OUKA
The University of Osaka
Institutional Knowledge Archive

Title	Effects of Strain Rate and Thermal Processing on Mechanical Properties of 17-4 PH Stainless Steel Processed by Selective Laser Melting
Author(s)	Lebrun, Tyler Christopher
Citation	大阪大学, 2015, 博士論文
Version Type	VoR
URL	https://doi.org/10.18910/52050
rights	
Note	

The University of Osaka Institutional Knowledge Archive : OUKA

https://ir.library.osaka-u.ac.jp/

The University of Osaka

Effects of Strain Rate and Thermal Processing on Mechanical Properties of 17-4 PH Stainless Steel Processed by Selective Laser Melting

Tyler Christopher LeBrun

March 2015

Effects of Strain Rate and Thermal Processing on Mechanical Properties of 17-4 PH Stainless Steel Processed by Selective Laser Melting

A dissertation submitted to

THE GRADUATE SCHOOL OF ENGINEERING SCIENCE
OSAKA UNIVERSITY

in partial fulfillment of the requirements for the degree of

DOCTOR OF PHILOSOPHY IN ENGINEERING

Tyler Christopher LeBrun

March 2015

Abstract

The following thesis presents an investigation into the mechanical behavior of 17-4 PH stainless steel powder processed by selective laser melting, an additive manufacturing technology. Tensile evaluation of material produced as part of this study was performed across a range of strain rates to identify the relationship between mechanical performance and this processing method. In addition to evaluating the strain rate sensitivity, the efficacy of post-production aging heat treatments was measured for specimens processed in accordance to and apart from industry standards. Measurements made of the as-fabricated and thermally processed microstructure indicate a high volume fraction of metastable austenite amidst the primary lath martensite. The presence of this phase effects both mechanical performance and thermal processing results.

Relatively high volume fractions of face centered cubic austenite in excess of 36% were measured within the as-fabricated structure. Retention of this phase was found to significantly reduce yield strength of the as-fabricated material. However, the yield stress was found to monotonically increase with strain rate. Ultimate tensile strength was found to be susceptible to temperature that occurs with plastic deformation. In tensile testing where the strain rate is sufficiently high, the increase in specimen temperature due to adiabatic heating prevents the strain-induced transformation of austenite to martensite. This inhibits the transformation-induced plasticity observed in isothermal tensile evaluation at quasi-static strain rates. This thermal stabilization mechanism was verified by elevated temperature testing at quasi-static strain rates.

Measurements of alloy distribution in the as-fabricated condition are also presented in addition to characterization by transmission electron, scanning electron, and optical microscopy. Consistent segregation of austenite stabilizing elements is found along fusion boundaries between each melt pool as developed during selective laser melting. However, the volume fraction of austenite retention measured precludes this as the primary source of its stabilization. The evolution of the dual phase material and the formation of the desired precipitation hardening with thermal processing are investigated. From tensile testing it is found that relative strength increases are reduced for specimens with initially high volume fractions of austenite. Fully martensitic specimens following solution heat treatment achieve greater increases in relative strength via aging. Austenite significantly inhibits age hardening by maintaining higher solubility of the precipitating alloying element that is otherwise in a saturated state in the primary martensite. Additionally, non-standard thermal processing progressively revert austenite to martensite by relieving residual thermal stresses related to the selective laser melting process. This significantly alters the mechanical performance at yield and subsequent work hardening in these cases.

Table of Contents

	Abstract	i
	Table of Contents	ii
1.	Introduction	1
1.1	*Thesis Structure*	1
1.2	*A Disruptive Manufacturing Technology*	2
2.	Purpose	4
3.	Additive Manufacturing	6
3.1	*Definition*	6
3.2	*Importance*	7
3.2.1	Economic	8
3.2.2	Design	8
3.2.3	Materials Engineering	9
3.3	*Varieties*	10
3.3.1	Solid State Sintering	10
3.3.2	Liquid Phase Sintering	11
3.3.3	Full Melting	11
3.3.4	Chemical Induced Binding	11
3.4	*Operation of Selective Laser Melting*	12
4.	Background of 17-4 PH Stainless Steel	14
4.1	*Introduction*	14
4.2	*Alloy Composition*	15
4.3	*Phase Transformation and Resultant Structure*	17
4.4	*Crystal Structure Change from γ–α'*	19
4.5	*Metastable Austenite*	21
4.5.1	Chemical Stabilization	22
4.5.2	Thermal Stabilization	23
4.5.3	Mechanical Stabilization	24
4.6	*Delta-Ferrite*	25
4.7	*Precipitation Hardening*	26
4.7.1	Standardized Methods	26
4.7.2	Precipitation Structure and Resultant Strengthening	27
4.7.3	Particle Strengthening Theory Overview	31
5.	Processing by Selective Laser Melting	35
5.1	*Preface*	35
5.2	*Raw Material*	35
5.3	*Processing to Form Bulk Material*	38
6.	Microstructure of 17-4 PH Processed by Selective Laser Melting	44
6.1	*Preface*	44
6.2	*Optical Microscopy*	44
6.3	*Scanning Electron Microscopy*	52
6.4	*Transmission Electron Microscopy*	52

6.5	*X-Ray Diffraction*	55
6.6	*Electron Probe Micro-Analysis (EPMA)*	57
6.7	*Discussion*	64
7.	Experimental Investigation I: Initial Characterization of Mechanical Properties and Anisotropy	67
7.1	*Purpose*	67
7.2	*Introduction*	67
7.3	*Theory*	68
7.3.1	Thermally Activated Plastic Deformation	68
7.3.2	Strain Rate Effects of Uniaxial Stresses	74
7.4	*Experimental Setup*	77
7.4.1	Choice of Tensile Specimen Design	77
7.4.2	Quasi-Static Strain Rate Testing Equipment	78
7.4.3	Intermediate Strain Rate Testing Equipment	79
7.4.4	Dynamic Strain Rate Testing Equipment	80
7.5	*Material Preparation*	88
7.5.1	Tensile Specimen Production	88
7.5.2	Tensile Sample Thermal Processing	88
7.6	*Results and Discussion*	89
7.6.1	Mechanical Properties	89
7.6.2	Embedded Flaws	96
7.7	*Conclusions of Experimental Investigation I*	102
8.	Experimental Investigation II: Effect of Metastable Austenite on Mechanical Properties	104
8.1	*Purpose*	104
8.2	*Introduction*	104
8.3	*Testing Hardware*	104
8.3.1	Intermediate Strain Rate Tensile Testing: Dropping Weight Machine	105
8.4	*Tensile Specimen Preparation*	107
8.4.1	Tensile Specimen Orientation	107
8.4.2	Tensile Specimen Thermal Processing	108
8.5	*Results and Discussion*	109
8.5.1	Mechanical Properties, Quasi-Static Strain Rate	109
8.5.2	Mechanical Properties, Strain Rate Dependency	119
8.5.3	Mechanical Properties, Temperature Sensitivity	131
8.5.4	Schematic Summary	135
8.5.5	Fractography	139
8.6	*Conclusions of Experimental Investigation II*	152
9.	Conclusions and Final Remarks	154
Works Cited		157
Appendix A: Equation of State During Dynamic Tensile Analysis		161
Appendix B: Development of Selective Laser Melting Materials Processing		167
List of Publications, Conferences and Awards		188

1. Introduction

1.1 Thesis structure

The body of presented work contained within this thesis is organized so as to present the information in a logical and cohesive manner. However, it is prudent to present a structural outline upfront so as to prepare the reader for the contents to follow.

The proceeding chapters will present the following content as titled, in the order as they appear here:

2. Purpose: The central motivation for this research effort and what its results show will be explained.

3. Additive Manufacturing: A relevant discussion on the technology as it currently exists within industry. A brief overview of the variety of technologies and methods will also be presented. A general overview of the processes within additive manufacturing will also be discussed.

4. 17-4 PH Stainless Steel, Background Of: An overview and technical discussion of the working material focused in this study. A discussion on the properties and secondary processing mechanics will be made.

5. Processing by Selective Laser Melting: The initial effort at processing of the powdered material by selective laser melting will be outlined. The parameters used to form the bulk material later evaluated microstructurally and mechanically will be explicitly detailed. Differences between the lots of material fabricated will be highlighted. Detailed analysis of the processing is presented in the appendix.

6. Microstructure of 17-4 PH Processed by Selective Laser Melting: The effort to characterize the microstructure of the as-fabricated and thermally processed selective laser melted 17-4 PH will be detailed. Additionally, other characterization techniques, such as transmission electron microscopy, x-ray diffraction, and electron probe microanalysis as they relate to the later mechanical evaluation, will also be included. Differences between the processing lots mentioned in the previous section will be identified in this section.

7. Experimental Investigation I – Initial Characterization of Mechanical Properties and Anisotropy: The first experimental work to investigate the properties of 17-4 PH stainless steel as processed by selective laser melting will be discussed. Applicable theory to this section will also be outlined as necessary.

The results of this work influenced the subsequent experimental work and the next chapter.

8. Experimental Investigation II – Effect of Metastable Austenite on Mechanical Properties: Further mechanical evaluation throughout standard and non-standard thermal processing techniques will be discussed. The effects of phase transformations on mechanical properties will be outlined. Solutions to shortcomings in testing hardware identified in the previous section will be discussed.

9. Conclusions and Final Remarks: A summary of the conclusions made from this study will be detailed.

1.2 A Disruptive Manufacturing Technology

Science and engineering are limited only by one's imagination and the tools available to craft and create. The depth of humankind's innovativeness has remained bottomless throughout antiquity, an inexhaustible well from which to draw. However, the tools at the disposal of creators and makers evolve and improve, and yet, continue to remain their greatest limitation. With every improvement in the collective ability to fabricate and to manufacture, new goods and services have come forth. Most refinements with manufacturing have remained incremental, small changes to existing tools and processes that either improve upon accuracy, precision, speed, or cost. However, there occasionally comes a technology that is so fundamentally different that our newly enable ability to manufacture extends beyond our ability to apply it, to maximize its potential. Arguably, this is what has occurred with the development and rapid growth of additive manufacturing technologies (AM) since their inception in the late twentieth century. Only now have various industries begun to integrate AM into the suite of tools available to produce goods and services. Motivation to do so stems from the desire for production capacity that may be faster, cheaper, and entirely different than before. With continued refinement, the practical implementations and applications of this manufacturing process will also continue to grow.

Machine tools for manufacturing tangible goods from bulk materials have remained largely unchanged when reduced down to their most basic function: subtractive manufacturing. Traditional fabrication techniques have commonly relied on transforming raw materials into any part of a larger assembly or individual product by removing unwanted material until a final form and shape is achieved.

This stayed relatively unchanged throughout the 19th and most of the 20th centuries. However, as of 1980, a process that enabled the freeform fabrication of nearly any solid geometry from powdered bulk materials by means of directed laser energy had been developed [1]. This marked the beginning of an alternative method for producing goods: *additive manufacturing*.

The importance of this technological leap can be understood when reviewing the past several hundred years of industry. Mechanization and the harnessing of highly dense forms of energy (namely steam power) transformed much of the West from an agrarian based economy to one of industry driven by mass production. Replaceable parts were a milestone of this transition –– a testament to the accuracy and precision of machine tools. However, the capability to produce nearly any near-net shape from smaller, bulk material constituents is a testament to the universality of additive manufacturing fabrication (AM). One person can operate an additive manufacturing machine, potentially producing hardware in a fraction of the time that is required of traditional, machine tools-based subtractive methods.

Additive manufacturing is, by itself, not a revolution of the scope and scale as the Industrial Revolution. However, it is a perfect example of an enabling technology. Producing manufactured goods may no longer be limited by their machinability, but by designs and ideas crafted by the creative minds inside and outside the engineering community. Fabricating what was once impossible by subtractive manufacturing and producing highly customized, low-quantity designs are now possible or economically within reach. The potential of this method to produce goods has yet to be fully tapped. This is mostly a consequence of its short history and gradual, incremental maturation of the technology following its invention by Dr. Carl Deckard and Dr. Joseph Beaman at the University of Texas at Austin in the mid-1980s.

Already there has been evidence that the penetration of this technology has exceeded the realm of research and traditional engineering and made its mark on the individual consumer and hobbyist. “3D printing” and “rapid prototyping” has entered popular culture lexicon. People who are not engineers by formal education or experience can now design, fabricate, and sell their ideas in a physical form. This technology has the potential to democratize the product development lifecycle and take away what has traditionally been the realm of established companies, brands, and industries. As the technology continues to mature with the push of research and pull of industry, it has the potential to make designers of us all.

2. Purpose

Many are quick to believe that at the current level of maturity, AM can replicate the functionality and potentially displace traditional manufacturing technologies outright. Popular culture sees it potentially supplanting most of the existing production capability for an endless variety of products, predicting it will become and embody the very science fiction that may have inspired it. However, with every new technology, expectations often outpace the realities of its capability. And in this case, AM is no different.

First and foremost, the various technologies that make up AM are still largely considered "emerging". And for many within industry, the technical readiness assigned to these materials processing methods is still considered as unreliable or unverified for the purpose of producing salable goods. And at present the industries that might benefit greatest from this technology, namely aerospace and biomedical, are highly resistant towards changes in manufacturing flow chains with unproven technologies. Ergo, both industry (in the generic sense) and the research community continue to work towards establishing a solid understanding of the fundamentals at work within AM. The end result of this effort would be to establish demonstrable predictability at processing materials into whatever shapes and volumes needed. And yet, forming the proper shape is not sufficient litmus for the successful maturation of AM. The behavioral properties of these processed materials must also be predictable, but preferably comparable, or better still, improved over traditional counterparts. Establishing these properties and the relationships between them and the materials processing method are largely considered the foundation for vetting AM as a trusted tool. This serves as the impetus for the body of research work presented here.

As part of establishing the mechanical behavior of materials produced via AM, the expectations of non-engineers on this manufacturing tool must be made to match its capability. A good analogy may be made using the niche market for replacement automotive parts. In cases where custom hardware is necessary or replacement parts difficult to acquire, AM may be turned to as a relatively inexpensive alternative to traditional machining when fabricating near-net components. Hypothetically, an end-user of an AM machine may incorrectly assume that since the replacement part is produced from the same material as the original and of the exact same design and shape, it will perform equally as well. However, because bulk material produced via AM is formed by means entirely different from any previous method, it is reasonable to assume that

mechanical properties may be influenced and characteristic of that forming process. And where safety is a concern in this analogy, unknown or sub-standard performance may prove to be dangerous. Establishing what those properties are in relation to standardized benchmarks of traditional forming methods is paramount in the greater engineering and research effort of maturing AM as a method of materials processing.

The purpose of the research effort of the past two years, as outlined and detailed in this thesis, is to contribute towards that material characterization effort in the way most appropriate in the laboratory available. These studies focused on a metallic material common throughout various industries for its versatility, high strength, corrosion resistance, and ability to tailor its mechanical properties through additional thermal processing (aging). For these reasons, it and other similar alloys are attractive for applications where fabrication via AM is appropriate. However, because AM is an emerging technology, the existing body of published research on this material is relatively sparse. All of these aspects provided a variety of research pursuits largely unexplored. The strengths and experiences of faculty and previous student-led research in the Kobayashi-laboratory were leveraged to maximize the effectiveness of any study pursued. Consequently, the types of experimental evaluation appropriately explored through this effort, namely dynamic strain rate tensile testing, are nonexistent for materials processed by AM. Performing these series of mutually supporting studies characterized this material in ways never before attempted.

The results of these investigations are important for a variety of independent, but complimentary reasons. Establishing the dynamic mechanical response of any material produced via AM has never been undertaken. In applications where dynamic loads are experienced, such as energy absorbing features of automotive structures or ballistic protection, understanding the mechanical behavior at these speeds is critical. Yield and ultimate tensile strengths are expected to vary with the rates of strain. Lastly, generalized mechanical behavior across all strain rates observed as part of this study has never before been documented for material of this chemistry. The effects on the resultant microstructure by AM directly influence the mechanical properties. This thesis investigates and documents that mechanical behavior.

3. Additive Manufacturing

3.1 Definition

The American Society for Testing and Materials, International (ASTM), has defined additive manufacturing in narrow but modern language as it applies to existing technology and manufacturing processes. This definition can be found in the standard ASTM F2792 [2], as developed by the subcommittee on additive manufacturing terminology, F42.91.

additive manufacturing (AM), *noun* – a process of joining materials to make objects from 3D model data, usually layer upon layer, as opposed to subtractive manufacturing methodologies. Synonyms: additive fabrication, additive processes, additive techniques, additive layer manufacturing, layer manufacturing, and freeform fabrication.

This term encompasses the suite of manufacturing and materials processing technologies that conform to the sequential formation of a larger shape from smaller constituent, raw materials. However, the definition presented is limited. The language describing three-dimensional programming as a desired volume's definitional source excludes any of the hand-operated variants that currently exists. Also, not all machines necessarily operate in a layer-based manner. In short, the technology is rapidly evolving and the definition presented here is more exclusive and limited to machines operating on the principles of AM from ten years ago. A more inclusive definition in the spirit of the production process, one that is less a description of the machines themselves and more of the material processing method, is appropriate. A different definition is submitted here that preserves the material processing method as the root of the definition, while still encompassing its history and potential expansion in the future.

additive manufacturing (AM), *noun* – a collection of technologies that unites raw material of smaller volume into a larger, near-net shape of desired form or function.

This rewording of the definition maintains the intent of that proposed by ASTM, but also does not exclude the variations of AM that have since emerged in recent years that don't strictly follow those aforementioned processing mechanics. While the nuances are largely based in semantics, the intent of the

definitions are plainly clear. Inherent to its name, AM is a method of creating a larger whole from a series of parts typically done in a sequential or piecewise process. Recently, the term “3D Printing” has been used to describe all of AM. While this method of fabrication is but one variety under the umbrella-term as defined above, it does accurately depict the nature of these processes as being an assemblage within a three-dimensional space rather than a subtraction from a larger whole.

Historically speaking, the technology conceived by Carl Deckard at the University of Texas at Austin would later become what is known as AM. However, it was initially intended as a method of “rapid prototyping” (RP). And for many years it continued to provide that role to industry. Early commercial versions of these self-contained machines produced non-functional, demonstrative pieces of hardware as engineering aids. However, the lexicon has recently expanded along with its capability to include “rapid tooling” (RT) and “rapid manufacturing” (RM) [3-6]. This gradual shift in capability occurred as the technology improved. In very specific and limited cases, AM is turned to as a method to fabricate nearly complete pieces of hardware (also known as near-net) intended for use in functional assemblies [7]. This has enabled some organizations to work towards bypassing much of the existing manufacturing supply chain. Much of the excitement surrounding this technology is because of this potential.

The focus of the body of research presented within this thesis is limited in scope to one type of AM known as “selective laser melting” (SLM). However, to better frame this technology and the significance of the research presented herein, a brief and general overview of the variety of similar technologies will be detailed in a following section.

3.2 Importance

As introduced, many industries are looking towards AM as an alternate means of fabrication. This attention has the potential to replace well established manufacturing supply chains that rely on traditional machining technologies. Despite the demonstrated capabilities of heritage materials processing and manufacturing tools, the allure of AM is warranted for a variety of reasons. There are three distinct advantages of AM.

3.2.1 Economic

In cases where production volume is high, AM is simply not affordable. Economies of scale work against AM's cost structure. In cases where goods are better suited to mass production, the up-front engineering and tooling associated with developing these manufacturing flows reduces the per unit cost (e.g., injection molded or stamping dies). However, in cases where demand for a single product is low, the cost structure favors AM [8,9]. Industries that benefit from this are those that rely on highly customized goods typically with a quantity of one or high-cost, low volume industries with low production volumes. Examples of these cases where AM has previously demonstrated useful for customized hardware include medical prosthesis [10] or patient-customized surgery aids [11]. Similarly, low volume production is prevalent in the aerospace industry with the production of satellite, rocket transport, or scientific hardware. All of which stand to benefit from circumventing the time and costs associated with traditional manufacturing.

3.2.2 Design

In the case above, many business accountants see AM as an attractive method to produce existing designs more cheaply. However, some design engineers see it as a way to produce what may have been previously impossible. Because AM is constructive and not subtractive, some design features that are not producible by traditional means are now accessible and attainable. This advantage over subtractive manufacturing technologies is best explained by example. Figure 3.1 highlights an example presented by Simchi [12]. This prototypical product would benefit from being produced via AM. His example included a helical cooling channel built internal to the bulk-solid of a cutting mill head grip. In this case the integrated features, such as cooling channels or other flow passageways, are needed within the bulk volume of a part. Traditional machining using multi-axis, computer numerically controlled machines simply has limited or no access. Instead, AM can build said part with these design elements additively. With further maturation to the technology, designs can be optimized to take advantage of this production technique.

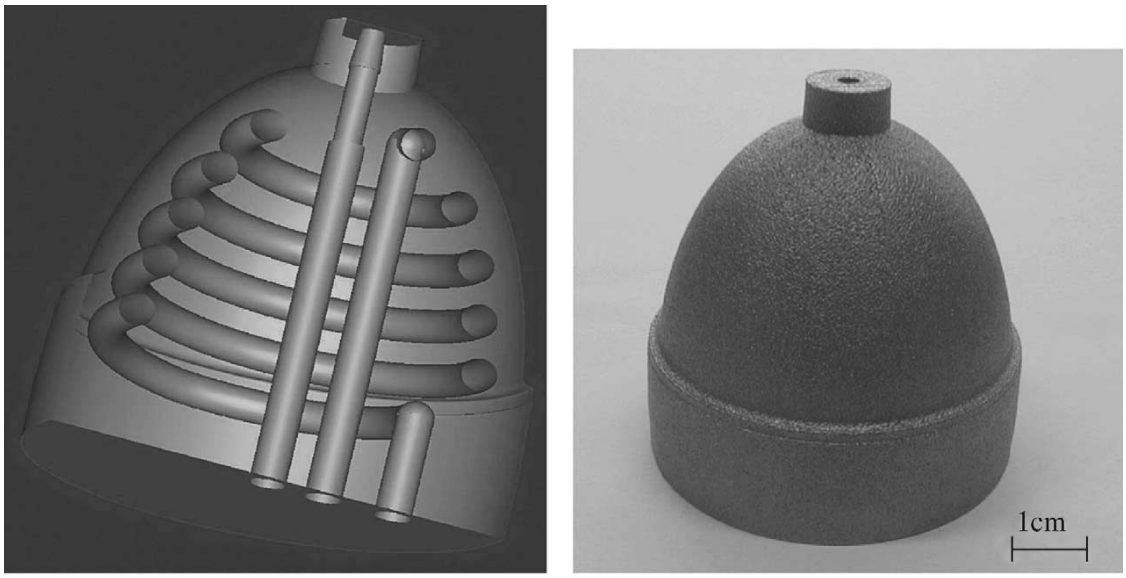


Figure 3.1: Complicated part geometry not feasible by traditional manufacturing methods. (a) CAD geometry and (b) physical part produced by SLM. [12]

3.2.3 Materials Engineering

A less understood, but potentially more disruptive capability of some AM technologies is their ability to engineer the as-fabricated material microstructure as a part of its production. Murr accurately described this as expanding the conventional materials science and engineering tetrahedron representing the connections between material structural-properties-processing-performance to a new pyramid paradigm [13]. By including an additional dimension of microstructural architecture by means of processing methods and technology, greater control of the resultant material performance could be enabled. Figure 3.2 schematically illustrates this change in approaching materials science as a consequence of greater control enabled by AM technologies.

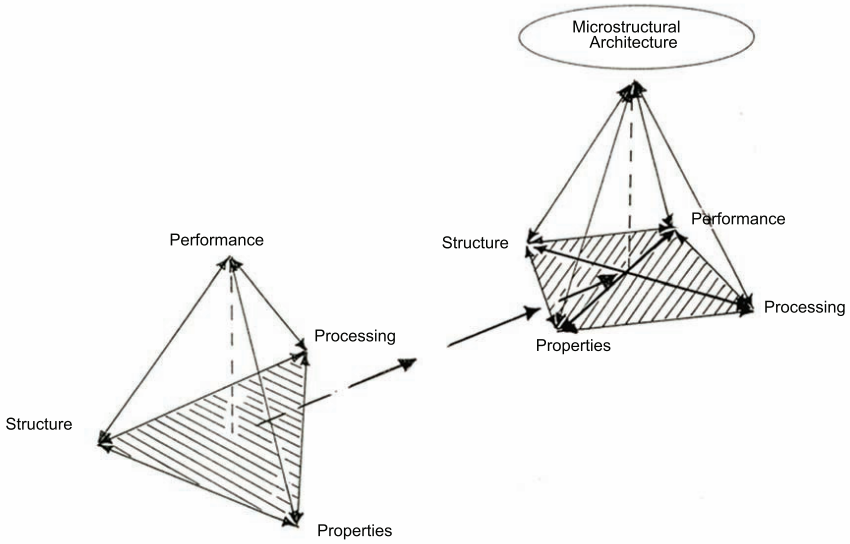


Figure 3.2: Extension of the materials science and engineering tetrahedron to a pyramid scheme with the introduction of microstructural architecture as proposed by Murr. [13]

Macro-scale mechanical properties may be controlled by varying the microstructure, phase, or embedded porosity of a material. In effect, the material architecture and the engineering design where it is used may enable hardware more efficiently constructed for their respective application. Similarly, if AM parameters are varied throughout the build operation we may more readily fabricate functionally gradient materials. All of these pursuits are largely unexplored and far from real-world application.

3.3 Varieties

The manufacturing process of AM spans several material classes: metals, plastics, and ceramics. The vast majority of these utilize powdered forms of their respective working material. Binding mechanisms vary widely from process to process and material to material, but can be described as one of four types: solid state sintering, liquid phase sintering – partial melting, full melting, or chemically induced binding. Powders take various forms that depend heavily on the intended binding mechanism.

3.3.1 Solid State Sintering

Sintering without the phase change or chemical activation of particles is known as solid state sintering (SSS). The binding mechanism of this form of AM is entirely reliant upon atomic diffusion between neighboring particles (volume

diffusion, grain boundary diffusion or surface diffusion). This mechanism is rarely used in layer-based AM as its binding mechanism is slow and not compatible with the high laser scanning velocities typically used for the rapid production of hardware [3].

3.3.2 Liquid Phase Sintering

A variety of binding mechanisms are possible under the mechanism of liquid phase sintering (LPS). However, in general this process can be described as partial melting of powdered particles such that necking is formed without complete melting of all particles by laser energy in the powder bed. Molten material will spread through vacancies between particles rapidly due to strong capillary forces. The melting associated with this process can be from a binder material as a separate particle, coating on a structural particle, or composite powder with a micro-composite structure contained within each particle. The material that does not melt usually acts as the structural component of the resulting sintered bulk material.

3.3.3 Full Melting

As its name implies, the entire powder bed is targeted for complete melting as part of the consolidation process. Intense thermal gradients and high densification ratios may result from this process, which may ultimately induce severe, trapped thermal stresses or distortion of completed geometry. Despite this risk, the advantage of this process is to not require further thermal processing for densification. The powders used in this process are usually a pure or pre-alloyed material.

3.3.4 Chemical Induced Binding

The final category of binding mechanism is not commonly used in layer-based AM, but has been demonstrated in laboratory settings. One such example includes the utilization of laser energy to make aluminum powder react with a nitrogen gas atmosphere to create an aluminum-nitrogen (AlN) binder phase to hold the remaining aluminum particles in place. The University of Queensland has used such a mechanism during post-sintering in a N2 furnace, rather than during the initial SLS phase itself, at which stage a sacrificial polymer binder was

used to consolidate the green Al part [3] [14]. This binding mechanism, however, has not seen wide-scale industrial application.

3.4 Operation of Selective Laser Melting

Simply put, the process of producing a bulk solid from a powder source by way of one of the aforementioned binding mechanisms, sequentially, layer by layer, by way of directed laser energy, is one form of additive manufacturing. The machine that accomplishes this task cannot be so simply explained. Because of the variety of AM technologies and techniques, the process of selective laser melting will only be described in detail.

Fabrication of near-net designs by way of selective laser melting begins before formal, physical fabrication – in the digital space of a computer aided design (CAD) software package. Modern CAD software enables any designer to create a three dimensional object that is exported to a file format known as a stereolithography (STL) file (STL is also an abbreviation for the Standard Tessellation Language appropriately used at reducing geometries generated in three-dimensional space to a series of smaller, discrete triangular shapes to define outer surfaces). Most commonly, these file types are not the native format for the CAD software, but an optional format for export when being used for a variety of specific user-defined purposes – as in this case, import and utilization for AM.

Completed designs that have been successfully exported into the requisite format are then interpreted by either helper-software on a standard desktop computer or by an onboard software suite hosted on the SLM machine itself. Ignoring variations from one vendor's machine to the next, all receiving software will take the provided STL file and segregate the geometric data into discrete, sequential slices or cross-sections. These cross-sections extracted from the STL file, when recombined in order, approximately reproduce the same geometry as originally designed in the CAD environment. The approximate representation is a byproduct of the piecewise re-defining of the geometry. The accuracy is only limited by the resolution capability of the SLM machine and physical process itself. As a result, it is necessary that the thickness of each of these cross-sections be defined as part of the operational parameters of the machine. Thicker layers of the powdered working material will generate a coarser representation of the defined part to be fabricated, especially around curved features of the to-be-built geometry.

Following a successful import of the file's geometry, the actual fabrication process can proceed. The SLM fabrication takes place within a machine that houses two vessels in immediate proximity to each other. Each vessel has a moveable floor whose height is controlled by a piston or actuator. One vessel's floor is raised completely such that the volume is near zero. The other vessel's volume is at its maximum extent with the piston retracted completely. This latter vessel houses the working material powder. The other, near-zero-volume container, is the working build-space. The floor of this vessel is usually some removable metal substrate held in place by bolts or screws. Incrementally lowering the build-space piston by the previously determined and computer specified layer thickness exposes the first volume for the working powder. The powder source vessel's floor will raise a similar amount, thereby exposing a volume of powder for this purpose. A rolling, wiping, or depositing mechanism will fill this exposed volume in the build space with the working material. This freshly deposited powder layer is then selectively exposed to the directed laser energy in a raster pattern specified by the helper-software mentioned earlier. The area exposed at this layer corresponds to only one slice of the part to be fabricated. The process repeats until the production is complete.

Following production, the completed part and baseplate must be removed from within the bed of un-used powder. The fabricated design must then be mechanically separated from the baseplate. Further post-production processing on the near-net shape is typically required before service. However, the intent with this production technique is to circumvent much of traditional machining to arrive at this nearly finished part geometry.

A more detailed discussion on the processing, laser-powder interaction, and the parameters used to produce the bulk material in this study will be presented in Chapter 5.

4. Background of 17-4 PH Stainless Steel

4.1 Introduction

Steel alloys are used throughout engineering applications because of their relatively inexpensive cost and for their predictable and diverse properties. Through the tailoring of chemical composition and thermal processing, the properties of steel alloys may be adjusted to suit the intended application. Of the wide variety of steel alloys available, stainless steels represent a class of materials that are turned to for their corrosion resistance while still maintaining high strength and ductility. To be classified as a "stainless" steel, chromium content is maintained at a minimum of 11% by weight in the alloy chemistry. The formation of a chromium-rich oxide layer is what protects the underlying iron within a stainless steel. Additionally, this oxide layer forms spontaneously upon surface damage to stainless steels and acts a self-healing mechanism to further protect the material from corrosion. Additional alloying elements may be added to further control the presence of phases, inclusions, and resultant mechanical properties.

Of the classes of stainless steels, precipitation hardenable (PH) stainless steels include a group of alloys commonly utilized throughout a variety of industries. Within the class of PH stainless steels, a sub-category of martensitic stainless steels exists. The focus of this body of research is on one such alloy, 17-4 PH (AISI grade 630). Martensitic PH stainless steels, as their name implies, exist principally as martensite at room temperature and within their normal operating temperature range. In addition to this phase, several others may be present, but typically not intended. These other phases include metastable austenite, δ-ferrite, and other, small inclusions with compositions including intermetallic elements, carbon or nitrogen. Chemical composition and thermo-mechanical processing are turned to as ways to control the presence of these phases. The existing body of literature on the processing of 17-4 PH by SLM is relatively small by comparison to other traditional methods. Consequently, there is little research on the subsequent thermal processing and aging performance of 17-4 PH when formed by SLM. However, there are some studies that detail the systems of precipitation of copper in wrought varieties. The following sections on 17-4 PH will discuss the compositional and processing effects of this material on the phase and microstructure with the corresponding mechanical properties. This will be discussed in the context of currently understood theory and established experimental evidence as presented in the literature.

4.2 Alloy Composition

Because of its widespread use, the chemistry has long since been established and standardized across a variety of materials and mechanical engineering organizations. The alloying composition of 17-4 PH is shown in Table 4.1 as outlined by the ASTM standard A564/A564M-10 [15].

Table 4.1: Alloy composition of 17-4 PH by weight percent

C	Mn	P	S	Si	Cr	Ni	Nb	Cu	Fe
0.07	1.00	0.040	0.030	1.00	15.00-17.00	3.00-5.00	NS	3.00-5.00	bal.

Numbers shown are limits, unless otherwise listed as a range

NS – Not Specified

Stainless steel chemistry, such as that outlined for 17-4 PH, is used to control the presence of intended phases. Chromium levels, while necessary to establish the "stainless" quality through enhanced corrosion resistance, result in the presence of delta ferrite when at excessively high concentrations (as is also the case with elements such as silicon and molybdenum). The chromium levels are therefore balanced against nickel (with additional influence by manganese and silicon additions). Carbon is used as a strengthening addition, but must also be closely managed alongside nitrogen, as they are both very strong austenite stabilizers. Viewing changes to the Fe-X phase diagrams can better summarize the effect of these elements on phase stability with temperature. Figure 4.1 shows the binary phase diagrams for the various alloying elements added therein [16]. Note the change to the γ-iron loop across the various alloying elements.

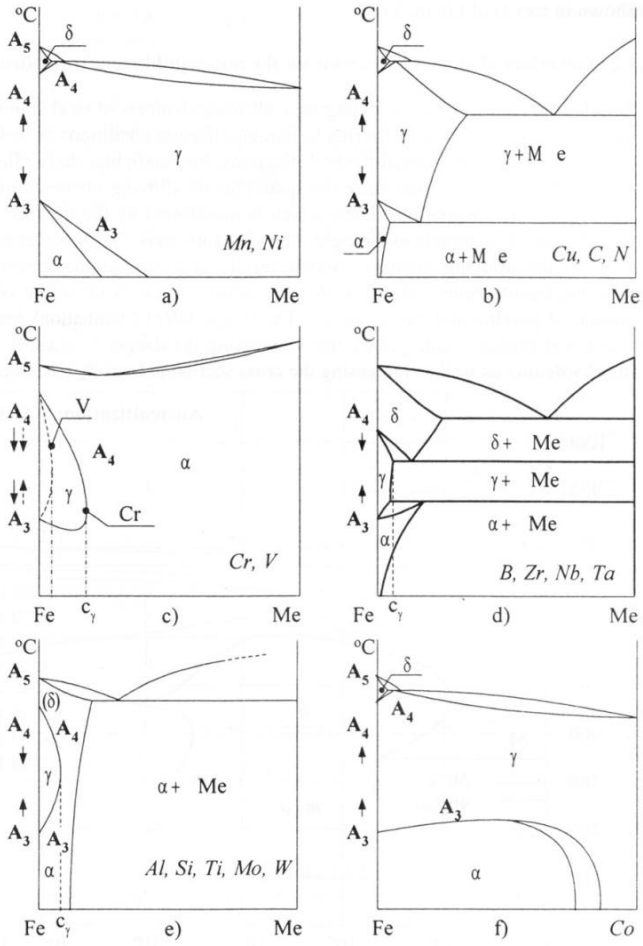


Figure 4.1: Fe-X phase diagrams. (a) Mn, Ni; (b) Cu, C, N; (c) Cr, V; (d) Zr, Nb, Ta; (e) Al, Si, Ti, Mo, W; (f) Co. [16]

Of particular note is the changing nature and size of the γ-field (austenite). With excessive concentrations of various elements, the austenitic field may be stabilized as low as room temperature and permit the presence of this phase. This, for martensitic PH stainless steels, is not typically intended. However, for other varieties of stainless steels, such as the aptly named austenitic stainless steels, the γ-loop is open and austenite is stable at room temperature.

Aside from the two primary alloying elements of nickel and chromium, the other addition of significant importance to 17-4 PH is copper. The strengthening mechanism associated with the nucleation and growth of a secondary phase relies on the diffusion and restructuring of this element into fcc structured Cu-rich precipitates. This solute element is of sufficient concentration that it exists in a saturated state within bct martensite. The initiation of precipitation only requires sufficient thermal energy through heat treatment to increase diffusion rates and aid in the restructuring of the lattice at local sites.

4.3 Phase Transformation and Resultant Structure

The discussion on microstructural phase composition and transformation is best framed in the context of the initial transition of the liquidus to solidus phase and subsequent cooling of molten 17-4 PH. Prediction of the solidification mode in stainless steels can be best described with the solute equivalent equations given by Suutula [17] that have been employed by Cieslak [18] and Ritter and Savage [19] for niobium containing steels [20]. These equivalents are shown as:

Cr_{eq} = Cr + 1.37Mo + 1.5Si + 2Nb + 3Ti (in wt%)

Ni_{eq} = Ni + 0.31Mn + 22C + 14.2N +Cu (in wt%)

When the ratio of Cr_{eq} to Ni_{eq} is less than 1.5, austenite is the stable primary solidification phase. If the ratio is above 1.5, primary ferrite is the stable solidification phase. Using the values of composition present in the powdered 17-4 PH, this ratio is calculated to be 1.69. This value effectively puts 17-4 PH in the primary ferrite solidification mode. However, solidification to a metastable phase is usually encountered in the solidification of stainless steel weldments or in laser or electron beam welding. Under high cooling rate conditions (such as is the case with selective laser melting), it has been observed that the solidification mode changes from primary ferrite to primary austenite [21-23]. This requires solidification to a metastable phase austenite with an undercooling under the metastable austenite solidus. For the present discussion on 17-4 PH, the transformation behavior will be discussed in this context.

Continued cooling of the now solid material results in a phase transformation to the face centered cubic structure of austenite. From this phase the material will initiate an allotropic transformation to martensite starting at a critical temperature known as the martensitic start temperature (M_s). The temperature dependence of this phase transformation is strongly reliant on the composition of the constituent alloying elements. However, empirical relationships have been established to assist in calculating the start of this transition. Eichelman and Hull developed a well known empirical relationship to define this transition start temperature based on research with 18Cr-8Ni steels [24] (the most appropriately fitted to this research effort):

$$M_S\,(C^\circ) = 1302 - 42(\%Cr) - 61(\%Ni) - 33(\%Mn) - 28(\%Si) - 1667(\%[C+N]) \quad (4.1)$$

Whereas Pickering provided the following variation on this relationship for austenitic stainless steels [25]:

$$M_S\,(C°) = 502 - 810(\%C) - 1230(\%N) - 13(\%Mn) - 30(\%Ni) - 12(\%Cr) - 54(\%Cu) - 6(\%Mo) \quad (4.2)$$

And still a third[1] by Honeycombe and Bhadeshia [26,27]:

$$M_S = 539 - 423(\%C) - 30.4(\%Mn) - 17.7(\%Ni) - 12.1(\%Cr) - 7.5(\%Mo) \quad (4.3)$$

These are only a small handful of the various empirical relationships that attempt to identify the start temperature based on chemistry (and there are many). Despite their variation, they all commonly identify the elements whose solute concentrations most strongly affect the phase presence and transformation temperature. Note the relative sizes of the coefficients for carbon and nitrogen to those of the other alloying elements in the respective equations 4.1 through 4.3. Regardless of the variation in modeling and empirical-based methods at characterizing this transformation, in general, the vast majority of expressions identify a transition start temperature of approximately 90-100 °C for 17-4 PH.

With cooling below the M_S temperature, the austenite will continue to transform into martensite (α') until a martensitic finish temperature (M_f) whereupon all transformation has ceased. Empirical M_S equations do not make predictions as to the M_f temperature as cooling rates between these two temperatures will largely influence the volumetric fractions and subsequent microstructural morphology of retained austenite and martensite [28]. However, a generally accepted temperatures for the completion of the M_f temperature for 17-4 PH is approximately 32 °C [29]. Accurate measurements of these two are typically done via dimensional changes resulting from constant rates of temperature change via dialometry equipment [27].

[1] This particular empirical equation appears to well overestimate the start temperature as indicated by the work of Hsiao, Chiou, and Yang [27] and other empirically driven calculations because it does not account for the stabilizing effects of copper.

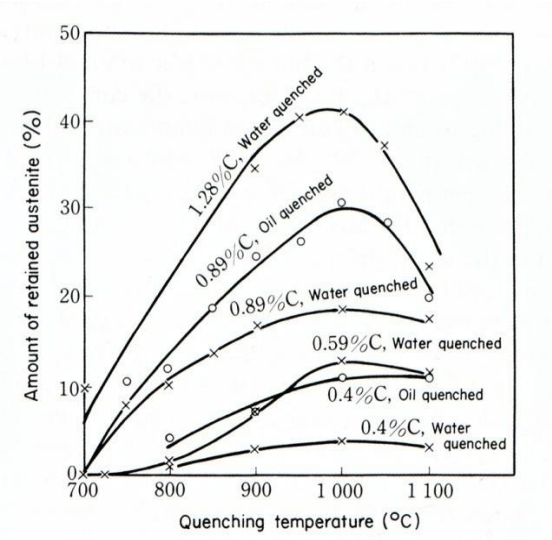


Figure 4.2: Effect of quenching rate on the M_S temperature and volume fraction of retained austenite (After Tamaru and Sekito).

4.4 Crystal Structure Change from $\gamma - \alpha'$

The transformation of austenite (γ-iron) to martensite (α') upon quenching is a result principally of the presence of interstitial alloying elements (specifically carbon) and their distortional effects. This phase change is a diffusionless transformation (allotropic) in the crystal structure and can be described as a restructuring of austenite's face centered cubic shape. Upon transformation to martensite, the structure becomes body centered tetragonal, closely resembling body centered cubic, but with one edge of the structure elongated due to the presence of the interstitial atoms. The resultant structure of the martensite exhibits a similar structure to the parent austenite from which it transforms [30]. For 17-4 PH this transformation commonly follows what is known as the Nishiyama-Wassermann relationship and has been observed experimentally [27] [30]. Figure 4.3 depicts this transformation and illustrates the lattice structure. The relationship between these two phases and their lattice structures can be described as [17]:

$$\{111\}_\gamma \parallel \{011\}_m$$

$$< 11\bar{2} >_\gamma \parallel < 01\bar{1} >_m$$

This transformation, along with the schematic illustrated in Figure 4.3, identifies the transition of the family of planes in the {111} orientation for γ-iron

as they become {011} for the now bct structure of α' martensite. Similarly, the set of directions <11$\bar{2}$> can now be notated as <01$\bar{1}$> post-transformation.

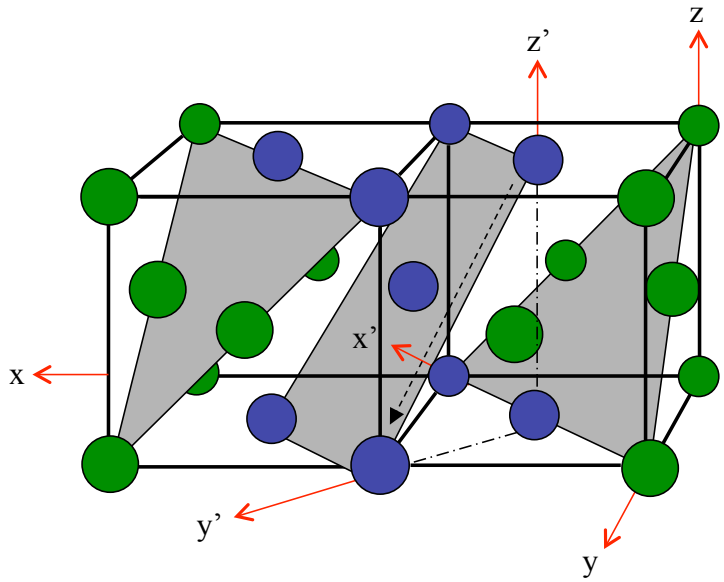


Figure 4.3: The Nishiyama-Wassermann orientation relationship. Blue spheres represent atoms of a bct unit cell. Green sphere represent atoms of the fcc unit cell. Red arrows indicate part of the motion that initiates the transformation. The dashed arrow indicates the invariant direction that is shared by the parent, austenite, and resultant martensite phase. [31]

In steels with relatively high percent weights of carbon, the martensitic microstructure is heavily strained with a large ratio of the *c* and *a* axes shown in Figure 4.4. However, in the case of low-carbon 17-4 PH, the resultant bct structure closely resembles bcc with a ratio between these axes nearly equal to unity.

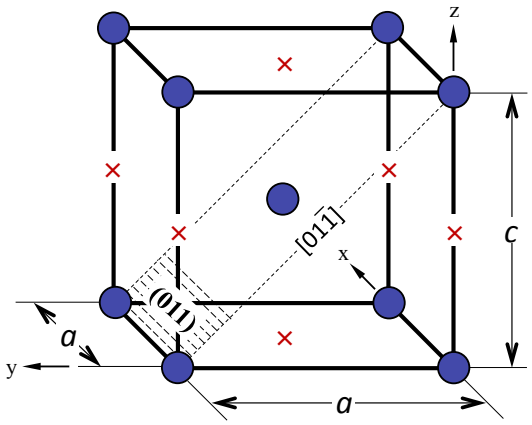


Figure 4.4: The resultant bct structure of α' martensite post transformation. Interstitial site that may be occupied with carbon are indicated by a red "x". Iron and their substitutional alloying equivalents occupy the sites indicated by the blue spheres. Note the variation in structure lengths "a" and "c" associated with the strain induced by the carbon interstitials.

Twinning, as a means to accommodate local strain in adjacent lath structures, is occasionally observed in some studies [27]. However, unlike other steel alloys with greater percent weights of carbon, the presence of twinning is more the exception than the rule for this alloy's martensitic microstructure. Several studies do not indicate or make note of the absence of twinning in the resultant martensitic structure [30,32].

4.5 Metastable Austenite

Within the bulk martensitic microstructure there are two, path dependent varieties of austenite that may be present at room temperature. Upon initial forming of the material, the volume fraction of austenite that does not transform into martensite upon cooling and remains present at room temperature is known as *retained* austenite. Martensitic transformation from austenite is considered an asymptotic process across a temperature regime. Under idealized conditions the entire volume of austenite will finish transforming into martensite upon achieving the M_f temperature during quench. To help clarify this relationship between M_S and M_f temperatures in the context of volume fraction of the two phases, Figure 4.5 schematically illustrates the transformation of austenite to martensite in volume percent with respect to the two bounding, transition temperatures.

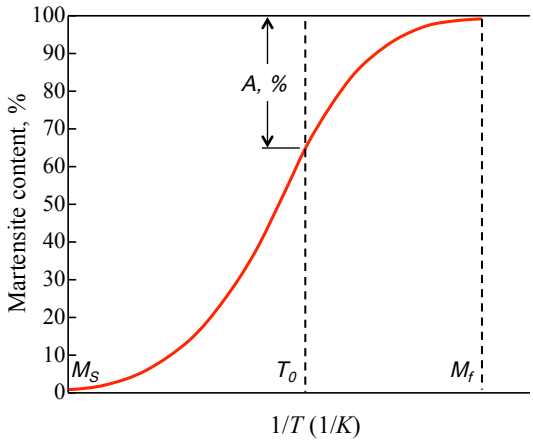


Figure 4.5: Sigmoidal relationship between the M_S and M_f temperatures.

The transition from one phase to another is not instantaneous across the volume, but progressive. When described as a change in volumetric percent between the two phases, this transition is sigmoidal in shape bounded by the start and finish temperatures. As a result, control of the M_S and M_f temperatures is critical to controlling phase presence at room temperature (or operational environment temperature). And in the case of some alloys where the finish temperature is near room temperature, specialized quenching or post-

processing treatments (such as refrigeration) are necessary to assist and complete the transformation. Retained austenite in alloys that should otherwise be free of this phase has been identified to show significant reductions in yield [33,34].

The other path dependent variety of austenite is known as *reverted* austenite. Under the influence of applied heat, typically during subsequent thermal processing, some martensite will invariably revert back to austenite and remain stable following subsequent cooling to room temperature. Typically, this is a result of the localized chemical stabilization by diffusion of solute atoms that favor the martensitic reversion by locally reducing its M_f temperature [30].

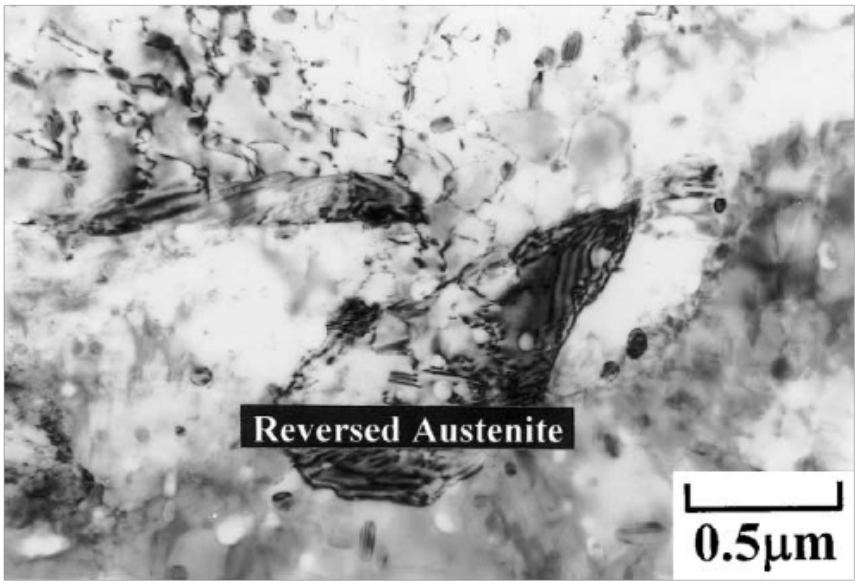


Figure 4.6: Transmission electron micrograph showing copper precipitates as globular or circular structures and a reversed austenite grain obtained from a sample aged at 620°C for 4 hours. (From Hsiao, Chiou, and Yang)

In practice, the retention of austenite following forming is considered to have a deleterious effect on the mechanical performance of the material. Austenite lacks the strength associated with properly aged martensite. Additionally, the austenite phase will retain copper, the notable precipitating alloying element, and inhibit local hardening. Nishiyama described three mechanisms by which austenite is capable of being retained despite the driving forces associated with its transformation to martensite [35]. These mechanisms include chemical stabilization, thermal stabilization, and mechanical stabilization.

4.5.1 Chemical Stabilization

The process of retaining austenite until room temperature via chemical stabilization comes as a result of local variations in concentration of the constituent alloying elements. Of the alloying elements that are used in the

development of 17-4 PH there are several that are known to act as “austenite stabilizers”. The elements highlighted in a previous section, nickel, carbon, nitrogen, and manganese, all work to reshape, expand and open the austenite field of the Fe-X binary phase diagram. Each has their own varying degree of influence on the phase retention, but local segregation of all is a concern. This is especially true for castings and welding of 17-4 PH [36].

With initial cooling of molten material, the alloying elements tend to solidify via the formation of dendritic structures. As a result, it is common to encounter micro-segregation from the chemical partitioning of solids forming with certain composition and structure at different rates within the liquid.

4.5.2 Thermal Stabilization

In the context of 17-4 PH, thermal stabilization usually refers to the holding of the material at an elevated temperature above the M_f temperature at which austenite remains stable. It is at this temperature that the transformation process is incomplete for the chemistry provided. However, the scope of “thermal stabilization” is much more nuanced than just holding at elevated temperatures indefinitely. Aging at temperatures slightly above the M_S temperature have been found to result in a variety of stabilization mechanisms that are maintained after quenching to room temperature for certain steel alloys. Okamoto and Okada discussed the holding of an Fe-1.06% C-1.63% Cr steel at 250°C for extended time periods and noted via dialometry a varied, but distinct change in M_S temperature with aging period [37]. Figure 4.7 shows the results of their work regarding the rapid reduction of M_S following the formation of bainitic structures. And similarly for Izumiyama working with a Fe-3.08% Ni-1.05% C alloy, a variety of stabilization mechanisms evolved over time. These included elastic interactions between dislocations in austenite and interstitial atoms, obstruction of dislocation movement via fine precipitates, relaxation of stress in α’ (by a rise in the transformation temperature), and increase in energy at the γ-α’ boundary [38]. The various methods by which austenite is stabilized through extended aging at elevated temperatures is nearly as varied as the chemistries studied.

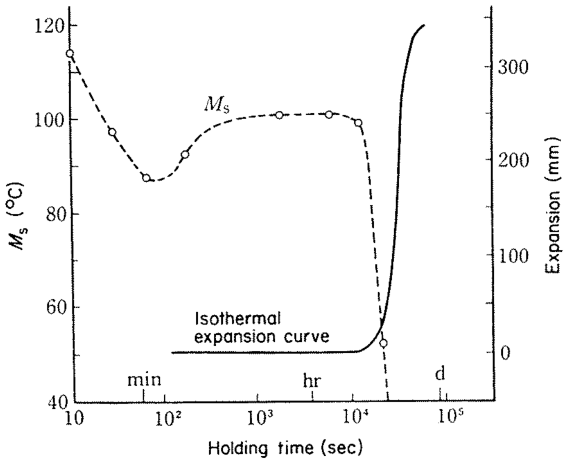


Figure 4.7: Effect of aging at 250°C (>M_S) on M_S temperature (Fe-1.06% C-1.63% Cr) (After Okamoto and Osaka).

4.5.3 Mechanical Stabilization

Both pressure and temperature determine the state of materials. In cases where the hydrostatic pressure is great, there is a nontrivial change to the interatomic spacing of the elements in the crystal lattice. This shrinkage in distance would also affect the electron distribution and cause an appreciable change in the transformation temperature [35]. Hillard and Cahn showed the change in the Fe-C binary phase diagram and the effective eutectoid point and temperature with changes in pressure. At 1 atm the eutectoid temperature was observed to be at 727 °C. However, with an additional 34 katm, the eutectoid temperature had both fallen to 645 °C and shifted in concentration for percent weight of carbon [39].

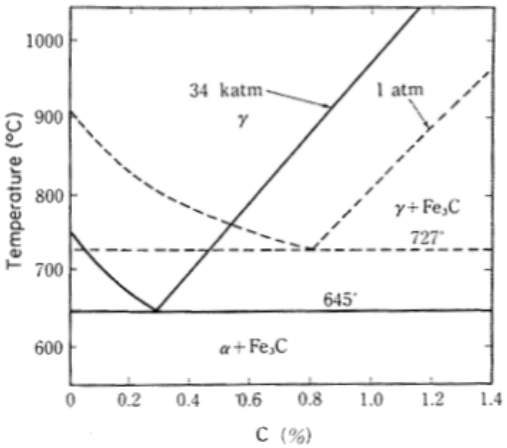


Figure 4.8: Effect of pressure on Fe-C phase diagram. (After Hilliard and Cahn)

Even under cases where quenching is done at 1 atm, the formation of martensite exerts a compressive stress on the surrounding austenite because of volume expansion during transformation. And similarly, with the presence of a

hydrostatic pressure, either from an external source or internally driven by lattice structure volumetric changes, the reverse formation of austenite from martensite is favored at lower temperatures [40].

4.6 Delta-Ferrite

As previously explained, cooling rates from the initial solidification largely determine the volume fractions of both martensite and austenite. However, sufficient segregation of solute atoms within the material may also promote the formation and stabilization of δ-ferrite at room temperature. This particular phase is commonly found in larger cross-sections of bulk material where cooling rates are sufficiently slow and final solute segregation sufficiently large enough to promote its formation. These phases are typically in the shape of stringers or islands within the martensitic matrix. Additionally, these inclusions commonly coincide with orthotropic or oriented microstructures produced in the bulk material's forming process. One such example is the elongated stringers observed in drawn rod with a long axis oriented parallel to drawing direction. However, the formation of eutectic ferrite is still possible with this material's chemistry. Consulting a Schaeffler diagram indicates that the microstructure has the possibility of containing both martensite and ferrite upon solidification [41]. Figure 4.10 shows such a diagram and approximate location of the Ni_{eq} and Cr_{eq} position for the 17-4 PH powder chemistry.

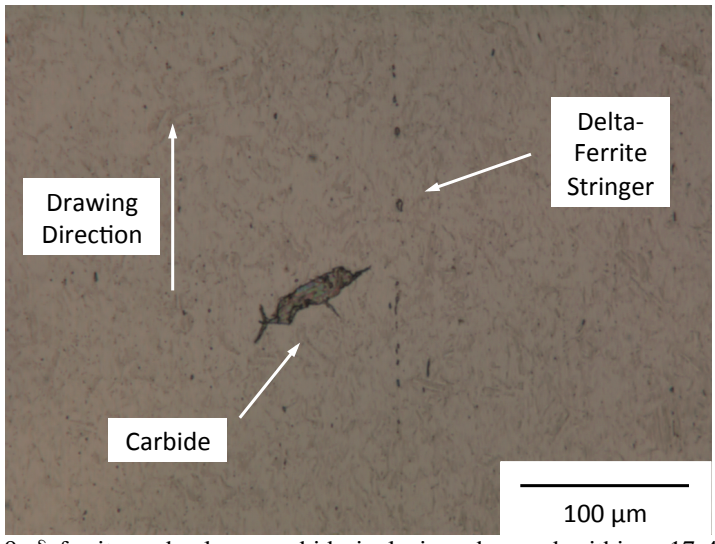


Figure 4.9: δ-ferrite and a large carbide inclusion observed within a 17-4 PH hot-drawn rod in the Condition A state. Note the elongation of the δ-ferrite in the drawing direction. Sample was etched using Vilella's reagent.

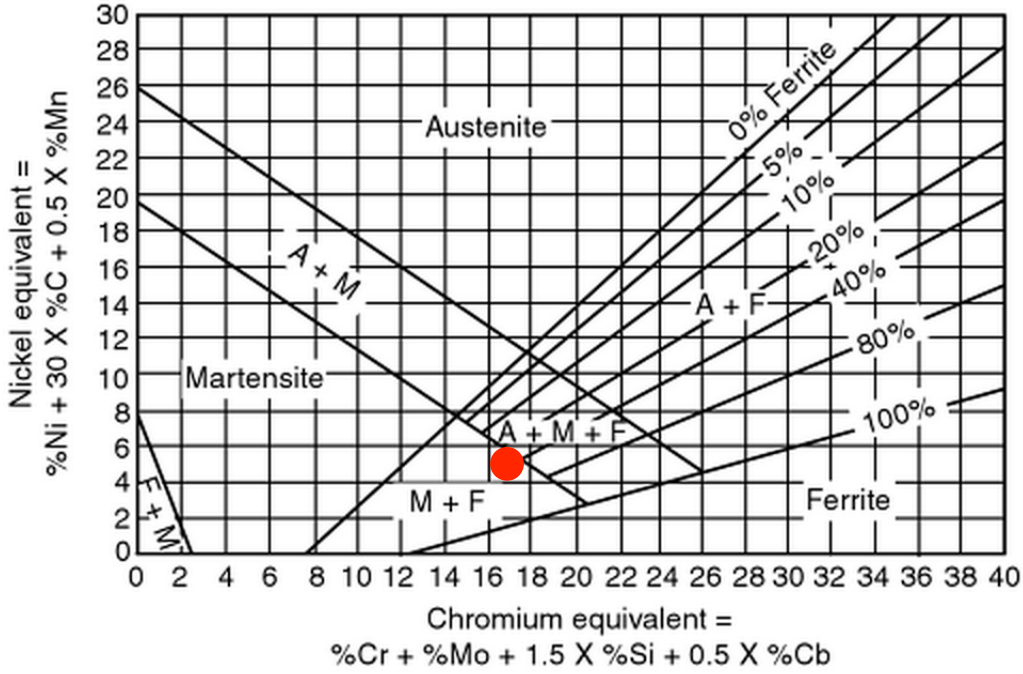


Figure 4.10: Schaeffler Diagram annotated with the location of Nieq and Creq and the predicted phases. (adopted from Kou)

4.7 Precipitation Hardening

4.7.1 Standardized Methods

The namesake of precipitation hardenable stainless steels comes from their ability to further tailor strength and toughness via the controlled growth of secondary phase particles. The strength of 17-4 PH arises from both the primary martensitic microstructure, with its high density of dislocations, and the capacity to nucleate and grow Cu-rich precipitates. Before discussing the kinetics of this process, it is useful to establish the industry-recognized mechanical property minimums associated with the various different tempers of 17-4 PH. Table 4.2 outlines the recommended aging treatment temperatures and duration, and the corresponding expected properties.

Table 4.2: Standardized heat treatments with associated minimum mechanical properties

Condition	Aging Treatment (Temperature, °C / Time, h)	Tensile Strength (MPa)	Yield Strength (MPa)	Elongation (%)	Hardness (Rockwell C / Brinell)
H900	480 / 1.0	1310	1170	10	40 / 368
H925	495 / 4.0	1170	1070	10	38 / 375
H1025	550 / 4.0	1070	1000	12	35 / 321
H1075	580 / 4.0	1000	860	13	32 / 311
H1100	595 / 4.0	965	795	14	31 / 302
H1150	620 / 4.0	930	725	16	28 / 277
H1150M	760 / 2.0, air cool + 620 / 4.0	795	520	18	24 / 255
H1150D	620 / 4.0, air cool + 620 / 4.0	860	725	16	24 / 255 33 max / 311 max

These standardized heat treatments are advised to be performed on a material following an initial solution heat treatment at 1040 °C for 30 minutes (additional time as necessary for thicker cross-sections). This state is referred to in the material standards as “Condition A” [15]. The general purpose of the solution heat treatment is to establish a fully austenitic microstructure at the elevated temperature and work towards the redistribution of solute elements from whatever segregated state they may exist after initial forming. The duration over which this treatment is conducted is relatively short and subsequent recovery, recrystallization, and grain growth is minimal.

Following the prescribed solution heat treatment, aging is performed at one of the defined temperatures for either 1.0 or 4.0 hours. Following the aging treatment, material must be quenched to sufficiently low enough temperatures to ensure the completion of the martensitic transformation.

4.7.2 Precipitation Structure and Resultant Strengthening

Formation of copper precipitates has been found to progress from coherent fcc structures that transform into incoherent fcc-ε copper precipitates with observable shape and morphology via transmission electron microscopy (TEM). For temperatures below ~400 °C, copper precipitates form as coherent bcc-structures with dimensions ≤1 nm. However, with increasing temperature and exposure time, these structures progressively growin in size and transform into

the stable fcc Cu phase when dimensions typically exceed 5 nm [42,43]. Coherency and small lattice strains associated with the fine precipitates make them difficult to osbserve at low temperature and short-duration heat treatments. These two characterisistcs are largely a result of similar atomic radii between and lattice parameters between both γ-iron ($a \cong 0.36\ \text{nm}$) and copper ($a \cong 0.36\ \text{nm}$). However, studies conducted on early-stage aging treatments have been successful at imaging these structures and identifying the kinetics associated with their formation.

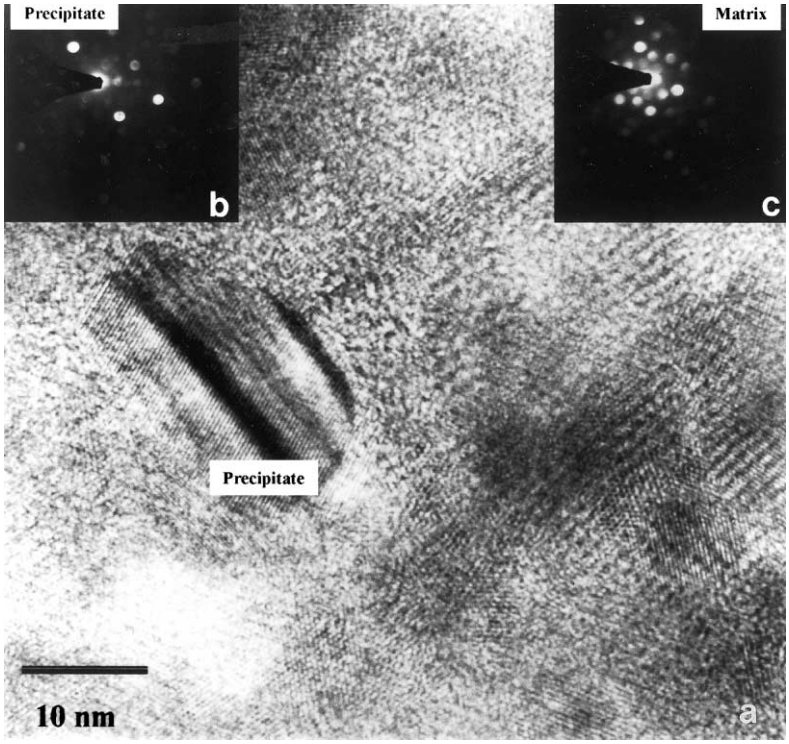


Figure 4.11: FEG-TEM bright field image and corresponding diffraction patterns for copper precipitate obtained from a specimen aged to the peak-age condition (480 °C for 1 hour). (a) bright field image, (b) and (c) corresponding diffraction patterns of the precipitate and surrounding matrix. (From Hsiao)

As it is has been historically noted, the high density of dislocations within martensitic 17-4 PH promotes the transit of copper along these microstructural features by pipe diffusion [30,42,44,45]. Precipitation sites tend to favor (but are not limited to) individual lath boundaries or along dislocation lines, but there is no one-to-one correlation between the two. As copper precipitation structures precede the formation of reversed austenite with high temperature heat treatments, the formation of austenite is suggested to occur at the localized reduction in M_S [27,30]. With the depletion of copper from the central regions of lath block structures towards their boundaries, the reversion of austenite is believed to be a chemical stabilization by higher concentrations of this alloying element.

The formation of these precipitate structures follows the typical Johnson-Mehl relationship for phase transformations [46]:

$$y = 1 - \exp(-kt)^n \tag{4.4}$$

Where y is the volume fraction of the secondary phase formed at time, t, k is the rate constant, and n is also a constant [47].

Extensive experimental work has been performed at characterizing the resultant hardness for 17-4 PH aged at various temperatures and times [34]. And it is generally well accepted that the peak-age condition occurs at approximately 450 °C (850 °F) for 1 hour of exposure. Incidentally, the ASTM standard previously outlined instructs readers to follow an aging treatment of 480 °C (900 °F) for the same period of time [15]. This is likely done so as to avoid the embrittlement that typically accompanies the true peak-aged condition [36]. Nonetheless, the peak-age condition may be achieved outside of the standardized heat treatments, but careful attention to the combination of exposure time and temperature is necessary when treating at higher temperatures than the identified 480 °C. Figure 4.12 shows the relative hardness from the solution heat treated condition associated with varying treatment times and temperatures.

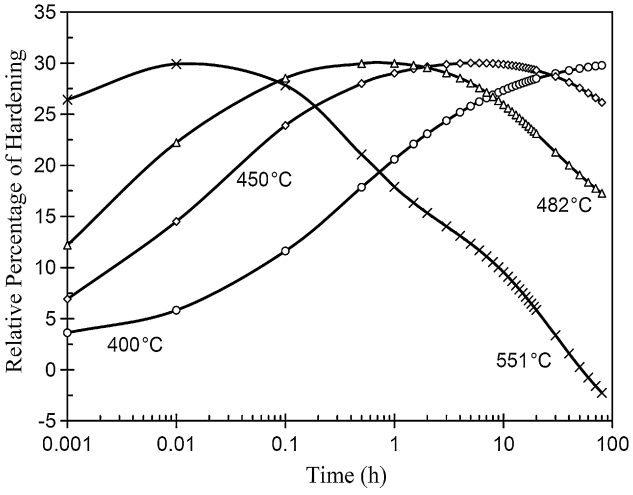


Figure 4.12: Effect of aging time on the hardening behavior at various temperatures for 17-4 PH. (After Mirzadeh and Najafizadeh)

Because standardized heat treatments are typically performed across a wide range of temperatures and time durations, direct comparisons between the resultant mechanical properties as a result of different heat treatments are not readily possible. It is therefore useful to normalize the exposure conditions into a

single parameter. And common to discussing the effects of heat treatment, the Hollomon-Jaffe parameter is typically used (also known as the Larson-Miller parameter). This parameter is effectively a time-compensated temperature term.

$$P = T(C + \log t)\times 10^{-3} \tag{4.5}$$

where T is the absolute temperature in Kelvin and t is the tempering time in hours, while C is the materials constant in the range of 10 to 20 (in many applications it is considered to be 20) [48,49]. The units of this parameter are not relevant in this discussion, only the tabulated value is of consideration, but the parameter effectively permits comparisons across various thermal processing temperatures and times. This is typically plotted against the relative hardening due to precipitation structure development. Relative hardening is typically defined as:

$$H_t = \left(\frac{H - H_{st}}{H_{st}}\right)\times 100 \tag{4.6}$$

where H and H_{st} are the measured hardness of aged and solution-treated specimens, respectively. An aggregated plot across many experimental studies of 17-4 PH cataloging this relationship is shown in Figure 4.13.

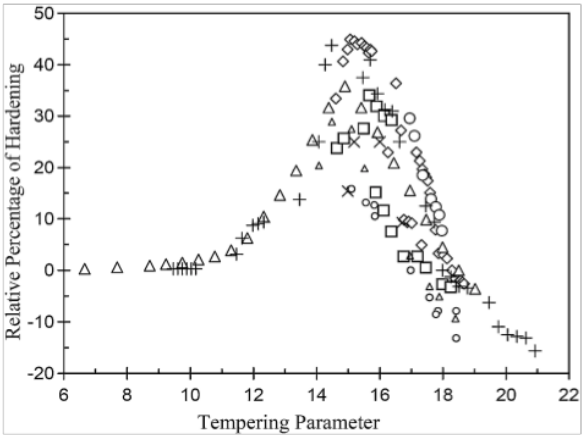


Figure 4.13: Effect of tempering parameter on aging behavior for 17-4 PH stainless steel (adopted from Mirzadeh and Najafizadeh).

As shown by the above figure, increasing time and higher temperatures result in a relative weakening of the material that correlates with a reduction in relative hardness. At extended aging times, this relative strengthening turns negative (although, this is typically accompanied by an increase in ductility,

uniform plastic elongation, and total elongation). This behavior fits well with classical precipitation hardening theory (to be discussed in the subsequent sub-section), but the macroscopic material behavior is not solely a result of coarsening precipitates. As previously discussed, the precipitates typically beget austenite reversion. And has been noted, austenite is a significantly weaker phase. Owing to this change in volume fraction of austenite and a propensity to favor particle bypass over dislocation pinning and cutting for these coarsened Cu-precipitates, we observe a reduction in mechanical strength.

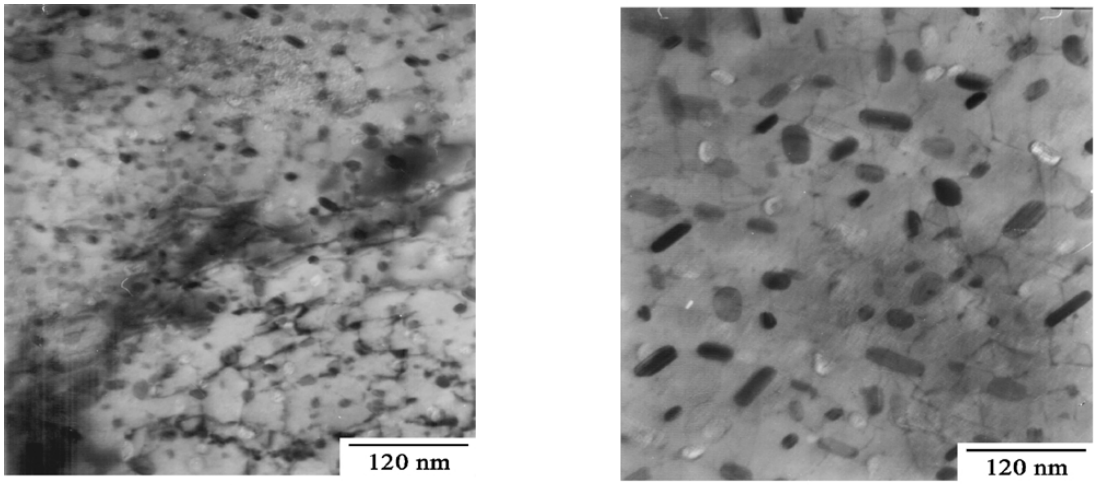


Figure 4.14: TEM micrographs of microstructure in Condition A of 17-4 PH stainless steel exposed at 600 °C for (a) 0.25 hours and (b) 32 hours. Note the coarsening and elongation of Cu-precipitate structure with increasing time. (from Wu and Lin) [50]

4.7.3 Particle Strengthening Theory Overview [51]

17-4 PH stainless steel benefits from strengthening following the nucleation and growth of precipitates dominated in composition by copper. These form from a saturated concentration throughout the material when exposed to elevated temperatures. Increased diffusivity rates and diffusion paths at elevated temperature over appropriately timed exposure durations assist the diffusion of these atoms to initially form spherical precipitates that lead to substantial increases in strength. Strengthening by these secondary phase particles depends on a variety of physical characteristics of the particles themselves within the larger matrix material and can be described by classical particle strengthening theory.

As plastic deformation of 17-4 PH stainless steel is dominated by dislocation motion[2], these particles contribute to the overall strengthening by acting as barriers to such dislocation motion through the matrix material. The relative increase in strength is dependent on a variety of properties for these particles relative to the matrix material. Strong particles can only be overcome by sharp changes in direction or curvature for a dislocation line. In contrast, coherent particles may permit passing of a dislocation by cutting, but at much higher stress levels than through the matrix material. The means of bypassing a particle, either by cutting or change in dislocation curvature/orientation, are largely dependent on the particle size and distribution. There are six properties of particles that can affect the ease by which they are sheared:

coherency strain

staking fault energy

ordered structure

modulus effect

interfacial energy and morphology

lattice friction stress

This research effort does not directly study the micro-scale interaction of particle strengthening on 17-4 PH, but simply as a consequence of thermal processing on the macro-scale properties. However, it is useful to illustrate the transition between relative strengthening and softening of a material due in large part to changes in precipitation particle sizing [52]. Figure 4.15 shows a schematic illustration of the relative tradeoff between the two mechanisms, particle shearing and particle bypassing, over which strengthening is found to peak.

[2] As opposed to grain boundary sliding.

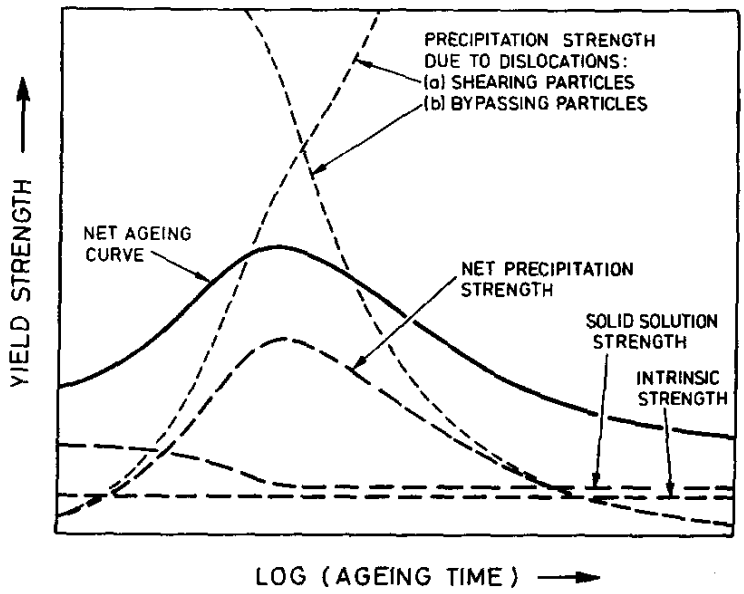


Figure 4.15: A schematic diagram of the relative contributions to the full ageing curve of the intrinsic strength, solid solution strength, and precipitation hardening due to shearable and non-shearable particles; note that the effective mechanism of precipitation hardening is the one requiring the least shear stress , with a smooth transition between the two. (From Shercliff and Ashby)

As precipitation particles nucleate, their relative size to the matrix is extremely small. At this size and if the relative hardness (modulus) of the particle is less, dislocations may cut through a particle. Contribution to the strength of the alloy involves a combination of the resistance to shearing, the density and distribution of said particles, and the flexibility of the dislocation with which they interact. This is known as the “Friedel effect”. In its most basic form, this effect may be described as a change in yield stress by the following equation:

$$\Delta\sigma_Y = cf^m r^n \tag{4.7}$$

where *f* is the volume fraction of the particles, *r* is the particle radius, *c, m,* and *n* are constants. For most dislocation-particle interactions, both *m* and *n* have a value of 0.5 [52].

With the increase in size of precipitates, the spacing also begins to increase. With increased inter-particle spacing and resistance to cutting, there comes a point where a dislocation will bow between neighboring particles within the slip plane. In this case the energy required to bow, break, and re-align a dislocation is less than shearing through them. The bowing stress is described by the following:

$$\Delta\sigma_B = \frac{c'G\mathbf{b}}{l} \tag{4.8}$$

where c' is a material constant, G is the shear modulus, **b** is the Burgers vector and l is the inter-particle spacing. The inter-particle spacing within a slip plane may be described by the following:

$$l = c'' \frac{r}{f^{1/2}} \tag{4.9}$$

These two expressions both show the relationships between yield stress, bowing stress of a dislocation around a particle, and the particle size. As previously shown in Figure 4.15, the yield stress increases monotonically with resistance to particle shearing as it is related to the particle size. However, this is only maintained so long as the stress required to bow around a particle is greater than to shear through it. At a particle size where these are equal, an exchange to favor particle bypassing by bowing occurs. Increasing particle size does not contribute to the alloy strength and we see a reduction in strength from a peak-age condition with further particle growth.

5. Processing by Selective Laser Melting

5.1 Preface

The results of research into the properties of material produced via AM are strongly path dependent. Said another way, the results and behavior observed of any one material processed in this manner is strongly influenced by the steps and inputs taken both in the forming of the bulk material and in testing done upon it. The chemistry of the working material may be the same between studies, but there exist a tremendous variety of parameters and factors that influence the final result. While work into finding commonality, scalability, and fundamental behavior between experimental investigations is ongoing, the results of one researcher commonly differ from the next. The experimental work presented as part of this thesis is no different. Therefore, careful attention will be given in the description of the raw material and all processing performed upon it.

This research effort undertook two independent mechanical studies of material processed by SLM. For both of these studies, sourcing of the raw material was made from the same supplier. However, for reasons outside of the author's control[1], processing of this powdered material was done by two different external entities for the two studies performed. The equipment available for the densification of the powdered material at these locations and the processing parameters used were different and subsequently produced variations in the resultant, as-fabricated material. Therefore, the following sections within *Processing by Selective Laser Melting* will detail these inputs and parameters associated with the processing of each lot of bulk material by SLM. Material produced for the first and second experimental studies will be referred to as "Batch One" and "Batch Two".

5.2 Raw Material

Before discussing the actual processing of the material by selective laser melting (SLM), it is important to discuss the working powder in so far as how it interfaces with the machine. AM methods that process metal materials do so by handling powder or wire as the initial working material state. Of those that utilize powder there exist two methods by which machines may access and

[1] Altering the processing environment/machine was also a change not intended.

deploy the working material: layer-based distribution and metal deposition. Layer-based machines require a build chamber whose floor is sequentially lowered at discreet increments to accommodate a growing volume of powder distributed by wipers or rollers [5,53]. Metal deposition techniques require hopper-supplied and pneumatically pressurized feed jets on the end of a two or three-axis computer numerically controlled head that sprays powder at the site of directed energy in the form of a high power laser [54,55]. Wire-fed machines also operate in a manner similar to that described by powder-based metal deposition with the exception that the wire is heated and effectively extruded and laid in a predetermined three-dimensional pattern. These wire-fed machines also share the same name as the powder deposition counterparts [56].

For the purpose of both lots of fabricated bulk material, Batch One and Batch Two, a layer-based approach utilizing pre-alloyed 17-4 PH stainless steel powder was used. This raw material was sourced from the Kobe Steel Company (Kobe City, Hyogo Prefecture, Japan). The supplier produced the pre-alloyed powder via an atomization machine in a standard "V-jet" configuration. V-Jet water atomization relies on flat streams of water introduced into a chamber with an acute angle between. A molten stream of metal intended for processing falls into its vertex and is struck by the streams of water. Atomization by this means is a cost-effective method to produce powder in large quantities for use in compacts and die forms for solid-state sintering [57]. However, water atomization is not ideally suited for use in SLM applications. Irregular particle shapes commonly result from rapid quenching by impingement with water or steam. These particle morphologies result in lower packing densities than spherical, gas-atomized powders [58]. As has been demonstrated by early testing of simple iron powders, gas atomized variants perform better at achieving higher resultant densities [59].

The powder was further processed by the supplier using a mechanical sieve so as to reduce the maximum powder size. Figure 5.1 details the powder as imaged by scanning electron microscopy (SEM). As-received powder chemistry and particle size distribution data according to supplier inspection is provided in Tables 5.1 and 5.2. The pre-alloyed powder chemistry meets ASTM required minimums and ranges outlined for 17-4 PH stainless steel [15]. The characteristic particle distribution was measured at d_{90}= 32.98 µm, d_{50}= 21.12 µm, and d_{10}= 13.95 µm.[2] The SEM imagery of the working material highlights the

[2] Common in powdered metallurgy, powder dxx values specify the size under which the volumetric fraction is listed as the subscript (xx). For example, a d50 value of 21.12 µm indicates that 50% by volume of the powder is of a size less than 21.12 µm.

two shape morphologies of the water-atomized powder (see Figure 5.1). The predominant morphology is a jagged and irregular shape consistent with the water-atomization process. The secondary shape takes the form of a smooth spheroid resulting from surface tension forces acting on free falling droplets of molten metal not immediately quenched by water or steam [57]. Alloy composition of the two shapes was verified by energy dispersive x-ray spectroscopy to be consistent (i.e. not a mixture of different materials).

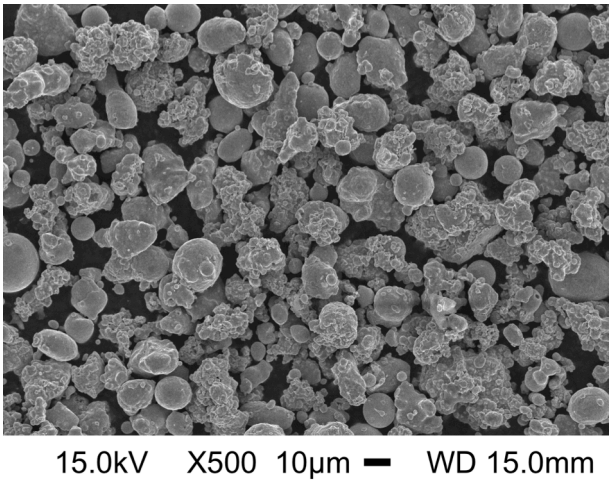


Figure 5.1: Two-form morphology of the water-atomized 17-4 PH powder.

An additional sourcing of hot-drawn rod meeting the same industry standard for chemistry was procured from an additional supplier. This material, hereafter referred to as the "reference material" in the remainder of this text, was utilized as the baseline for mechanical testing comparisons to that of the SLM processed powder. For reference, the chemistry of the drawn rod is also outlined in Table 5.1.

Table 5.1: Chemical composition of the powdered material and reference (weight %)

	Working Powder	Reference Material	ASTM A564/A564M Limits [9]
C	0.054	0.05	0.07
Mn	0.18	0.85	1.00
P	0.011	0.034	0.040
S	0.005	0.004	0.030
Si	0.41	0.30	1.00
Cr	16.51	15.66	15.00-17.00
Ni	4.16	4.26	3.00-5.00
Nb	0.42	0.32	NS
Cu	3.97	3.30	3.00-5.00
O	0.33	NS	NS
N	0.09	NS	NS
Fe	bal.	bal.	bal.

Limits are in percent maximum unless shown as a range.

NS – not specified

Table 5.2: Powder distribution

Powder Diameter Range (μm)	<2.8	2.8-3.9	3.9-5.5	5.5-7.8	7.8-11	11-16	16-21	21-31	31-44	>44
Percent Weight	0.0	0.0	0.0	0.5	2.8	15.2	36.9	31.9	9.5	3.2

5.3 Processing to Form Bulk Material

Methods to consolidate the working material into a free form shape vary based on the morphology and composition of the material being processed. In

the case of metal deposition, a full-melt of the processing powder or wire is typically required [56]. Layer-based machines, however, may depend on selective full-melt and densification or particle-to-particle sintering as the consolidation mechanism [3,5]. Energy sources and controllable environmental conditions differ between machine types. Those that rely on high-powered lasers, such as CO2 or Nd:YAG, may work to form bulk material out of the powder bed by either selective laser melting (SLM) or selective laser sintering (SLS), the former being more common. Material processing by laser energy typically occurs within an inert, oxygen-minimized atmosphere. An alternative process known as electron beam melting (EBM) relies on a focused electron beam operating in a high vacuum. EBM is capable of processing virtually any electrically conductive material, even those with high optical reflectivity that performs poorly with other, laser-based energy sources. Processing environment, irrespective of other machine settings, has been documented to affect the resulting microstructure by varying the rate of heat transfer away from the melt pool within the build chamber [13,32].

All other processing parameters within the laser or electron-beam equipped machine are varied to directly affect the interaction between energy source and working material. Most notably of these interactions are the resulting linear and volumetric energy densities [59,60]. With respect to SLM and EBM, layer thickness, energy power, spot diameter, scanning speed, hatch spacing, and powder morphology all work in concert to establish a working melt pool and its size, control its wetting characteristics, and establish penetration both horizontally and vertically within the build volume [61-63]. Too little energy and melt pool kinetics may prevent proper wetting performance and subsequently generate enlarged pores [59,62]. On the other hand, too much energy may generate a plasma of the inert atmosphere or vaporize the working material and generate an expanding shock front that expels material away from the build spot [64-66]. As a consequence of these inputs, crystallographic microstructure and microstructural-scale artifacts can also vary in size, phase, and orientation [13,67].

Bulk material produced in the first lot, Batch One, was produced by SLM via an M2 LaserCusing® machine (Concept Laser, GmbH, Germany) operated by JMP (Takatsuki City, Osaka Prefecture, Japan). Figure 5.2 details a schematic outline of the features and processing steps used by this particular SLM machine deployed. The M2 utilizes a fiber laser with a wavelength of 1075 nm and a maximum power of 200 W in continuous wave mode. An attached gaseous nitrogen generator or external supply of either nitrogen or argon may be used to

ensure a continuous, inert processing environment. Materials produced in this study were done under a nitrogen protective atmosphere sourced from pressurized tanks to the sealed building chamber. Machine measured oxygen content ranged between 0.5 and 0.7% throughout. As has been previously introduced, laser-powder interaction is of the highest importance to the liquid metal kinetics, consolidation, and resulting microstructure; ergo, the machine settings utilized in this study were 190 W in continuous wave mode with a scanning speed of 700 mm/s. The laser spot diameter was set to 150 µm. Hatch spacing (scanning line offset) in this particular case was set at 70% of the laser diameter. The layer thickness generated by incremental lowering of the building chamber's floor was set to 30 µm. It should be noted that while the layer thickness is set below the maximum particle diameter per Table 2, proper distribution of the working material is not prevented. More powder than what is required for each layer's build volume is made available from the powder reservoir. Excess powder is then tumbled by the distribution wiper until it reaches a catchment on the far side.

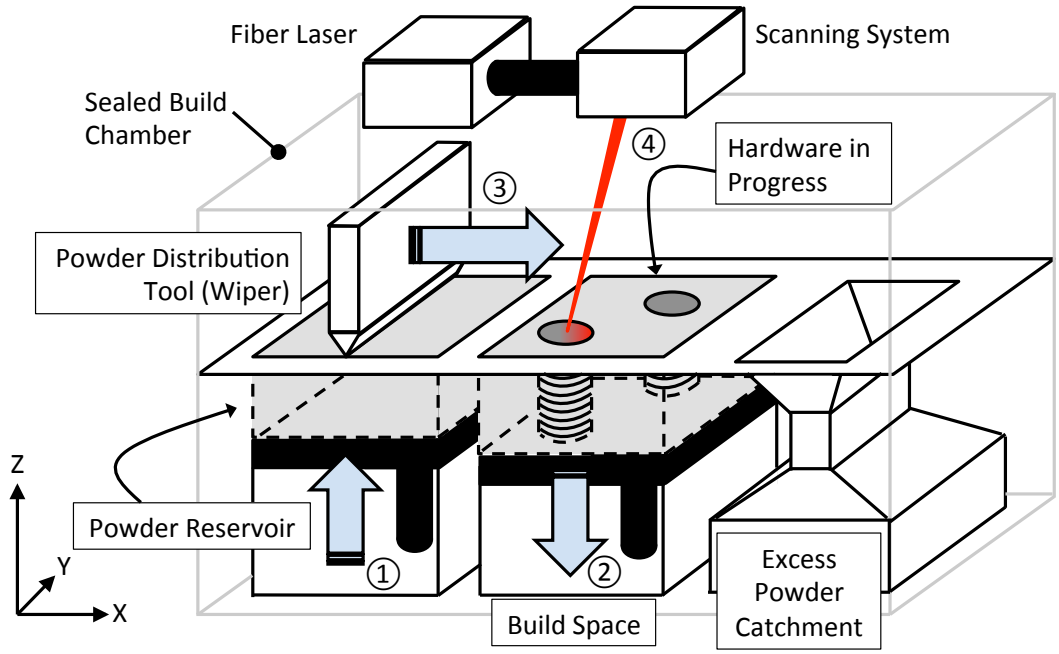


Figure 5.2: Schematic of a typical SLM machine. Operation runs in sequence from (1) through (4). (1) The reservoir chamber floor is raised to elevate powder above the building plane. (2) The building chamber floor is lowered the designated layer thickness. (3) The powder distribution tool is used to collect and lay the powder from the reservoir into the build chamber. Excess powder is swept into the catchment. (4) The current layer's cross-section is scanned by the laser system. The process repeats from (1) – (4) until the entire part volume is complete.

As a method to improve consolidation and minimize warpage resulting from thermal stresses, scanning patterns have been of interest to some researchers [68]. While not a focus of this study as it does not change the overall energy

density, the scanning pattern used did have an influence on the as-fabricated microstructure. For completeness, the scanning pattern used in the production of Batch One will be detailed here and graphically outlined in Figure 5.3. Bulk material, as discretized by their layer thickness, had each layer's cross-sectional area pre-planned by the assistive software "Magics" (also provided by LaserConcepts as part of the workflow with the M2). Each cross-sectional layer's area is divided into squared 5 mm "island" units. Laser scanning directions within each square are parallel and alternating in direction to each other. The four squares that share the same edge of any one square have their scanning directions oriented normal to the one at center. This creates a "checkerboard" pattern across the surface of every layer as it is rastered at random by the laser (adjacent islands are not commonly rastered in sequence). And if the machine axes are delineated as right to left for positive-X and near to far as positive-Y (all relative to the operator), this checkerboard pattern was rotated +45° from the x-axis. Every subsequent layer is built with a 1 mm +X and +Y shift in the pattern (the boundary of each cross-section does not translate, only the pattern therein). This is done to ensure that pattern features and scan paths do not directly overlay each other from one layer to the next. In addition to the 5 mm square pattern elucidated above, each laser track will extend an additional 15% of the spot diameter beyond the square's 5 mm dimension in both directions. This is done to provide some overlap between adjacent squares and minimize a seam forming between perpendicular scanning paths. Following the scanning of the complete pattern, the laser will trace the outer perimeter (and any internal, enclosed perimeters) of the cross-section, exposing this trace of material to directed energy a second time.

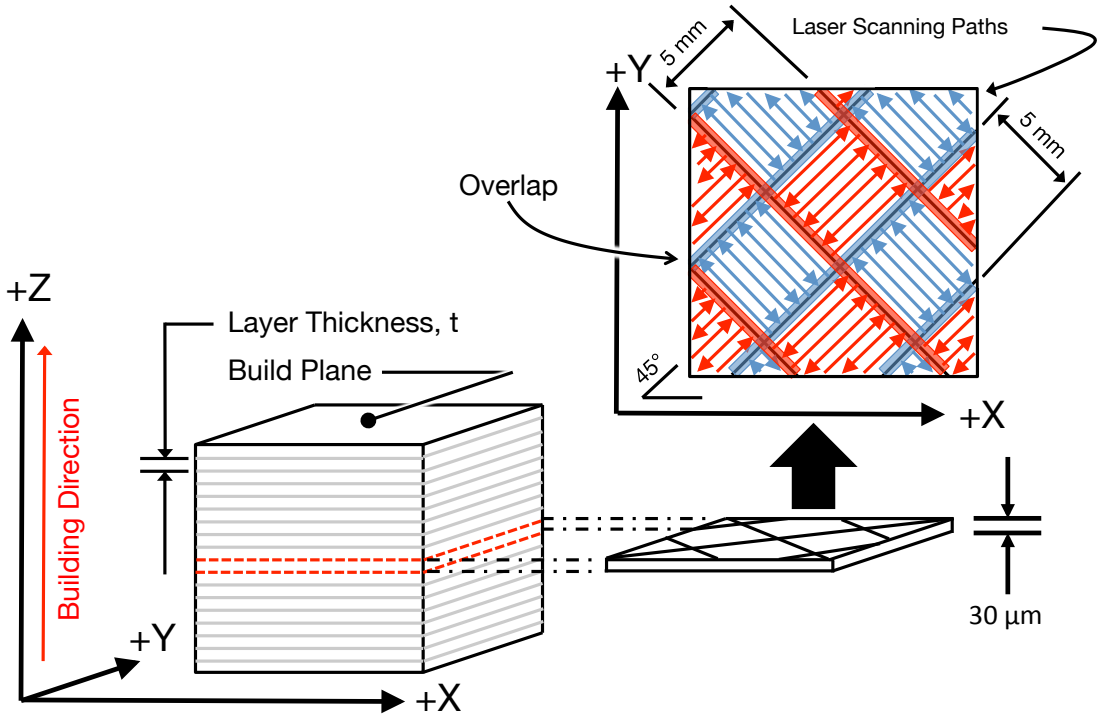


Figure 5.3: Schematic illustrating the scanning pattern utilized on each layer to fabricate the full volume of an arbitrary shape. This scanning pattern was utilized in the production of Batch One.

The production of Batch Two was performed under very similar parameters in an effort to duplicate the results obtained. The fabrication of Batch Two was performed using a EOS M280 (EOS, GmbH, Germany) Direct to Metal Laser Sintering machine (DMLS). The technicians at the Osaka Prefectural Technology Research Institute (TRI) (Izumichuo City, Osaka Prefecture, Japan) oversaw operation of this machine. This machine also operated using a fiber laser with similar operational characteristics as M2. However, this machine was limited to a layer thickness resolution only as small as 40 µm. As a result, a similar energy density was targeted to try and achieve the same resultant densification. The operational parameters used to produce Batch Two were a laser spot diameter of 100 µm, laser power of 190 W, laser scanning speed of 787 mm/s, and a scan offset 0.110 mm from centerline to centerline of adjacent scan paths. The scanning offset effectively put a 10 µm gap between the subsequent scans of the laser. The scanning pattern deployed for this lot of material was far less complicated than the first. Every layer was a series of parallel scan lines. Each subsequent layer was rotated 60 degrees from the previously scanned cross-section. This machine was also operated with an external nitrogen supply to ensure a protective gas environment during operation. Table 5.3 summarizes the operational parameters between the two machines.

Table 5.3: Operational Parameters Summary

	Batch One – M2	Batch Two – M280
Laser Power (Watts)	190	190
Laser Diameter (µm)	150	100
Laser Scanning Speed (mm/s)	700	787
Scan Line Offset (µm)	70	110
Layer Thickness (µm)	30	40

6. Microstructure of 17-4 PH Processed by Selective Laser Melting

6.1 Preface

Despite the differences in processing parameters deployed between the builds of Batch One and Batch Two, the observed microstructure and alloy distribution were very similar. For the sake of brevity, discussion of microstructure with accompanying figures will focus on Batch One. Any differences that have arisen between the two builds will be identified and explained.

6.2 Optical Microscopy

Preparation for and observation by optical microscopy was performed in accordance with standard laboratory procedures. Metal samples were sectioned, ground and polished using progressively finer grit sandpaper atop a rotating polishing wheel. Final buffing to a mirror finish was performed atop a rotating buffing wheel using a suspension of alumina powder in water with progressively finer particle sizes. Depending on the features to be observed, samples were etched using a variety of techniques to highlight certain phases or microstructural features.

To help establish a baseline of comparison, Figure 6.1 shows a typical micrograph for the reference material used throughout the mechanical evaluations across the experimental investigations. This particular micrograph is of a reference sample in the Condition A state. Again, the reference material samples and specimens were taken from 17-4 PH hot-drawn rod meeting the same material standard for chemistry (with small variations from the powdered material used in SLM). Figure 6.1 showing the microstructure of the reference specimen was prepared with the viewing plane normal to the direction of drawing. The microstructure observable here is fairly equiaxed in this view without any indication of directional biasing. Approximate prior austenite grain size of the reference material is 30 μm in size with occasional grains 40 μm in size. Individual boundaries between grains are clear and distinct at this magnification. With a clear microstructure, individual parent austenite grains are easily traceable using optical microscopy.

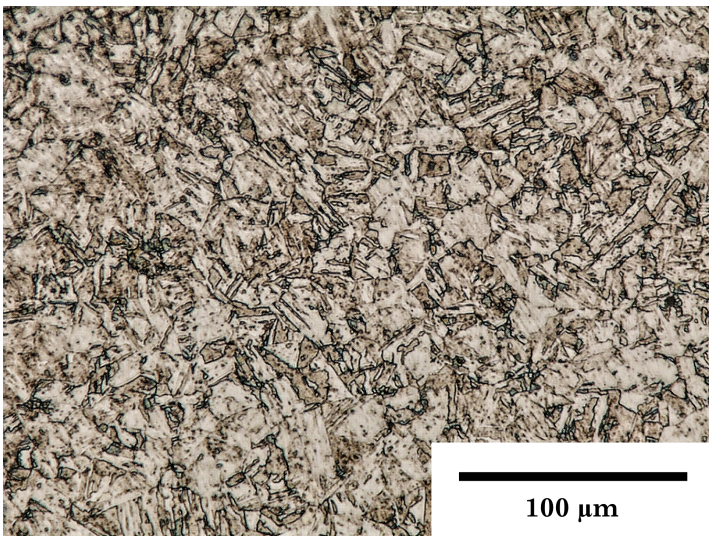


Figure 6.1: Lath martensitic microstructure as observed in the drawn-rod reference material treated to the Condition A state. The viewing direction is normal to the drawing direction. 1000x magnification. Etched using Kalling's #1.

Figures 6.2 and 6.3 show optical micrographs of the as-fabricated SLM 17-4 PH as viewed in the vertical and horizontal reference planes at high magnification. The building direction of the SLM material is indicated in Figure 6.2 by the white arrow. A relatively smaller grain size to that of the reference material is observable in both orientations. The approximate prior-austenite grain size ranged from 1-5 µm (with the occasional elongated structure approaching 10 µm oriented in-line with the building direction). Differences in grain size and direction coincide with the SLM process. Longer grains containing lath bundles are observable and oriented roughly in-line with the building direction. This coincides well with the expected thermal gradients within individual melt pools (oriented normal to the fusion boundary between individual melt pools, generally in a radial direction). Other researchers have observed directional structures in similar fashion relating to the building direction [32,67].

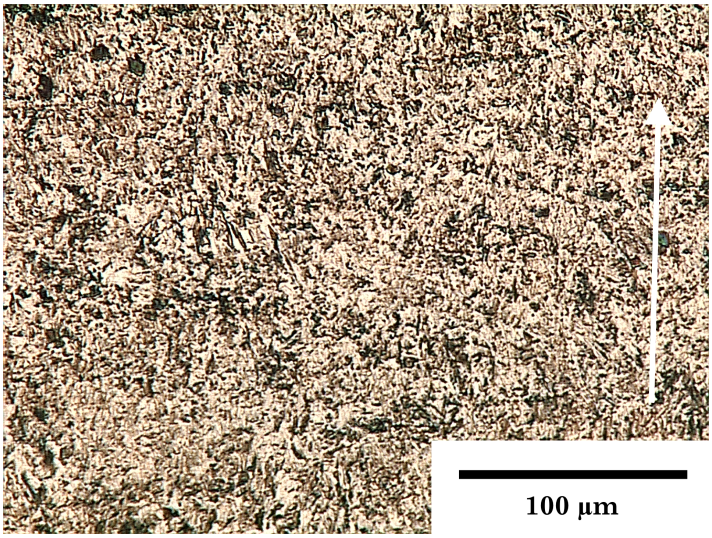


Figure 6.2: As-fabricated microstructure of SLM 17-4 PH. Image taken in the vertical reference plane with the building direction indicated by the white arrow. 1000x magnification. Etched using Kalling's #1.

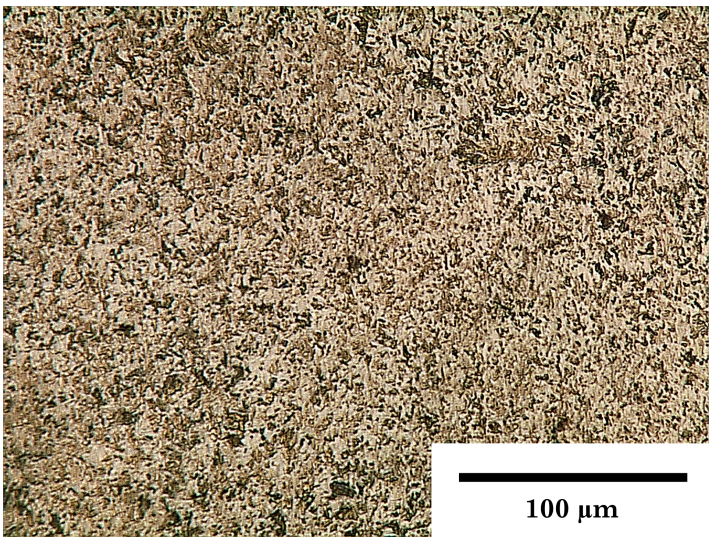


Figure 6.3: As-fabricated microstructure of SLM 17-4 PH. Image taken in the horizontal reference plane. Building plane shown. 1000x magnification. Etched using Kalling's #1.

At lower magnification, the patterning that results from the scanning by the laser system is clear. Figure 6.4 and 6.5 show a low magnification image of the microstructure as observed in the vertical and horizontal reference planes, respectively. Circular features observed in Figure 6.5 are points within the scanning pattern where the laser stopped its traverse and turned off to begin its trace in an opposite direction. Additionally, this figure illustrates the intersection between two checkerboard islands of the pattern deployed. Hence the opposing scanning pattern directions at right angles to each other. While in Figure 6.4, the layered structure and scanning pattern are visible. Mild banding is shown in this

image. As expected, these bands that traverse the imaged region were measured to coincide with the machine set layer thickness of 30 µm in the case of Batch One. However, the final layer, visible as a lighter band at the top of the image is considerably thicker.

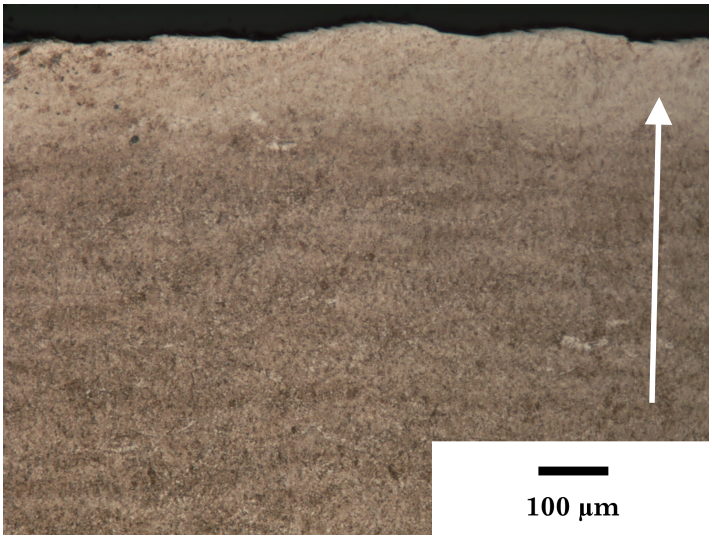


Figure 6.4: As-fabricated microstructure of SLM 17-4 PH. A light-dark banding pattern is observed corresponding to the building direction. Image taken in the vertical reference plane (XZ) with the building direction indicated by the white arrow. 300x magnification. Etched with Kalling's #1 reagent.

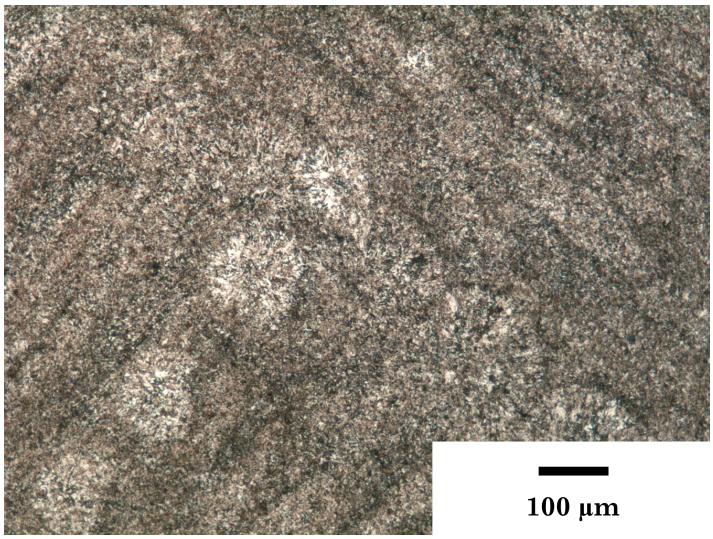


Figure 6.5: As-Fabricated microstructure of SLM 17-4 PH. Image taken in the horizontal reference plane. 300x magnification. Etched with Kalling's #1 reagent.

Measurements made of the final layer were found to vary between 100 and 130 µm. Figure 6.6 shows a magnified view of the final layer. Individual scan paths are observable as crescent shape arcs in the microstructure. These can be

interpreted as the fusion boundary between the molten material and the previously consolidated material below. Close examinations of other micrographs in the vertical reference plane occasionally show locations of these fusion boundaries, but with distances of approximately 30 μm separating each (corresponding to the layer thickness).

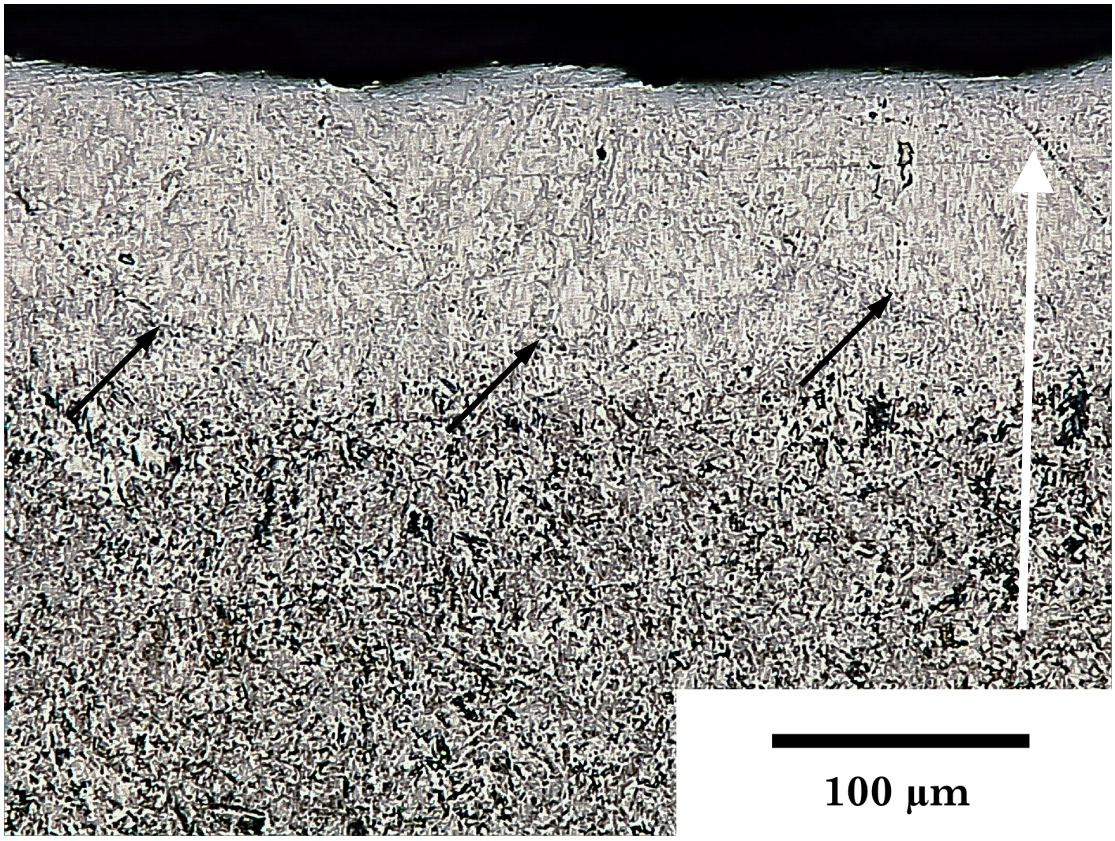


Figure 6.6: As-fabricated microstructure of SLM 17-4 PH. Image taken in the vertical reference plane. Building direction indicated by the white arrow. Individual fusion boundaries between the final layer's scan paths are indicated by black arrows. 700x magnification. Etched with Kalling's #1.

Based on measurements and observations of the final layer, a few inferences may be made about the SLM process. Individual scans by the laser not only melt the working powder with each new layer as-deposited, but integrate several layers previously consolidated into the working melt pool. Under the processing parameters utilized to produce the bulk material in Batch One, the melt pool penetration depth exceeded a single layer and re-integrated upwards of two to three additional layers with each pass of the laser. Prior austenite grains within the final layer are larger, but are still found to follow the predicted radial thermal gradients. And a comparison of the structures between sub-surface material and the final layer found similar structure, but of largely different sizes. Consolidated material was "finished" being reintegrated into the melt pool with the processing

of a third or fourth layer above it. The volume of material not re-integrated by subsequent laser scan passes was a region in height equal to that of the layer thickness extending from the tip of a fusion boundary crest to the next layer above it. Cooling rates of molten material would be expected to be at their peak in the extremities of a melt pool as a consequence of their proximity to the consolidated material below acting as a thermal sink. Therefore, the material not re-integrated with the building of each new layer cooled expeditiously quickly and is found to contain grains smaller than the final layer. However, the bulk of the material is built of these thin crescents. As a result, the bulk material demonstrates smaller grain sizes than that observed in the final layer. The final layer was observed to contain prior austenite grain sizes on the order of 30 μm. The cooling rates at these 30 μm tall, crescent-shaped local sites that make up the bulk volume of the material would be predictably much higher than an entire melt pool.

Figure 6.7 and 6.8 show microstructure of the SLM processed 17-4 PH following an initial solution heat treatment to Condition A. These figures illustrate the effects of a high temperature, short duration heat treatment on the microstructure. Patterning and residuals observable via optical microscopy have been minimized and largely eliminated. Initial recovery, recrystallization, and mild grain growth of the microstructure is observed. However, the structure is only found to coarsen to an average prior-austenite grain size of approximately 8 – 10 μm.

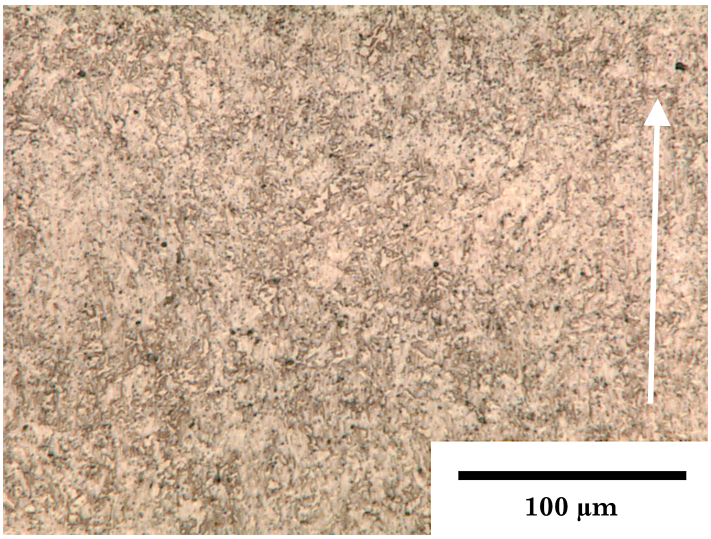


Figure 6.7: Microstructure of SLM 17-4 PH following solution heat treatment to Condition A. Image is taken of the vertical reference plane (XZ) with the building direction indicated by the white arrow. Etched with Fry's reagent.

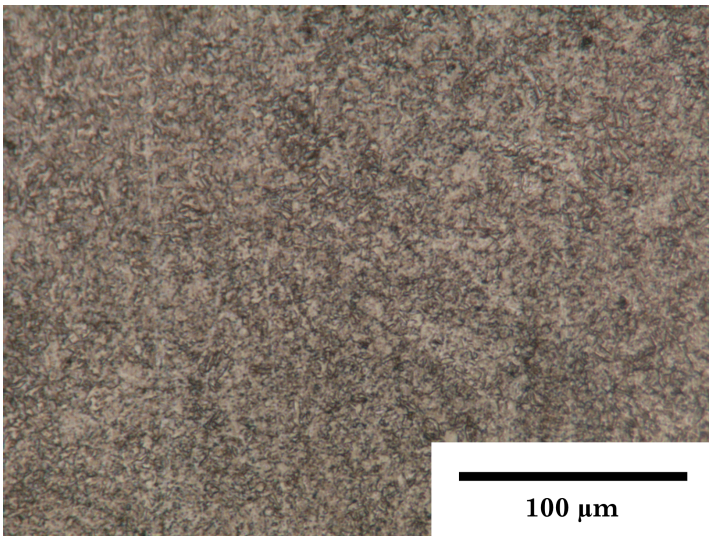


Figure 6.8: Microstructure of the SLM 17-4 PH following solution heat treatment to Condition A. Image is taken of the horizontal reference plane (XY). Etched with Fry's reagent.

Figures 6.9, 6.10, and 6.11 show the microstructure through the progressively longer and hotter aging heat treatments performed, H900, H1025, and H1150, respectively. These images are only of the vertical reference plane. Clear coarsening of the microstructure is observed across the treatment conditions. Differences between the H1025 and H1150 treatments as observed via optical microscopy are minimal (difference is only 70 °C in processing temperature for the same duration).

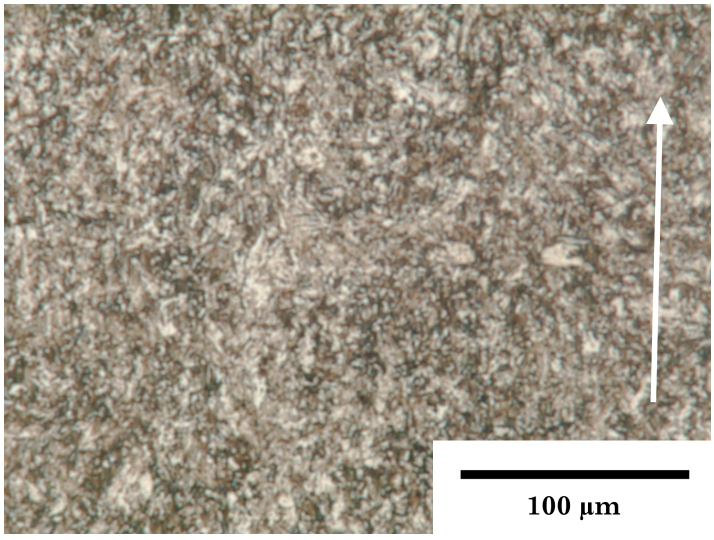


Figure 6.9: Microstructure of the SLM 17-4 PH following solution heat treatment and aged to H900. Image is taken of the vertical reference plane (XZ). Etched with Fry's reagent.

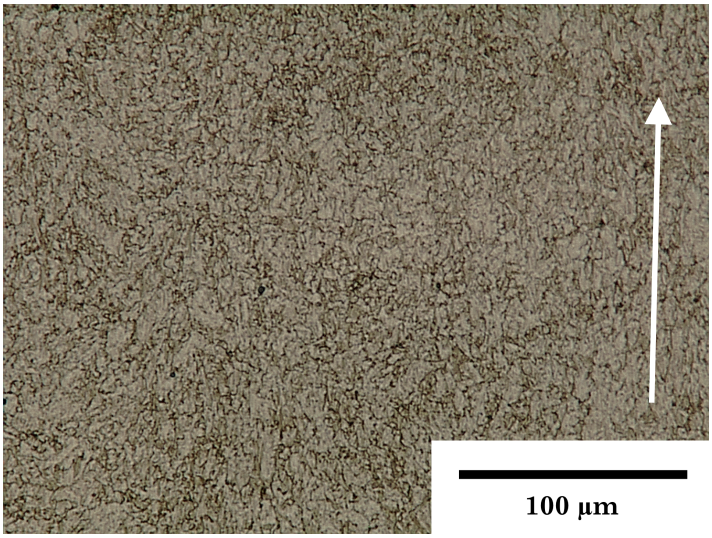


Figure 6.10: Microstructure of the SLM 17-4 PH following solution heat treatment and aged to H1025. Image is taken of the vertical reference plane. Etched with Fry's reagent

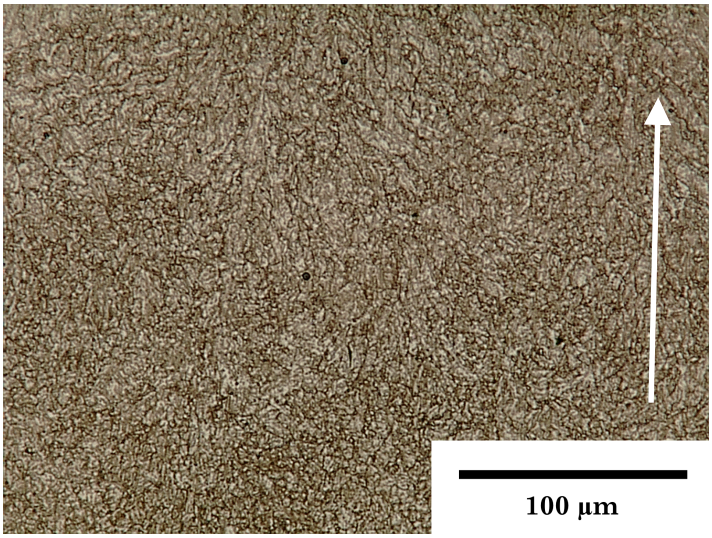


Figure 6.11: Microstructure of the SLM 17-4 PH following solution heat treatment and aged to H1150. Image is taken of the vertical reference plane. Etched with Fry's reagent

These three previous images detail the microstructures for the aged conditions under which copper-rich precipitates are intended to nucleate and grow. However, as previously described in the Chapter 4, precipitates remain extremely small and coherent and are not visible via optical microscopy.

6.3 Scanning Electron Microscopy

Because the microstructure is small, proper observation of the martensite and prior-austenite structure is best done by SEM. Figure 6.12 shows an image of the as-fabricated microstructure with the building direction indicated by the white arrow. Despite the rapid solidification and cooling understood to occur with SLM, ferrite may still be present in the microstructure. Figure 6.12 also highlights with small black arrows possible sites of eutectic ferrite in the otherwise lath martensite. This ferrite is roundish in morphology and its location suggests it formed as a result of eutectic solidification. This morphology was observed by Ozbayasl and Inal [20] in laser welding of 15-5 PH stainless steel. Vermicular or dendritic ferrite was not observed in this SEM imagery. The likely cause for their absence is again the speed of solidification. Observations by the previous researchers were made of material processed at two orders of magnitude slower laser scanning speeds and in the core of a molten material pool. Under these circumstances, cooling rates are much slower and permit the segregation of solute to form larger ferrite structures. That is not the case observed here.

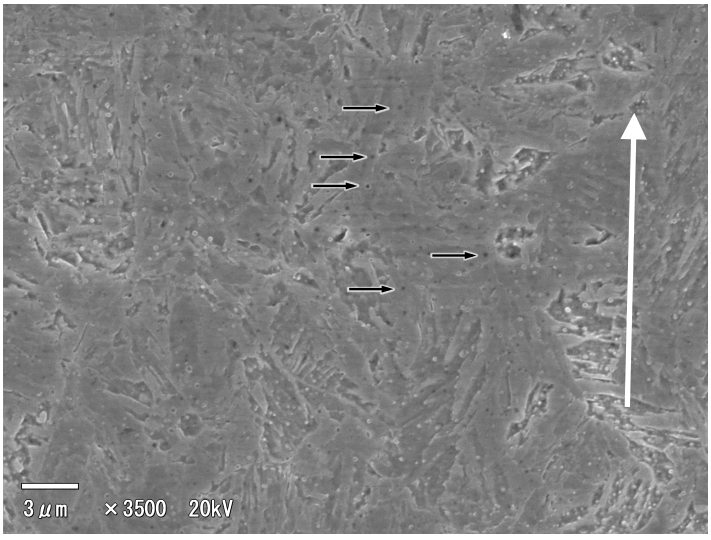


Figure 6.12: As-fabricated microstructure observed by scanning electron microscopy. Image at 3500x magnification. Surface etched using Fry's reagent. The large white arrow indicates the building direction. Small black arrows identify possible eutectic ferrite.

6.4 Transmission Electron Microscopy

Observations of the dislocation structure, phases, and the lath geometries of martensitic microstructures are best made by transmission electron microscopy. Additionally, both ferrite and martensite structures are bcc and bct with nearly

the same lattice parameters.[1] This makes them difficult to distinguish from secondary area diffraction (SAD) patterns during TEM. Therefore, observations of the dislocation and boundary morphology may be used to distinguish the structure in bright field images. Figure 6.13 shows a bright field image of the as-fabricated structure with a SAD inset. Figure 6.14 shows an enlarged view of the SAD with accompanying lattice interpretation.

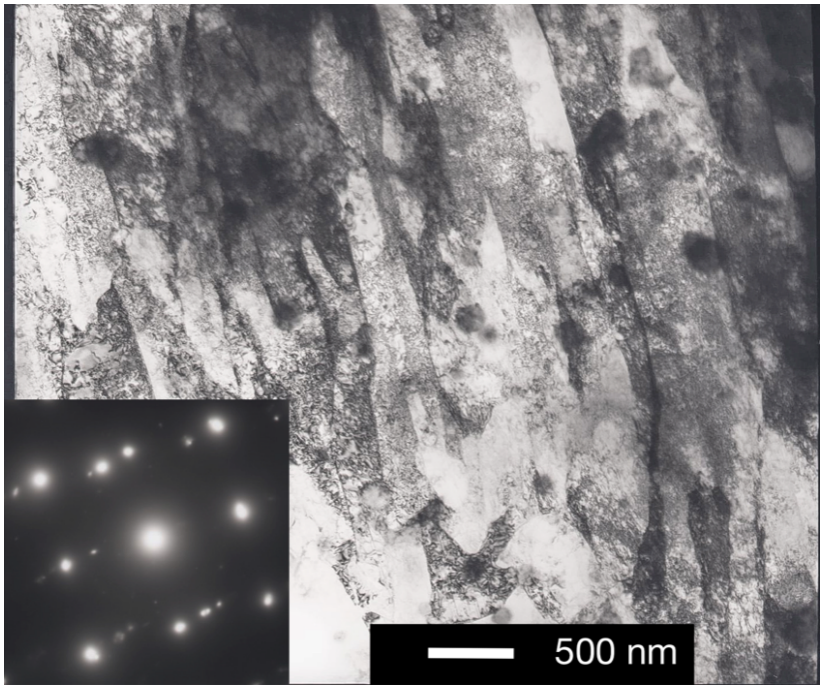


Figure 6.13: Transmission electron microscopy bright field image of the as-fabricated microstructure with SAD inset.

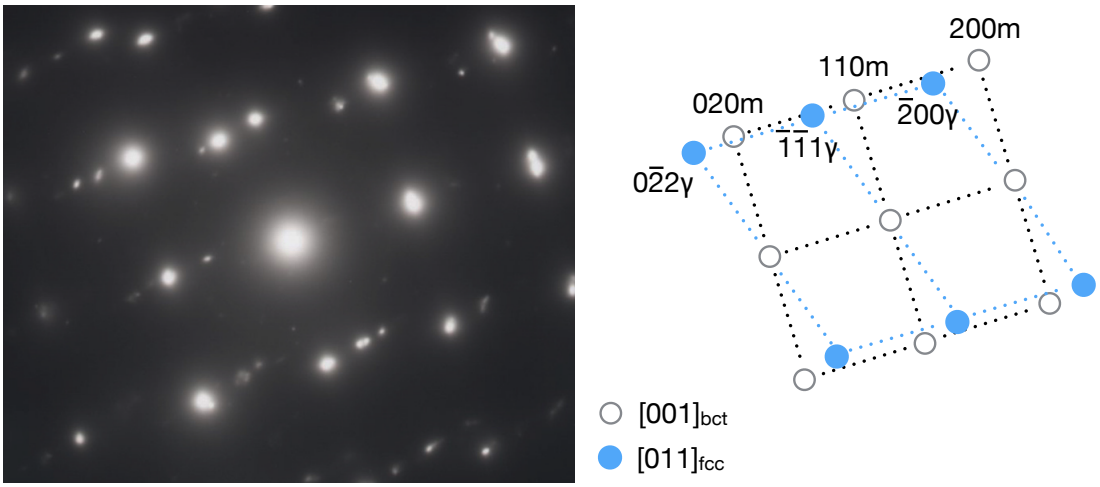


Figure 6.14: SAD pattern of the previous TEM imagery.

[1] Distortion by trapped interstitial carbon is what accounts for the difference between the bcc and bct structures. However, this difference in lattice parameter along the distorted axis is small.

From observations of the SAD pattern, the secondary phase of austenite is clearly visible as the rotated structure about the center bct. Therefore, a dark field image in the fcc reflection (without bct overlap) point is shown in Figure 6.15 with the isolated point obscured in the inset SAD pattern (Circled for reference). Between these three images the resultant lath structure is visible at higher magnification. Fine, columnar martensitic laths are observable with high dislocation densities throughout. Islands of austenite are observed to be interspersed rather than ribbon-like features occasionally observed on lath boundaries of aged microstructure. SAD imagery would suggest the presence of twinning by the secondary sources and smearing of the primary reflections. Figure 6.16 shows a magnified view of the twinning as observed in the bright field image showing the austenite grains. Twinning in austenite is not unexpected as it has appreciably lower stacking fault energy compared to martensite. Lattice strain is relieved by twinning deformation and is observable typically by TEM. Twinning within the martensite, while observed by other researchers who have also examined SLM processed 17-4 PH [32], are not immediately observed in these specimens at the magnification presented. However, again the SAD pattern does suggest their presence by the smearing of the bct spots.

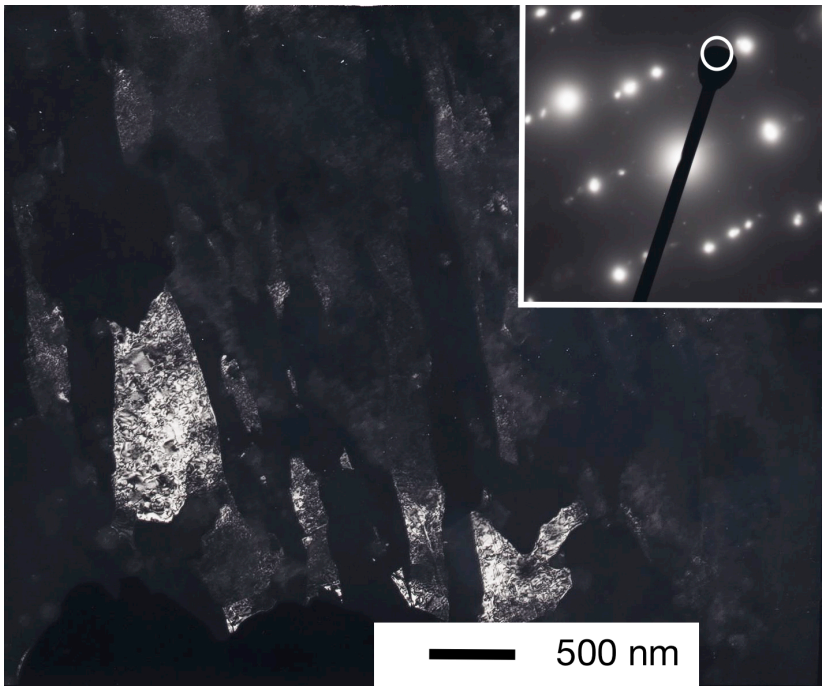


Figure 6.15: Dark field image of the fcc reflection from the previous TEM imagery. Inset is of the SAD pattern and reflected point obscured.

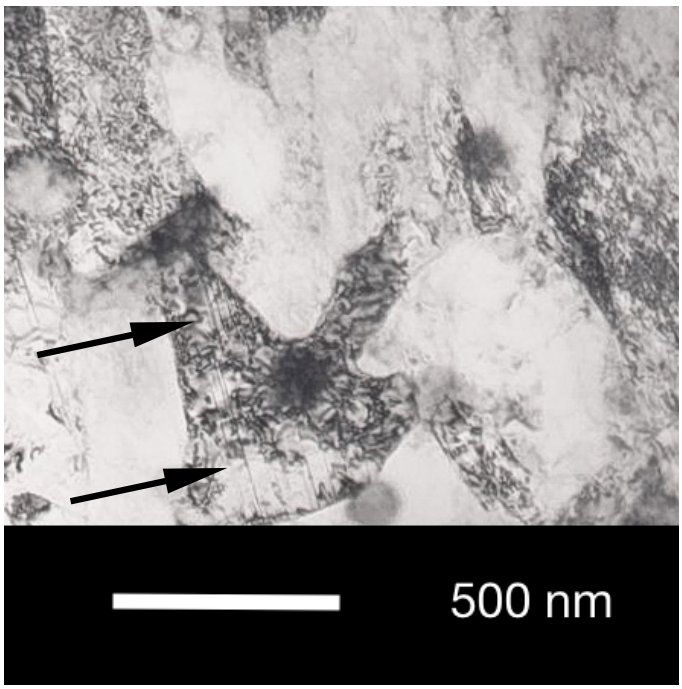


Figure 6.16: High magnification image of the bright field image shown in Figure 54. Austenite grain twinning is indicated by the arrows.

6.5 X-Ray Diffraction

In an effort to better qualify and quantify the primary lath martensite and observed metastable austenite phases, x-ray diffraction (XRD) was performed on the as-fabricated microstructure. Figure 6.17 details the normalized spectra of the vertical and horizontal reference planes respectively (Cu K(α) source was used). It is understood that mechanical methods used to prepare specimens for XRD analysis may unintentionally disturb the austenite grains and initiate a transformation to martensite. Therefore, measured peak intensities and the corresponding volumetric fractions of the phase are at best under-reported to the actual values.

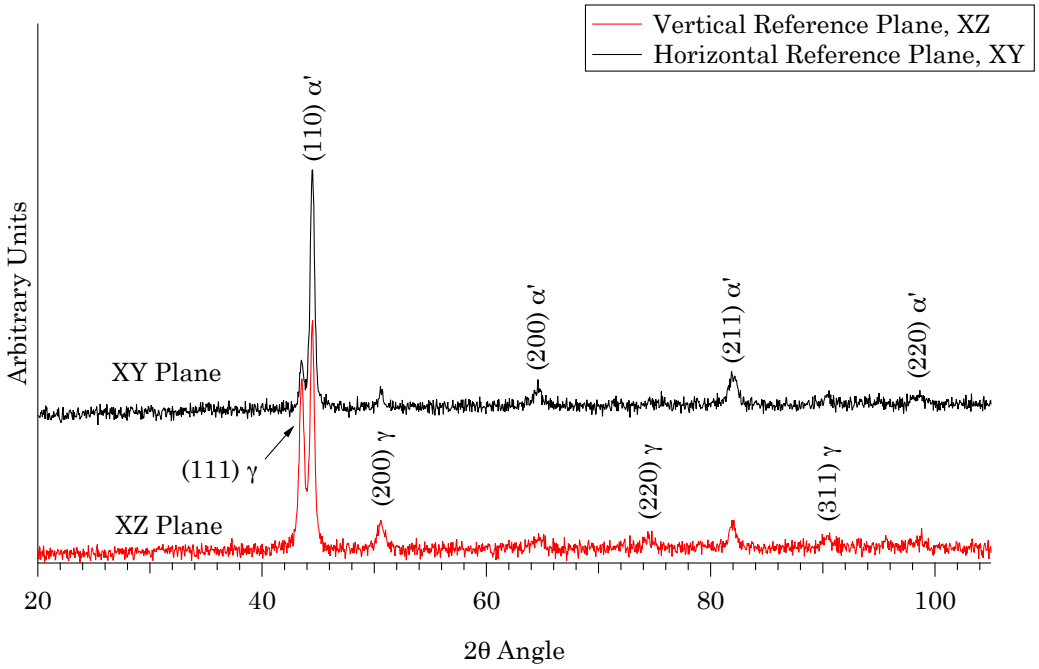


Figure 6.17: XRD spectra as measured in the horizontal (XY) and vertical (XZ) reference planes of an as-fabricated specimen.

The two spectra indicate a mild texturing between the austenite based on the relative height differences for the primary austenite peak at the miller index (111). It is likely that the texturing is an indication of the directional nature of the thermal gradients that result during cooling and the preferred alignment of the (111) to that of the cooling direction. Texturing and spectra patterns observed of the material samples prepared in this study did not exhibit the severity of texturing observed by Murr et al [32], but in that case different operating environments and processing parameters likely altered the cooling rates and liquid-solid metal kinetics (the author does not identify processing parameters). But comparisons between optical micrographs of that study and this one indicate a much less directional microstructure in material produced as part of this study. Comparison of processing conditions to establish a root cause was not possible because of their absence in the published literature. Based on quantitative Rietveld analysis of the measured XRD spectra, the volumetric phase fraction of austenite was measured to peak at 51.6 percent for material fabricated as part of Batch One. In the case of Batch Two, volumetric fraction measurements were repeatable at approximately 36 percent. Previous researchers reported retained austenite as high as 72 percent [69] using similar SLM production techniques. It is clear that the processing conditions have a tremendous effect on the resultant microstructure and phase fraction and

morphology, but again the processing parameters were unavailable for comparison.[2]

Figure 6.18 shows an XRD spectrum for measurements made of the upper-most layer in a bulk material sample. This spectrum indicates an absence of the fcc austenite structure. Suspected seasons for the difference between this final layer and the internal, bulk material will be discussed in the discussion section.

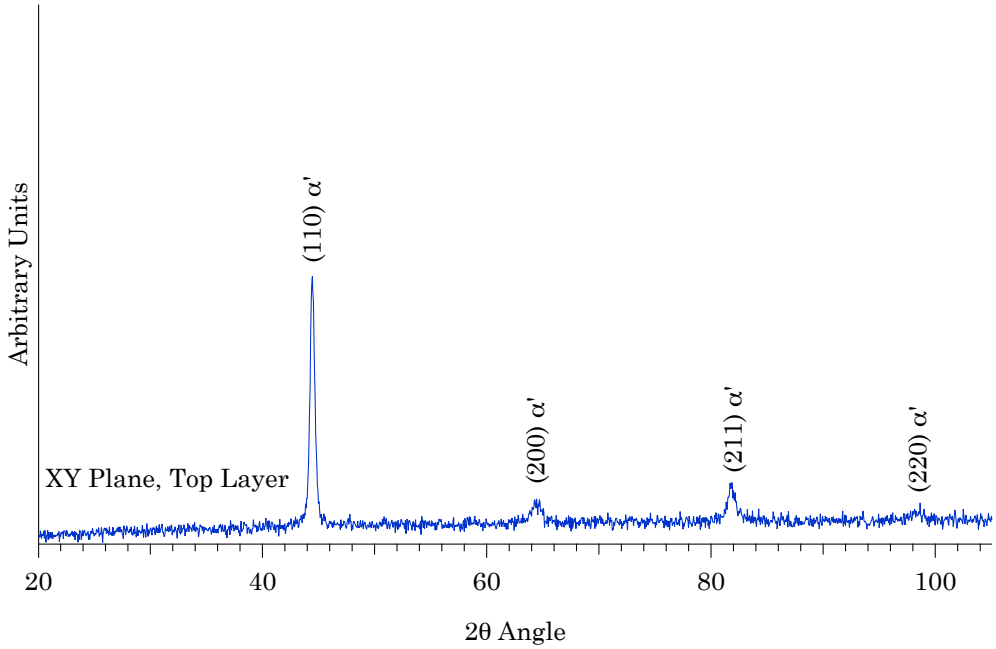


Figure 6.18: XRD spectrum for the upper-most layer of an as-fabricated specimen. Measurement was made in the horizontal reference plane, XY orientation.

Additional measurements of samples solution heat treated to the Condition A state show no traces of retained austenite. Thermal processing at 1040 °C is sufficient to relieve the thermal stresses associated with the retention of austenite. Upon cooling to room temperature, the resultant microstructure is fully martensitic.

6.6 Electron Probe Micro-Analysis (EPMA)

In Chapter 4 the possibility of stabilizing austenite to room temperature via redistribution and segregation of the solute elements was discussed. This chemical stabilization effectively lowers the M_S and M_f temperatures and may permit the retention of austenite at room temperature. So as to investigate the possibility of austenite retention by these means, material samples were

[2] Other authors do not commonly discuss material sample preparation techniques. It is not clear if their specimens are exposed to the same potential for accidental initiation of the martensitic transformation.

prepared for electron probe micro-analysis (EPMA). Measurements made by EPMA are similar to those by electro dispersive x-ray spectroscopy, but are typically done for a discreet set of elements and can quantitatively measure their concentration over a one or two-dimensional region (line or area scan). These can then be recompiled to examine the distribution as a function of the morphology within a spatial reference frame.

Figure 6.19 shows scans made of a region 250 by 50 μm, oriented in the vertical reference plane of an as-fabricated specimen. The top-most surface of the specimen is within the first 20 μm of the upper edge of the image.[3] The building direction during SLM is from the bottom to the top of the images. All of these images are of the same region (scanning is made simultaneously or with additional passes by the electron probe). The scanning resolution per pixel is 500 nm, square. The excitation area of the electron beam was approximately 1 μm in diameter. Figure 6.19 is for the elements of carbon, copper, nickel, chromium, niobium, and silicon.

Analysis of these qualitative images reveals some other information about the microstructure not readily observable via optical or scanning electron microscopy. Carbides and other intermetallic inclusions are easily recognizable as point sources of high intensity in carbon, chromium, niobium, and silicon maps. The size is relatively small compared to larger inclusions observed in the reference material, on the order of 10 μm in diameter. Absence of measured intensity in both the nickel and copper maps also show the negative relief of where these inclusions are located. Large-scale segregation of all alloying elements is not observed as a result of the liquidus to solidus phase transformation. However, mild banding and medium-scale segregation is observed along the fusion boundaries for both the nickel and copper element maps. Concentration gradients indicate an increase in concentration within solid solution of both of these elements just inside the fusion boundary and a similar depletion just outside. The exact boundary between the liquid and solid substrate is difficult to determine based on these measurements. Figure 6.20 is an image taken via SEM of this microstructural feature as etched (but not of the region scanned via EPMA).[4] This image does not identify a sharp boundary, but rather a banding effect in the etching of the specimen.

[3] Edge effects associated with the specimen geometry are certainly present and concentrations at this location are suspect. This is especially true for measurements made of carbon.

[4] Etching surfaces prior to EPMA analysis may artificially shift measured intensities for each of the elements. Therefore, samples prepared for EPMA analysis must be polished to a high degree of planarity.

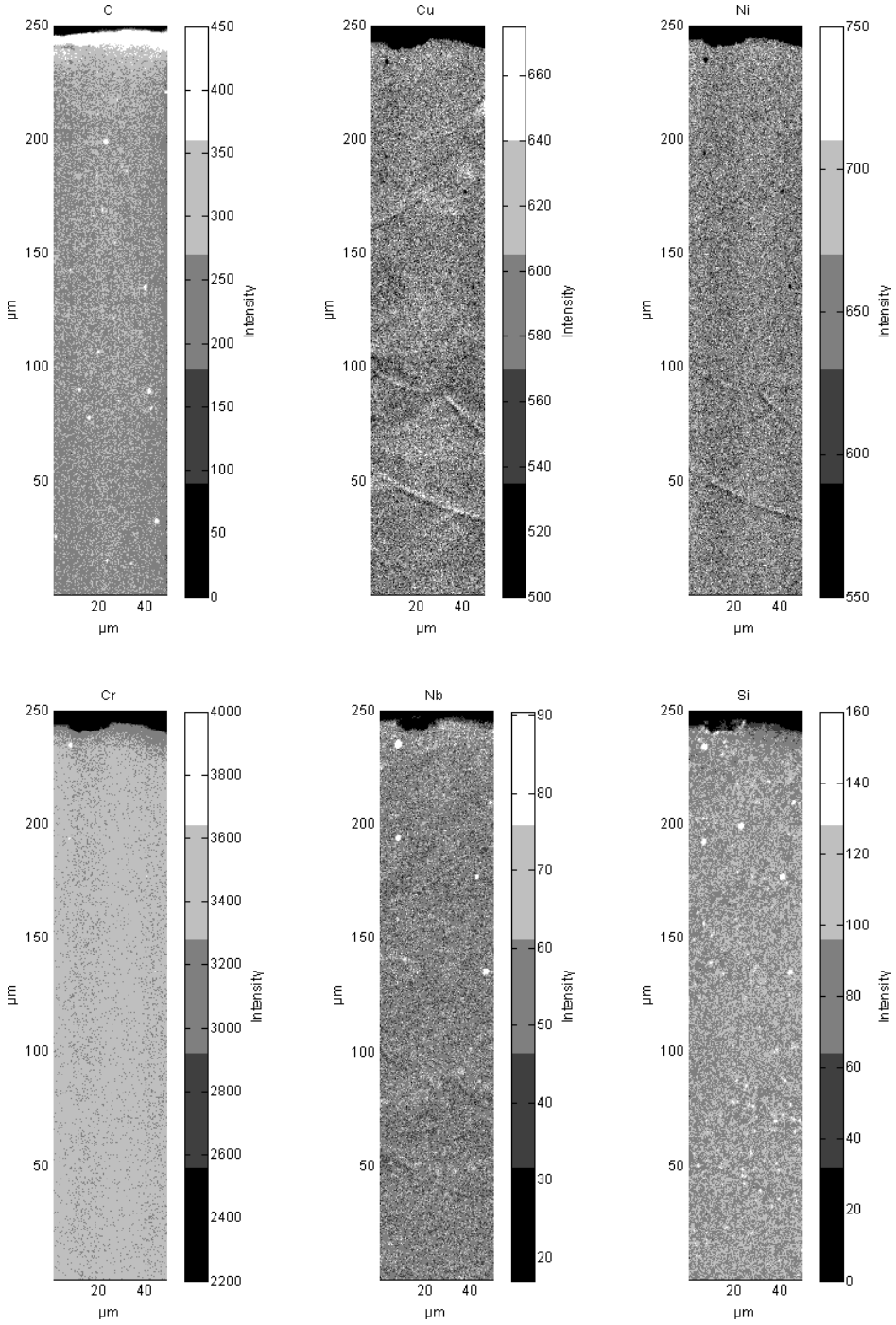


Figure 6.19: Qualitative mappings over a 50 x 250 μm area in the vertical reference plane of an as-fabricated material sample. Maps are for C, Cu, Ni, Cr, Nb, and Si.

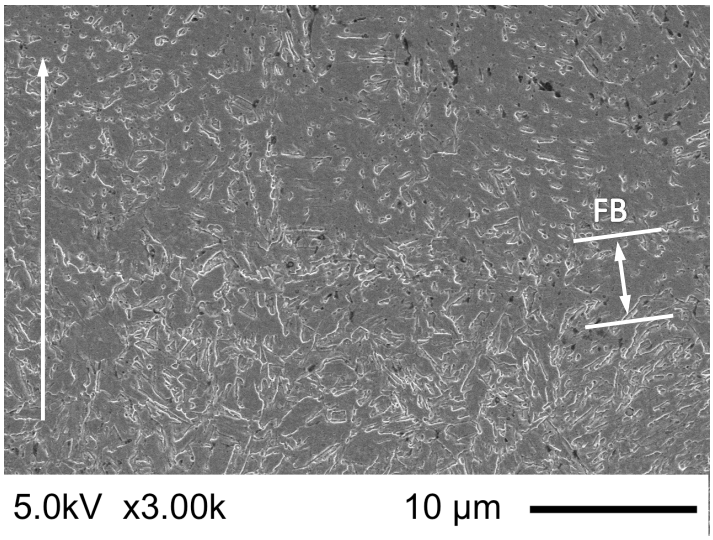


Figure 6.20: SEM image of the as-fabricated microstructure observed in the vertical reference plane. The building direction is indicated by the white arrow. The fusion boundary is marked with "FB". Sample was electro-etched using a solution of Oxalic acid in water for approximately 30 seconds.

Scanning and imaging resolution limitations prohibits identifying micro-scale segregation on the order of individual lathes or grains due to the refined microstructure. Excitation area of the electron beam in EPMA measurements is on the order of 1 µm in diameter. At best, these scans can identify the segregation behavior in a collection of several grains at any given measurement. However, the concentrations observed for both nickel and copper deserved a more thorough measurement. Figure 6.21 (a) through (c) show a secondary square-area scan of copper with quantitative linear scans across one highly contrasted fusion boundary for both copper and nickel. The scanned area map has been rotated to show the building direction as left to right. The corresponding line graphs are for concentration measurements of the two measured elements by percent weight.

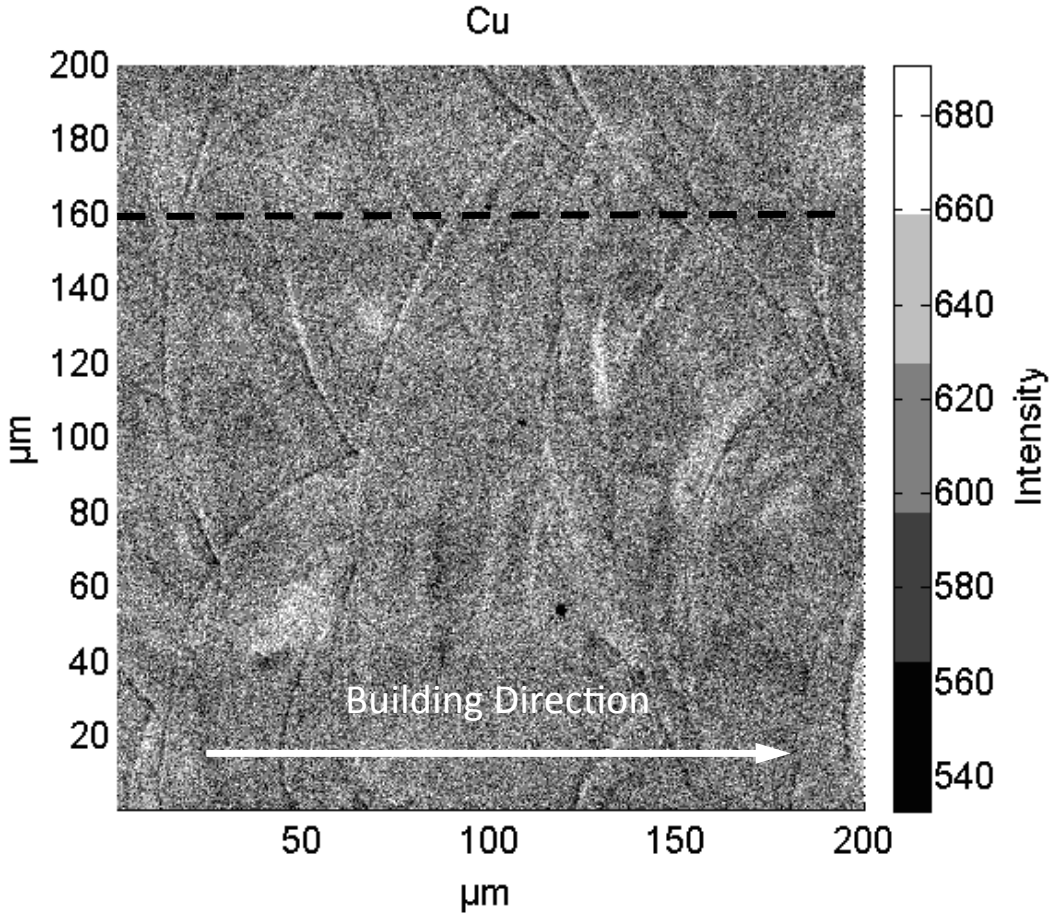


Figure 6.21 (a): Large 200 x 200 μm scanned area located below the surface of an as-fabricated specimen in the vertical reference plane (XZ). Intensity mapping data is for copper. The white arrow indicates the building direction. The dashed line represents the linear, quantitative scan performed for both copper and nickel as shown in Figure 6.21 (b) and (c).

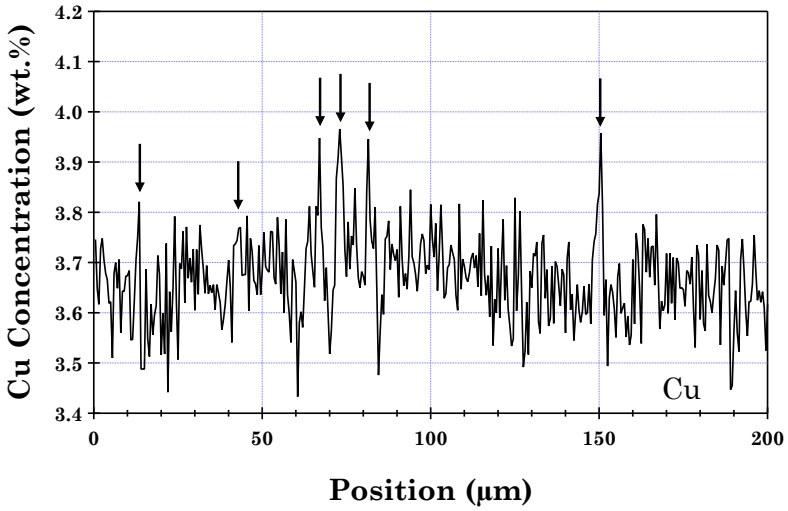


Figure 6.21 (b): Concentration by percent weight of copper along the linear scan shown in Figure 6.21 (a). Fusion boundaries indicated by the arrows.

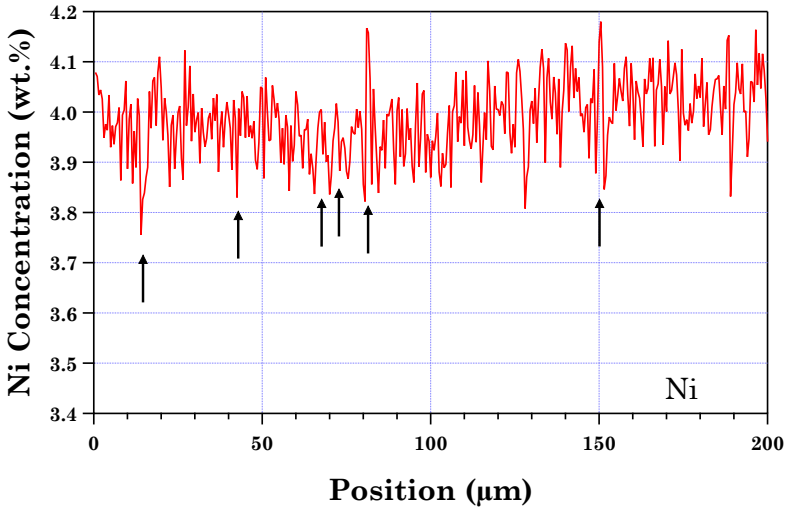


Figure 6.21 (c): Concentration by percent weight of nickel along the linear scan shown in Figure 6.21 (a). Fusion boundaries indicated by the arrows

Both copper and nickel act as austenite stabilizers of moderate strength (not as strong as carbon and nitrogen). Their concentration within the material is of interest to the possible intermediate-scale retention and morphology of austenite. However, the measured percent weight for both of these elements, while detectible here, translate into relatively limited changes in the M_S temperature. From calculations made using the empirical relationship generated by Eichelman and Hull [24] (Equation 4.1), an approximate 61 °C change is predicted in the M_S temperature for every 1 weight percent change in the concentration of nickel. However, a change in one solute element is typically compensated with a relative change in another across a moving solidification front [70] – the mechanism for this segregation observed here. In this case, chromium is the likely filler solute (as its weight percent is nearly 17%). If

changes in concentration of either copper or nickel are mirrored with opposite concentration changes of chromium, the effective change in M_S as predicted by the empirical relationship is less than simply varying the expression for concentrations of nickel and or copper alone. So, the magnitude of the predicted change in M_S that would result with the observed concentration changes of the austenite stabilizing elements observed here is likely to be small. If the relative concentration change of nickel (for example) is balanced with an equal change in chromium, the real change in the M_S temperature is only 19 °C per percent weight (for a one-to-one equivalency in concentration). And considering the concentration changes observed here via EPMA and knowing the approximate start temperature for the powdered 17-4 PH chemistry, this still puts the M_S temperature above room temperature. Austenite should not be stabilized at the percentages measured by XRD, throughout the bulk material, largely as a result of the segregation observed at the fusion boundaries.

For completeness, Figure 6.22 (a) and (b) show both a qualitative copper and nickel map as imaged in the horizontal reference frame. These maps also clearly show fusion boundaries, but within a different oriented view of the material sample. A wave-like structure in copper concentration is observed within the central region of one scan pass as it is bounded by the two concentration gradients on either side. Changes in concentration within the central regions of individual scan paths can be attributed to the liquid metal flow prior to solidification. And as a result of rapid solidification, the larger-scale solute segregation that might be common with dendritic or bainitic formations in cast steels with slower cooling rates is not observed.

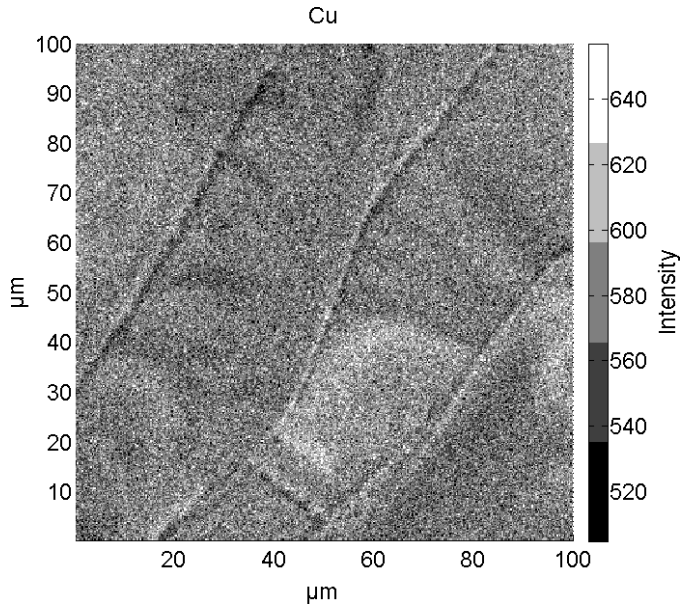


Figure 6.22 (a): Moderately sized scanned region of 100 x 100 μm of an as-fabricated specimen in the horizontal reference plane (XY). A qualitative concentration of copper is represented.

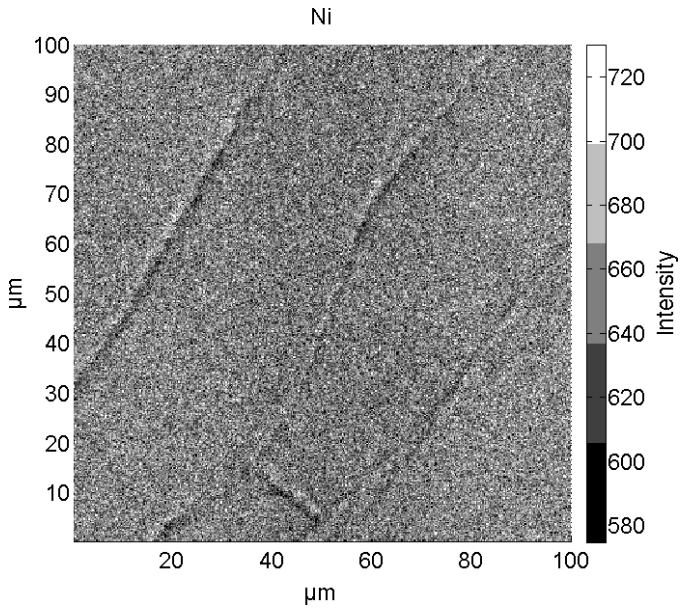


Figure 6.22 (b): Moderately sized scanned region of 100 x 100 μm of an as-fabricated specimen in the horizontal reference plane (XY). A qualitative concentration of nickel is represented.

6.7 Discussion

Observations of the microstructure directly by optical microscopy indicate a highly refined grain structure throughout. Within the fine grains a primary lath martensitic structure exists alongside a relatively high volume fraction of retained, metastable austenite. TEM imagery highlights the high dislocation

densities characteristic of martensite and establishes grain shapes for the retained austenite. EPMA measurements of solute element concentrations do not indicate any large-scale segregation of austenite stabilizing elements as a result of SLM. This lack of evidence at gross alloy segregation throughout the structure effectively eliminates the possibility of chemical stabilization being the primary mechanism for this phase's retention at room temperature at volumetric fractions as large as measured. The only other alternatives would be thermal or mechanical stabilization. And, because this material has not undergone any elevated temperature processing that results in changes of the M_S temperature similar to those previously described, thermal stabilization may be effectively eliminated. This leaves mechanical stabilization as the remaining, possible mechanism for the room-temperature retention of austenite.

Other researchers have noted through both experimental [67] and numerical simulation [71] the propensity for directed energy-based, layer AM methods to introduce significant thermal stress and resultant strain within processed materials. It can be concluded that the residual thermal stresses associated with the process are primarily responsible for retention of austenite. XRD analysis establishes a couple of supporting pieces of evidence for this argument. Measurements made of the upper-most surface indicate the absence of austenite. The last layer is effectively unbounded with a free surface. Thermal expansion and contraction is not limited in the way that previously consolidated layers are. From this, it can be asserted that the martensitic phase transformation is permitted to occur completely at this final layer. Similar observations are reported by Facchini [72]. Solution heat treatment for as little as 30 minutes has been demonstrated as an effective means to eliminate this phase by relaxing the residual thermal stresses. As will be shown in the following section, this solution heat treatment does not negatively impact the strength characteristics of the refined microstructure; however, in Chapter 8, the mechanical performance differs significantly when austenite is permitted to remain present. Other researchers have investigated the general critical temperature at which thermal stresses are relieved by measuring warpage in thin plates produced of 17-4 PH by SLM [67]. Their observations point to a temperature as low as 650 °C as a possible stress relief heat treatment[5], but still note the retention of high volume fractions of austenite. Retention of the phase is believed to be possible until the temperature exceeds the transus temperature of the α-γ (primary ferrite to austenite) transformation of 727 °C for 17-4 PH. The observations regarding the

[5] Also, this temperature is recommended by one of the SLM machine suppliers for this material.

thermal stress relieve are somewhat supported by experimental work presented in Chapter 8.

7. Experimental Investigation I:
Initial Characterization of Mechanical Properties and Anisotropy

7.1 Purpose

As has been introduced, the means and methods by which material processed by AM greatly influences the resultant microstructure and corresponding mechanical properties of fabricated bulk material. It is for this reason that a thorough mechanical evaluation of 17-4 PH be performed. Characterizing the material produced using the specific machine parameters is critical to understanding the inherent effects of SLM on material produced by it (the development of these machine parameters is outlined in Appendix B). The purpose of this initial experimental investigation was to determine basic mechanical properties and identify any performance characteristics directly affected by the additive layer manufacturing method.

7.2 Introduction

Mechanical characterization of engineering materials may be performed across a wide variety of machines and testing methods. The most fundamental of these testing methods is the uniaxial tensile test. From this single testing method, much about the material may be understood and further extrapolated using more complicated or detailed experimental approaches. But from the humble tensile test, properties such as yielding behavior, local and uniform plastic deformation, strain hardening, ultimate tensile strength, deformation mechanics, and elongation, just to name a few, may be established. And it is through this rigor that SLM processed 17-4 PH material was subjected.

Because this research effort focused on an already established material chemistry processed in a relatively new manner, it was useful to make a direct comparison to a reference baseline. And rather than simply reference established literature for this comparison, parallel testing using specimens of the same chemistry produced by traditional means and processed in parallel to the SLM material was not only useful but prudent. As previously outlined, this reference material was commercially sourced hot-drawn rod meeting the same industry standards for 17-4 PH chemistry. All preparatory processing and testing performed on the SLM-fabricated material, mechanical and otherwise, was also performed on a duplicate set of specimens produced from this reference material.

A particular focus of this experimental investigation was identifying any directional component to the mechanical behavior of SLM processed 17-4 PH. As previously outlined, the fabrication method was layer-based in an additive fashion; it is quite plausible to encounter mechanical behavior and anisotropic residuals within the material that reflects this processing method. And leveraging the background of faculty and equipment available, this initial experimental effort sought to identify any strain rate sensitivity inherent to 17-4 PH produced via SLM. Similarly, this effort sought to identify any differences from those expected and observed when compared against the reference material.

Prior to outlining the observations from the experimental work, the following sub-sections will discuss the associated theory of thermally activated plastic deformation, strain rate sensitivity, and provide some initial background on non-standard mechanical evaluation (namely, testing using a split-Hopkinson tensile bar). Following the theoretical discussion, the experimental procedure and associated results will be discussed at length.

7.3 Theory

7.3.1 Thermally Activated Plastic Deformation [51]

The plastic flow of material under an applied load may be treated as a thermally activated process [73]. The interrelationship between the activation energy of plastic deformation and stress, temperature, strain, strain rate, and secondary phase concentrations are commonly looked to for establishing the basis of theoretical models pertaining to dislocation mechanics in solids. Experimental work relating the temperature and strain-rate dependence of flow stress can show a link to dislocation behavior within the material.

It is useful to describe this system in a symbolic way. Taking the aforementioned relationships further, let a system under load be described as having an externally applied shear stress[1]. This may be represented as τ. Internally, there exists resisting forces acting counter to the applied external load. These may be collectively represented as τ_i. The sum of the two, external and internal shear stresses symbolically represents the effective shear stress, τ_{eff}, acting upon the material under inspection ($\tau - \tau_i$). These internal, resisting

[1] It is useful to remember that shear stress can be commonly defined as $\tau = \sigma/2$, where the shear strain is similarly approximated as $\gamma = 1.4\varepsilon$.

shear stresses can be further categorized as either long-range or short-range obstacles to plastic deformation. In the case of long-range obstacles, barriers to plastic deformation are too great for the naturally occurring thermal fluctuations to assist any dislocation in overcoming it. Short-range obstacles, on the other hand, are capable of being surmounted by these same thermal fluctuations. These typically represent some obstacle within 10 atomic diameters away from any particular dislocation. As a result of being uninfluenced by naturally occurring thermal fluctuations, barriers to dislocation motion of the long-range variety are also referred to as *athermal barriers*. These types of obstacles are not affected by variations in temperature or applied strain rate (except for the variation of flow stress as it applies to the decrease in shear modulus G with increasing temperature). The internalized stress fields associated with these long-range barriers can be notated as τ_G. Stress fields from other dislocations within the material and large, incoherent secondary-phase particles contribute to the magnitude of τ_G. When examined with respect to a material's history, τ_G is largely dependent on the composition of the material, thermal processing, and dislocation structure (inherent or developed via applied work). Short-range obstacles as previously introduced have the appropriate name of *thermal barriers* and exhibit the opposite sensitivity to temperature compared to those of the athermal variety. These barriers to dislocation motion are strongly influenced by either the applied strain rate, temperature or both. The stress fields stemming from short-range barriers may be notated as τ^*. Sources that contribute to τ^* include the stress fields of coherent particles and solute atoms, the Peierls-Nabarro force needed to move a dislocation within the lattice structure, cross slip, dislocation climb, and other intersections between dislocations present.

$$\tau_{eff} = \tau - \tau_i \tag{7.1}$$

Total internal stresses may be expressed as a sum of both the athermal and thermal components and is given by:

$$\tau_i = \tau_G + \tau^* \tag{7.2}$$

To explain this phenomenon further, a schematic illustrating the resistance to flow over a fluctuating long-range stress with wavelength λ is presented in

Figure 7.1. Short-range, thermally dependent stress fields are illustrated as perturbations in the long-range stress wave. The sum of these internal stress fields may work to enhance or impede dislocation motion. A positive value for τ_i would represent a resistance to dislocation motion, while a negative value would enhance it. When determining rate-controlling mechanisms for dislocation motion, the largest obstacles will establish the energy requirement necessary for continued plastic flow. Said another way in the context of the presented schematic, the magnitude of peaks of the short range obstacles atop the crest of the long-range varying stress field will determine the rate controlling process of continued plastic deformation.

Short-range thermal barriers and the corresponding stress fields are sensitive to temperature. For example, if the temperature of the system were at absolute zero, 0 K, there would be no thermal fluctuations to assist the applied stress in overcoming short-range obstacles. Therefore, the applied stress, τ, would need to be equal to or greater than the greatest barrier found at the top of a long-range stress wave and any additional short-range, local stress field. The sum of these two internally resisting stresses would be τ_0 and is illustrated in Figure 7.1. However, with temperature above 0 K the naturally occurring thermal fluctuations present would assist the applied stress in overcoming these short-range obstacles. And with ever increasing temperature, the needed applied stress for continued dislocation motion would decrease. The red region of Figure 7.1 indicates this difference between the applied stress and that needed by thermal fluctuations. A limit exists where $\tau = \tau_G$ and all short-range obstacles are overcome by the supplied thermal fluctuations. At this point, all internally resisting stress fields are determined to be athermal in kind and independent of applied temperature or strain rate.

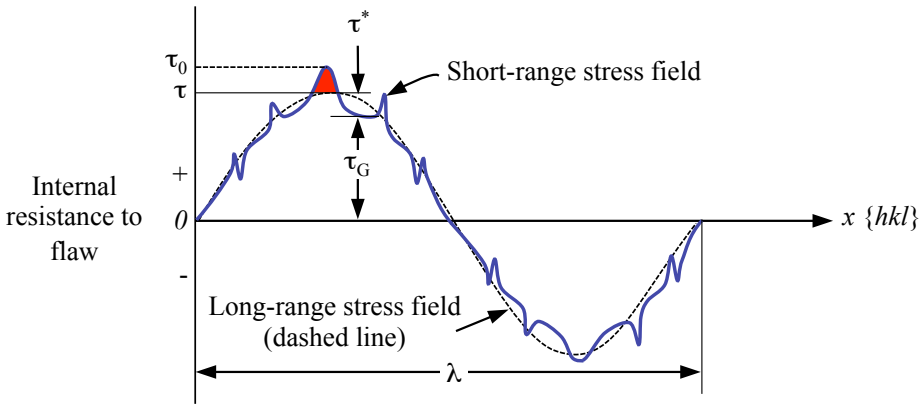


Figure 7.1: A symbolic representation of the long-range and short-range obstacles to

plastic deformation. Short-range obstacles are indicated by small variations in the general sinusoidal curve representing the long-range character of the material. The dashed line indicates the idealized long-range resistance to plastic deformation. (Adopted and modified from Conrad [74])

When examining these short-range barriers in detail, the seminal text by Seeger [74] appropriately outlines the energy requirements necessary to overcome them. This work describes a common type of barrier with an activation energy not described simply in terms of τ^*. Seeger examines in detail the volumetric requirements necessary for a dislocation to overcome a short-range barrier of the kind commonly referred to as a jog or a dislocation intersection. Speaking in terms described above, when τ is greater than the τ_G associated with the athermal, long-range barriers, a dislocation is positioned with a force amplitude at an intermediate value necessary to exceed the resisting force of the immediate short-range barrier. Schematically, this is illustrated in Figure 7.2 with an obstacle depicted as a rising and falling slope. Force equivalent to τ does not quite overcome the short-range barrier, but is positioned along its slope. This intermediate position is identified as x_o with the corresponding force value of F. The force value, F, is determined to be the product of $\tau^*\mathbf{b}l^*$, where $\mathbf{b}$ is the Burgers vector of the dislocation and l^* is the length influenced by the thermal fluctuation. The energy that then must be supplied to the system in the way of thermal fluctuations is characterized as ΔH and is represented as the red region of Figure 7.2. The total work done by this thermal fluctuation across this barrier can similarly be described as

$$W = \tau^*\mathbf{b}(x_0^* - x_0) = \tau^*\mathbf{b}d^* \tag{7.3}$$

$$\Delta H = \int_{x_0}^{x_0^*}\left[F(x) - \boldsymbol{\tau}^*\mathbf{b}l^*\right]dx = \Delta H^* - v^*\boldsymbol{\tau}^* \tag{7.4}$$

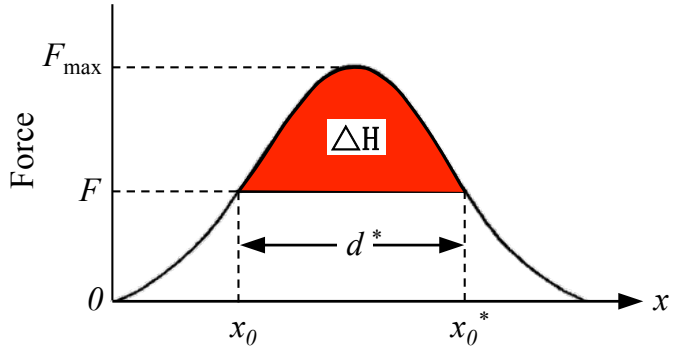


Figure 7.2: A schematic representation of the force necessary to overcome a short-range obstacle with respect to its one-dimensional linear distance x. Force required by thermal fluctuations is identified as ΔH and is shown in the figure as the red region. The externally supplied stress acting upon this dislocation, τ, is represented as the force level of F. (Adopted and modified from Conrad [74])

ΔH represents the area under the force-displacement curve from x_0 to x_0^* less the work done by the applied stress when thermally activated. The term ΔH^* describes the activation energy when there is no externally applied stress. The *activation volume* over which the dislocation is perturbed by the thermal fluctuation is represented by v^* and represents the average volume of dislocation structure taking part in the deformation process at this local site. And referencing Figure 7.2, $v^* = l^* \mathbf{b} d^*$ for a process that does not vary with stress across the length l^*. For this expression, $l^* \mathbf{b}$ is the atomic area involved in the flow process and d^* is the distance the atoms move during the dislocation process. Activation volume has a definite value and related stress dependence for each atomistic process and is therefore an important quantity when characterizing the deformation mechanism through a crystalline solid.

These relationships outline the symbolic interactions between temperature and dislocation motion within a solid. However, with respect to the strain rate dependency, the effect of temperature may be described in a different manner. Equation 7.5 relates the shear strain rate with dislocation velocity and is commonly known as the so-called Taylor-Orowan expression.

$$\dot{\gamma} = \rho \mathbf{b} \bar{v} \tag{7.5}$$

Where $\bar{v}$ is the average dislocation velocity, ρ is the average dislocation density, and $\mathbf{b}$ is the Burgers vector. Both $\bar{v}$ and ρ will depend on the applied

stress, time, temperature, and prior thermo-mechanical history. The strong temperature dependence of shear-strain rate can be described as

$$\dot{\gamma} = Ae^{-\Delta G/kT} = \rho \mathbf{b} s v^* e^{-\Delta G/kT} \tag{7.6}$$

where

ΔG = the change in Gibbs free energy of the system

A = the overall frequency factor

v^* = the frequency of vibrations of the dislocation segment involved in the thermal activation process

s = the average distance a dislocation moves after every successful thermal fluctuation

k = the Boltzmann constant

T = the temperature

Furthermore, the activation volume as previously described may be related to this expression, (7.6), by the following:

$$\upsilon^* = kT\left[\frac{\partial \ln(\dot{\gamma}/A)}{\partial \tau}\right]_T = -\left(\frac{\partial \Delta G}{\partial \tau}\right)_T \tag{7.7}$$

From these expressions it can be understood that the shear strain rate maintains an exponential relationship with the reciprocal of temperature. Dislocation velocity, previously described as simply $\bar{v}$ can now by unbundled to describe its relationship with temperature. While the slowest mechanism to dislocation motion will act as the rate limiting process, one symbolically represented as being the largest thermal barrier in Figure 7.1, these mechanisms are strongly related to temperature as identified in previous section on thermal activation of dislocation motion and plastic deformation. With increasing temperature, a greater frequency of thermal fluctuations necessary to overcome barriers is made available and similarly translates into a greater shear strain rate at a given applied stress.

How dislocation motion and strain rate interact, producing macroscopic-scale behavior, can be summarized thusly. For a given applied stress where the assisting force available by thermal fluctuations permits dislocation motion, deformation will be observed. With increasing temperature, tensile testing can

measure a reduction in the applied stress necessary to produce the same resultant deformation (strain). However, these thermal fluctuations have a temporal frequency, the rate over which they may assist dislocations at overcoming obstacles. This frequency may be slower than the rate over which the stress is applied. At speeds where the thermal fluctuations at a given temperature occur at a frequency to small to assist with plastic deformation, greater applied stress is necessary to continue dislocation motion and by extension, greater plastic flow. The opposite is also true. Reduced strain rates will see over time a greater occurrence of the assisting thermal fluctuations that translate into dislocation motion. At lower strain rates a smaller stress will be measured for the same plastic deformation due to the greater time over which thermal fluctuations may assist at overcoming the greatest barriers to their dislocation motion. A material's sensitivity to this thermally activated nature of dislocation motion at these different strain rates is commonly referred to "strain rate sensitivity". Most of this discussion is made in terms of the rate of applied stress. However, most tensile testing is strain rate controlled. So, in turn, the measurement of stress required to continue plastic deformation at a given rate is measured.

7.3.2 Strain Rate Effects of Uniaxial Stresses [76]

Returning to the Equation 7.5, it may be further expanded and rewritten to the following[2]:

$$\dot{\varepsilon}^P = \mathbf{b}\rho_m(\varepsilon^P, \sigma_S)\bar{v}(\varepsilon^P, \sigma_S) \tag{7.8}$$

where again, **b** is the Burgers vector, ρ_m is the density of mobile dislocations, and $\bar{v}$ is the average dislocation velocity. The terms ρ_m and $\bar{v}$ are now notated with $(\varepsilon^P, \sigma_S)$ and said to be functions of stress and plastic strain. Standard practice is to perform tests at constant strain so as to measure strain rate sensitivity.

Strain rate sensitivity has been measured experimentally to vary significantly when defined as a function of flow stress. The following expression is typical of strain rate sensitivity analyses:

[2] The previous expression for the Taylor-Orowan relationship was written in terms of γ and τ. However, when describing macroscopic behavior, it is more convenient and relatable to speak in terms of stress (σ) and strain (ε).

$$\sigma = K(\dot{\varepsilon})^{\beta_\varepsilon} \tag{7.9}$$

where K is a constant and β_ε is the strain-rate sensitivity parameter. It may also be expressed as

$$\beta_\varepsilon = \left(\frac{\partial \sigma}{\partial \log \dot{\varepsilon}} \right)_\varepsilon \tag{7.10}$$

From Equation 7.8 it is clear when mobile dislocations, ρ_m, begin to saturate the microstructure, or if the average dislocation velocity, $\bar{v}$, becomes limited in some way, the constant-strain, strain-rate sensitivity, β_ε, will change noticeably. For many experimental works [77,78] β_ε is indeed found to increase significantly with increasing $\dot{\varepsilon}$, but typically when it exceeds 10^3 s^{-1}. However, below that range, β_ε either does not increase or the changes are irregular. Explanations for this effect include dislocation drag associated with the saturation of $\bar{v}$ or by its limitation. Previous work by Follansbee [79] using a compressive split-Hopkinson bar on face-centered cubic metals and alloys concluded that increased rate sensitivity arose from the sensitivity of *structure evolution* rather than from a change in deformation mechanism.

Figure 7.3 (a) illustrates a common method of displaying this strain rate sensitivity data. This figure illustrates the sensitivity of copper at various strains and over a range of strain rates. Similarly, Figure 7.3 (b) shows the same kind of information for Nitronic 40 and 316L stainless steels as produced in tests performed by Follansbee [79]. It is clear from these two figures the dramatic differences across the various materials for effects of dislocation motion and their sensitivity to strain rate. Copper demonstrated a clear sensitivity above 10^3 s^{-1}, while Nitronic 40 and 316L clearly show an increased sensitivity as early as 10^2 s^{-1}. It should be noted that these tests were performed under compressive loading.

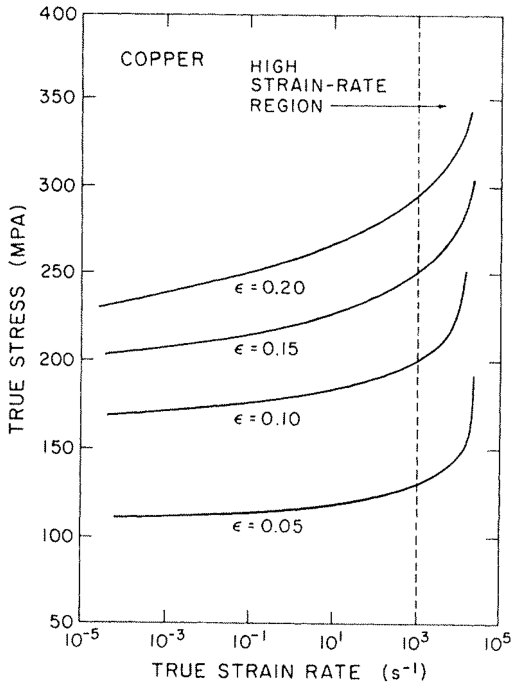


Figure 7.3 (a): Flow stress versus strain rate of copper measured at various strains. [79]

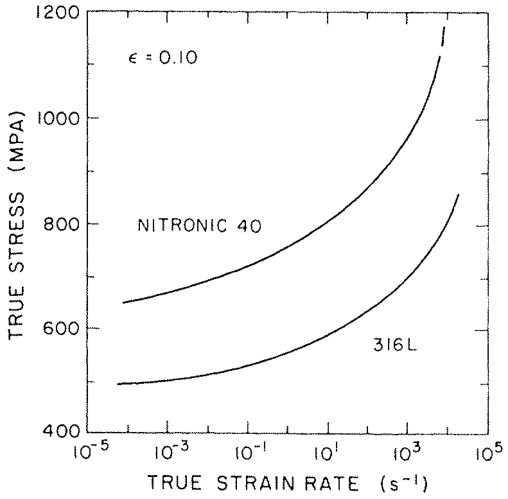


Figure 7.3 (b): Flow stress of Nitronic 40 and 316L stainless steels measured at constant strain. [79]

Strain rate sensitivity is commonly characterized for materials throughout the regions of uniform plastic deformation, excluding behavior observed during non-uniform deformation (e.g. necking of a tensile or torsional test specimen). The previous expression, Equation 7.10, may then be relied upon to characterize how strain rate sensitivity evolves over the change in uniform plastic deformation between tests at different strain rates, but at very specific points of strain (such as that depicted in Figures 7.3 (a) and (b)). However, in cases where the range of strain over which uniform plastic deformation occurs is extremely short, Equation 7.10 may be slightly modified and applied differently. The alternative version of this expression may be used to determine strain rate sensitivity for

key mechanical properties across different tests to establish differences between processing characteristics of the same material (e.g. heat treatment or aging). The mechanical property typically examined is ultimate tensile strength (UTS), regardless of the variations in strain value at which it is achieved. The altered form of the previous expression when used to evaluate strain rate sensitivity, is shown below [80]

$$m = \left(\frac{\log(\sigma_1 / \sigma_2)}{\log(\dot{\varepsilon}_1 / \dot{\varepsilon}_2)} \right) \tag{7.11}$$

Here the subscripts of σ, 1 and 2, refer to the two tests' mechanical property evaluated (again, UTS is common). For $\dot{\varepsilon}$, the subscripts refer to the corresponding strain rate over which these two tests were performed. *m* is commonly used in the literature when describing the sensitivity in this way. But as with the previous equation, this strain-rate sensitivity parameter is non-dimensional. This form of strain-rate sensitivity is especially useful when establishing a quantitative comparison of the strain rate sensitivity between various conditions of the same material tested in the same manner when flow-stress may not be easily used.

7.4 Experimental Setup

7.4.1 Choice of Tensile Specimen Design

To establish the resultant mechanical properties and strain rate sensitivity of SLM processed 17-4 PH several pieces of testing equipment were utilized. All testing was performed under uniaxial tension testing across a series of strain rates at room temperature. Strain rates on the orders of 10^{-3}, 10^{-1}, 10^{1}, and 10^{3} s^{-1} were investigated. Because of the variety in equipment required to test at the various strain rates, it is important to note that all tensile specimens were of the same design. This was done so as to eliminate any unknown size or geometry effects stemming from the test sample itself or the way it interfaced with the testing apparatuses. However, to rely upon a single test specimen geometry requires that all test equipment be capable of accepting it into whatever grips or jig-interface available. Ergo, the equipment most limiting in its ability to accept a tensile specimen determined the shape for all other tests performed. This most limiting piece of equipment was the split-Hopkinson tensile bar (SHTB)

(description to follow). The specimen geometry for this purpose and all subsequent testing is defined in Figure 7.4.

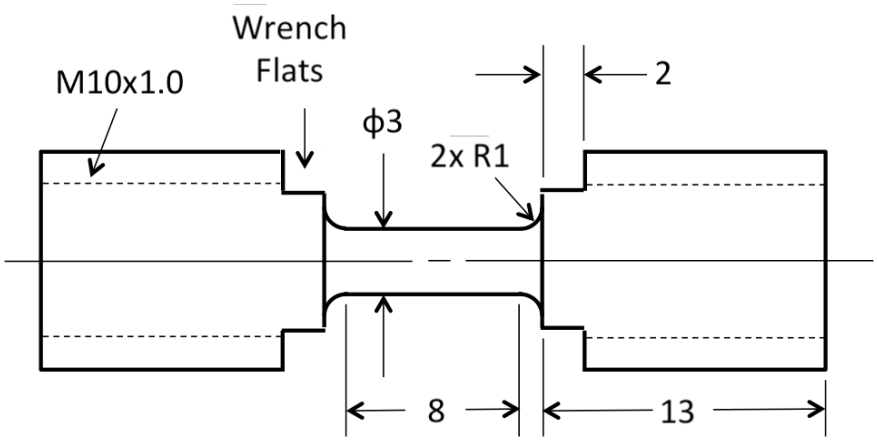


Figure 7.4: Specimen shape used across all tensile evaluation.

Understandably, the specimen shape and aspect ratio do not conform to standardized testing practices for uniaxial tension testing [81]. Typically, length to diameter ratios of specimens typically range from four or five to one (4/1 or 5/1). In the experimental work presented, the ratio used was 2.67 to one (2.67/1). However, because the SHTB and other dynamic tensile testing equipment typically operate at constant load and not constant strain rate, achieving the order of strain rate desired requires modifying the specimen gauge length appropriately. Said another way, a specimen of a design with the same cross-sectional diameter as depicted in Figure 7.4, but with a L/D ratio of 5, would require a testing speed roughly twice that required for the shorter gauge length. And because the testing apparatus is only load controllable, to achieve this speed would require a proportional increase in the applied load. Under these conditions, testing equipment is at risk of incurring damage via plastic deformation at the specimen-equipment grip interfaces. Compromises made to the specimen design are therefore reflected across all testing at all strain rates. Impacts of this unusual specimen shape will be discussed when appropriate in the results sections to follow.

7.4.2 Quasi-Static Strain Rate Testing Equipment

At quasi-static strain rates (10^{-3} – 10^{-1} s^{-1}) all tests were performed using a standard screw-driven uniaxial tension-testing machine (Shimadzu Autograph, DSS-10T-S) using a custom designed testing jig. Load was recorded via a 2-ton

load cell integrated into the test equipment with an analog output directly to a recording oscilloscope. Because tensile samples were of the geometry outlined in Figure 7.4, direct measurement of elongation from the sample in situ was not possible. Sample geometry precluded any use of an extensometer due to the narrow gauge length. Therefore, measurement of sample elongation was performed by direct measurement of the machine's crosshead displacement via a laser position gauge. The corresponding elastic stretch of the machine and testing jig was calibrated prior to test and corrected in all displacement data post-test. The same oscilloscope also collected the laser gauge output in sync with the load cell output.

7.4.3 Intermediate Strain Rate Testing Equipment

Testing performed at intermediate strain rates at the 10^1 s^{-1} order was done using a custom-built, dropping weight machine. Figure 7.5 outlines a schematic depicting this machine and its general operation sequence. This particular testing machine was designed to test tensile samples under load generated by the falling of a weight at the end of a lever arm. Because of its non-standard design, its operation will be summarized here and is reflected by the number sequence in Figure 7.5:

1. Weight attached to the end of the lever arm is adjusted to generate the desired load during the test. The lever arm is secured by the testing frame by heavy gage copper wire (soft enough to be cut manually). The test is initiated by the cutting of this wire.
2. Immediately following the release of the weight, the lever arm is permitted to fall freely.
3. While in free-fall, the lever arm pivots about the fulcrum. The vertical travel of the long-end of the lever arm is reduced by a factor of eight and is reflected by the rise of the short-end.
4. The short-end of the lever arm will rise until the entire testing jig becomes restrained by the contact of the striker plate at the bottom of the testing equipment frame. Upon contact between the striker plate and the frame, the specimen and testing jig will begin to experience a tensile load with the continual fall of the unrestrained weights opposite of the fulcrum.
5. The elastic and plastic deformation of the specimen is measured by two laser displacement gauges situated 180 degrees separated about

the specimen[3]. A controller maintains these two laser displacement gauges simultaneously with data fed directly to a recording oscilloscope. An integral load cell built into the testing jig measures load experienced by the specimen. The analog output of the foil gauges contained therein are balanced by a wheatstone bridge before being fed into a strain bridge and ultimately the same recording oscilloscope.

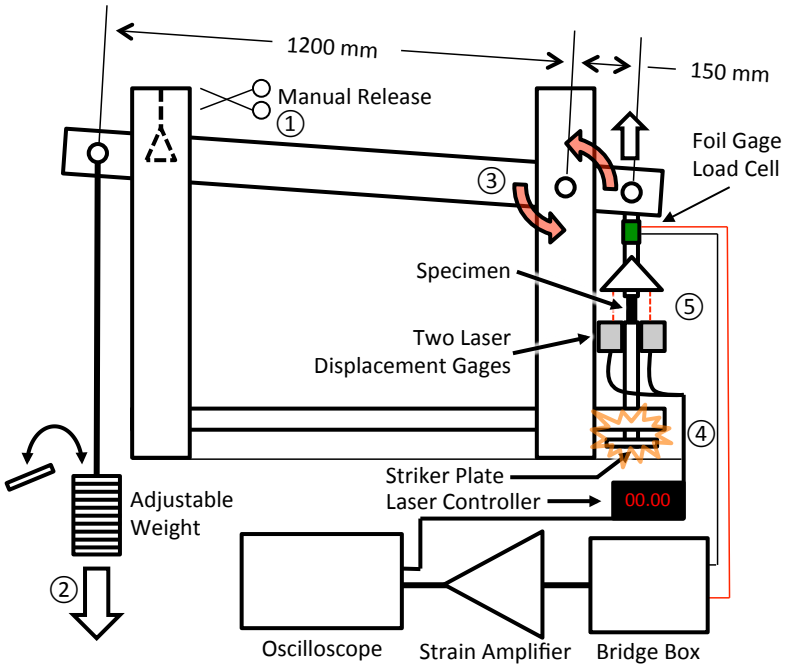


Figure 7.5: Dropping weight machine for use at testing specimens at intermediate strain rates (on the order of 10^2 s^{-1}).

Because the laser gauges utilized in this machine were situated immediately about the specimen, elastic calibration of test equipment was not necessary. Elastic stretch of the jig over the operating distance of the laser gauge was tabulated to be negligible with respect to displacement of the specimen.

The load cell was calibrated against a known analog standard using the quasi-static machine described earlier.

7.4.4 Dynamic Strain Rate Testing Equipment [82-84]

Tests conducted at dynamic rates of strain (on the order of 10^3 s^{-1}) were performed using a SHTB configured for tension testing of cylindrical test specimens with threaded interfaces. While the operation and data acquisition of

[3] Two laser gauges were used in this setup in an effort to mitigate bending observed in initial experimental trials of this testing machine.

a quasi-static test is straight forward, dynamic tests via SHTB are not as common and worth explaining in detail.

Figure 7.6 depicts a schematic representation of the SHTB used in this set of experimental work. The design of a SHTB for tensile testing of metallic materials requires two, axially supported cylindrical metal bars attached to the material specimen at its ends and located between the two bars. A third component, known as the striker tube, is a hollow cylinder situated within a concentric vessel surrounding the rest of the test equipment at one end. This vessel remains open towards the test apparatus's end, attached to a pressurized gas source and valve, and pointed away from the specimen. At strategic and carefully measured locations, strain gages in two wheatstone bridge configurations are affixed to both bars as they are attached to the tensile specimen (2 mm gage length, foil-type gages are used).

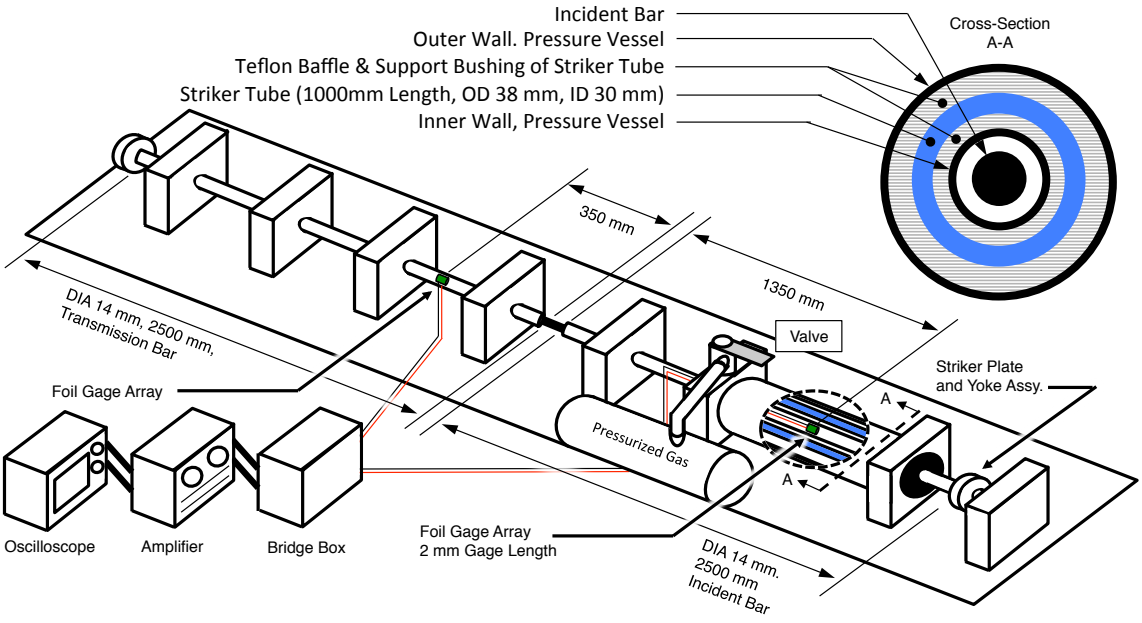


Figure 7.6: Schematic diagram of a split Hopkinson tensile bar with dimensional and configuration notation specific to this experimental setup.

Operation of a SHTB may be described as the following. Initiation of a dynamic tensile test requires the release of the pressurized air behind baffles attached to the striker tube. The striker tube then travels at high speed across the short distance between the open end of its containment vessel, along the axis of the test setup, and makes contact with a striker plate attached at the end of one of the two collinear bars. The bar affixed with the striker plate is known as the

“incident bar”. At the time of impact with the striker plate interface, a tensile pulse is generated in the incident bar and a compressive pulse is generated in the striker tube. This compressive pulse is then unloaded by its reflection as a tensile pulse traveling back down the length of the striker tube. Until this initial compressive pulse within the striker tube is unloaded by its reflection, a tensile load is maintained on the impact-end of the incident bar. The time duration for this to occur is twice the length of the striker tube divided by its sound speed.

Amplitude of this pulse is proportional to the striker tube velocity at the time of impact. The tensile pulse continues and passes the initial set of foil gages, 1350 mm distant from the bar-specimen interface (Figure 7.6, from bottom-right to upper-left). Upon reaching the bar-specimen interface, some of the initial stress pulse is transmitted into and beyond the specimen. This fractional wave is carried further into the second bar known as the “transmission bar”, while the remainder is reflected and travels back down the incident bar. The transmitted stress wave is recorded by the second set of foil gages located 350 mm further down the axis from the specimen. What fraction of the initial tensile pulse is transmitted and not reflected is principally dependent on the response of the material being tested. Figure 7.7 illustrates schematically this time-position relationship of the stress behavior throughout the SHTB apparatus. Figure 7.8 is a detailed view of the area indicated in Figure 7.7. Here the specimen-bar interface is outlined. This detailed view also illustrates the relative change in tensile behavior when a specimen of a different sound speed than the SHTB is used. Note the change in slope of the stress pulse outlines. However, for the purpose of this body of experimental work, the sound speed between the bar (304 stainless steel) and that of the evaluated material were very similar.

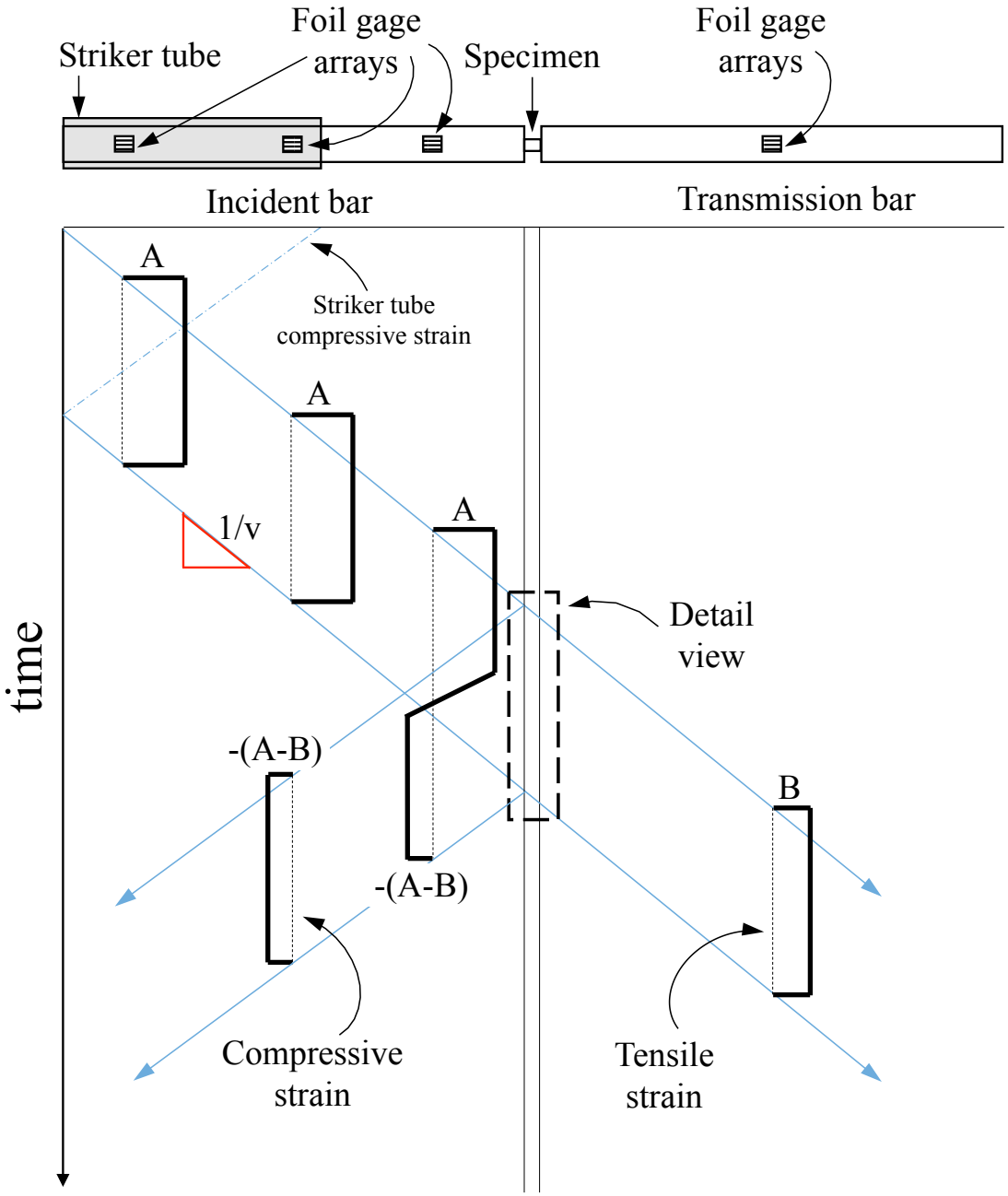


Figure 7.7: Schematic illustrating the time-position relationship of the different strain pulses, both tensile and compressive as they travel through the incident bar, specimen, and transmission bar.

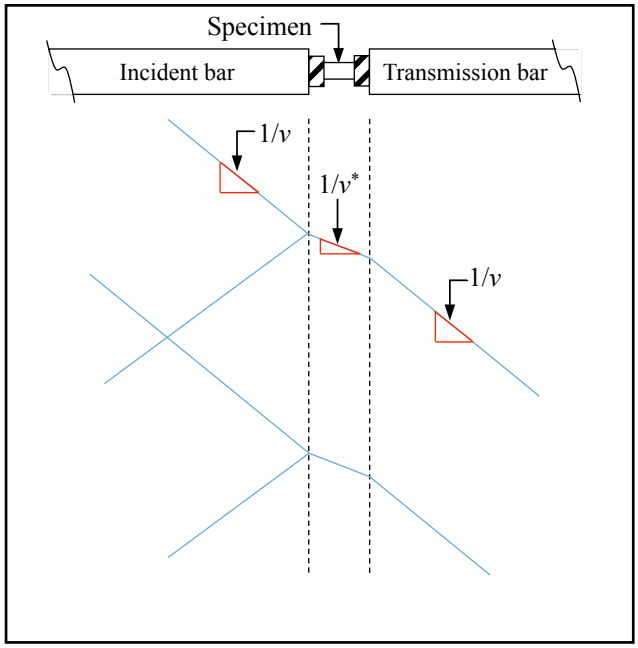


Figure 7.8: Detailed schematic of the region shown in Figure 7.7 at center.

The SHTB operates under the assumption that the strain gages affixed to both the incident and transmission bars represent the strain states of the sample as affixed to the ends of their respective bars (neglecting the effects of dispersion). As such, one-dimensional stress wave theory relates particle velocities at both ends of the specimen to the three measured strain pulses. This behavior is schematically detailed in Figure 7.9.

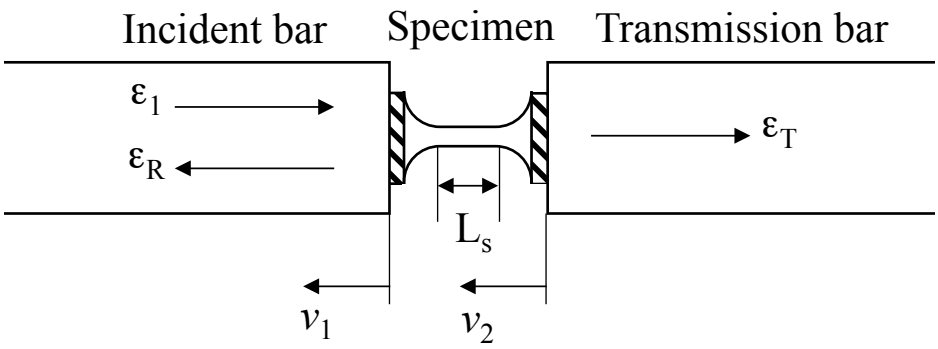


Figure 7.9: Schematic detailing the interaction of the strain pulses at the specimen-bars interface. It should be noted that the directions of V_1 and V_2 are shown in the same direction to preserve the relationship of their sign (+ or – relative to the bar axis). A negative relative velocity would travel in the opposite direction.

Particle velocities at the ends of the specimen may be summarized by the following expressions:

$$v_1 = C_B\left(\varepsilon_I - \varepsilon_R\right) \tag{7.12}$$

$$v_2 = C_B \varepsilon_T \tag{7.13}$$

Where the subscripts *I*, *R*, and *T*, represent the incident, reflected, and transmitted pulses, respectively. C_B represents the bar sound speed. The sound speed of the bar may be expressed as

$$C_B = \sqrt{\frac{E_B}{\rho_B}} \tag{7.14}$$

E_B and ρ_B are the Young's modulus and density of the bar material, respectively.

The average engineering strain rate and strain in the specimen are defined as

$$\dot{\varepsilon} = \frac{v_1 - v_2}{L_s} = \frac{C_B}{L_s}\left(\varepsilon_I - \varepsilon_R - \varepsilon_T\right) \tag{7.15}$$

$$\varepsilon = \int_0^l \dot{\varepsilon}\, dt = \frac{C_B}{L_s}\int_0^l \left(\varepsilon_I - \varepsilon_R - \varepsilon_T\right) dt \tag{7.16}$$

where L_s is the initial length of the specimen. It should be noted that the actual distance separating the bar-ends is greater than the gauge section of the tensile specimen. Exposed threads and non-constant diameter sections (transitionary radii from the gauge to the grips sections) are part of the separation distance. Therefore, these equations are only an approximation of the strain imparted onto the specimen itself. The stresses at both ends of the specimen are calculated with the following elastic relations

$$\sigma_1 = \frac{A_B}{A_s} E_B \left(\varepsilon_I + \varepsilon_R\right) \tag{7.17}$$

$$\sigma_2 = \frac{A_B}{A_s} E_B \varepsilon_T \tag{7.18}$$

where A_B and A_s are the cross-sectional areas of the bars and specimen, respectively.

The average stress state of the specimen may be described as the sum of these two expressions divided by two.

$$\sigma_{AVG} = \frac{E_B A_B}{2A_S}\left(\varepsilon_I + \varepsilon_R + \varepsilon_T\right) \tag{7.19}$$

Because the specimen is assumed to be in a state of stress equilibrium, the following condition must be met

$$\sigma_1 = \sigma_2 \tag{7.20}$$

$$\varepsilon_I + \varepsilon_R = \varepsilon_T \tag{7.21}$$

The establishment of this condition can be made by comparing the sum of the incident and reflected waves with the measured transmitted wave. Figure 7.10 shows an example of the three stress pulses as recorded by the two sets of strain gauges on the incident and transmission bars.[4]

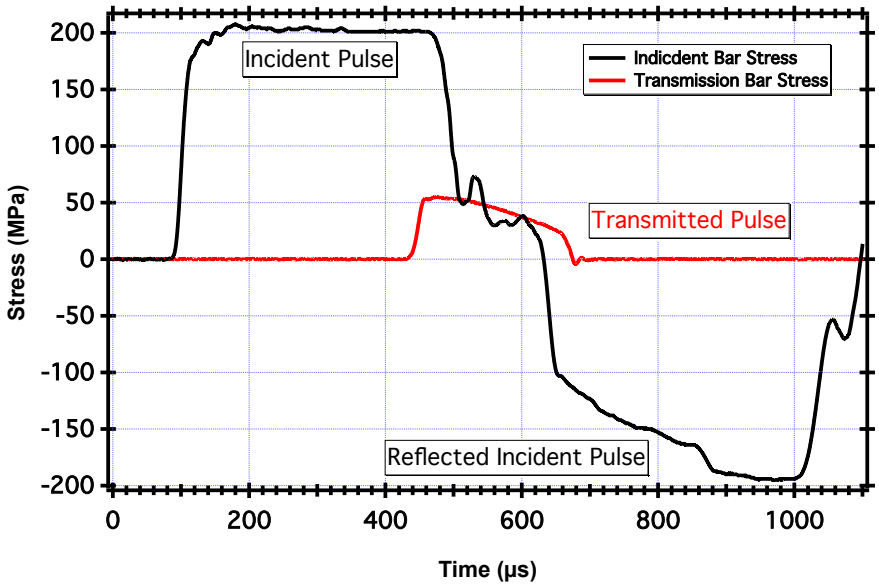


Figure 7.10: Stress within the incident and transmitted bars plotted with respect to time. Separation time between the signals is related to the physical distance between the strain gauges. It should be noted that strain gauges obviously measure strain, this plot reflects the calculated stress state within the bars using the relationship of Hooke's law and Young's modulus.

[4] Strain gauges measure strain, but for the convenience and the understanding, stress is reported here as it more meaningfully conveys the concept of a tensile load. Knowing the constant of proportionality between strain and stress (Young's Modulus), stress is simply calculated by Hooke's law.

Figure 7.11 shows the time-corrected comparison between the strain states at the ends of the incident and transmission bars. If dispersive effects are ignored, these strain states represent the states at the ends of the specimen at the time of test.

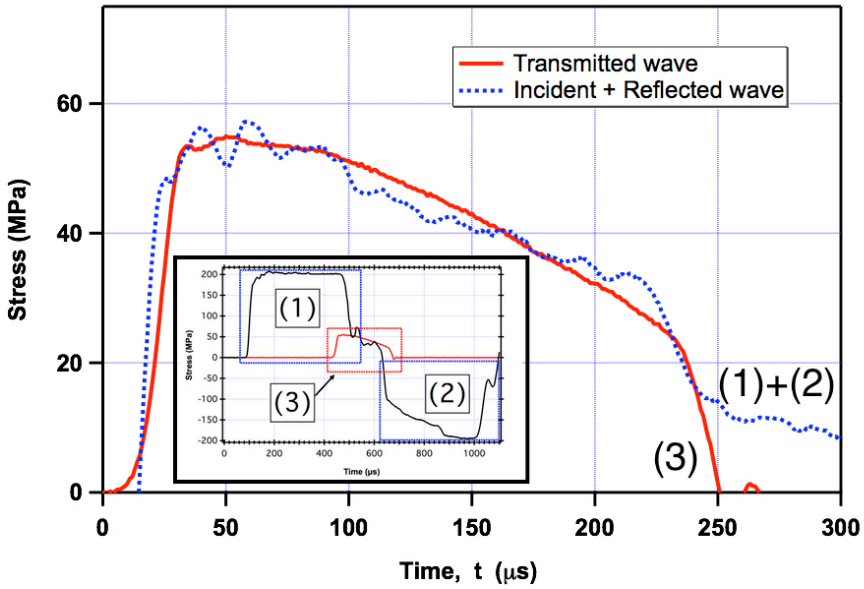


Figure 7.11: Comparison of the stress states in the transmission bar and the sum of the incident and reflected stress pulses. Specific waves are indicated by the inset figure.

Because of the relatively good agreement between the stress states observed, the conditions assumed in Equations 7.19 and 7.20 may be considered valid. With this condition met, the state of stress and strain in the specimen may be calculated by simplifying equations (7.14), (7.15), and (7.19) using (7.21) and become

$$\dot{\varepsilon} = -2\frac{C_B}{L_s}\varepsilon_R \tag{7.22}$$

$$\varepsilon = -2\frac{C_B}{L_s}\int_0^t \varepsilon_R \, dt \tag{7.23}$$

$$\sigma_{AVG} = \frac{A_B}{A_s}E_B\varepsilon_T \tag{7.24}$$

All of the above equations are derived from the conservations of mass and momentum with the assumption of one-dimensional wave propagation [82]. Further derivation of these expressions, as they relate to the idealized one-dimensional wave behavior, is available in Appendix A.

7.5 Material Preparation

7.5.1 Tensile Specimen Production

One of the aspects focused in this experimental investigation was the possibility of directionality in resultant mechanical properties. Therefore, tensile specimens fabricated from SLM processed 17-4 PH bulk material were made of two distinct orientations. Specimens were fabricated with a loading axis oriented normal to the building plane and with a loading axis oriented normal to the building direction (stacked layers are loaded in-plane for parallel oriented samples) of the SLM process were produced. These will hereafter be referred to as “perpendicular” and “parallel” specimens, respectively. Figure 7.12 depicts the general location from within the bulk material that these tensile specimens were produced to assist with understand their special orientation within the bulk material and corresponding production process.

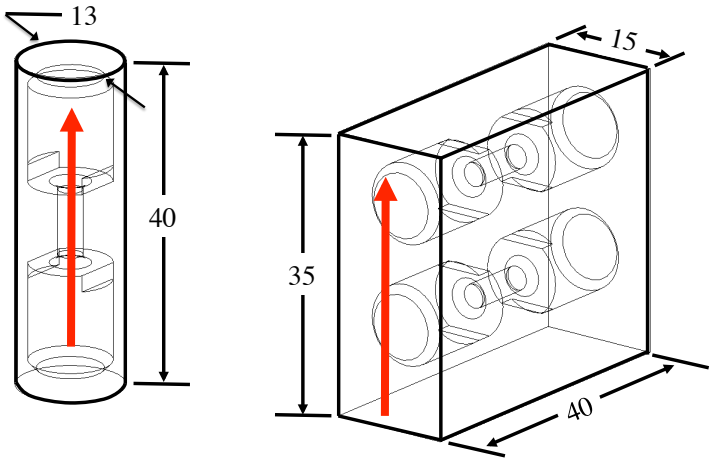


Figure 7.12: Tensile specimens as fabricated from within bulk primitives produced during the SLM process. The red arrow indicates the building direction. All dimensions are in mm.

7.5.2 Tensile Sample Thermal Processing

Prior to mechanical evaluation of 17-4 PH, all tensile specimens underwent a series of thermal processing. For this experimental investigation, all SLM and reference material specimens were treated in accordance with the material standard, ASTM A564/A564M–10 [14]. All tensile samples were initially treated to an austenizing solution heat treatment at 1040 °C for 30 minutes (referred to in the standard as “Condition A”). Half of the specimens were then further processed to the peak-age condition identified by the standard as H900. This

heat treatment was at 480 °C for 1 hour. All thermal processing was done within a quartz-chambered, vacuum electric furnace. Upon completion of the prescribed heat treatment, the furnace was opened and samples were exposed to laboratory air. Immediately following exposure to air, all samples were then quenched in water. Samples were left in the water bath until the temperature arrived to that of the water (typically municipal water is at a temperature below room temperature). This was done to ensure that the material finalized its martensitic transformation in a repeatable time scale of seconds across all specimens evaluated. The material standard makes allowances for the heat treatment to be done in air. This was not performed so as to avoid the formation of scale.

7.6 Results and Discussion

7.6.1 Mechanical Properties

Figure 7.13 shows the calculated engineering stress-strain relationships for specimens of both the parallel and perpendicular orientations as tested at 10^{-3} and 10^{3} s^{-1}. This figure depicts single curves that are representative of the family of tests performed at the conditions evaluated. These two speeds depict mechanical response at the bounds of strain rate evaluated in this first experimental effort. This figure also outlines the differences observed for the two thermal processing conditions, H900 and Condition A. From this plot, several points regarding the mechanical performance of the material can be made.

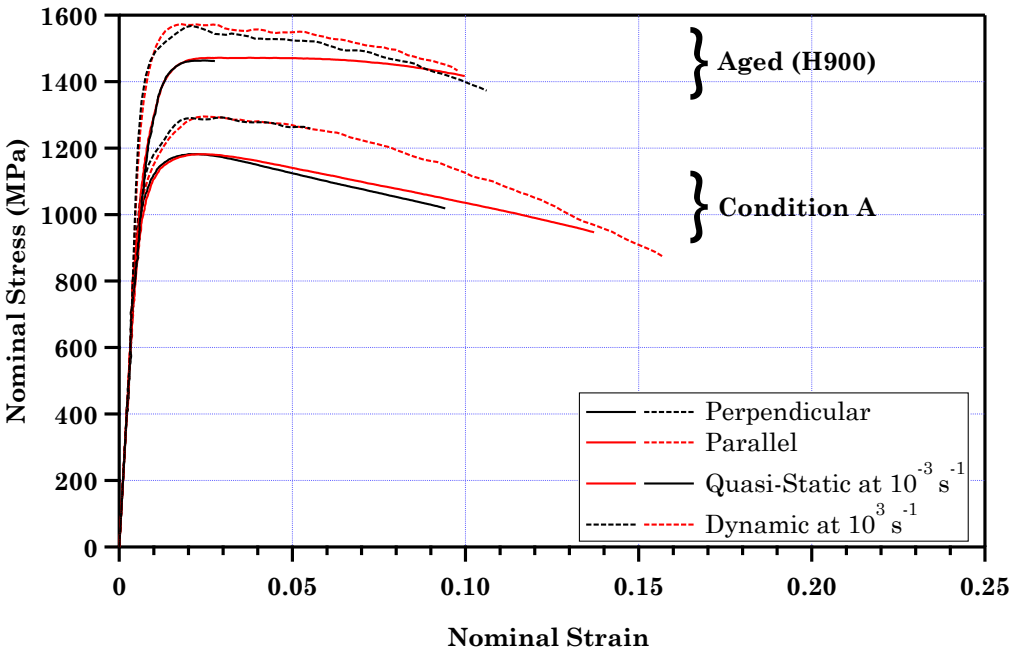


Figure 7.13: Nominal stress-strain curves for the two thermal processing conditions and the two evaluated orientations. Curves show data for both the slowest quasi-static strain rate of 1.04×10^{-3} s^{-1} and the dynamic rate on the order of 10^{3} s^{-1}.

The first observation that can be made is in regards to mechanical anisotropy, one of the principle aims of this study. Specimens of the two orientations examined did not exhibit any strength-based anisotropy in their response to either quasi-static or dynamic loads. Variations in yield strength and ultimate tensile strength were seen as insignificant at the scale presented. Regarding the efficacy of the heat treatment, controlled thermal processing of the material did demonstrate the desired precipitation hardening strength increase from the Condition A state. Additionally, as a consequence of the peak-age heat treatment, peak-stress values were observed to be held for greater extents of plastic strain. Also, the increases in strain rate produced the expected increases in both yield and ultimate tensile strength for this material. Curve shapes for Condition A and H900 aged 17-4 PH were found to be consistent with traditionally fabricated variants. While there were no perceivable differences in strength characteristics between the two orientations, Figure 7.13 begins to highlight the anisotropic response in elongation observed.

Perpendicular specimens were observed, regardless of strain rate, to demonstrate a greater tendency to rupture early in strain as compared to parallel specimens tested in the same manner. While not observed for every test, rupture occurred at earlier positions of strain after regions of uniform plastic deformation. At the onset of local plastic deformation, also referred to as necking, perpendicular specimens were observed to be intolerant of reductions

in area. This response was more pronounced for specimens hardened via aging. Further observations regarding this difference in plastic deformation are made in the section detailing porosity and fracture behavior.

Because the variation in observed mechanical properties for the two orientations was small, comparison of stress strain curves between the SLM material and the reference material are presented here with only the parallel specimen orientation. The extended range of elongation helps to clarify the differences between the traditionally processed material and the SLM version. Figures 7.14 and 7.15 show comparisons between parallel specimens and the drawn rod reference material at the two thermal processing conditions and at the two strain rates previously displayed, 10^{-3} and 10^{3} s^{-1}.

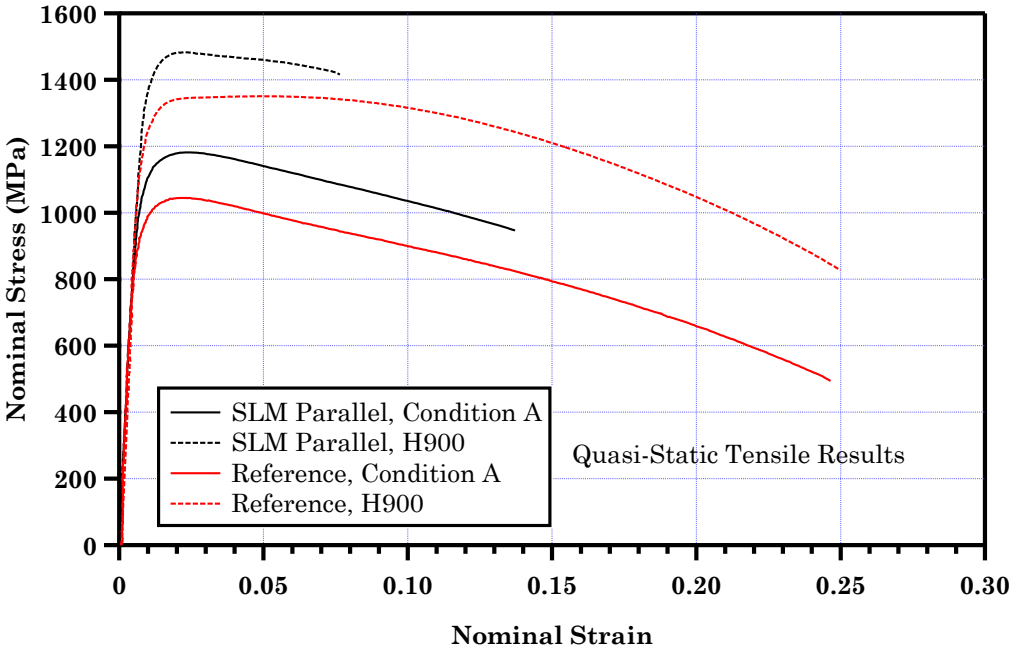


Figure 7.14: Nominal stress-strain plots for parallel and reference material specimens of both the Condition A and H900 treatments evaluated at the quasi-static strain rate of 10^{-3} s^{-1}.

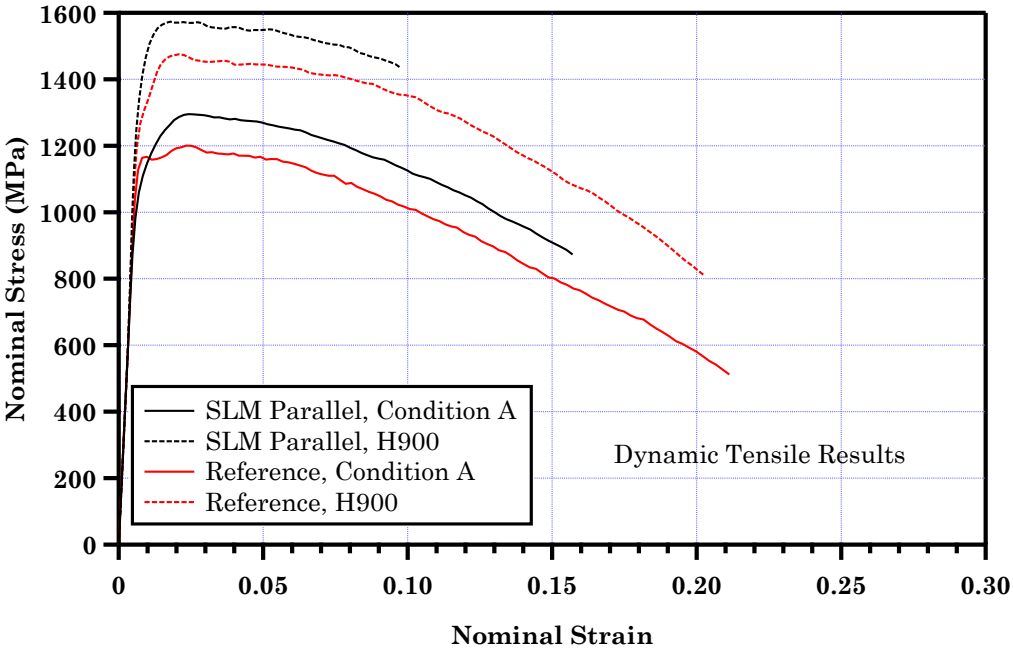


Figure 7.15: Nominal stress-strain plots for parallel and reference material specimens of both the Condition A and H900 treatments evaluated at the quasi-static strain rate of 10^{-3} s^{-1}.

Differences between processing method are clear. Both yield and ultimate tensile strengths for the SLM processed varieties demonstrate significant increases over the traditional counterparts in both the solution heat-treated and aged conditions. Curve shapes are similar between the two and do not reflect differences in plastic deformation rates with elongation. Differences between the observed strength of two materials (with the same thermal processing histories) are attributable to the grain refinement observed in the microstructure. As previously identified in the chapter detailing as-fabricated and thermally processed microstructure, grain sizes were appreciably smaller for both the Condition A and H900 states of SLM processed material samples. The effective increase in strength is a demonstration of the Hall-Petch relationship on the basis of mechanical strength via grain size refinement. Dislocation motion throughout the lath martensitic microstructure is inhibited with the greater density of grain boundaries. Energy requirements and the necessary stress level for a dislocation to transit through a grain are smaller than those necessary for it to change direction at a high-angle grain boundary or penetrate into an adjacent grain [85]. As a result of the reduced grain sizes observed throughout the SLM specimens, it is not unexpected to observe a significant increase in mechanical strength. Yield strength of lath martensite may be characterized by the following equation [86]:

$$\sigma_Y = \sigma_0 + \sigma_P + \sigma_S + \sigma_\rho + k_{HP} d^{-1/2} \quad (7.25)$$

where σ_0 is the friction stress for pure iron, σ_p the precipitation hardening, σ_s the solid solution hardening, σ_ρ the hardening of dislocations within the laths and in the low angle boundaries (lath boundaries and sub-block boundaries), and $k_{HP}d^{-1/2}$ is the grain boundary strengthening (k_{HP}: Hall–Petch slope; d: the effective grain size or the spacing of high angle boundaries). Because both tensile specimen groups, SLM and the reference material, underwent solution heat treatment, differences between them are principally in grain size (formation of copper precipitates does not occur at this temperature). This relative dissimilarity can account for the differences in the observed strength. Variations in solution hardening (via chemical compositional differences), corresponding precipitation hardening, and dislocation hardening are all considered small.

Hardening via aging treatments for the SLM material, while similarly increasing yield and ultimate tensile strength, also increase the susceptibility of premature rupture by stress concentrations at the peripheries of embedded flaws. These embedded flaws were commonly of the form of SLM generated porosity. SLM specimens with embedded porosity demonstrated appreciable reductions in elongation following secondary thermal processing before tensile evaluation. Tests of the SLM material frequently failed to exceed 15% and 10% elongation in the solution heat-treated and H900 conditions, respectively.

For additional clarity, Figures 7.16, 7.17, and 7.18 detail the measured YS, UTS and elongation as a function of strain rate. Individual tests are depicted as data points, while the averages of each data set, both of strain rate and the corresponding strength characteristic measured (YS or UTS), are depicted as piecewise linear curves through the tabulated mean. These plots also show the results of the reference material for comparison.

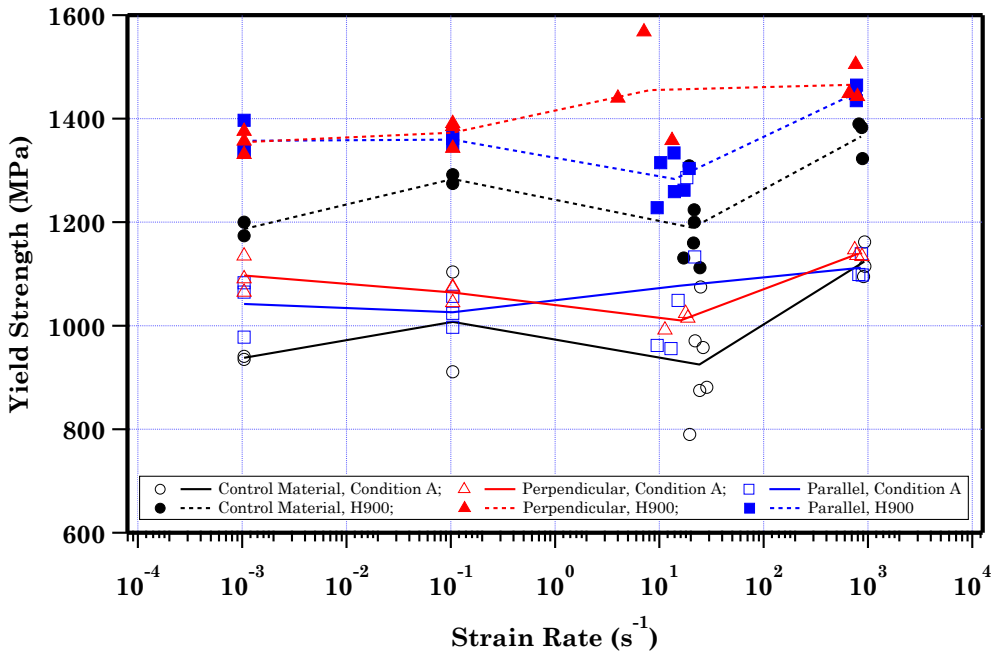


Figure 7.16: Summary plot of yield strength versus strain rate. Individual tests are identified by points with lines as their averaged mean.

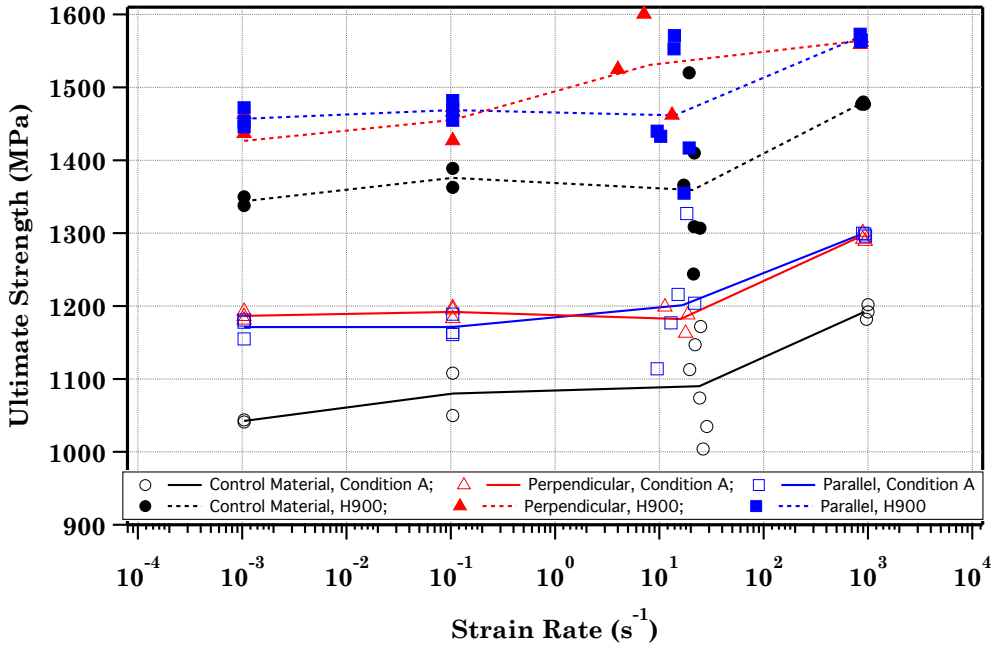


Figure 7.17: Summary plot of UTS versus strain rate. Individual tests are identified by points with lines as their averaged mean.

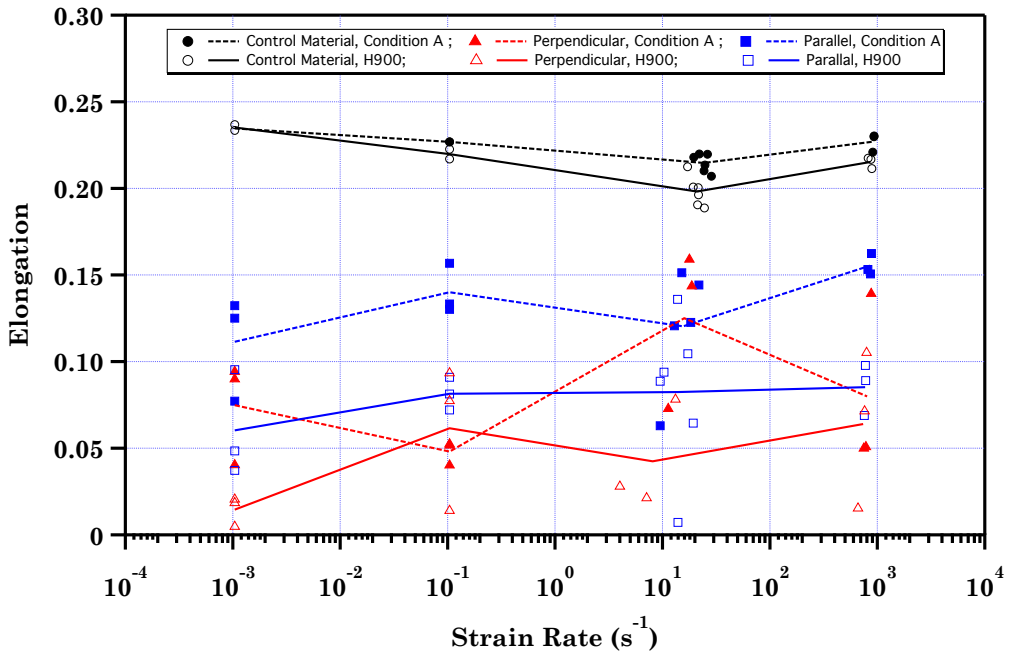


Figure 7.18: Summary plot of elongation versus strain rate. Individual tests are identified by points with lines as their averaged mean.

From these additional summary figures, some additional observations and commentary can be made. At all strain rates evaluated and despite the scatter observed at 10^{-1} s^{-1} strain rate, the absolute increase in both yield and ultimate tensile strength over traditionally processed equivalents is clear. Additionally, as previously reported, this strength increase is independent of SLM-layer orientation. Increases in strength persist across the quasi-static, intermediate, and dynamic rates evaluated. Generally, converging or diverging behavior of YS and UTS with increasing strain rate is not observed. Elongation to failure does not demonstrate any dependence on strain rate. However, there is a stratification of the data between the two orientations evaluated. This reinforces the aforementioned observation that perpendicular specimens failed at lower values of strain more frequently than the parallel oriented counterpart.

The observations regarding strength increases illustrate changes to the athermal barriers to dislocation motion through the material as a result of SLM material processing and the secondary thermal processing. These athermal barriers are observed to be the introduction of a greater density of grain boundaries. The strain rate sensitivities between the various materials do not show significant disparity. However, it is useful to quantify this sensitivity. Equation 7.10 is relied upon to present this change in sensitivity in strain rate. Table 7.1 outlines the calculated strain rate sensitivity parameter, *m*, across quasi-static and dynamic strain rates of 10^{-1} and 10^{3} s^{-1} for the property of ultimate tensile strength. The mean calculated value for the sensitivity

parameter is reported for comparisons between strain rates of the same material kind and orientation. The scatter observed at 10^1 s^{-1} precluded its inclusion into the strain rate sensitivity calculations shown here.[5]

Table 7.1: Strain rate sensitivity, 10^{-1} to 10^3 s^{-1}

	Strain rate sensitivity parameter, *m*		
	Perpendicular	Parallel	Control
Condition A	0.0084	0.0103	0.0183
H900 temper	0.0077	0.0072	0.0074

Table 7.1 also demonstrates the similarity in strain rate sensitivity across the specimen conditions evaluated. What may be visible in Figures 7.16 and 7.17 are numerically apparent in this table. Layer orientation had little influence on the sensitivity to changes in strain rate. The effect of thermal processing on the sensitivity of strain rate was also observed to be negligible. In contrast, the reference material demonstrated marginally greater resistance to plastic flow in the Condition A state. But again, this difference was not great. The changes observed as a consequence of microstructural refinement via SLM did not translate into great differences in sensitivity to strain rate.

7.6.2 Embedded Flaws

A common residual of the SLM process is the formation of porosity within the densified material [3,66,87,88]. While the material produced for this experimental study was measured to be of high density (greater than 99.5% compared to fully densified material), the presence of porosity was found to strongly influence the elongation response of machine tensile specimens. Observations of post-test fracture surfaces and sectioned bulk material samples identified several repeating characteristics of these pores. Figure 7.19 shows measurements made of porosity when observed within the bulk material in the vertical reference plane (layers are oriented from top to bottom). Individual pores were found to be limited in the vertical, building direction by the layer

[5] The dropping weight machine as designed and used in this initial experimental investigation demonstrated a significant tendency to induce bending into the specimen during the tensile test. This was observed in the dual laser gauge measurements made in tandem, 180 degrees apart, across the specimen. As a result of this observation, a new machine design was needed. The results of this re-design and tensile testing are documented in the second experimental investigation. The inclusion of the data here is to demonstrate the improvement in testing capability of the laboratory as a result of this experimental work.

thickness used during the material fabrication (30 μm). However, similar measurements made of pores in the horizontal reference plane (parallel to the building layer) and direct observations of fracture surfaces of perpendicular specimens (where layers are oriented normal to the loading direction) found porosity to not be limited by any feature of the SLM process or controllable parameter. Figure 7.19 shows porosity as viewed from a section material sample when viewed in the horizontal reference plane.

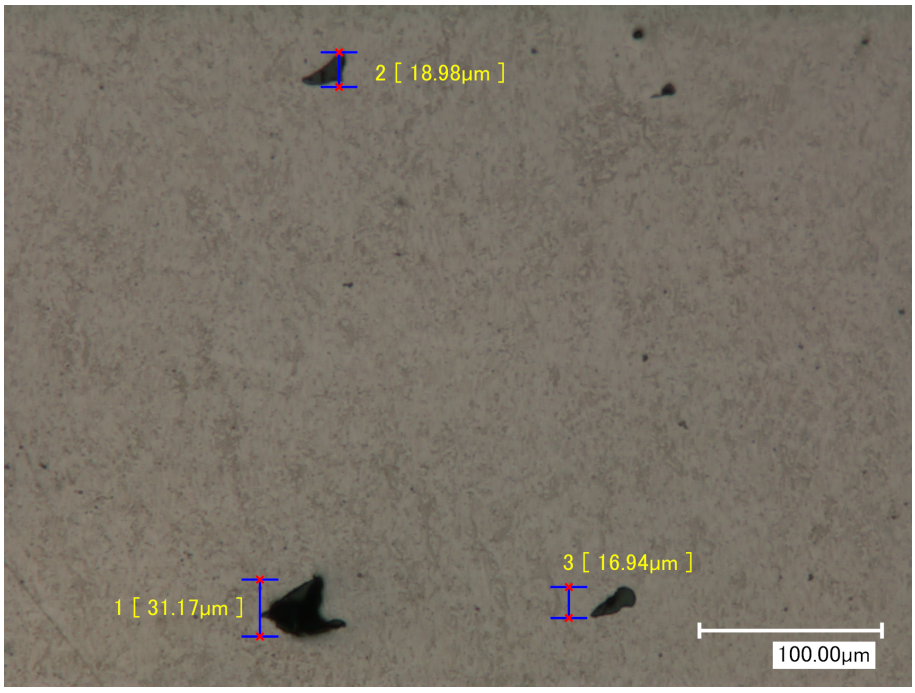


Figure 7.19: Porosity as observed within a bulk sample, viewed in the vertical reference plane (XZ). Layers are oriented on-edge to this image.

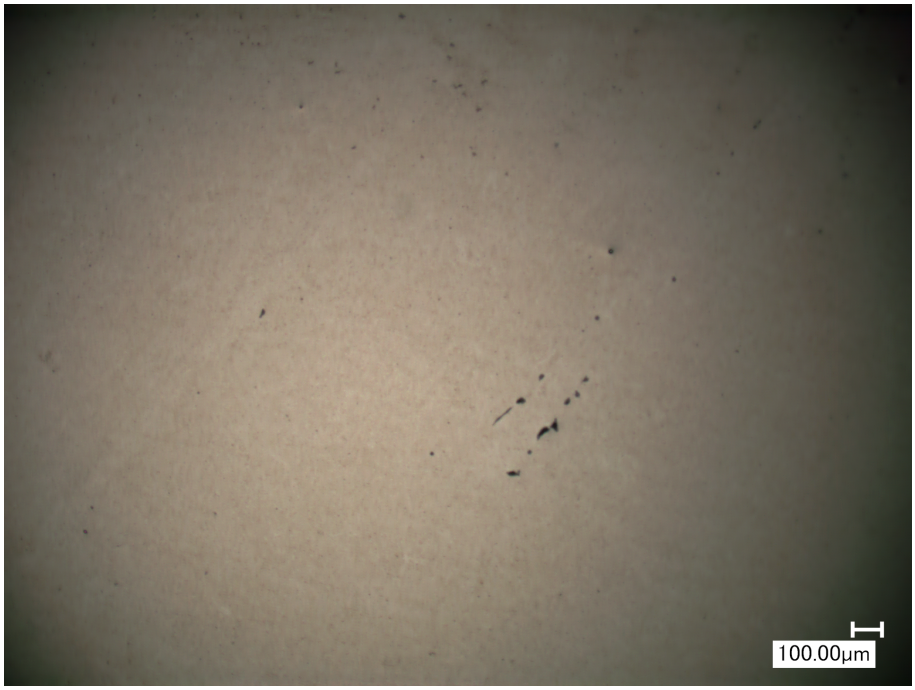


Figure 7.20: Porosity as observed within a bulk sample viewed in the horizontal reference plane (XY). Layers are oriented normal to the image.

Figures 7.21 (a) and 7.22 (a) show fracture surfaces of a parallel and perpendicular specimen, respectively. The effect of observable porosity morphology and orientation becomes more apparent when fracture behavior is considered. Figures 7.21 (b) and 7.22 (b) show the corresponding macro-scale images of the same specimens containing their related pores. What is most clear from these images is the surface fraction of the fracture surface over which the pore is visible. Figure 7.23 shows a schematic of the embedded porosity and its deducible effect on potentially limiting elongation of specimens.

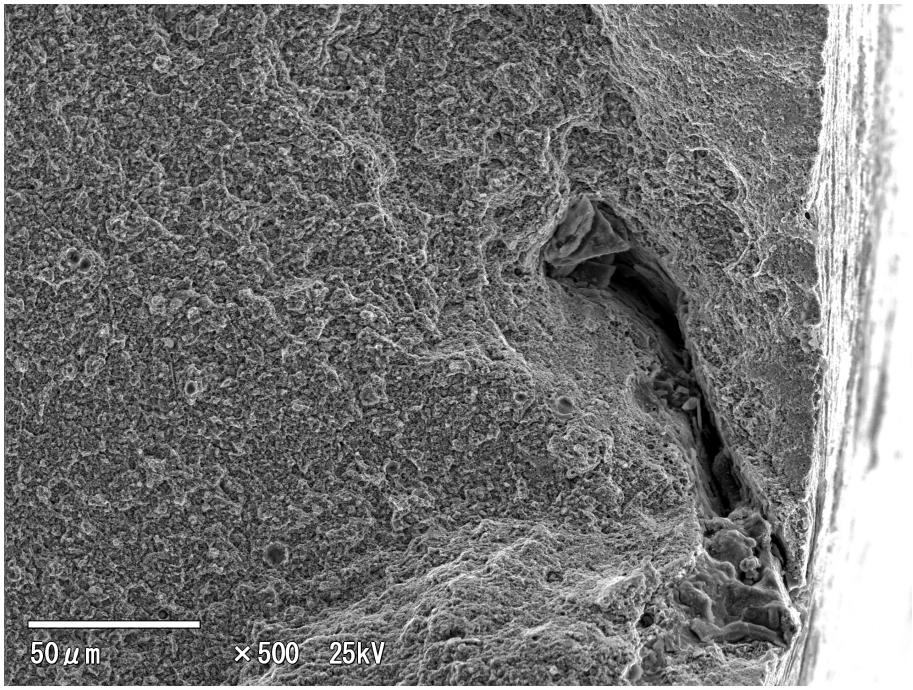


Figure 7.21 (a): Detailed view of a pore visible on the fracture surface of a parallel specimen. Note the depth of penetration of the pore relative to the fracture surface.

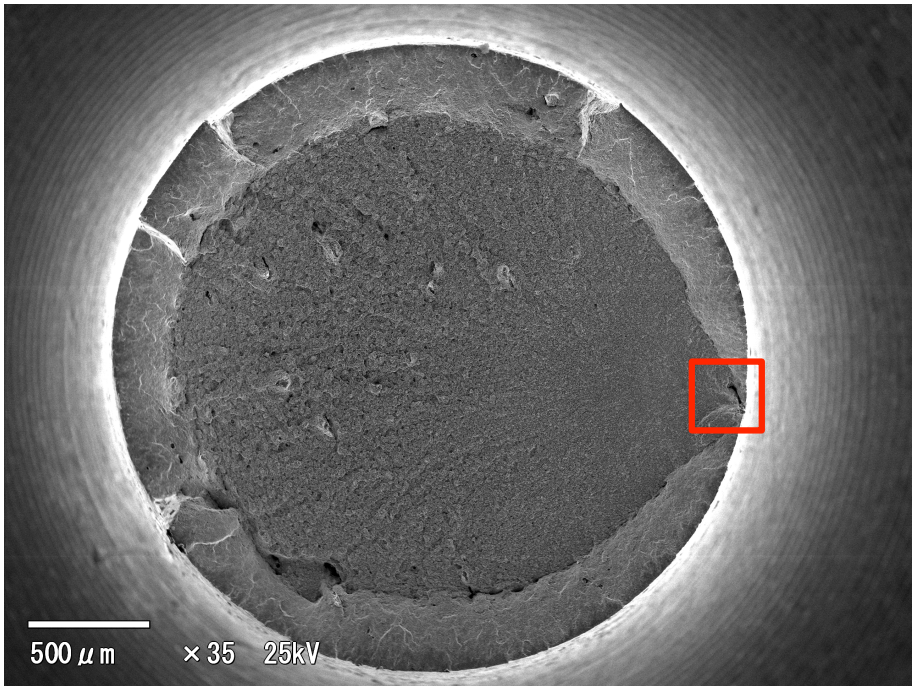


Figure 7.21 (b): Macroscopic image of the previous image detailing the embedded pore. A river pattern is observable on the fracture surface that points to this particular pore as the site of rupture.

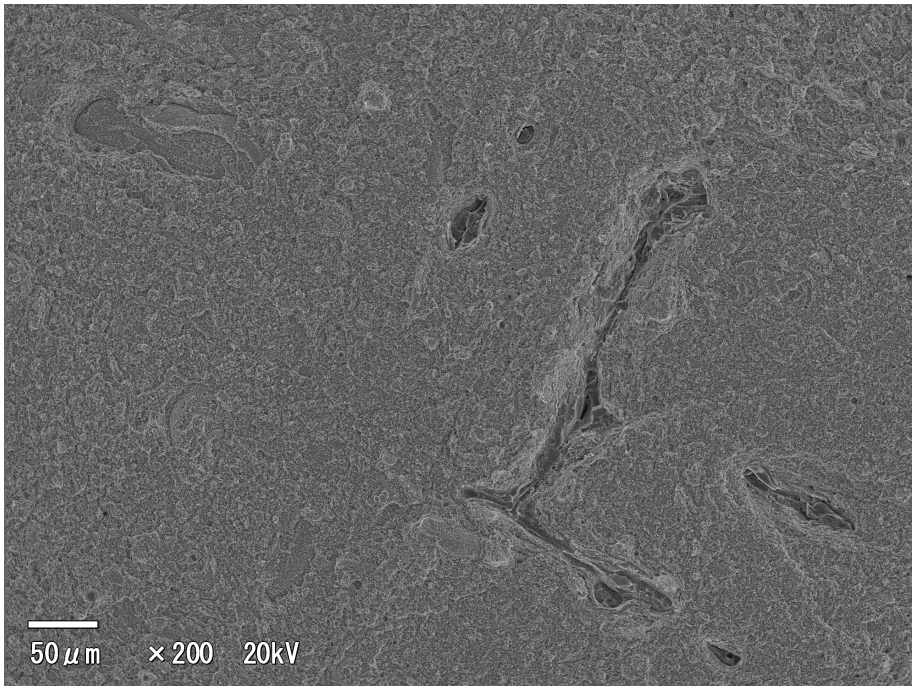


Figure 7.22 (a): Detailed view of a pore visible on the fracture surface of a perpendicular specimen. Note the depth of penetration of the pore relative to the fracture surface

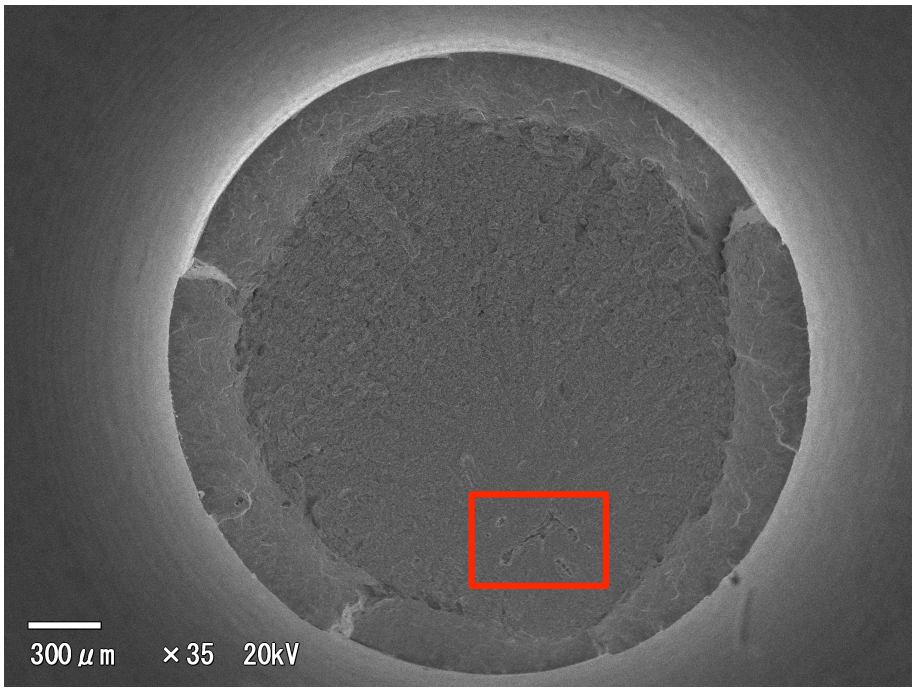


Figure 7.22 (b): Macroscopic image of the previous image detailing the embedded pore. A river pattern is observable on the fracture surface that points to this particular pore as the site of rupture. The macro-scale image appears inverted due to images taken of the reverse side of the fracture surface.

Because pores were limited in size in the building direction, their effect on the mechanical behavior was principally a result of relative loading direction. As shown by the preceding images, these flaws were observed to be disc or string-like in shape, but consistently limited within an individual layer thickness. Of the three directional degrees of freedom that a pore could expand, only two were unlimited (these two directions coincided with the plane that also denotes the building plane). As a result, perpendicular specimens always maintained an orientation of their internal layer and porosity structures normal to the loading direction. This translated into the orientation of the largest feature-of-size for every pore in a perpendicular specimen to be normal to the applied load at every test. Persistently early fractures were traceable to the associated stress concentrations proportional to the effective flaw size underdoing Mode I crack separation. Whereas parallel specimens had no such forced alignment of all pores' largest features to the applied load. Coincidentally, all parallel specimens in this experimental investigation had loading axes oriented in the same relative direction to the scanning pattern used to produce the material (approximately at +/- 45 degrees to the checkerboard scanning pattern described in Chapter 5). Therefore, observable pores on fracture surfaces of parallel specimens are seen as elongated structures that penetrate at-angle into the gauge section of the sample below the fracture plane. Perpendicular specimens are observable as shallow features that frequently span lengths on the fracture plane.

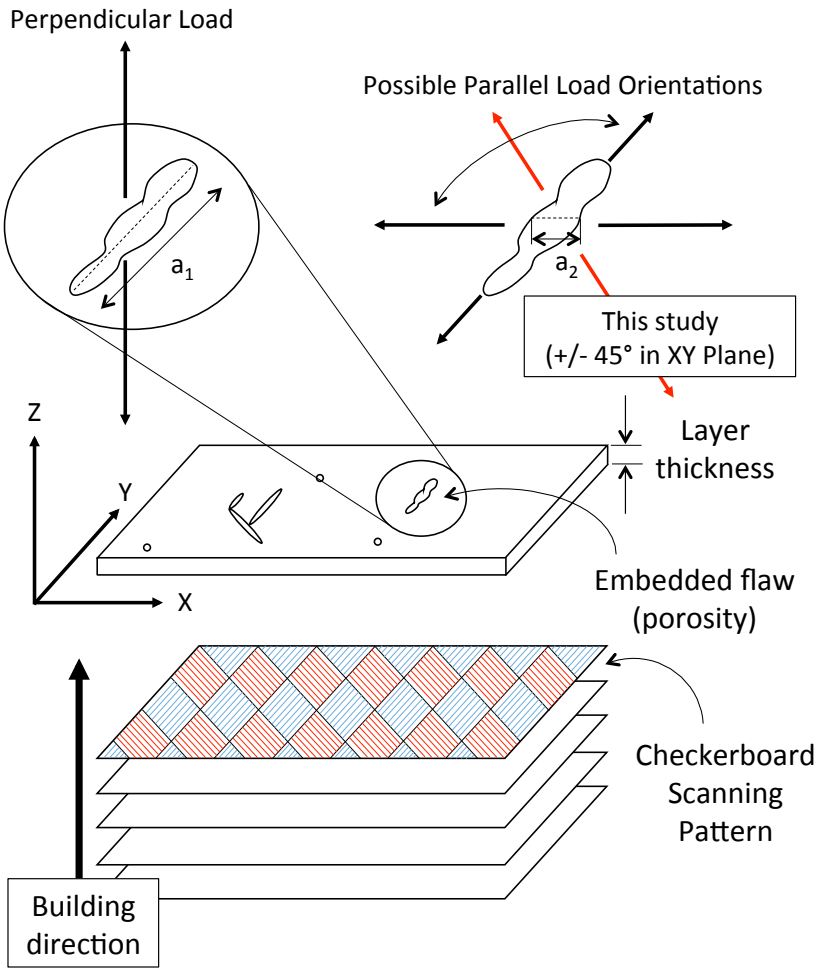


Figure 7.23: Schematic illustrating the relationship between the scanning pattern, embedded porosity, and eventual loading based on tensile specimen orientation.

Thermal processing of samples was not observed to have a discernable effect on the morphology of the porosity. However, as stress concentration increases with the product of the applied stress and the square root of the embedded flaw length, aged specimens demonstrated greater sensitivity to the embedded flaws during localized plastic deformation where true stress increases rapidly with the reduction in load bearing area. This is also borne in the tensile testing results with the reduced elongation to failure for specimens in the peak-age condition, H900 temper.

7.7 Conclusions of Experimental Investigation I

The focus of the first experimental effort was to understand the mechanical performance of SLM-processed 17-4 PH with respect to *standardized* thermal processing. Because the SLM process is directional by design, anisotropy in the mechanical response of the material was of interest. In order to evaluate both

cardinal orientations, across four strain rates, and following two sequential heat treatments, a large quantity of mechanical tensile specimens were prepared. The conclusions of this investigation are as follows:

1. Both yield and ultimate tensile strengths were observed to be considerably higher for specimens made of SLM processed 17-4 PH. This mechanical behavior was consistent for both the solution heat-treated condition and the peak-age condition (also referred to H900 temper). The increase in strength is a result of the grain refinement observed over traditional processing methods. This refinement in microstructural size results in an increase to athermal barriers to dislocation motion.
2. Layer orientation did not significantly affect the measured strength of specimens via tensile testing.
3. Tensile strength of both the reference and the SLM material increase with strain rate across the range investigated (10^{-3} to 10^{3} s^{-1}). Increasing tensile strength with strain rate is consistent regardless of the thermal processing conditions.
4. Strength increases related with aging of the SLM material were noted and illustrate the efficacy of the heat treatment. However, relative increases in strength were observed to be less than those of the reference material. Absolute increases were similar.
5. Porosity morphology and its orientation relative to the applied load influenced the elongation to failure tremendously. Perpendicular specimens failed at lower values of plastic strain than parallel specimens. Both conditions were found to fail earlier than the reference material.

8. Experimental Investigation II: Effect of Metastable Austenite on Mechanical Properties

8.1 Purpose

Initial evaluation of the mechanical properties of SLM processed 17-4 PH following standardized heat treatment procedures identified a variety of basic characteristics common of materials processed in this manner. It also established a relative comparison to a traditionally processed reference material. The second experimental evaluation was intended to further expand the scope of knowledge surrounding the thermal processing and sensitivity to strain rate. Of focus to this experimental work was the as-fabricated structure with its high volume fraction of retained austenite and the significance of a solution heat treatment on further aging efficacy and subsequent mechanical behavior.

8.2 Introduction

The theoretical basis for this experimental work is no different than previously outlined in Chapter 7 and will not be repeated here. Testing methods have also not changed as part of this experimental effort; however, some changes were made to the testing equipment and will be detailed along with their associated impacts on the results. Much of the previous discussion on the material's microstructure and phase characterization will be of importance in this section.

8.3 Testing Hardware

Between the completion of the first experimental work and this second investigation both the quasi-static machine and dropping weight machines were replaced. The new quasi-static tensile testing apparatus, a Shimadzu AG-Xplus 100kN screw driven machine, operates no differently than the previous machine and its description will be omitted here. However, in an effort to address the inadequacies of the dropping weight machine, the design was changed significantly. Because testing at the intermediate strain rate of 10^1 s^{-1} is of relative difficulty compared to quasi-static and dynamic materials testing, it is worth describing in detail the machine and its design.

8.3.1 Intermediate Strain Rate Tensile Testing: Dropping Weight Machine

To mitigate the effects of bending, the previous iteration of the dropping weight machine relied upon two clevis joints, each with a degree of rotational freedom 90 degrees apart in a plane normal to the tensile load. This was intended to eliminate bending along the axis of the tensile test. As is evident by the data collected, the degree of scatter reflected the lack of success in this effort. Additionally, this scatter proved unacceptable for a proper representation of the stress-strain relationship at the intended strain rate. As a way to address the bending during the tensile test, an external third party produced a new design. This design relies on a rigid cage structure to mechanically restrict bending along the loading axis. The load is transferred to the specimen through this by a co-axial tube and integral grip-platen arrangement to effectively push-pull one end of the specimen away from the other. The other end of the specimen is restrained by a female threaded grip interface and is integral to the load cell attached to the moving end of the lever arm. Because of the relative increase in complexity and to visually clarify this textual description, Figures 8.1 and 8.2 detail the design of this machine with additional notations.

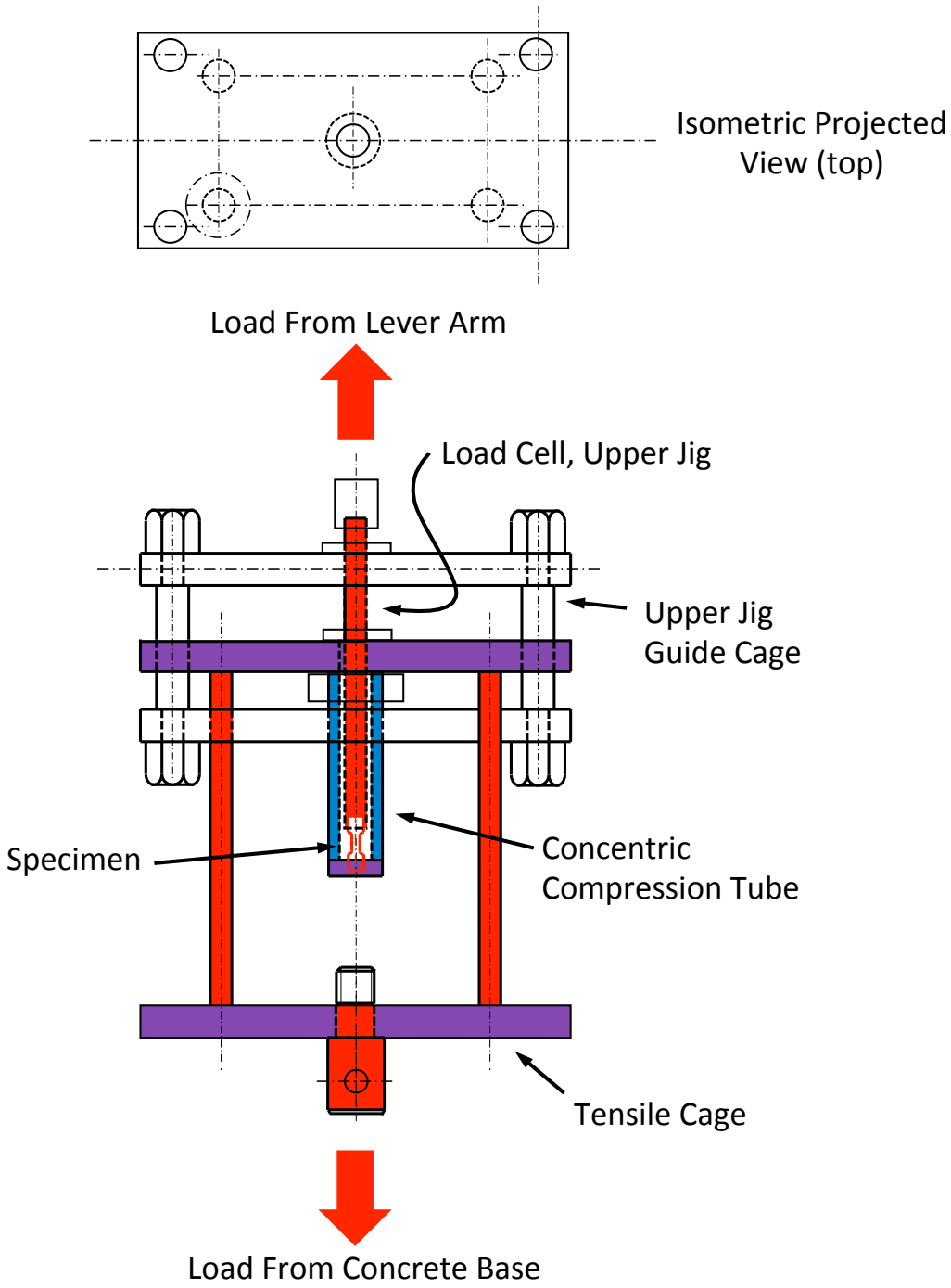


Figure 8.1: Front and top views of the redesigned dropping weight machine jig used in tensile testing at intermediate strain rates. Items in the color red are under tension during operation. Items in blue are under compression. Items in purple experience bending. And items in white are not intended to be loaded during the test except after the rupture of the specimen. The upper guide cage, as depicted in white, is intended to restrict the angularity of the upper jig and load cell relative to the centerline of the specimen. Both the upper cage and lower tensile care are free to slide relative to each other.

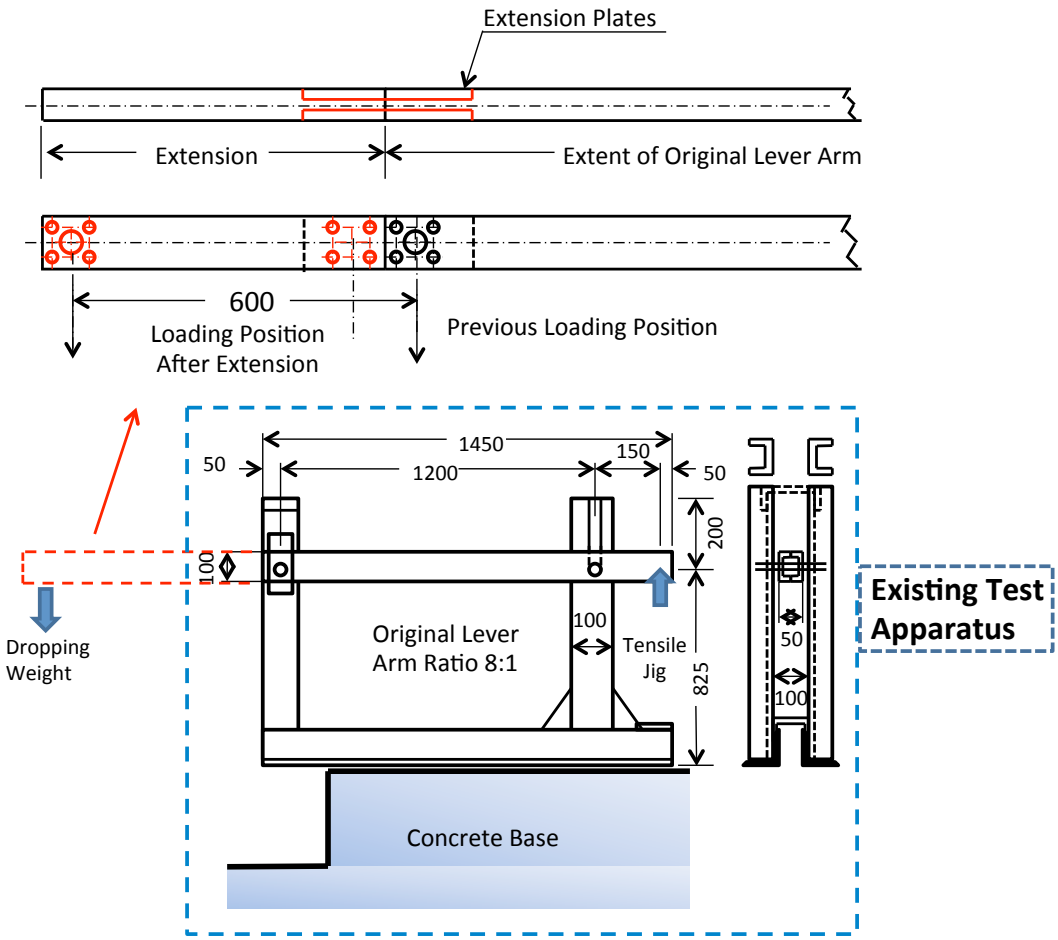


Figure 8.2: Side view of the dropping weight machine structure with additional extension to the lever arm on the side of the fulcrum loaded by the falling weight. Previous loading ratio was 8 to 1. The new design increased this to 12 to 1.

Results of testing conducted on this machine were far more repeatable and consistent across the tensile specimen families evaluated. These results will be presented in the following sub-sections.

8.4 Tensile Specimen Preparation

8.4.1 Tensile Specimen Orientation

The focus of this experimental effort was to characterize the as-fabricated microstructure and the effect of solution heat treatment on further aging across a range of strain rates. Because the mechanical properties of tensile specimens evaluated during the first experimental effort were found to be independent of orientation except for a sensitivity to porosity expressed in elongation, it was determined to limit all tensile testing to specimens produced to the orientation described previously as “parallel”. It was believed that mitigating the effect of

porosity would permit the measuring and further analysis of the material across greater ranges of strain and not the effect of porosity on it. Additionally, these specimens were produced from the fabrication lot previously described in Chapter 5 as Batch Two. The resultant density of this lot of material was measurably lower (approximately 98.8%).

8.4.2 Tensile Specimen Thermal Processing

Specimens prepared for tensile evaluation were segregated into three different groups.

1. As-fabricated with no additional thermal processing
2. Specimens immediately treated with standardized aging treatments without a prior solution heat treatment
3. Specimens treated to a solution heat treatment prior to aging

The aging heat treatments considered for both groups 2 and 3 were the H900, H1025 and H1150. For summary, their temperatures and durations are outlined here in the following table.

Table 8.1: Aging treatment temperatures and durations

Aging Condition	Temperature	Duration
H900	480 °C (900 °F)	1 hour
H1025	550 °C (1025 °F)	4 hours
H1150	620 °C (1150 °F)	4 hours

Thermal processing was performed using the same equipment as prior treatments described in Chapter 7. To minimize confusion and disambiguation, specimens of group 2 are referred to by their aging treatment name only. While those of group 3 have the prefix “CA-“ added as a way to identify them with a prior solution heat treatment to the Condition A state (e.g. CA-H900).

8.5 Results and Discussion

8.5.1 Mechanical Properties, Quasi-Static Strain Rate

Figure 8.3 shows engineering stress-strain relationships for specimens treated to a solution heat treatment prior to aging and evaluated at a strain rate of 10^{-3} s^{-1}. A curve representing the solution heat treated condition is included for reference as the initial condition prior to aging. These traces effectively demonstrate the expected mechanical response of 17-4 PH in accordance with industry standard practices for additional thermal processing. Two exceptions to typical behavior are observed. First, the increase in yield and ultimate tensile strengths over traditionally fabricated counterparts is substantial and coincides with the results presented in Chapter 7. And second, the only criterion not meeting the associated material standard is, again, elongation. Specimens suffering from premature rupture due to embedded porosity demonstrate an inability to plastically deform beyond ultimate tensile strength. Only the CA-H1150 specimen were capable of meeting minimum requirements for elongation.

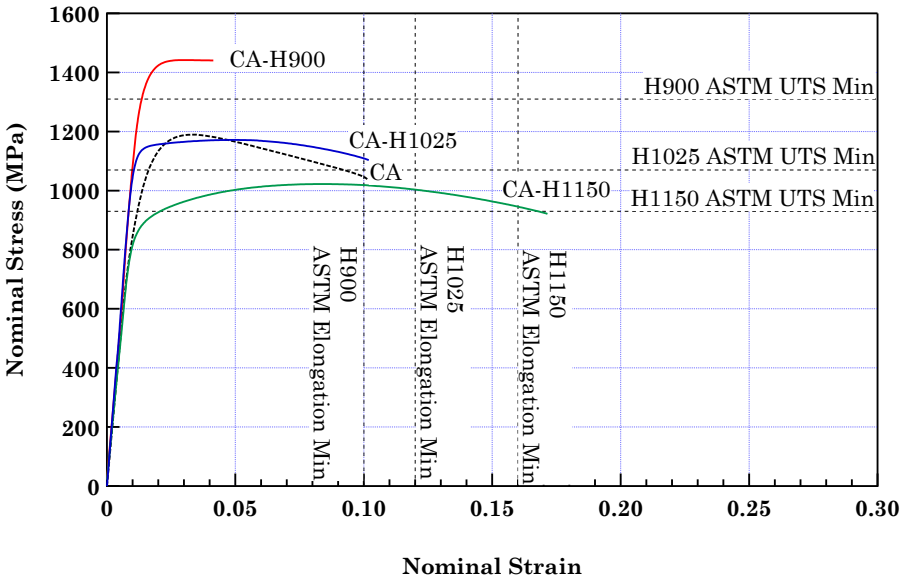


Figure 8.3: Nominal stress-strain plots from tensile testing at a strain rate of 10^{-3} s^{-1} for specimens with a prior solution heat treatment and aged to the three various conditions: CA-H900, CA-H1025, and CA-H1150. A reference curve of the Condition A state is included as the baseline from which secondary thermal processing was performed. The horizontal and vertical dashed lines indicate ASTM A564/A564M standard minimums for UTS and elongation respectively.

To help further clarify the similarity between traditional and SLM variants of 17-4 PH when properly processed (i.e. performing an aging treatment from the Condition A state), Figure 8.4 shows flow stress curves for the family of tensile tests depicted by the individual traces shown in the previous figure. These are

also plotted alongside the reference material heat treated in the same manner. Flow stress is defined as the instantaneous stress required to maintain continued plastic deformation within the range of strain described as uniform plastic deformation (up to the limit of UEL) and may be described by a simple power law expression like the one below:

$$Y_f = k\varepsilon^n \tag{8.1}$$

Where both *k*, the strength coefficient, and *n*, the strain hardening exponent, are both constants. These constants are typically determined empirically from plots of true stress and true strain on a log-log scale plot (as shown in Figure 8.4).

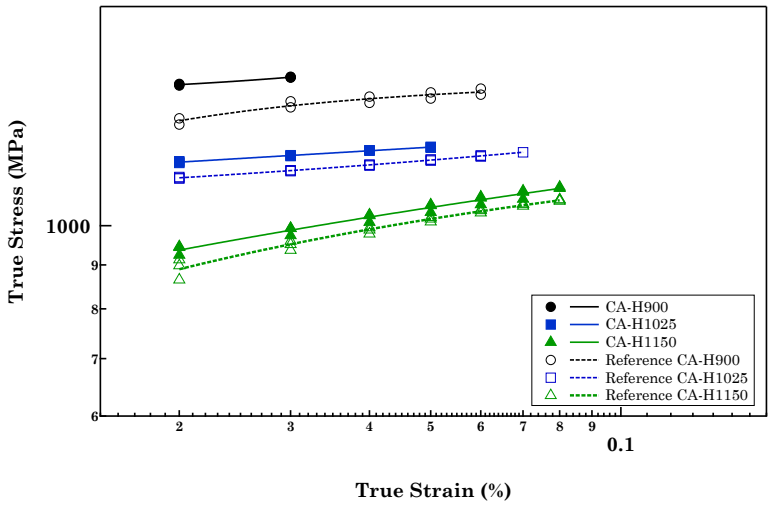


Figure 8.4: A log-log scale plot of true stress versus true strain for strain locations extracted from tensile data through the region of uniform plastic deformation. This plot includes data from CA-H900, CA-H1025, and CA-1150 of both the SLM and reference material specimens.

Constants for this power-law expression as determined from the plots of Figure 8.4 are shown in Table 8.2. From Figure 8.4 it is observed that the flow stress levels are higher in the case of SLM fabricated material. This is also reflected in the engineering stress-strain plots of Figure 8.3. Additionally, the power-law trend lines applied to the data points for the two specimen types indicates good similarity between the strain hardening constant. This would suggest that the rate-limiting method for continued plastic deformation between the two specimens types is the same. Additionally, the effect of heat treatment, beyond modifying the underlying grain size of the SLM fabricated material, has the same effect on flow stress between both specimen types.

Table 8.2: Flow Stress Power Law Expression Constants

Material Condition	k	n
CA-H900	1769.7	0.049
Reference CA-H900	1741.5	0.070
CA-H1015	1408.7	0.044
Reference CA-H1025	1402.5	0.054
CA-H1150	1499.3	0.120
Reference CA-H1150	1506.8	0.134

Between the Figures 8.3 and 8.4 several general observations about thermal processing can be made. The CA-H900 treatment, also referred to as the peak-age condition, is achieved with the highest relative strengthening as a result of the growth of finely dispersed copper precipitates. CA-H1025 and CA-H1150 indicate a reduction in relative strengthening off of the peak age condition. CA-H1150 demonstrates a negative relative strengthening, but with an appreciable increase in uniform plastic deformation. Peak strength is delayed until approximately 9% engineering strain and accompanied by an increase in local plastic deformation well past UTS. Increased ductility with extended aging is a result of the coarsening precipitates and a decrease in their relative spacing within the microstructure. This transitions the material from off of the peak age condition where a balance is struck between the slicing or bypassing of these precipitates. With coarsened precipitates, the required stress to bend around a dislocation becomes less than the force required to cut through them. Additionally, with diffusion and localized concentration of copper into precipitate structures we see an increase in austenite reversion. Local chemical stabilization is enabled by the segregation to lath boundaries [30]. Austenite also demonstrates a higher solubility limit of copper and nickel and effectively begins to deplete the martensite, further enhancing the reversion process. Line analysis of XRD spectra from SLM material samples aged to the same conditions as these tensile specimens indicate an increase in austenite from 0% in the Condition A state to 3.3%, 4.7%, and 20.4% for the CA-H900, CA-H1025, and CA-H1150 states respectively. This effectively demonstrates the progressive reversion of austenite from martensite with continued aging treatment.

Figure 8.5 and 8.6 shows the same set of information as Figure 8.3 and 8.4, but for specimens aged without an initial solution heat treatment, treated to the same tempers but immediately from the as-fabricated condition. Similarly, a curve representing the as-fabricated condition is shown here for reference as the initial starting condition prior to thermal processing. The engineering stress-strain relationships for these conditions of material significantly differ from those observed previously. Despite the relatively high volumetric fraction of retained austenite in the as-fabricated condition (51.6% for Batch One and 36% for Batch Two), the H900 aged condition demonstrates a sizeable increase in strength. As previously discussed, austenite does not age-harden; copper precipitates do not form within austenite grains, as their solubility is higher. As a result, age hardening is expected to be inhibited [30]. Relative changes in nominal strength for the peak-age condition as measured from the pre-treatment condition are lower when compared to the CA-H900 material. Curves depicting flow stress also indicate a large departure from the behavior of those specimens with a solution heat treatment. The as-fabricated and H900 treated specimens can not be fit with a power-law expression for the behavior observed. The lack of a power-law fit to flow stress highlights a change in the underlying method of continued plastic deformation for these specimen types.

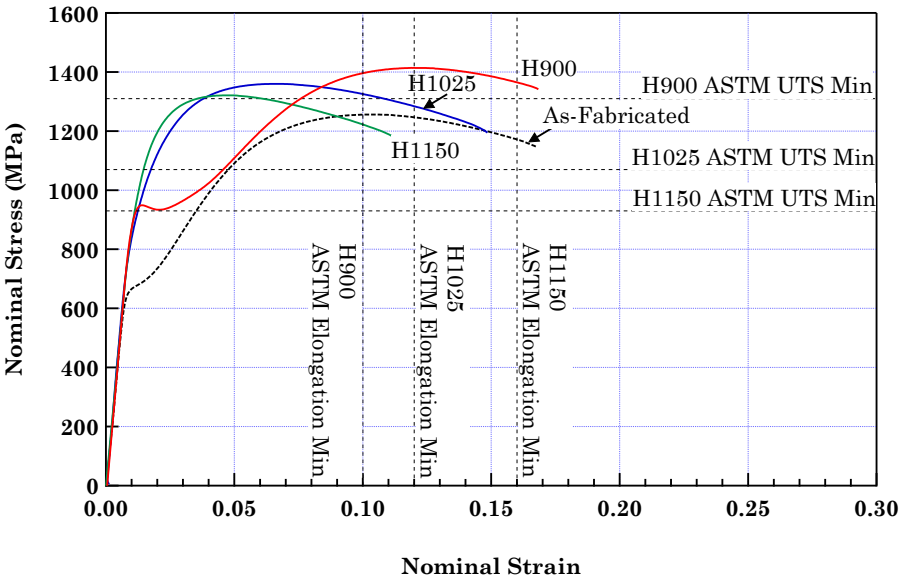


Figure 8.5: Nominal stress-strain plots from tensile testing at a strain rate of 10^{-3} s^{-1} for specimens **without** a prior solution heat treatment and aged to the three various conditions: H900, H1025, and H1150. A reference curve of the as-fabricated condition is included as the baseline from which secondary thermal processing was performed. The horizontal and vertical dashed lines indicate ASTM A564/A564M standard minimums for UTS and elongation respectively.

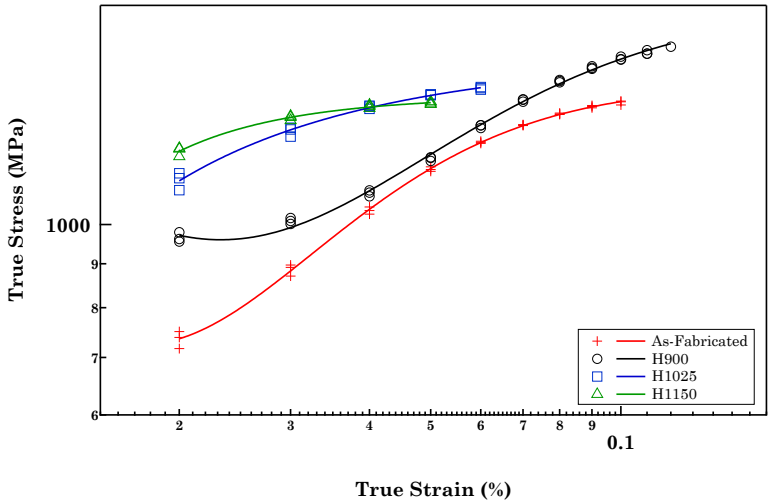


Figure 8.6: A log-log scale plot of true stress versus true strain for strain locations extracted from tensile data through the region of uniform plastic deformation. This plot includes data from SLM specimens processed to the H900, H1025, and 1150 conditions. The as-fabricated condition is included for reference.

Table 8.3 summarizes the observed mechanical properties for the tensile evaluations performed at the quasi-static strain rate of 10^{-3} s^{-1} across all the specimens and their respective thermal processing conditions. All testing was performed at room temperature.

Table 8.3: Summarized Mechanical Properties (Average of Three Tests)

Condition	Proof Stress (0.2% Elastic Offset) (MPa)	Ultimate Tensile Strength (MPa)	UEL (%)	Total Elongation (%)
As-Fabricated	661±24	1255±3	9.9±0.2	16.2±2.5
H900	945±12	1417±6	11.7±0.8	15.5±1.3
H1025	870±25	1358±8	6.5±0.03	13.3±1.5
H1150	1005±15	1319±2	4.8±0.0	11.1±0.4
CA-H900	1352±18	1444±2	2.9±0.1	4.6±0.4
CA-H1025	1121±9	1172±2	4.8±0.1	9.6±1.7
CA-1150	859±11	1017±15	7.7±0.3	16.6±1.2

Figure 8.7 and 8.8 show the evolution of the measured phases as observed via XRD. Increasing heat treatment exposure temperature generates the expected reversion to the fcc-structured austenite from martensite for samples with an initial solution heat treatment depicted in Figure 8.7. Whereas, in the case of

those without a solution heat treatment, a more complicated evolution of structure occurs across the aging treatments. At the relatively low temperature, H900 aging treatment (480 °C, 1 hour), the concentration of austenite is observed to increase. This temperature is too low to relieve thermal stresses [67], but still high enough to initiate diffusion of copper within the martensite. Precipitates form, but are also likely to initiate the reversion of additional martensite to austenite via chemical stabilization. Hence, an increase in the volumetric fraction of the austenite phase is observed. However, between the H900 and H1025 heat treatments a transition is observed in yielding behavior – the low yield point and clear yield shoulder in the H900 specimens has been eliminated. Sufficient relaxation of thermal stresses are likely to occur with these two higher temperature treatment conditions and result in the transformation of a larger portion of the mechanically stabilized austenite to martensite upon cooling to room temperature (below the M_f temperature). However, because the initial conditions of specimens aged to H1025 and H1150 contain high volume fractions of austenite prior to the start of aging, we continue to see inhibited aging kinetics. The coarsening of precipitates that would normally be expected to occur throughout the microstructure only occurs within the martensitic phase. After returning to room temperature, the austenite that has been released from mechanical stabilization is free to undergo shear transform to the martensite phase starting at the M_S temperature. This increasing fraction of both aged and non-aged martensite results in the mechanical responses observed in Figure 8.5 for the H1025 and H1150 specimens. Continued coarsening of precipitates in the H1025 and H1150 aged treatments contributes to a reduction in observed UTS. A greater fraction of austenite that is free to transform to martensite upon cooling increases the yield strength. It should be noted that none of the treated conditions in Figure 8.5 demonstrate a negative relative strengthening that would be expected with uniform over-aging. This is in contrast to the behavior observed from the CA-H1015 and CA-H1150 specimens. To assist with this understanding, Table 8.4 is a summary of the calculated volumetric fractions of austenite and martensite per the collected XRD data for material produced as part of Batch Two after thermal processing. It should also be noted that the highest temperature heat treatment (H1150) does not exceed the expected Austenite-start (A_S) temperature. It is at this temperature that the martensite is expected begin reverting to austenite (just as austenite converts to martensite upon cooling, the A_S and A_f temperatures indicate the reverse process, but at

higher temperature[1]). As a result of this mixed phase microstructure, we see unusual and imperfect aging performance.

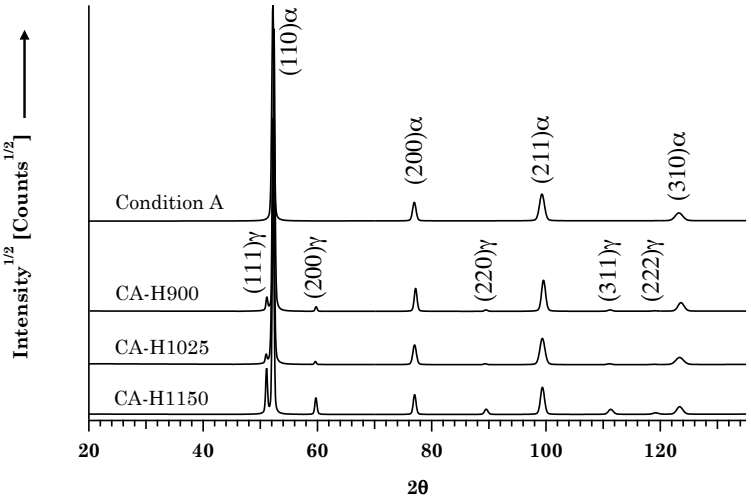


Figure 8.7: Progression of austenite reversion with increasing temperature and aging treatment duration from the initial Condition A state.

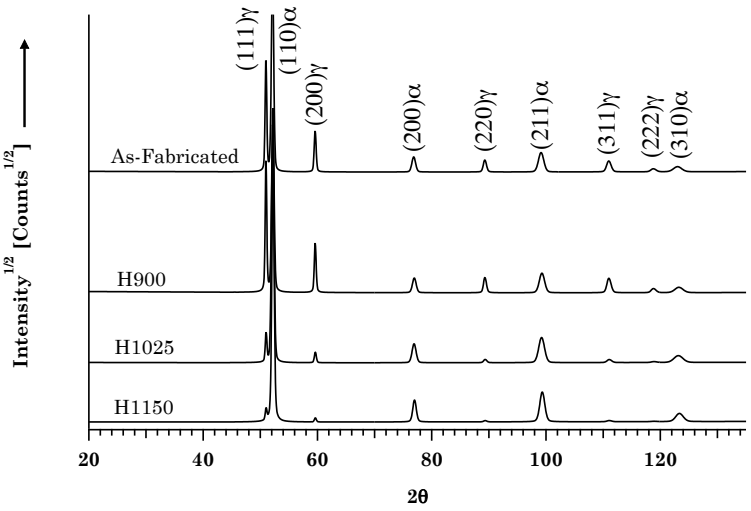


Figure 8.8: Phase evolution with increasing temperature and aging treatment duration from the initial as-fabricated state.

[1] These temperatures are not established for 17-4 PH in the literature, but can be estimated using chromium and nickel equivalent concentrations and other reference curves for simple Fe-Ni binary alloy systems [30].

Table 8.4: Volumetric fraction post thermal processing

Condition	Martensite (α') (vol. %)	Austenite (γ) (vol. %)
Condition A	100	0
CA-H900	96.9	3.1
CA-H1025	95.0	5.0
CA-H1150	79.6	20.4
As-Fabricated	64.0	36.0
H900	59.5	40.5
H1025	89.6	10.4
H1150	94.4	5.6

It is useful to compare the aging condition paths (with and without solution heat treatment) against their relative strengthening performance. By combining the heat treatment conditions (temperature and time) via the Hollomon-Jaffe parameter and plotting against the relative strengthening, we can see the efficacy of the heat treatments. Traditionally, relative strengthening is done using change in hardness values from the initial condition to the post-aged state. In the absence of this, the true stress value at the point of UEL (uniform elongation[2]) is instead used as a way to gauge the increase in relative strengthening. Figure 8.9 shows a plot of the relative strength versus the time-compensated temperature term, the Hollomon-Jaffe (HJ) parameter, *P*. The peak age condition, identified by a HJ value of 15, shows the reduced strengthening achieved for specimens without a solution heat treatment. And with higher values of P, those specimens without a solution heat treatment do no over-age as intended, but instead increase in volumetric fraction of martensite with cooling. Plotting the information in this way helps to illustrate the case that the aging kinetics are inhibited when the initial microstructure contains a large volume fraction of a phase that does not age-harden in a way typically intended. Figure 8.9: Plot of the relative strengthening achieved against the time compensated temperature Hollomon-Jaffe parameter, P.

[2] Also referred to as the extent of uniform plastic deformation.

[3] The difference in yield between 10^{-4} and 10^{-5} is smaller than what is observed for all other neighboring strain rates, but the increased scatter does not lend confidence to making any determined conclusions on the actual value.

[4] Tests at 10^{1} s^{-1} are the only strain rate with 4 data points available. All other tests are averages of three test

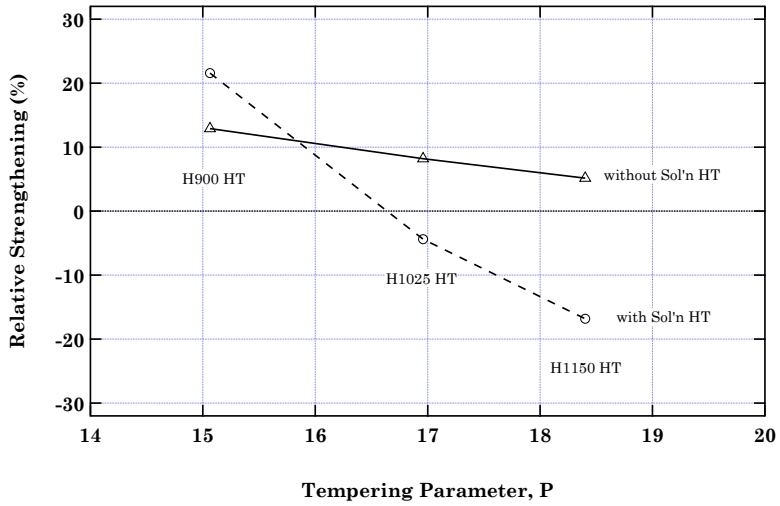


Figure 8.9: Relative strength from initial conditions prior to the application of aging treatments plotted against the time-compensated-temperature Hollomon-Jaffe parameter, P.

In addition to identifying the effects of this increased volumetric fraction of austenite on heat treatment performance, it is worth examining in more detail the effect on mechanical behavior. Figures 8.10 and 8.11 show the work hardening rate of all specimens heat treated with and without the initial solution heat treatment, respectively. High initial densities of dislocations associated with the martensite phase and the finely dispersed precipitates significantly impede dislocation motion in the CA-H900 specimens and result in a rapid transition in the work hardening rate from yield to UTS. Increased softening of the microstructure with over-aging and increased austenite reversion in specimens treated to CA-H1025 and CA-1150 reduces the rate of transition between yield and UTS. These cases demonstrate a prolonged work-hardening curve for greater ranges of plastic strain. This trend is reversed for those without an initial solution heat treatment, where greater fractions of metastable austenite transform to martensite (H1025 and H1150) with increasing heat treatment temperature. For the as-fabricated and H900 treated specimens with high volume fractions of austenite, a significantly different trend in behavior is observed. A rapid work-hardening transition is observed at the point of yield. However, a region of relatively low flow stress immediately follows. And in the case of the H900 specimens, an observed negative work hardening relationship is measured. This would indicate work softening occurs where reduced stress levels are required to maintain dislocation glide or accommodate plastic strain by twinning within the relatively softer austenite grains with lower stacking fault energies. Following the initial shoulder at yield, the H900 and as-fabricated materials appreciably work harden until achieving a maximum, post-yield rate. Following this reversal after yield the rate begins to decline again until reaching

their respective UTS and local plastic deformation dominates continued elongation. This demonstrates a strong capacity for strain-induced hardening. And as a consequence of the high initial volume fraction of austenite, we observe stress-induced transformation of austenite to martensite in this metastable, dual phase microstructure.

The behavior of strain induced transformation has been extensively studied in austenitic stainless steels where the stable microstructure at room temperature is the austenite phase, but may transform to the ε-phase at low values of strain and further to α' martensite at higher strain [89]. For precipitation hardenable, martensitic stainless steels, however, this transformative behavior of phases is rarely encountered in practice, as it is not the stable bulk material behavior. To verify this, a tensile specimen of the as-fabricated condition tested at a strain rate of 10^{-3} s^{-1} was sectioned and prepared for XRD. The volumetric fraction of austenite within the grip section where no plastic deformation occurred was found to be unchanged from the previously reported value of 36%. Whereas in the gauge section, adjacent the site of rupture, the volumetric fraction of austenite was found to have been reduced to 5.2%. This measurement was made within the region identified as uniform plastic deformation where the diameter remains relatively constant. It is expected that measurements made within the region of local necking, the volumetric fraction of austenite would be lower still.

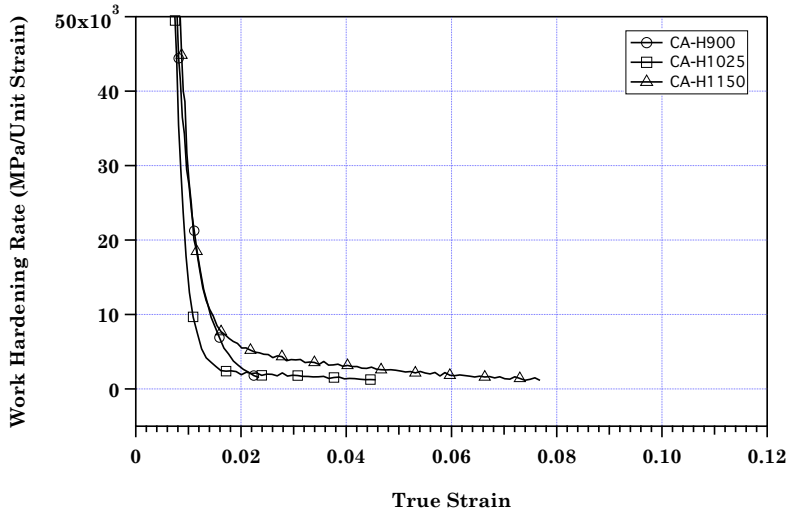


Figure 8.10: Work hardening rates for specimens with an initial solution heat treatment and evaluated at a strain rate of 10^{-3} s^{-1}.

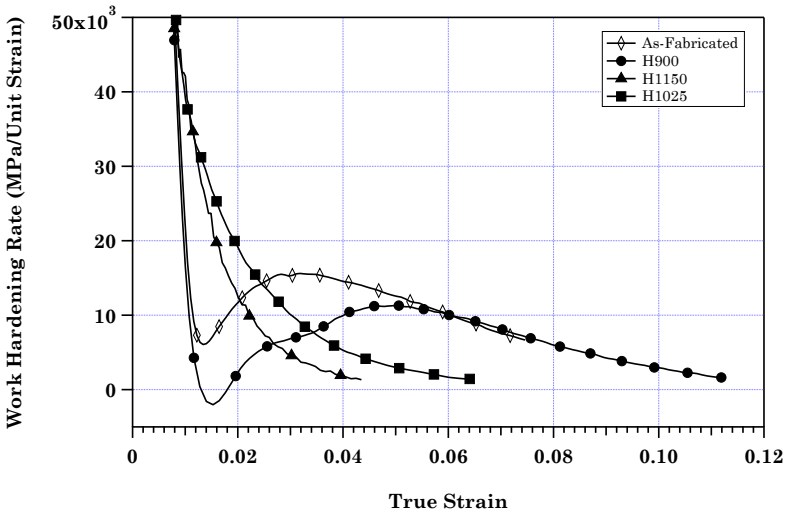


Figure 8.11: Work hardening rates for specimens **without** an initial solution heat treatment and evaluated at a strain rate of 10^{-3} s^{-1}.

8.5.2 Mechanical Properties, Strain Rate Dependency

Figures 8.12 and 8.13 show trends in measured YS and UTS for specimens with and an initial solution heat treatment across the four principle strain rates investigated, 10^{-3}, 10^{-1}, 10^{1}, and 10^{3} s^{-1}. And similarly, Figures 8.14 and 8.15 show the same data, but for specimens without an initial solution heat treatment across the same conditions evaluated. Behavior observed in Figures 8.12 and 8.14 show the expected increase in YS that accompanies increasing strain rate. For all specimen types evaluated, this trend in behavior is consistent. However, the sensitivity to these changes in strain rates is markedly different between the two groups of specimens.

Generally, increases in both yield and ultimate tensile strength are observed with increases in strain rate for those specimens initially treated with a solution heat treatment prior to aging. Dislocation motion is impeded by the previously described grain, dislocation, and precipitate structures. Available thermal fluctuations at the temperature evaluated (room temperature, 24 °C) are incapable of assisting dislocations over short-range thermal barriers at a rate fast enough to permit plastic flow. Therefore, as plastic deformation is considered a thermally activated process, we expect increases in yield to accompany the increases in strain rate. However, Figures 8.13 and 8.15 show some unexpected differences in behavior. While the trends in yield strength continue to monotonically increase with increasing strain rate, measured UTS between the specimen types begins to diverge. More specifically, for the two specimen types with austenite volume fractions greater than 35% (as-fabricated and H900), UTS is observed to decrease through the range of quasi-static strain

rates evaluated (10^{-3} and 10^{-1} s^{-1}), increase at the intermediate strain rate (10^{1} s^{-1}), but continue to fall again with dynamic testing (10^{3} s^{-1}). This erratic behavior is not what was initially expected. To better understand this relationship, additional measurements across a greater range of strain rates and at intermediate speeds for the as-fabricated condition were performed as a proxy to understand the effect of austenite fraction on strain rate sensitivity in SLM processed 17-4 PH.

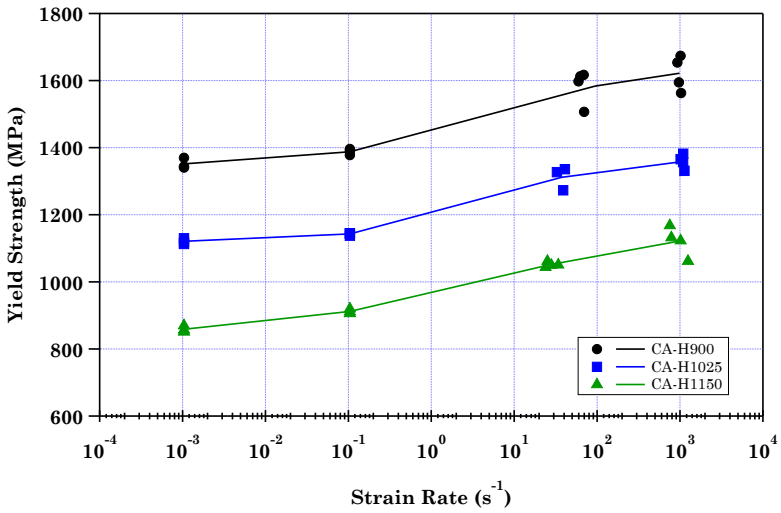


Figure 8.12: Yield strength plotted against changes in strain rate. The three conditions shown here are the CA-H900, CA-H1025, and CA-H1150 heat treatments. Strain rates evaluated are on the order of 10^{-3}, 10^{-1}, 10^{1}, and 10^{3} s^{-1}.

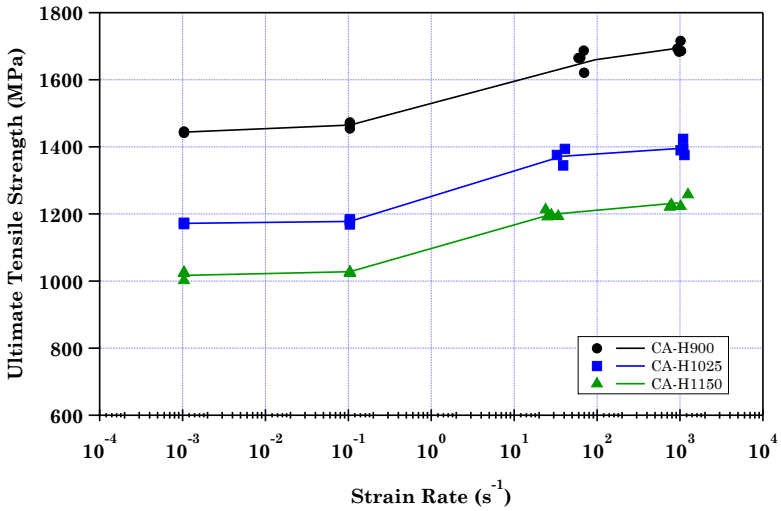


Figure 8.13: Ultimate tensile strength plotted against changes in strain rate. The three conditions shown here are the CA-H900, CA-H1025, and CA-H1150 heat treatments. Strain rates evaluated are on the order of 10^{-3}, 10^{-1}, 10^{1}, and 10^{3} s^{-1}.

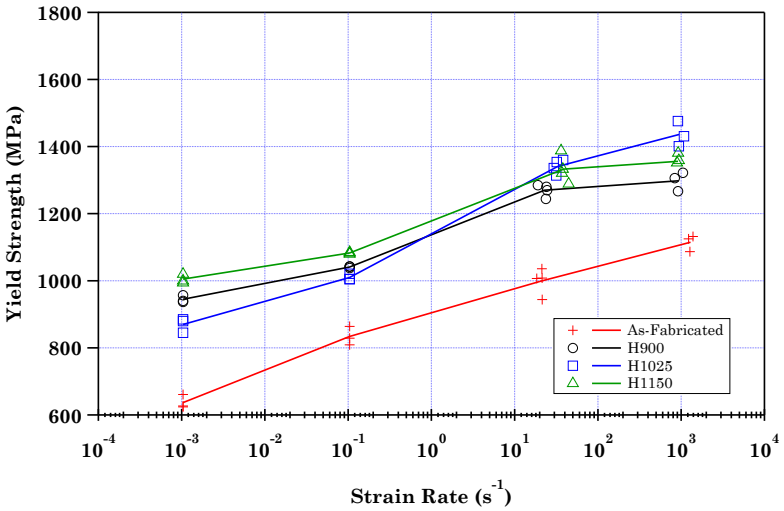


Figure 8.14: Yield strength plotted against changes in strain rate. The three conditions shown here are the H900, H1025, H1150 heat treatments, and the as-fabricated condition. Strain rates evaluated are on the order of 10^{-3}, 10^{-1}, 10^{1}, and 10^{3} s^{-1}.

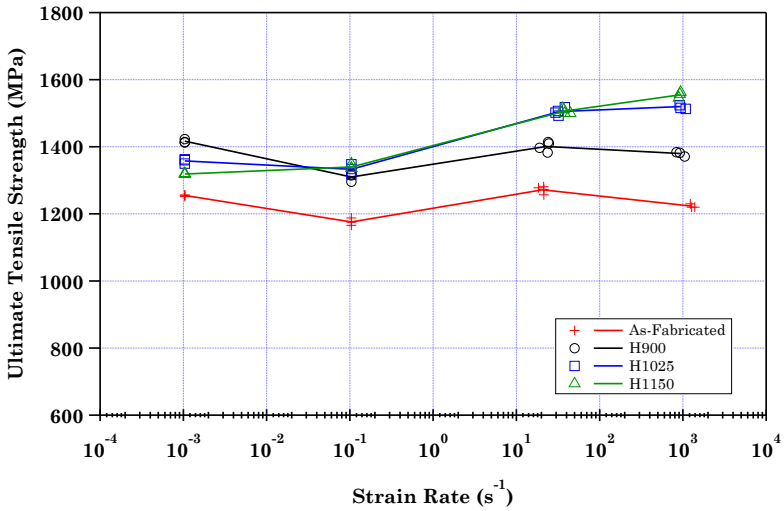


Figure 8.15: Ultimate tensile strength plotted against changes in strain rate. The three conditions shown here are the H900, H1025, H1150 heat treatments, and the as-fabricated condition. Strain rates evaluated are on the order of 10^{-3}, 10^{-1}, 10^{1}, and 10^{3} s^{-1}.

Figure 8.16 shows a combined plot of both the YS and UTS as measured for as-fabricated specimens across the following strain rates: 10^{-5}, 10^{-4}, 10^{-3}, 10^{-2}, 10^{-1}, 10^{0}, 10^{1}, and 10^{3} s^{-1}. As previously observed, increasing strain rates demonstrate increasing yield strength. However, the yield strength is not observed to asymptote towards at any lower value. Across the entire range of testing speeds evaluated, yield strength is observed to nearly increase or decrease in proportion to the logarithm of the testing speed.[3] UTS is observed to behave differently. From the slowest testing speeds evaluated, UTS is found to originate

[3] The difference in yield between 10^{-4} and 10^{-5} is smaller than what is observed for all other neighboring strain rates, but the increased scatter does not lend confidence to making any determined conclusions on the actual value.

at a peak value of 1395 MPa. With increasing tensile testing speed the maximum obtainable stress level is observed to drop. At an intermediate testing speed of 10^1 s^{-1} the UTS is observed to increase. However, at the one dynamic speed evaluated, another reduction is noted. Figure 8.17 clarifies the stress-strain relationship for the as-fabricated material across all strain rates evaluated. This figure plots the true stress value as a function of strain rate along iso-strain lines (i.e. each line indicates a particular value of strain). For clarity, the ε values of 0.02 and 0.03 are of a different color to aid in following their path. Points along the iso-strain lines are an average of 3 or more tests.[4]

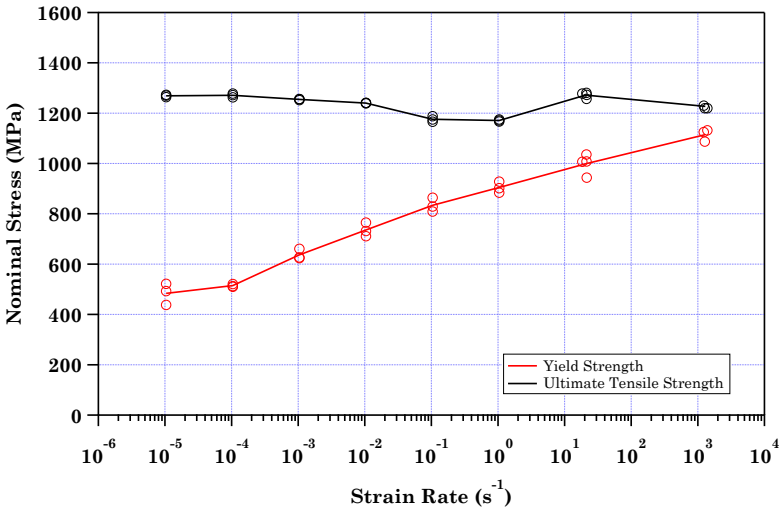


Figure 8.16: Combined plot of yield and ultimate tensile strengths of the as-fabricated material when tested across a wide range of strain rates.

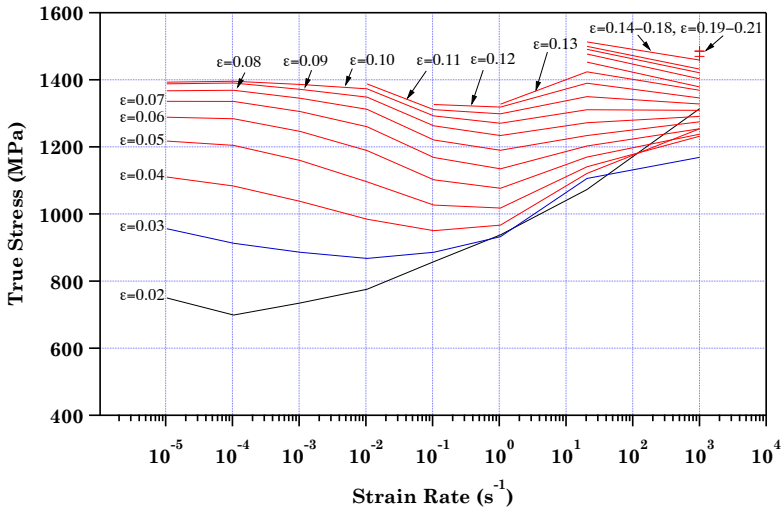


Figure 8.17: Iso-strain lines of true stress plotted across the range of strain rates evaluated for the as-fabricated specimen. Iso-strain lines of 0.02 and 0.03 are colored differently to aid in following their path.

[4] Tests at 10^1 s^{-1} are the only strain rate with 4 data points available. All other tests are averages of three test specimens.

At dynamic tensile strain rates, the yielding behavior is observed to introduce an upper and lower yield point. This behavior is occasionally observed for testing via SHTB and can be sometimes attributed to an oscillating incident stress wave. However, the upper-lower yielding phenomenon is also observed at strain rates lower than those performed on the SHTB. As such, it is believed this is a material effect relating to dislocation glide en mass or a high degree of strain induced twinning within the austenite grains where initial stress is relieved by strain at reduced stress levels. This behavior is observable in Figure 8.17 by the crossing of the iso-strain lines at low values of strain (namely at 0.02 and 0.03) where a high yield point is followed by a reduction in stress before subsequently rising with additional strain.[5] To aid in understanding Figure 8.17, traditional engineering stress-strain plots are shown for the 10^{-5}, 10^{-3}, 10^{-1}, and 10^{3} s^{-1} strain rates in Figure 8.18. These illustrate individual tests and their characteristic behavior for the family of tests at their respective strain rates. For clarity, only a single test from the subset of the strain rates are shown.

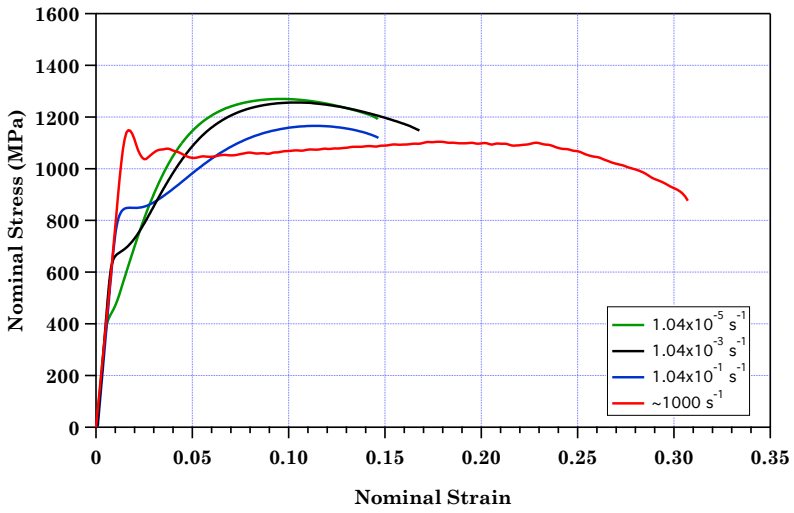


Figure 8.18: Nominal stress-strain curves for as-fabricated specimens evaluated at 10^{-5}, 10^{-3}, 10^{-1}, and 10^{3} s^{-1}.

Close scrutiny of Figure 8.17 begins to illustrate the differences in work hardening across the strain rates evaluated. However, Figure 8.19 shows this information directly and in greater detail. Here the rates at which the specimens work hardened through the range of strain until UEL is displayed. Work hardening rates for specimens tested at the slowest of strain rates show the greatest rates upon yielding. And it is for this reason that we can observe comparatively smaller ranges of UEL. Figure 8.20 shows UEL as a function of

[5] Scatter in the yielding behavior at dynamic testing speeds may also account for some of the overlap observed at low values of strain.

strain rate. For specimens at low strain rates, the rate of work hardening and range of UEL is nearly constant. With increasing strain rate, however, the specimens are permitted to extend the range of strain over which work hardening occurs. This occurs alongside the observed reduction in UTS.

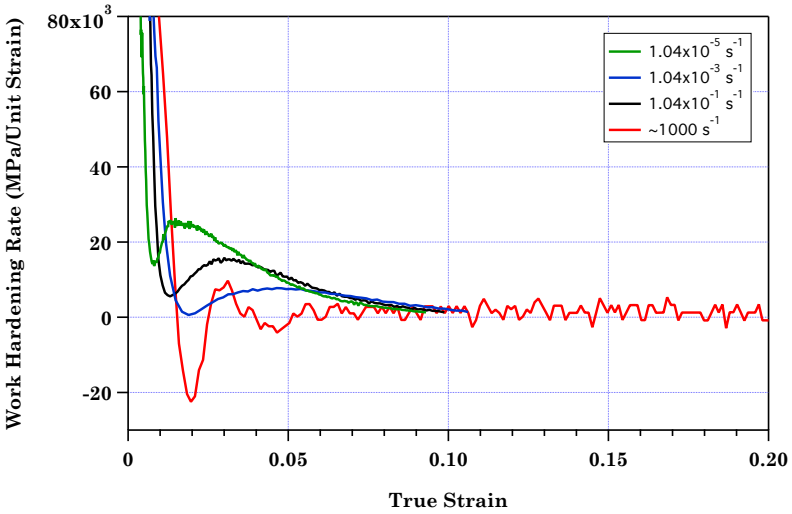


Figure 8.19: Work hardening rates as a function of true strain of as-fabricated specimens plotted evaluated at strain rates of 10^{-5}, 10^{-3}, 10^{-1}, and 10^{3} s^{-1}. Oscillatory behavior observed at the strain rate of 10^{3} s^{-1} is principally an artifact of electrical noise during test. The running mean value is just above 0.

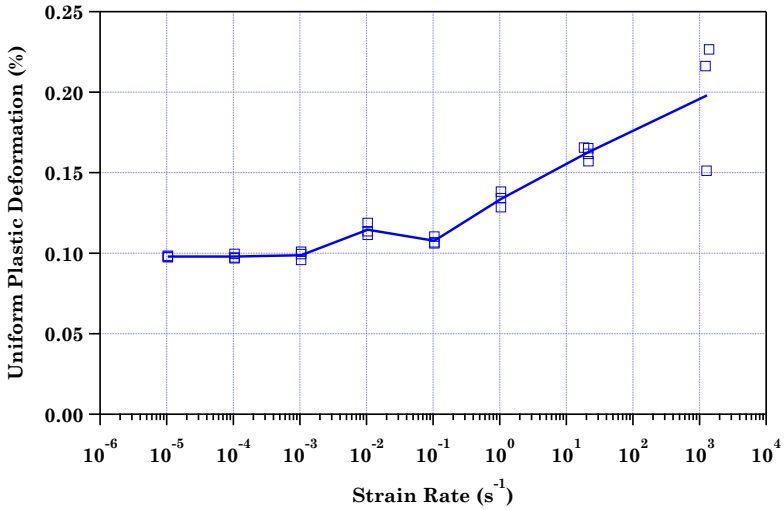


Figure 8.20: Uniform plastic deformation attained against strain rate evaluated for as-fabricated specimens.

The work hardening behavior observed in Figure 8.19 is shown as a function of true strain. However, to elaborate on the deformation mechanism, Figure 8.21 shows the work hardening behavior as it changes with respect to true stress on a natural log-log plot. This figure illustrates how the dual-phase steel plastically deforms through three distinct phases. The first stage is described as the initial working hardening and complementary plastic deformation at low stress and strain. The end of the first region is marked by a rapid decline in the rate upon

yield. Region two is characterized by a reversal from the initial decline in work hardening and a steady increase in its rate until a peak rate is achieved. From this peak rate the third region is defined as a gradual reduction in work hardening until the test specimen achieves ultimate tensile strength. At slow strain rates where the UTS is observed to remain unvarying with strain rate, work hardening rates all converge at the same peak stress value. However, due to the sizable sensitivity to strain rate at yield, the initiation of region one and the range of stress over which the transition from region two into three occurs is not consistent – at lower strain rates, this transition is larger. For faster strain rate tests where UTS remains constant, but the difference in YS and UTS is smaller, the transitionary work hardening rate between regions two and three is more acute. In other dual-phase steels [90], it is common to observe a similar change in work hardening rates with an accompanying transition from one phase largely undergoing plastic deformation alone to both phases together plastically deforming with additional applied stress. In other words, the softer phase undergoes plastic deformation alone until a critical stress value. At this point, both phases in the dual-phase material plastically yield together. It can be surmised that this behavior is occurring between the relatively soft austenite and very hard martensite phases here. Martensite is found to not plastically yield until much later in the deformation. And for a strain rate of 10^{-3} s^{-1}, this transition in work hardening rate is clearly observed. At 10^{-5} s^{-1}, the transition is less clear due to the gradual transition. However, it is found to occur after a region of nearly constant work-hardening. A single deformation mechanism isolated to the softer austenite is believed to be at work here. An additional observation of note in Figure 8.21 is the nature of the dynamic test. Work-hardening is seen to bypass all of these various regions described in the quasi-static case. It immediately drops from the high work-hardening rate at yield and is found to remain stable for a region of increasing stress.[6] This behavior and the reasons for it will be described in the following paragraphs.

[6] The observed two parallel lines for the curve identified as the 103 s-1 strain rate in Figure 8.21 are due to the electrical noise and sampling resolution during the high speed test. This will be corrected in a later revision of this thesis. The plot will be updated to properly reflect the work hardening derivative.

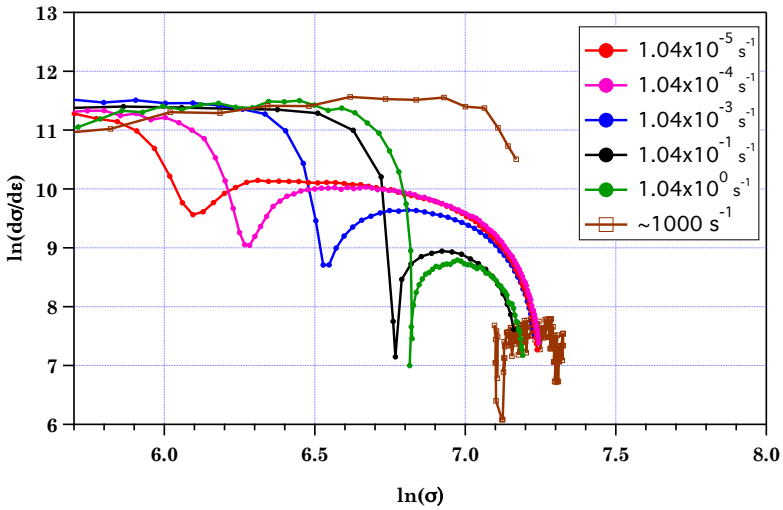


Figure 8.21: Logarithm of work hardening rate plotted against the logarithm of true stress. Strain rates of 10^{-5}, 10^{-4}, 10^{-3}, 10^{-1}, 10^{0} and 10^{3} s^{-1} are shown. The curve for 10^{3} s^{-1} is discontinuous due to the oscillatory behavior observed at the point of yield resulting in regions of the test not that cannot be evaluated by a natural logarithm.

Despite the changing plastic deformation behavior observed consistently between quasi-static tests, the transient nature of continued plastic deformation, work hardening, and maximum attainable stress (UTS) at ever increasing strain rates is a result of two competing material effects: thermal stabilization of the austenite phase and the strain rate sensitivity of the two-phase combination.

Tensile testing, among other forms of destructive material evaluation, is noted to generate heat as a part of the plastic deformation process. Equation 8.1 may be used to approximate the temperature change as a result of tensile deformation under the assumption of adiabatic conditions (i.e. no heat flux with the surroundings).

$$\Delta T = \frac{\beta}{\rho C_P} \int_0^{\varepsilon_f} \sigma_{avg}\, d\varepsilon \qquad (8.1)$$

Where β is defined as the efficiency factor (typically .9 or .95), ρ is the material density (the material density and not the relative density with porosity is used), and C_P is the heat capacity. This value can be calculated numerically by using the trapezoidal rule and a summation of tabulated temperature changes to integrate between the start and finish of the test as a function of stress and strain. Direct measurements during experimental work by Lichtenfeld et al [91], indicated that for strain rates orders of 10^{-1} s-1 and higher, this equation generally maintains good agreement with the actual measured value (within 5 °C) for austenitic

stainless steels.[7] Their measured values were found to be consistently higher than the calculated values by the above equation. Therefore, for the purpose of this experimental work, the equation is used to approximate the temperature increase for tests performed at strain rates of 10^{-1} s^{-1} and higher. Table 8.5 details the temperature of the specimen as calculated with respect to stress varying along strain across the four tests that met the criteria established above. The calculated temperature change has been rounded to the nearest whole degree centigrade. Because calculations involving true stress and true strain are only valid for regions of uniform plastic deformation, temperature estimations by Equation 8.1 are also only valid until UEL.[8]

Table 8.5: Estimated Temperature of Tensile Tests Evaluated

	Temperature (°C)			
Strain	$\dot{\varepsilon} = 0.104$ s-1	$\dot{\varepsilon} = 1.04$ s-1	$\dot{\varepsilon} \approx 10$ s-1	$\dot{\varepsilon} \approx 1000$ s-1
0	24	24	24	24
0.05	35	36	37	39
0.10	51	52	54	56
0.15	-	-	73	73
0.20	-	-	-	93

Absent values indicate rupture prior to the value of strain.

For these tests, the estimated temperature exceeds that identified as the approximate value as the martensitic finish temperature (M_f, 32 °C) with significant margin. Tensile specimens are increasingly elevated into a temperature regime where the martensitic transformation is ongoing. And as previously discussed in Chapter 4, the change is sigmoidal in shape across temperature with a rapid transition at some intermediate temperature between M_S and M_f. Changes in only a few degrees can result in large changes of phase stability. The result of higher fractions of austenite that remain stabilized and not undergoing the stress-induced phase transformation is a reduced or inhibited

[7] This was performed for 304L and 309 Stainless Steel. 17-4 PH has values for heat capacity and density that are similar to those for the other study's material.

[8] Nonetheless, temperature would still continue to increase after the onset of necking.

state of work hardening. In the case of the dynamic tests, little to no work hardening is observed in the engineering stress-strain plots beyond the initial oscillatory behavior at yield. For those specimens tested at strain rates slower that what may satisfy the condition of adiabatic heating, still indicate gradual reductions in UTS. This would suggest that a sufficient temperature rise still occurs to marginally stabilize austenite despite the heat flux through the tensile equipment and laboratory air.

As a result of these observations concerning the thermal stabilization of the austenite phase, a discussion about the strain rate sensitivity of as-fabricated 17-4 PH is increasingly more complex. The mechanical behavior observed as a result of this material evaluated across the wide range of strain rates tested clearly indicates a sensitivity to strain rate at low values of strain. Here, the temperature change due to plastic deformation is negligible. Specifically, the stress at the point of yield and shortly after is characteristic of the interaction between the microstructure and the applied strain rate. This reflects the thermally activated nature of dislocation motion when under load. Thermal fluctuations assist dislocations at overcoming internally varying short-range obstacles at lower levels of applied load. However, with the onset of continued plastic deformation and the expected temperature rise, the material instead undergoes a *temperature varying structural change* rather than a response to the change in the stress state of the material. When heat generated due to plastic generation is sufficiently balanced by heat flux away from the specimen, the continued stress-strain response is a result of ongoing stress-induced phase changes. However, with increases in temperature, the behavior observed is no longer a result of either the expected transformation from austenite to martensite or thermally activated dislocation motion alone. The changing nature of phase stabilization due to heat generated via plastic deformation with respect to strain rate determines the continued resistance to further plastic flow and macroscopic behavior. Under these circumstances, classical calculations that would describe the strain rate dependency of this material are no longer applicable.

Where we see this interaction between phase stabilization and strain rate sensitivity for the as-fabricated specimens is during the transitions between 10^0, 10^1, and 10^3 s^{-1} strain rates. At strain rates slower and including 10^0 s^{-1}, a steady reduction in work hardening and UTS is observed. However, at a strain rate of 10^1 s^{-1}, an increase in UTS is noted – a reversal in this trend. Both an increase in yield and UTS are observed with the subsequent increase in strain rate for the as-fabricated material. Similar behavior is observed across all other specimens of the various heat treatment conditions (especially the near fully martensitic

materials). A response in sensitivity to this change in strain rate is the likely cause for this reversal in the falling UTS value despite the increase in temperature. Figure 8.22 shows the nominal stress-strain curve for a test at a strain rate of 10^1 s^{-1}. Unlike specimens evaluated at dynamic rates, work hardening is still clearly observed, but not with a magnitude or rate observed from the slower quasi-static tests. Austenite stabilization has not been fully achieved. However, with an additional increase in strain rate to 10^3 s^{-1}, the continued rise in yield stress is still noted, but UTS has fallen again. In this final case, at the dynamic strain rate of 10^3 s^{-1}, the thermal stabilization is dominant at reducing UTS rather than the noted strain rate sensitivity that would otherwise raise it.

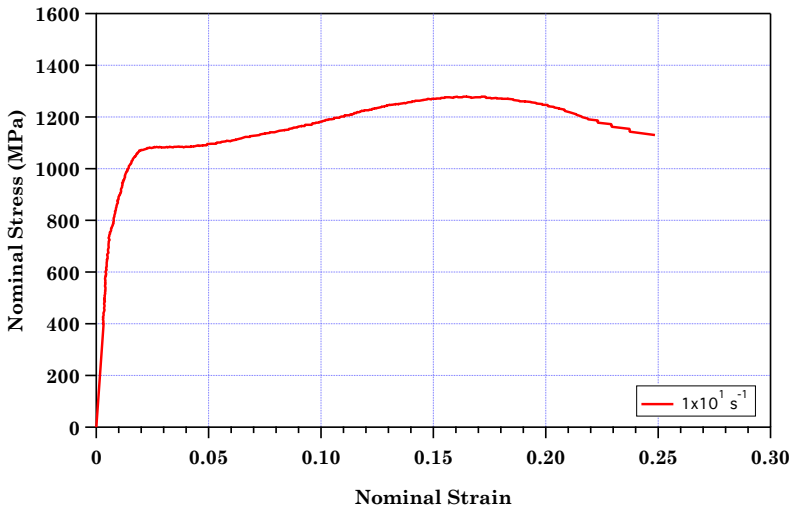


Figure 8.22: Nominal stress-strain plot for a single as-fabricated specimen evaluated at the intermediate strain rate of 10^1 s^{-1}.

Of particular note to tensile testing as-fabricated specimens at strain rates of 10^{-1} s^{-1}, as depicted in the stress-strain curve shown above in Fig. 8.22, is the formation of two yield points (approximately at 750 and 1075 MPa). This behavior was observed for both the as-fabricated and H900 specimens with high volumetric fractions of retained austenite. This yielding behavior is commonly seen for dual phase materials where a lower stress level initiates the yielding of the weaker phase, observed as a change in the slope of the elastic region, followed by a secondary yield point. At the upper yield point plastic deformation occurs for both the stronger and weaker phases together. For SLM processed 17-4 PH this behavior is not directly observable at slower strain rates for the following reason. In the material investigated here, metastable austenite and martensite are the two phases present, the latter being significantly stronger. The plastic deformation at quasi-static strain rates is not a plastic yielding of the weaker austenite phase, followed by the plastic deformation of the stronger

phase at elevated stress levels per se. Instead, the weaker phase is being progressively transformed into the stronger phase and the volumetric change associated with the transformation is the plastic strain measured. Actualized yielding of the martensite does not occur until the specimen achieves a critical stress value. The observed change in work hardening rates with respect to stress, as shown in Fig. 8.21, identify the stress level at which the martensite begins to yield irrespective of the austenite-martensite transformation (and it too increases with respect to increasing strain rate). These stress levels are identifiable in Fig. 8.21 by the deviation from the near-constant work hardening rates for 10^{-5} and 10^{-4} s^{-1} or by local maxima points of the work hardening rate post yield. At the increased strain rate of 10^{1} s^{-1}, there is insufficient time for the thermally activated transformation of austenite to martensite to occur at lower-stress levels. And because the temperature rise associated with plastic deformation has yet to increase to a level high enough to thermally stabilize the austenite phase, traditional yielding of the austenite phase by slip does not occur and instead remains a transformative process. Therefore, the stress levels are forced to rise without accommodating plastic strain. This results in the observed two-point yielding with the stronger martensite phase observed to yield at lower values of strain.

While temperature estimations that evolved with tensile testing, as presented earlier suggest the stabilization of the austenite phase, direct measurement is needed. Verification of this phase transformation process and the increasing stabilization of the austenite phase for tests across a range of strain rates was made by XRD. Tensile samples following test were sectioned and prepared for XRD. Measurements were made in both the grips and gauge section of the specimens. It can be reasonably assumed that no plastic deformation occurred in the grips sections of the tensile specimens. Their measurements of austenite volume fractions in that portion of the specimen agreed well with measurements of bulk material (36% for this lot of SLM fabricated material). Figure 8.23 shows the increasing volume fraction of austenite with increasing strain rate. This couples well with the observed change in mechanical behavior and plastic yielding during tensile testing

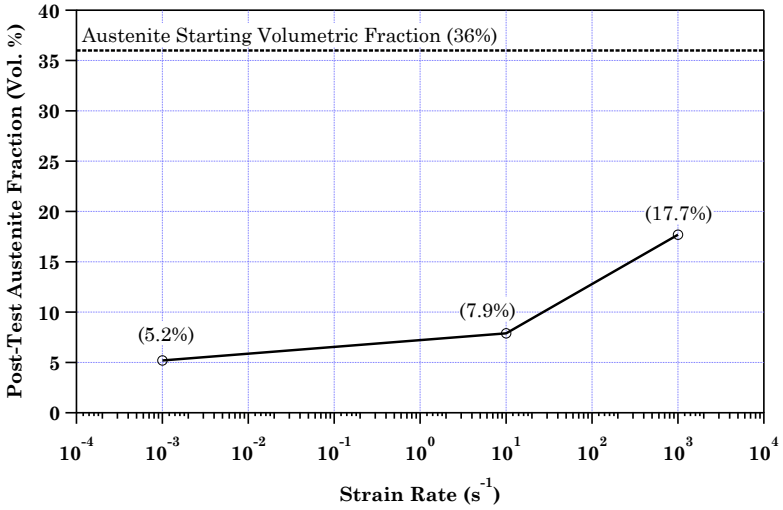


Figure 8.23: Change in volumetric fraction of Austenite with increasing strain rate as measured within the gauge section of ruptured tensile specimens.

8.5.3 Mechanical Properties, Temperature Sensitivity

A final validation of the thermal stabilization of austenite as the mechanism for the various changes in mechanical behavior observed across the strain rates evaluated, several quasi-static tests were performed at elevated temperature. Warm temperatures of 100 and 150 °C were selected to observe the changes in yield strength, ultimate tensile strength, and the intermediary plastic deformation of the specimens. Specimens were therefore evaluated using the screw-driven uniaxial tension testing machine in a manner similar to previous tests. An electric furnace was placed circumferentially around the specimen and testing jig with temperature levels maintained by a controller with an attached thermocouple adjacent to the specimen. To eliminate any temperature increase due to plastic deformation, the specimens were tested at a strain rate of 10^{-4} s^{-1}. In previous testing at room temperature, no significant changes were observed in the ultimate tensile strengths at this strain rate, suggesting no temperature-related stabilization of austenite occurred. Therefore, plastic deformation induced temperature changes at this and slower speeds were considered negligible and maintained an isothermal testing condition.

Figure 8.24 shows an engineering stress-strain plot of typical tests performed at 10^{-4} s^{-1} for specimens at room temperature (approximately 24 °C), 100 and 150°C. From this one plot, several observations on the plastic yielding behavior of the dual-phase material may be made. Increasing temperature has the effect of increasing the yield strength of tensile specimens while also reducing the

ultimate tensile strength. Total elongation is significantly altered (however, controlling for the effect of porosity on this behavioral characteristic is not possible with the material available and there may be differences between the temperatures not readily discernable). Both uniform and total elongation are observed to increase with the decreasing work hardening associated with the lack of phase transformation. For most other materials, an increase in the testing temperature below the homologous temperature would translate into a decrease of the yield strength of the material. As previously discussed in other chapters, dislocation motion is a thermally activated process. Dislocations are assisted over short-range obstacles by an increase in the available thermal energy associated with increases in the environmental testing temperature. However, for other alloys where metastable austenite is chemically stabilized at room temperature, this type of transitionary behavior is observed across temperature regimes that include the M_S and M_d[9] temperatures. Testing temperature ranges necessary to demonstrate this change in plastic yielding for such materials are across cryogenic temperatures [92]. In this case, where the chemically defined martensitic transformation temperatures are elevated above room temperature, the change in plastic yielding behavior may be observed at elevated temperatures.

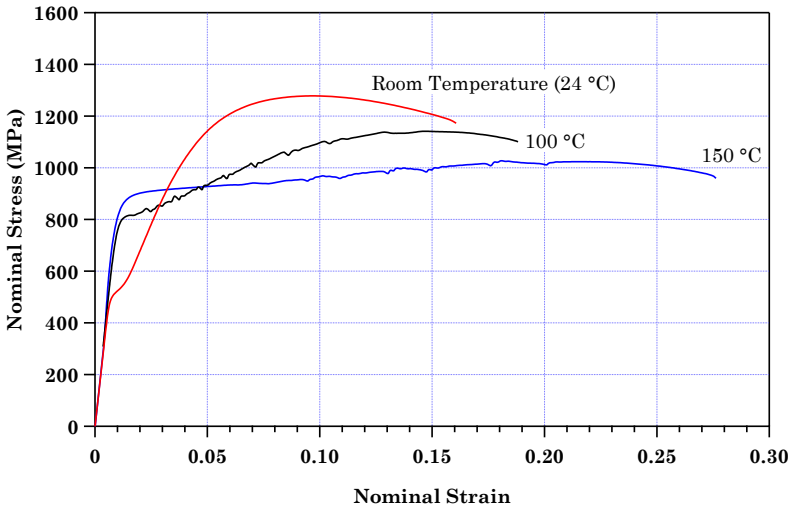


Figure 8.24: Nominal stress-strain plots at room temperature (24 °C), 100 °C, and 150 °C of the as-fabricated 17-4 PH.

[9] The M_d temperature, not previously introduced, is the temperature above which martensitic transformation due elevated stress or plastic strain does not occur. For 17-4 PH this temperature is not defined, as it is entirely martensitic at room temperature under normal conditions. M_d is at a temperature higher than M_S.

D. Fahr introduced nomenclature to describe the transition in behavior for metastable austenite based on the stability of the phase and the mechanism for its transformation [92]. The terms "stress-" and "strain-induced" formation of martensite with the corresponding plastic behavior as observed in the study performed by D. Fahr also apply here. As previously discussed, cooling 17-4 PH begins to spontaneously transform from austenite to martensite as a result of a large enough difference in the free energy between the two phases. Mechanisms for transformation, however, are not limited to the free energy difference, but include the applied normal stresses that may also initiate its formation at elevated temperature. In the case of 17-4 PH processed by SLM, the applied compressive stresses counter the driving force of the free energy difference that comes with lowered temperatures below the M_S temperature. At temperatures below M_S, however, the stresses required to initiate slip within austenite exceed those necessary to induce the phase transformation. However, as temperatures approach the M_d temperature, the stresses required to initiate the transformation to martensite exceed those necessary to induce slip within the austenite. Analogous to "stress-aging" and "strain-aging", the formation of martensite via applied stress or strain may be labeled as such, "stress-induced" or "strain-induced" transformation of austenite to martensite.

To be considered a "stress-induced" formation the applied stress level required to initiate the transformation is considered elastic and below the level necessary to yield the austenite ($\sigma_{\gamma \rightarrow \alpha'} < \sigma_{\text{yield-}\gamma}$). Whereas "strain-induced" transformation is the plastic yielding of the austenite grains by slip before the formation of martensite ($\sigma_{\gamma \rightarrow \alpha'} > \sigma_{\text{yield-}\gamma}$). The formation of martensite by plastic strain also may accommodate relaxation in the measured stress levels due to the volumetric change that occurs with its formation. This is observable as serrations in the plastic yielding behavior seen in the stress-strain plots that accompany the intermittent bursts of transformation amidst the continued slip within the austenite phase. "Stress-induced" transformation of austenite to martensite at lower temperatures occurs at stress levels lower than what is required to initiate slip. Plastic deformation is therefore free of serrations.

To summarize the temperature effects on mechanical behavior, Fig. 8.25 shows changes in both the yield and ultimate tensile strengths measured across the temperatures evaluated. Figure 8.26 shows work-hardening rates for the three temperatures with respect to strain. The observed transformation of plastic behavior with increasing austenite stabilization accompanying the increase in temperature is readily apparent.

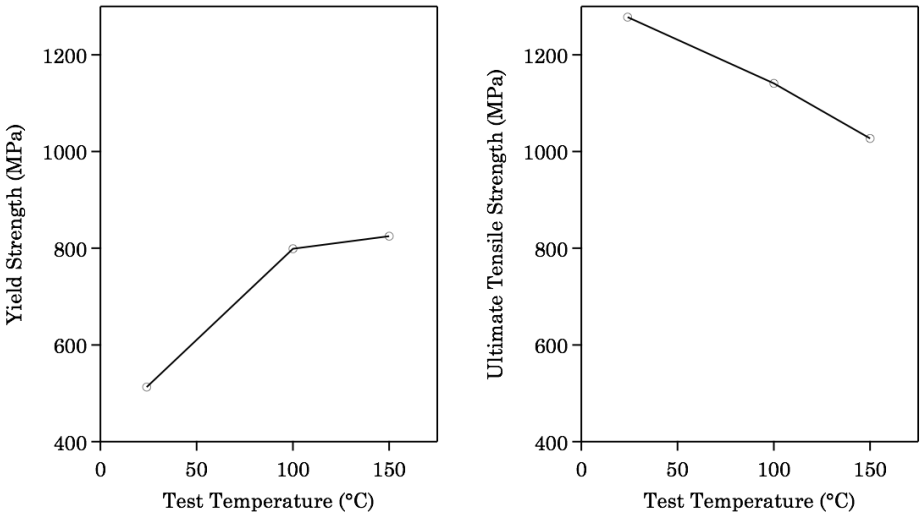


Figure 8.25: Changes in both yield and ultimate tensile strengths for as-fabricated specimens evaluated across changes in temperature.

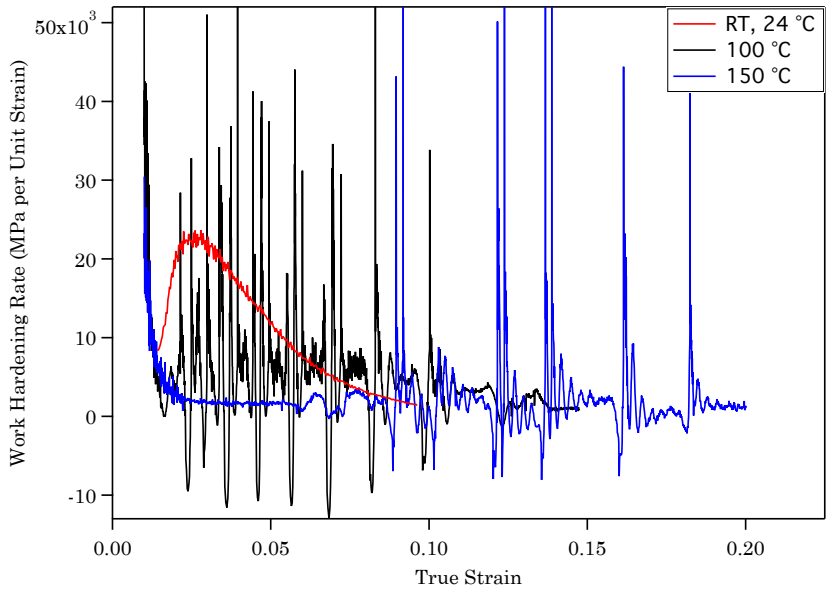


Figure 8.26: Work hardening rate with respect to true strain for the three temperatures evaluated. A strain rate of 10^{-4} s^{-1} was used for all tests. Serration bursts during plastic yielding are observable as oscillatory changes in the work hardening rate and denote the occurrence of strain-induced transformation of austenite to martensite. Stress-induced transformation of austenite to martensite at room temperature is free of these oscillations.

8.5.4 Schematic Summary

To summarize and condense the previous sections in this chapter to the information presented in the previous chapter detailing microstructure, it is valuable to schematically depict the behavior of the material with respect to the tensile testing performed. Figure 8.27 shows a single engineering stress-strain plot for an as-fabricated specimen evaluated at room temperature (24 °C) with a strain rate of 10^{-4} s^{-1}. A corresponding schematic representation of the microstructure for this material is shown in Figure 8.28 and illustrates the dual phase microstructure. The two phases, primary lath martensite and secondary retained, metastable austenite are labeled and may be identified by their patterning (parallel lines appropriately represent the lath martensite, but are not to scale).

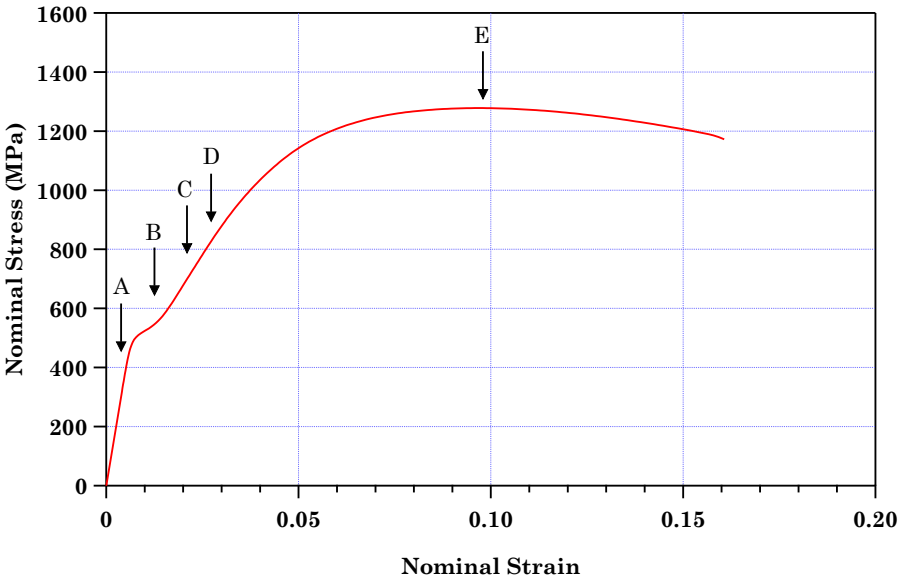


Figure 8.27: Nominal stress-strain plot for an as-fabricated specimen tested under uniaxial tension at a strain rate of 10^{-4} s^{-1} and annotated with particular microstructural events, A through E.

Event:

A. Initial load is applied to the tensile specimen and the stress levels are sufficiently low that specimen responds elastically. Typically, the slope of this region may be used to determine the proportionality constant for the material, Young's modulus (typical steels range from 190-200 GPa). However, measurement of Young's modulus by tensile testing is not commonly accurate at measuring this material property. Compliance within the testing apparatus, while largely compensated in this test, cannot be completely eliminated and results in a slope lower than what is considered. The distribution of austenite

and martensite remain unchanged from the initial state prior to test. No changes to the microstructure are made until event B.

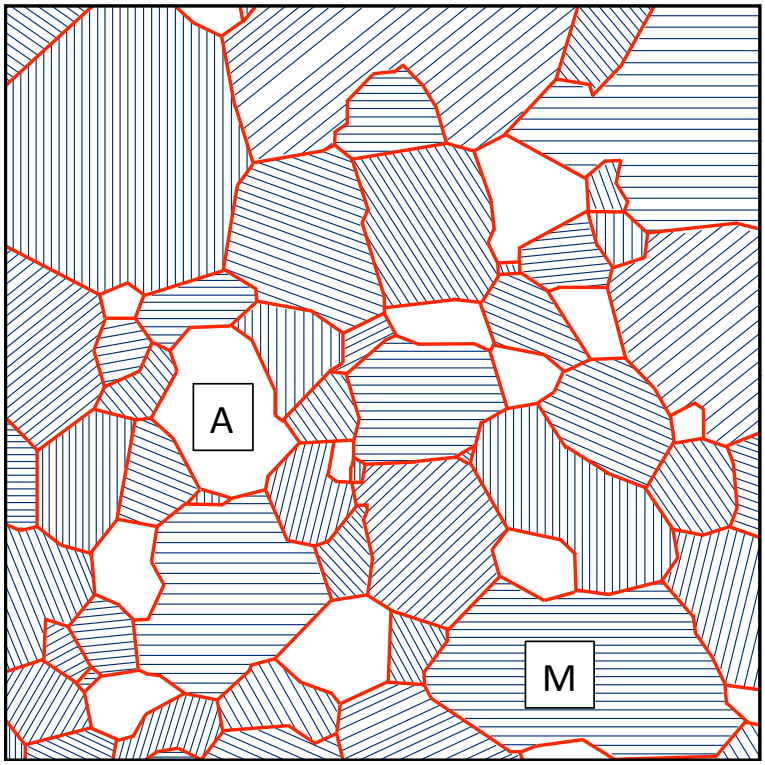


Figure 8.28 (a): As-fabricated material with the secondary austenite phase (identified as "A") and the primary lath martensite phase (identified as "M"). The red lines identify the prior austenite grain boundary structure. The black parallel lines within the grain symbolically represent the martensite lath structure. Martensite grains may in reality contain several "blocks" with groups of parallel laths that are antiparallel to other blocks within the same parent austenite grain boundary. This condition represents the unloaded and low-stress state of the material. Stress levels below "yield" do not affect the microstructure.

B. Yielding of the as-fabricated material is denoted by the shoulder and increase in measureable elongation to the tensile specimen. "Yield strength" is measured by a 0.2% strain offset intercept from the elastic region. The absence of a sharp yield point clearly highlights the behavior of the polycrystalline structure and the various lattice plane orientations relative to the applied load where deformation is preferred. The soft shoulder is a result of the varying shear stress necessary to induce deformation on these lattice planes at the their respective orientations to the applied load. "Yielding" is shown in quotations to indicate measurement of plastic deformation resulting from the stress-induced deformation of austenite to martensite and not the true yield of austenite grains by dislocation slip. Here, the transformation generates the measured change in

specimen length. The following rise in work hardening post-yield is characteristic of an over-stress condition where the rate-sensitivity of the transformation process requires excess stress to initiate the transformation due to a lack of available thermal fluctuations to assist with its initiation. Upon start of the deformation a reduction in work hardening accompanies an increase in plastic deformation at relatively reduced stress levels (in this case it is very small, but observable). Higher strain rates show an upper-lower yield point where this over-stress condition is larger. At lower strain rates, this yielding behavior is nearly non-existent. Austenite grains that transform to martensite are identified by the bold, blue lath structures within the existing grains.

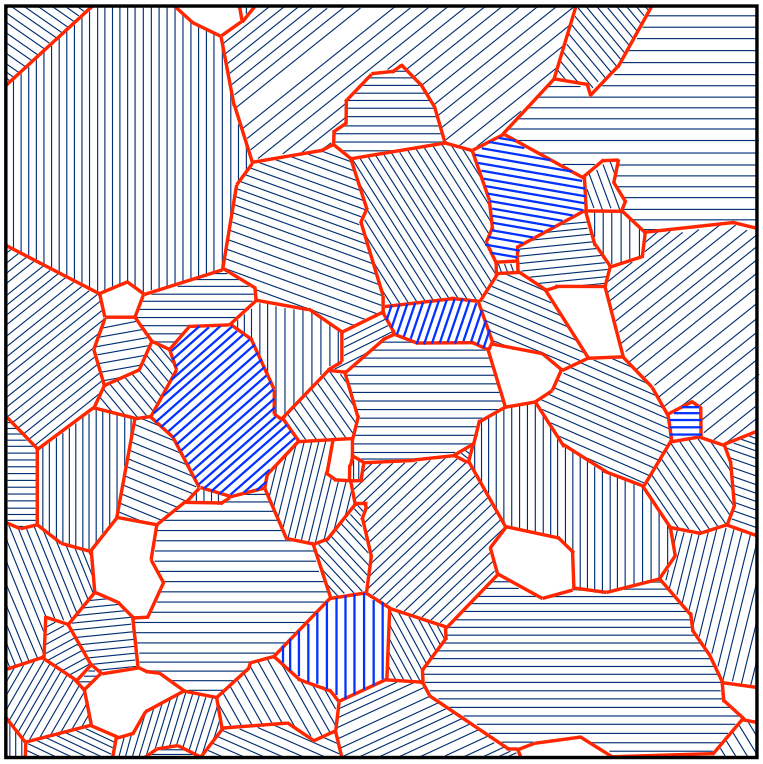


Figure 8.28 (b): "Yielding" of the softer austenite grains begins at stress levels below their normal yield strength. The deformation process is instead a transformation to martensite. The blue parallel lines schematically represent austenite grains where this transformation occurs.

C. Transformation of austenite grains to martensite effectively increases the resistance to further deformation via dislocation motion within these grains due to the increase in relative strength. Further transformations to martensite occur with the continued increase in stress levels. The process of dynamic transformation occurs continuously throughout the "yielding" of the specimen and may be denoted as a linear region of the stress-strain curve post-yield. This region is also seen as a constant work hardening rate with respect to stress on a natural log-log scale plot (as plotted in Fig. 8.21).

D. The inflection point noted as "D" in Figure 8.27 indicates the point at which work hardening rates are observed to begin falling. At these stress levels, the plastic yielding of martensite is believed to begin. This plastic deformation of the primary phase occurs alongside the continued transformation of remaining austenite to martensite. Both processes occur simultaneously. Transformation and plastic deformation continue until the load bearing capacity of largely martensitic structure is exceeded.

E. The point at which the structure can no longer maintain uniform plastic deformation is referred to as ultimate tensile strength (UTS). This is the peak stress attainable for the material. It is at this point in the plastic deformation that the onset of localized plastic deformation begins with incipient necking. It is likely that ongoing transformation of austenite to martensite continues in this region. However measurement of the phase fraction post-test (or at any intermediate point) is difficult due to the specimen geometry and the relatively small target for phase measurement via XRD.

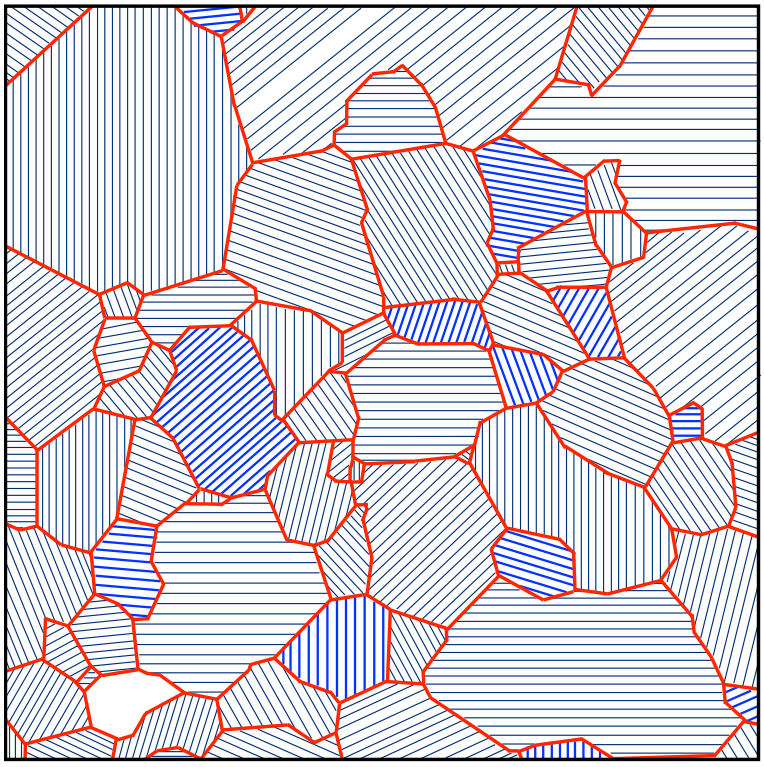


Figure 8.28(e): Near-complete transformation of the austenite phase to martensite has completed by the end of the test.

The test concludes with initiation of a crack and final rupture denoted by the end of the stress-strain curve.

8.5.5 Fractography

In addition to analysis made from data recorded as part of the tensile evaluation, observations on all specimens' rupture surfaces yielded information into the moments leading up to and at fracture. Throughout all the testing across the various heat treatment conditions and strain rates, several recurring observations were made at various size scales. In general, there existed three size levels of morphology at the surface of each fracture plane. These can simply be categorized as macroscopic features, intermediate texture, and highly localized, microscopic texture. And when discussing the fracture behavior these three size scales are a useful way to collectively compare and contrast the specimens. Macroscopic features typically existed as features of size on the order of 50 μm or larger. Intermediate texture typically ranged in size between 5-50 μm. And localized, microscopic texture typically existed sub 5 μm to the resolvable limit of the scanning electron microscope.

Figures 8.29 through 8.31 show the macroscopic morphology of the as-fabricated specimens' fracture surface at the 10^{-3}, 10^{-1}, and 10^{3} s^{-1} strain rates. Each figure contains a macroscopic image oriented normal to the fracture surface and a second image at angle to highlight its out-of-plane morphology.

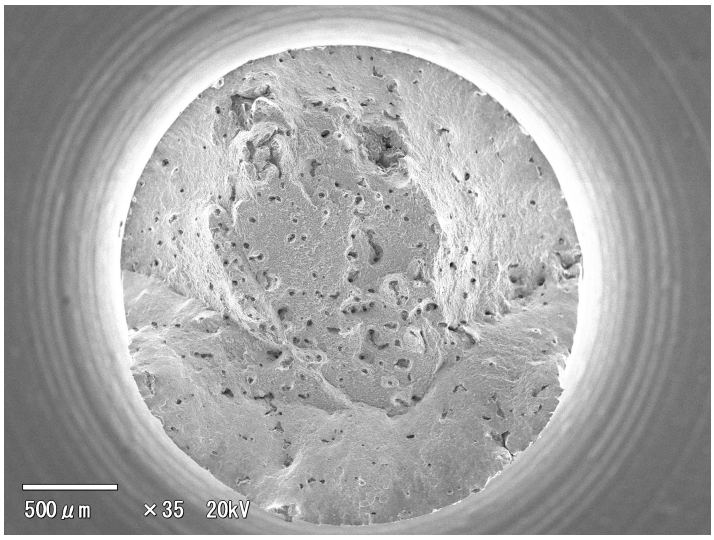


Figure 8.29 (a): Macroscopic Fracture surface of as-fabricated specimen evaluated at 10^{-3} s^{-1} strain rate. Tensile load was normal to the image taken.

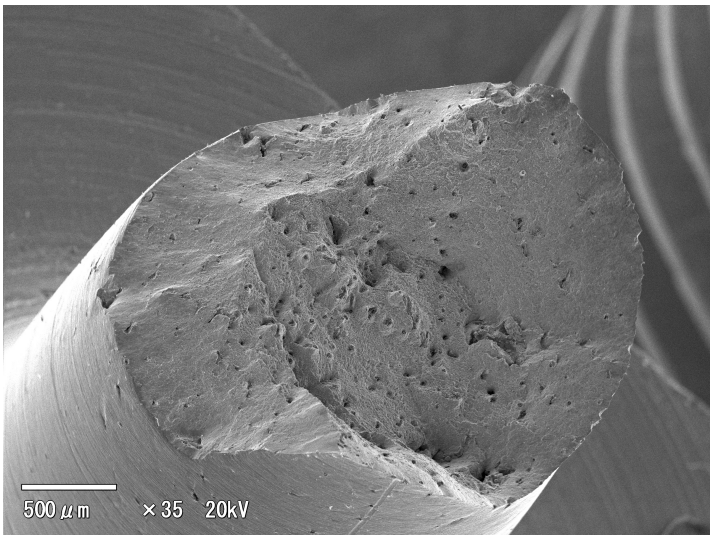


Figure 8.29 (b): Side view of the macroscopic fracture surface of as-fabricated specimen evaluated at 10^{-3} s^{-1} strain rate.

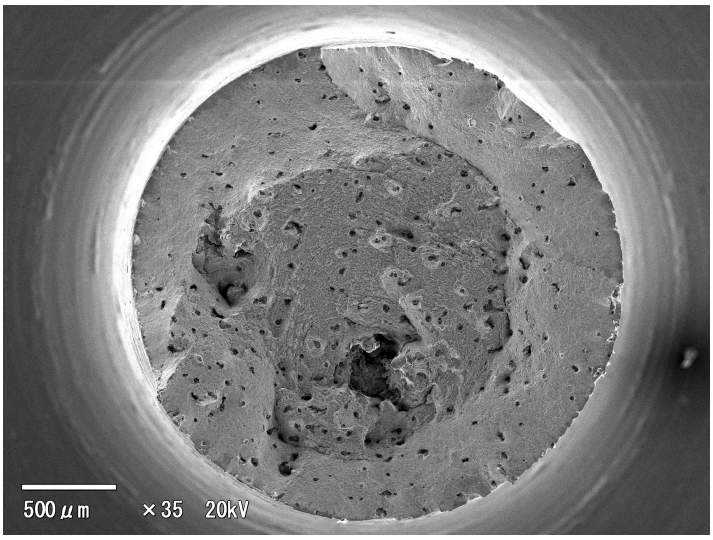


Figure 8.30 (a): Macroscopic Fracture surface of as-fabricated specimen evaluated at 10^{-1} s^{-1} strain rate. Tensile load was normal to the image taken.

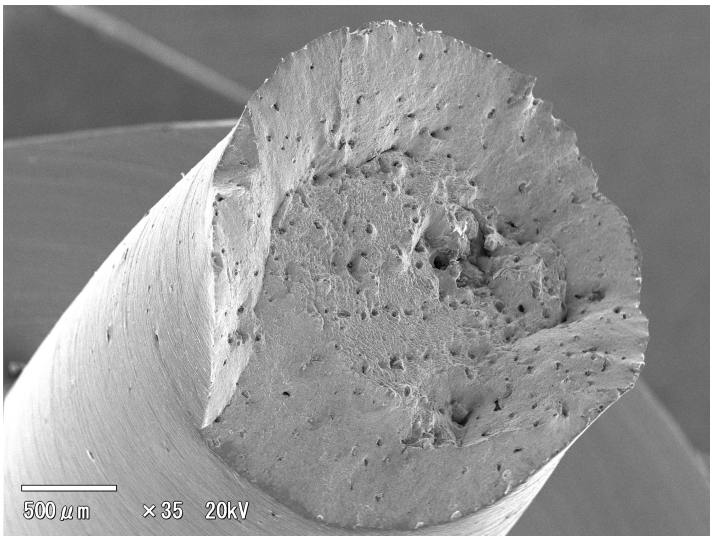


Figure 8.30 (b): Side view of the macroscopic fracture surface of as-fabricated specimen evaluated at 10^{-1} s^{-1} strain rate.

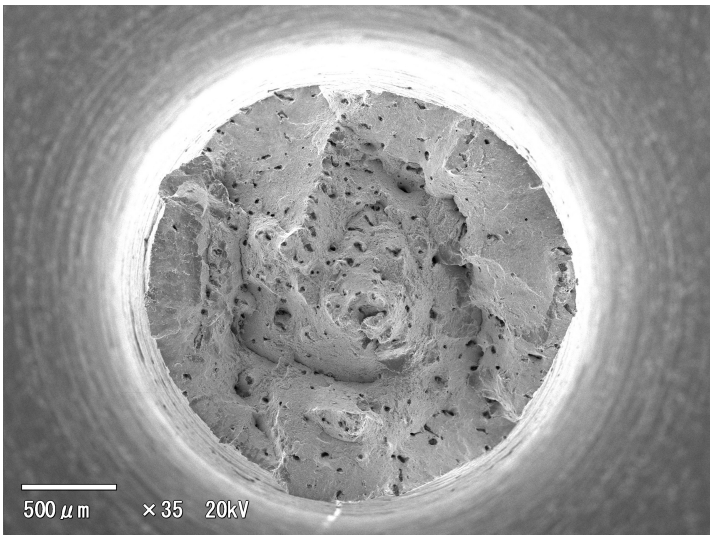


Figure 8.31 (a): Macroscopic Fracture surface of as-fabricated specimen evaluated at 10^3 s^{-1} strain rate. Tensile load was normal to the image taken.

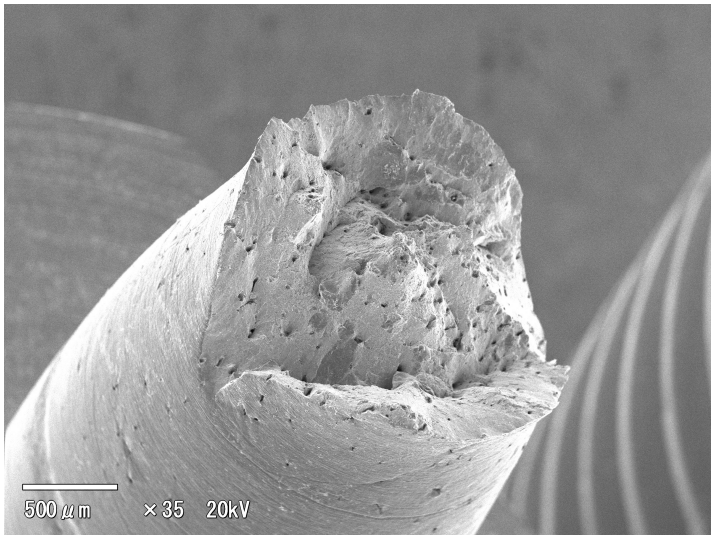


Figure 8.31 (b): Side view of the macroscopic fracture surface of as-fabricated specimen evaluated at 10^3 s^{-1} strain rate.

Across all three of these specimens it is clear that porosity is present at the fracture surface. At first glance, this porosity occasionally appears to occur in patterns. Fracture surfaces of specimens with high ductility appeared to prefer fracture planes that coincided with these pores. Coupled with the localized stress concentrations that would be surrounding these embedded flaws, load-bearing capacity would be diminished along paths where porosity was aligned. It is therefore reasonable to expect fracture planes to coincide with repeating pore structures when closely aligned with regions of critical resolved shear stress.

This behavior was more commonly observed for specimens with greater thermal stabilization of austenite with increasing strain rate (refer to Figure 8.31).

At lower, quasi-static strain rates fracture surfaces of the as-fabricated structure included greater fractional percent of planar surfaces oriented normal to the applied load. In contrast, dynamically tested samples were found to have greater instances of angular or out-of-plane macroscopic surface features. Close inspection of these angular surfaces occasionally indicated the presence of highly localized shear with asymmetric dimple texture characteristic of planar ductile shear. An example of this shearing surface texture is shown in Figure 8.32. Despite these macroscopic differences, all as-fabricated specimens maintained similar localized, microscopic texture regardless of strain rate. Figure 8.33 (a) (b) and (c) show examples of the dimpled texture observed on surfaces oriented normal to the applied load as a result of strain rates of 10^{-3}, 10^{-1}, and 10^{3} s^{-1} across three different magnification scales. These dimples were indicative of a ductile rupture, but only ductility as it applied locally. The growth of micro-voids and their coalescence into larger-scale dimples were not observed. Evolution of larger-scale dimple structures failed to occur despite the increased elongation to failure observed in dynamically tested specimens (where total elongation approaching 25-30%). This was in stark contrast to specimens of the reference material tested in the Condition A state. Figure 8.34 shows an example of a larger-scale dimple texture characteristic of the reference material. At the lower magnification in Figure 8.33 (a), the underlying intermediate-scale structure is observable as a granular texture not representative of the microstructure observed in previous micrographs (i.e. no clear representation of microstructure grain shape reflected in the fracture plane topography).

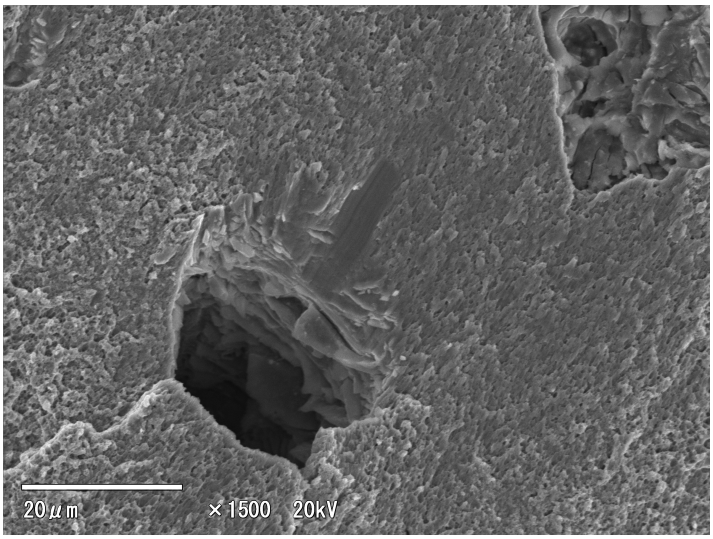


Figure 8.32: Localized shear occurring adjacent to a pore. Specimen is in the as-fabricated condition and tested at a strain rate 10^{-3} s^{-1}. Specimen loading direction is *not* normal to the image shown, but at an angle – note the direction of the elongated dimple structure for shearing direction.

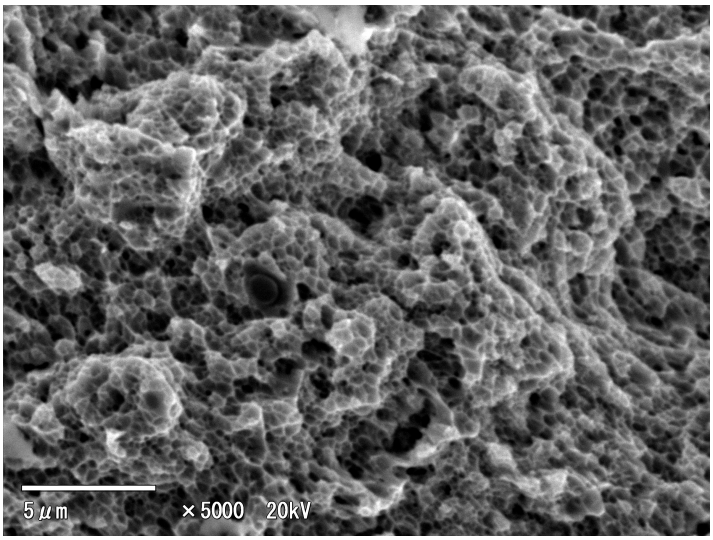


Figure 8.33 (a): Localized dimple texture on the surface of an as-fabricated tensile specimen evaluated at strain rates of 10^{-3} s^{-1}. Direction of the applied load is normal to this image.

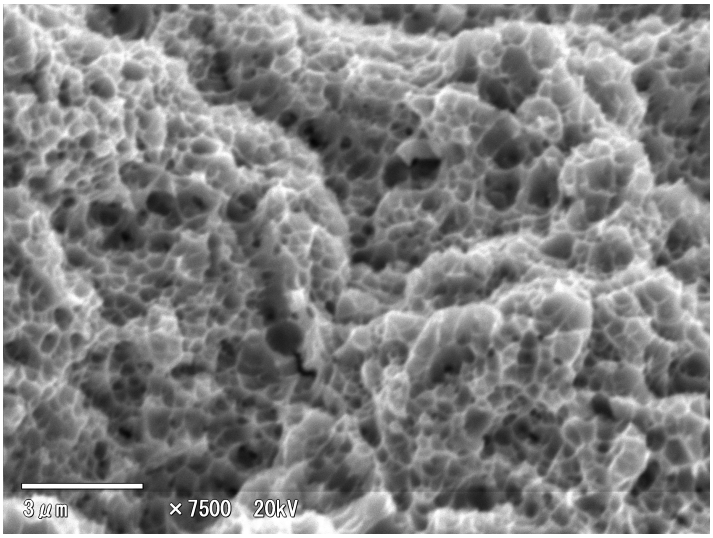


Figure 8.33 (b): Localized dimple texture on the surface of an as-fabricated tensile specimen evaluated at strain rates of 10-1 s-1. Direction of the applied load is normal to this image.

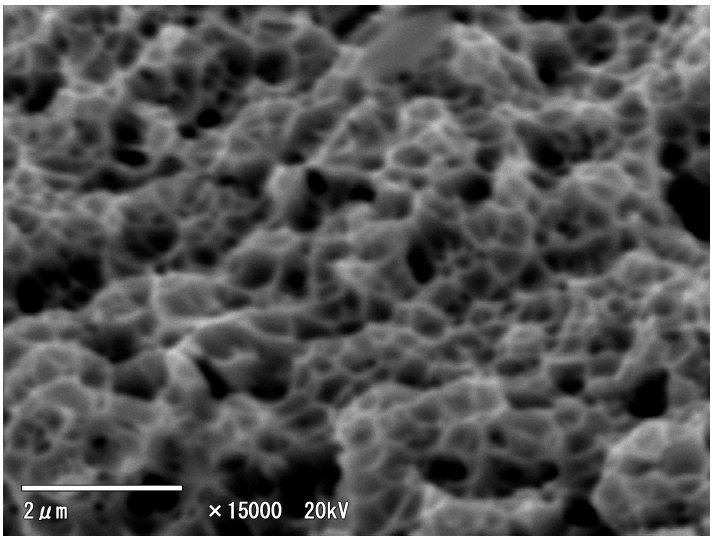


Figure 8.33 (c): Localized dimple texture on the surface of an as-fabricated tensile specimen evaluated at strain rates of 10^3 s^{-1}. Direction of the applied load is normal to this image.

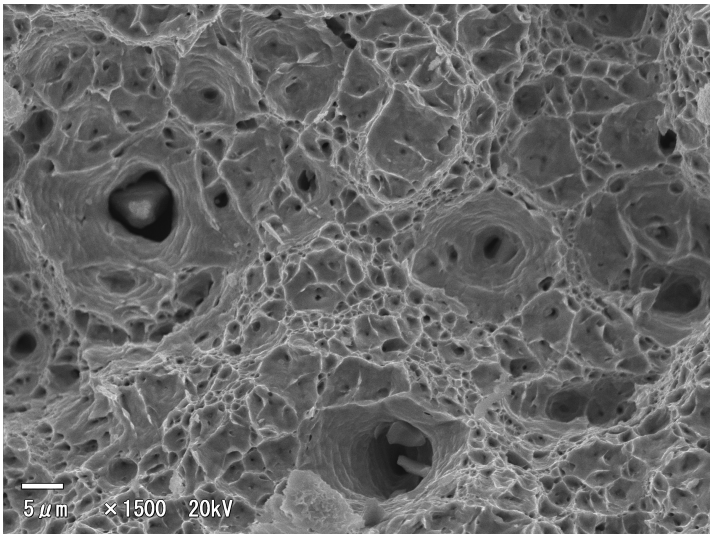


Figure 8.34: Dimple structure as observed on the rupture surface of a reference material specimen in the Condition A state and tested at a strain rate of 10^{-3} s^{-1}. Direction of the applied load is normal to this image.

Thermal processing was observed to dramatically alter the fracture behavior of the various specimens. Figures 8.35 through 8.40 show the angled macroscopic view of all thermally processed specimens as evaluated at a strain rate of 10^{-3} s^{-1}.

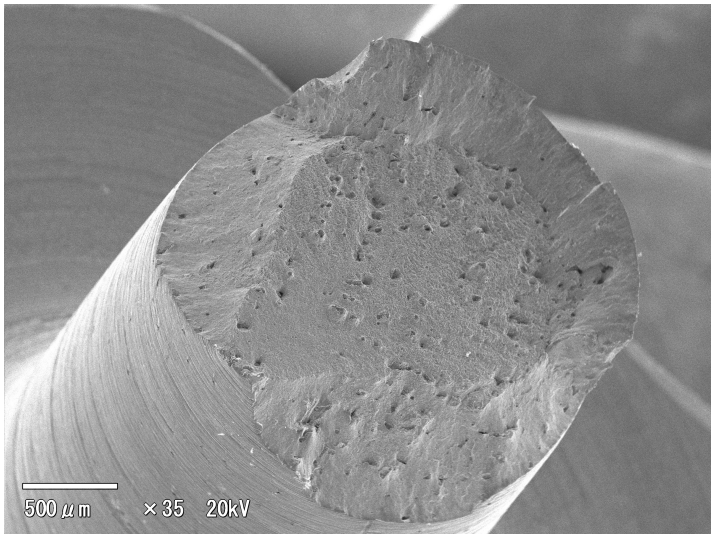


Figure 8.35: Side view of the macroscopic fracture surface of H900 specimen evaluated at 10^{-3} s^{-1} strain rate.

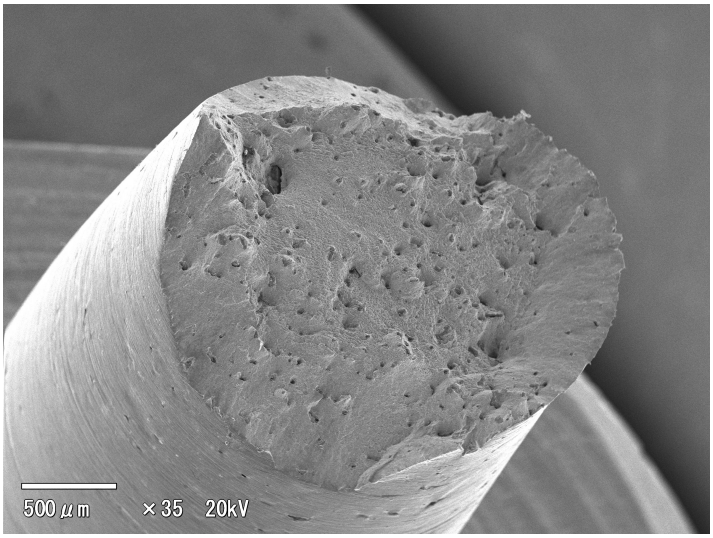


Figure 8.36: Side view of the macroscopic fracture surface of H1025 specimen evaluated at 10^{-3} s^{-1} strain rate.

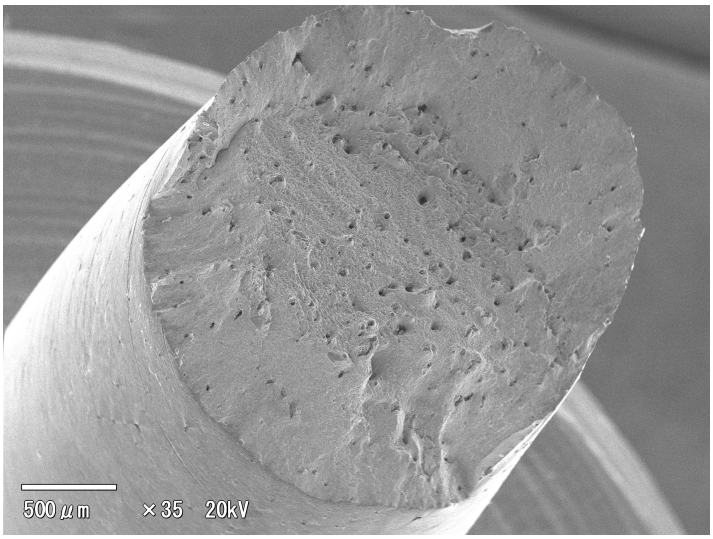


Figure 8.37: Side view of the macroscopic fracture surface of H1150 specimen evaluated at 10^{-3} s^{-1} strain rate.

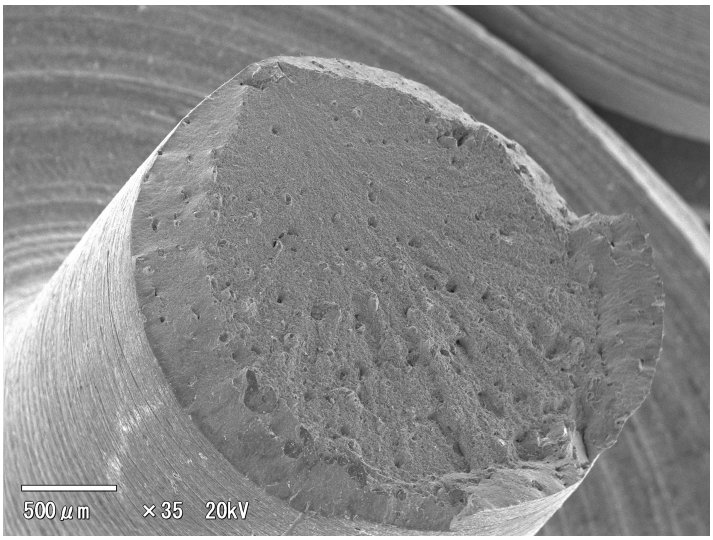


Figure 8.38: Side view of the macroscopic fracture surface of CA-H900 specimen evaluated at 10^{-3} s^{-1} strain rate.

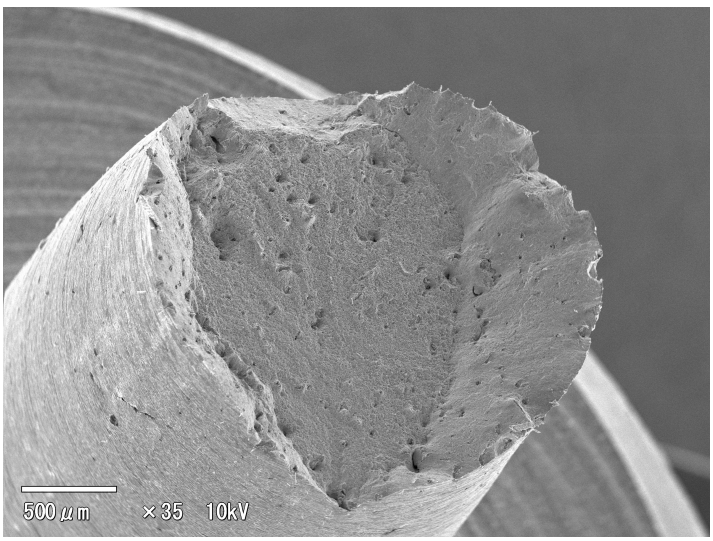


Figure 8.39: Side view of the macroscopic fracture surface of CA-H1025 specimen evaluated at 10^{-3} s^{-1} strain rate.

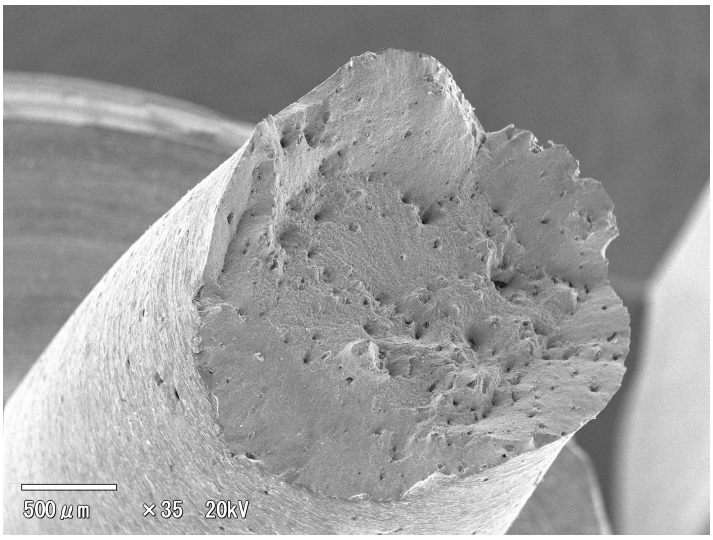


Figure 8.40: Side view of the macroscopic fracture surface of CA-H1150 specimen evaluated at 10^{-3} s^{-1} strain rate.

Peak-age conditions of H900 and CA-H900 specimens are found to regions of planarity in the fracture surface when flanked by the shearing surfaces along the periphery of the specimen. The peak-age condition is also commonly identified as an embrittled state. Images of the fracture surface support this description to a certain degree. The low degree of plastic flow and minimal local necking observed in stress-strain data is also reflected in what appears similar to a cleavage fracture. However, close inspection of the surface reveals local and intermediate texture similar to that in the as-fabricated specimens. On these highly planar surfaces of the peak-age conditions, the intermediate-scale texture could be used to easily identify sources for the initiation of rupture. "River patterns" were found to flow from these crack initiation sites and travel across the surface. Intermediate texture was found to grow in size with distance from these sources of fracture. However, the localized smallest-scaled texture with 500 nm – 1 μm sized dimples remained fairly constant across the entire surface. Figure 8.41 shows the texture as it changes on the fracture surface of a single CA-H900 specimen when viewed normal to the fracture plane.

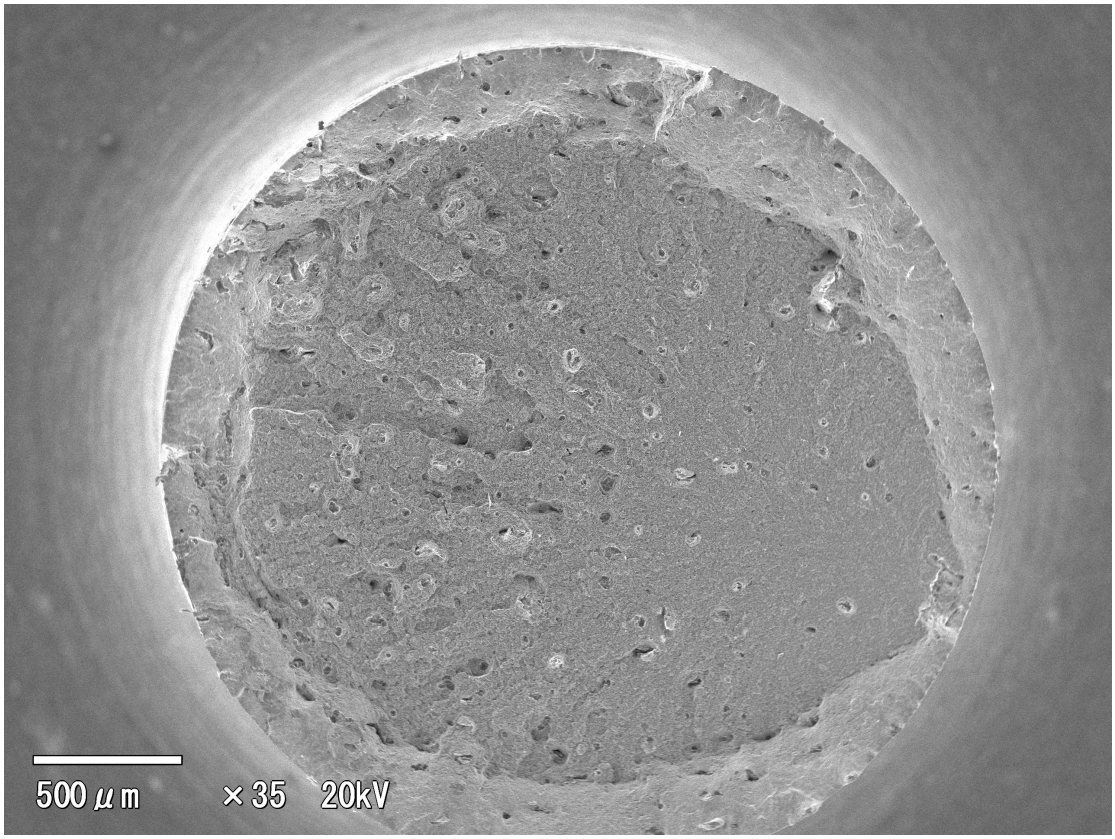


Figure 8.41: Normal view of fracture surface for a CA-H900 specimen with "river pattern" intermediate-scaled texture emanating from the source of the rupture.

Additional investigations of more ductile specimens include the observation that propagating cracks tended to meander below or above the plane normal to the specimen axis where the fracture initiated. Cracks were found to penetrate to nearby adjacent pores within the material. Figure 8.42 illustrates this behavior for an H1150 specimen. Figure 8.43 is the corresponding lower magnification view of the same specimen. This low-magnification image illustrates the relative frequency of this behavior for specimens of this type. These features appear as mounds or divots within the fracture plane with pores exposed at their peak or trough. In contrast, peak-age conditions with their embrittled cleavage-like fracture plane are nearly flat at the site of fracture initiation and do not penetrate in either direction to adjacent porosity. This fracture behavior also enhances the appearance of porosity in ductile specimens. Greater fractions of the observable surface area on the rupture surface are observed as porosity. In contrast, peak-age specimens appear with less porosity on their fracture surface than do those of greater ductility.

Despite the presence of porosity, mechanical performance did not appear limited by premature fracture for tensile samples with high volume fractions of austenite thermally stabilized during intermediate and dynamic tensile testing.

For these specimens, stress-strain curves routinely showed rapid necking post UEL, but necking was nonetheless observed. Specimens processed to the peak-age condition (CA-H900) demonstrated relatively small extents of plastic strain post-yield (very little necking). In these specimen types, where martensite was the dominant phase, porosity was found to have greater influence due to stress concentrations at their periphery. Stress concentrations will continue to exist in the case of specimens with high fractions of austenite, but that increase in localized stress is likely more tolerated by the dual-phase structure. Simply summarized, specimens with high degrees of austenite within their microstructure were less susceptible to flaws formed by SLM when austenite remains stabilized. This is observed by the significant increase in total elongation during intermediate and dynamic testing of as-fabricated and H900 specimens.

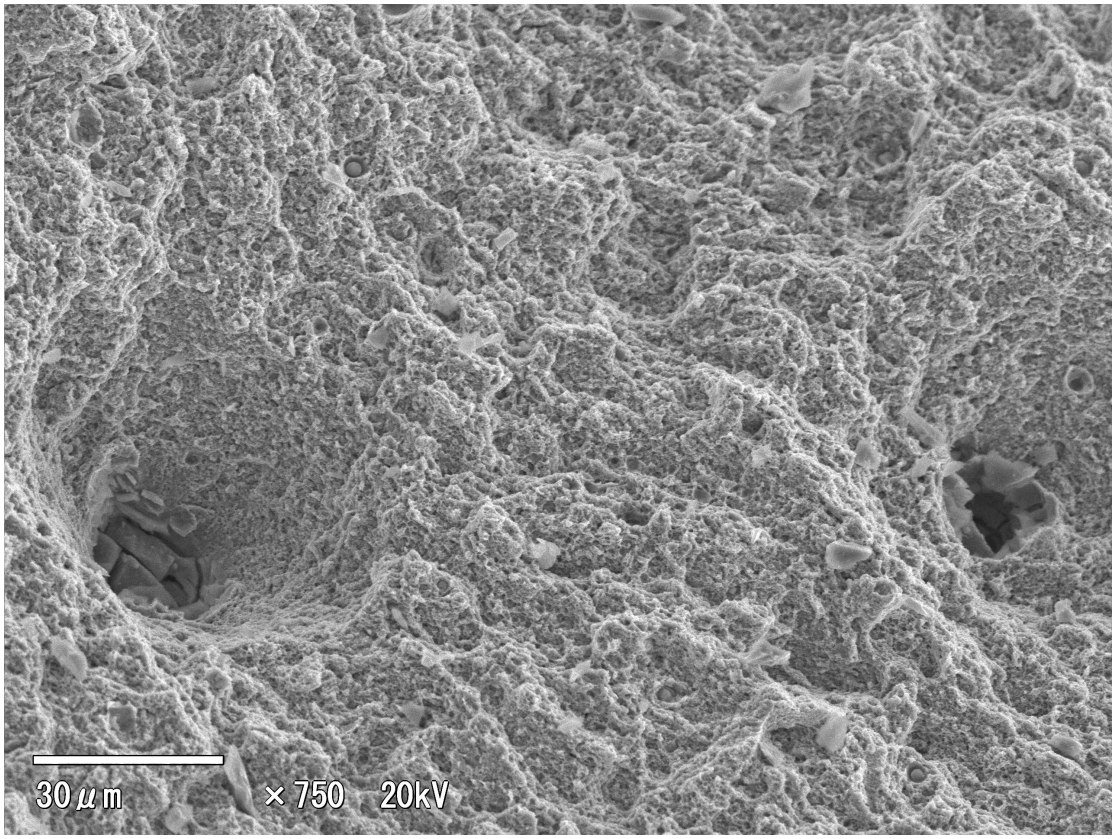


Figure 8.42: Divots of material removed towards underlying porosity at depths beyond the otherwise flat fracture plane. H1150 specimen evaluated at 10^{-3} s^{-1} strain rate.

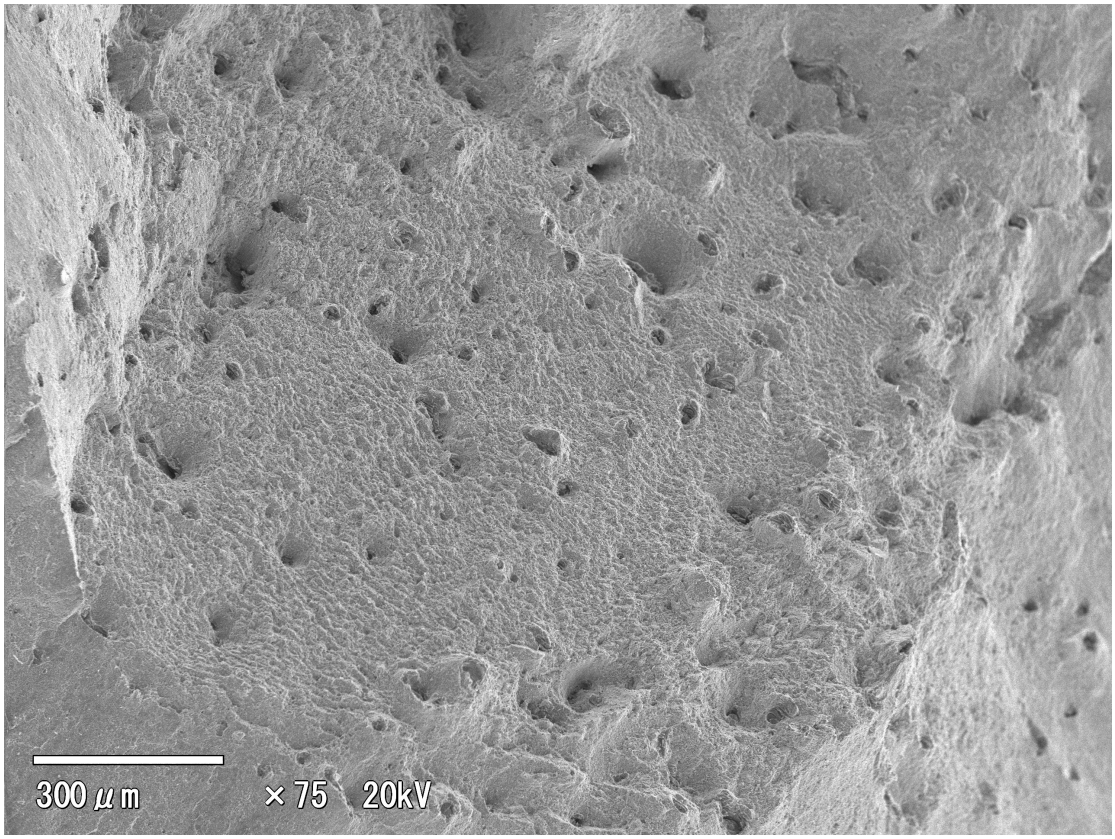


Figure 8.43: Lower magnification view of the macro-scale texture observed for the specimen shown in Figure 8.42.

8.6 Conclusions of Experimental Investigation II

Standard and non-standard thermal processing of specimens introduced a wide range in mechanical behavior as a result of the initial condition of the as-fabricated 17-4 PH material. The effect of high volume fractions of austenite relative to the typical lath martensitic microstructure were found to promote the following behavior:

1) A solution heat treatment performed on all specimens was sufficiently high enough in temperature and duration to adequately relieve thermal stresses associated with the SLM process. As a direct consequence of this, all metastable austenite was free to transform to martensite upon cooling. Mechanical properties of this material as aged to the CA-H900, CA-H1025, and CA-H1150 were observed to behave similarly to those of the reference material aged in the same manner. Differences were only found to be the relative increase in the underlying strength associated with grain size refinement from SLM processing and the associated Hall-Petch effect.

2) Austenite maintains a higher solubility of precipitating alloying elements. Specific to 17-4 PH is the precipitation of copper. Aging treatments on specimens without an initial solution heat treatment, at temperatures below those

determined necessary to relieve the mechanically stabilizing pressures on austenite grains, were found to have a smaller relative increase in strength. This is a result of the austenite maintaining in solution copper and preventing its heterogeneous nucleation and growth throughout the material.

3) Higher temperature aging treatments, specifically the H1025 and H1150 treatments, on specimens without an initial solution heat treatment were found to progressively relieve thermal stresses and permit greater transformation of austenite to martensite upon cooling. With greater volumetric fractions of un-aged martensite post-treatment, mechanical behavior (work hardening rates and flow stress) was found to approach those observed for material initially exposed to the austenizing solution heat treatment temperature. The expected reversion of martensite to austenite as a result of chemical stabilization directly related to the continued growth of copper precipitates was found to not be dominating of the mechanical behavior. Both uniform elongation and elongation to failure were observed to decrease with these higher temperature aging heat treatments. This behavior is opposite to those processed in accordance with the material standard by establishing a Condition A state prior to further aging.

4) The as-fabricated material demonstrated a high degree of sensitivity to strain rate, but not as a result of inherent thermal and athermal barriers to dislocation motion. Changes in mechanical behavior with changes in strain rate were principally a result of the structural changes associated with the microstructure. Yield strength was found to monotonically increase with strain rate, but ultimate tensile strength and uniform elongation were found to not behave similarly. Temperature rises associated with plastic deformation were found to thermally stabilize the austenite grains with similar increasing strain rates. Thermally stabilized austenite was prevented from strain hardening to the same degree observed during isothermal quasi-static tensile tests. This was observed across work hardening rates and flow stress behavior.

5) Porosity was observed across all specimens' fracture surfaces. However, with increasing specimen ductility, fracture surfaces were found to meander to include greater surface fractions of porosity. Peak-age specimens maintained comparatively flat fracture surfaces with characteristic "river patterns" identifying the source of fracture. Ductile specimens with highly angular and occasionally local shearing surfaces were not so easily analyzed for sites of fracture initiation.

9. Conclusions and Final Remarks

Bulk 17-4 precipitation hardenable stainless steel produced by selective laser melting was evaluated for its mechanical properties across various post-production processing treatments. These properties as they relate to the microstructure and its evolution with strain rate have been presented. The influence of the SLM process on the resultant properties with respect to established mechanical behavior for traditionally processed equivalents was also evaluated and discussed. From this body of experimental work, several conclusions and final remarks will be made.

The potential for additive manufacturing to be a powerful alternative to traditional machine tools is rapidly taking shape. Various industries have identified the capacity and capability, investing resources into its further maturation and adoption into existing product lifecycles and production planning. However, with the processing of materials by this relatively new suite of tools, it is natural to encounter unexpected effects on the resultant micro and macro-scale properties. 17-4 PH has demonstrated a large degree of sensitivity to processing by this method. Processing using SLM largely influences mechanical properties in the as-fabricated and further aged states. The results of these findings will be summarized here.

17-4 PH processed by SLM without any further thermal or mechanical treatment has been found to contain large volumetric fractions of metastable austenite. Typically, this microstructure should fully transform to martensite upon cooling from the initially molten state. However, because of a high degree of thermal stresses that reside within the material upon cooling, austenite grains are mechanically stabilized well below the start and finish temperatures commonly recognized for the allotropic martensitic transformation. Chemical stabilization as a result of solute segregation measured from bulk material processed by SLM was effectively dismissed as the mechanism for the large volume fraction of stabilization measured.

As-fabricated material demonstrated a large degree of stress-induced transformation of austenite to martensite when evaluated at quasi-static strain rates. Yield strength was observed to be at significantly lower levels compared to material entirely martensitic. However, with a rapid rise in the work hardening rate, the material was observed to strengthen to an ultimate tensile strength following an extended range of uniform elongation. Initial plastic deformation

behavior is believed to be a result of the much weaker austenite grains undergoing plastic deformation amongst the remaining martensite structure. At higher levels of strain and consequently stress, both materials plastically yield until reaching a peak stress where nearly the entirety of austenite has transformed to martensite. These observations on mechanical behavior are in contrast to a reference material produced via traditional fabrication techniques. The reference material exhibited a flow stress that was observed to remain consistent with power law behavior and no gross changes in work hardening rate were noted.

Strain rate sensitivity on macroscopic mechanical behavior was observed to be relatively high for the as-fabricated material. However, the sensitivity was not as a result of limitations to dislocation motion and their relative velocity through the material. Instead, however, the as-fabricated material demonstrated a structural sensitivity to thermal stabilization of the austenite grains with increasing temperature. The temperature rise noted as a result of plastic deformation resulted in specimen bulk temperature exceeding the finish and possibly start temperatures for the martensitic transformation. This suggests the austenite remains stabilized and not permitted to further transform into martensite with ongoing plastic strain. At low strain rates the achievable ultimate tensile strength at uniform elongation was found to plateau. Increasing strain rates demonstrated a reduction in the work hardenability of the material. And at dynamic testing speeds, little-to-no work hardening was observed post yield.

As-fabricated material exposed to various secondary thermal processing was found to demonstrate varying degrees of strengthening as a result of the initial microstructure and phases present. Solution heat treatments adequately relieved residual thermal stresses and permitted the complete transformation to martensite upon cooling to room temperature. The relative strengthening and stress-strain behavior noted for specimens with aging treatments performed following this initial solution heat treatment were found to be consistent with the reference material. However, elongation to failure was premature as a result of embedded porosity.

Maximum attainable strength via SLM processing of 17-4 PH was found to well exceed that demonstrable for the reference material. However, without further refinement in the development of the SLM processing parameters, porosity remains a negative drawback to this materials processing technique. Porosity was directly linked with inhibiting proper local plastic deformation well

beyond uniform plastic deformation. Porosity developed as part of the SLM process was found to generate mechanical fibering under select SLM processing parameters. Mechanical properties for specimens processed in accordance with industry norms were found to not show signs of material anisotropy reflected in mechanical behavior. However, elongation to failure was significantly reduced for specimens with planar and elongated pores oriented normal to the applied load. This occurs consistently for specimens with layers oriented perpendicular to the axis of the tensile specimens and by extension the applied load. As porosity tended to be produced with size, shape, and orientation reflecting the laser scanning strategy, specimens with layers oriented in-line with the loading direction were found to be susceptible to porosity based on the relative orientation of the scanning patterns and the applied load.

Despite these porosity-liked limitations observed in the mechanical properties, processing materials by additive manufacturing methods can result in reliable and predictable properties when industry norms are strictly adhered to. However, by expanding the academic and functional understanding between processing parameters and resultant microstructure, tailoring materials for the intended application and service environment is increasingly possible. Additive manufacturing of metallic materials enables a greater degree of property diversity and potential control over part or geometry-specific resultant macroscopic behavior. Ongoing research into the predictability and interrelationships between directed energy-based materials processing is necessary to see the further growth and application of this technology.

Works Cited

[1] C R. Deckard, "Method and Apparatus for Producing Parts by Selective Sintering," Process 4863538, Sep. 05, 1989.

[2] ASTM International, Standard Terminology for Additive Manufacturing Technologies, 2013, F2792.

[3] J -P Kruth, G Levy, F Klocke, and T H C Childs, "Consolidation Phenomena in Laser and Powder-Bed Based Layered Manufacturing," *CIRP Annals – Manufacturing Technology*, vol. 56, no. 2, pp. 730-759, 2007.

[4] Nannan Guo and Ming C Leu, "Additive Manufacturing: Technology, Applications and Research Needs," *Frontiers of Mechanical Engineering*, vol. 8, no. 3, pp. 215-243, May 2013.

[5] E Santos, M Shiomi, K Osakada, and T Laoui, "Rapid Manufacturing of Metal Components by Laser Forming," *International Journal of Machine Tools and Manufacture*, vol. 46, no. 12-13, pp. 1459-1468, 2006.

[6] Jouni Hanninen, "DMLS Moves from Rapid Tooling to Rapid Manufacturing," *Metal Powder Report*, vol. 56, no. 9, pp. 24, 26-29, 2001.

[7] E M Betts, D E Eddleman, D C Reynolds, and N A Hardin, "Using Innovative Technologies for Manufacturing Rocket Engine Hardware," NASA/MSFC, Huntsville, AL, Technical Report 2011.

[8] E Atzeni and A Salmi, "Economics of Additive Manufacturing for End-Usable Metal Parts," *The International Journal of Advanced Manufacturing Technology*, vol. 62, no. 9-12, pp. 1147-1155, 2012.

[9] J Allen, "An Investigation into the Comparative Costs of Additive Manufacture vs. Machine from Solid for Aero Engine Parts," Manufacturing Technology, Rolls Royce, Derby, UK, Public Release 2006.

[10] J Kruth, "Digital Manufacturing of Biocompatible Metal Frameworks for Complex Dental Prostheses by Means of SLS/SLM," *Virtual Prototyping and Rapid Manufacturing-Advanced research in virtual and Rapid Prototyping*, pp. 139-146, 2005.

[11] D Popescu and D Anania, "Design and Rapid Manufacturing of Patient-Specific Spinal Surgical Guides: A Survey," *Proceedings in Manufacturing Systems*, vol. 7, no. 2, pp. 115-120, 2012.

[12] A Simchi, F Petzoldt, and H Pohl, "On the Development of Direct Metal Laser Sintering for Rapid Tooling," *Journal of Materials Processing Technology*, vol. 141, no. 3, pp. 319-328, 2003.

[13] Lawrence E Murr et al., "Metal Fabrication by Additive Manufacturing Using Laser and Electron Beam Melting Technologies," *Journal of Materials Science & Technology*, vol. 28, no. 1, pp. 1-14, 2012.

[14] T B Schaffer and G B Sercombe, "The Production of ALuminum SLS Prototypes Via Infiltration," in *Proceedings of VRAP*, 2003, pp. 297-301.

[15] ASTM International, Standard Specification for Hot-Rolled and Cold-Finished Age-Hardening Stainless Steel, 2013.

[16] M Tisza, Ed., *Physical Metallurgy for Engineers*, 2nd ed. Materials Park, United States: ASM International and Freund Publishing House, Ltd., 2001.

[17] N Suutula, "Effect of Solidification Conditions on the Solidification Mode of Austenitic Stainless Steels," *Metallurgic Transactions A*, vol. 14, no. 1983, 1983.

[18] M J Cieslak, "Hot Cracking Mechanisms in CO2 Laser Beam Welds of Dissimilar Metals Involving PH Martensitic Stainless Steels," *Welding Journal*, vol. 66, pp. 57-60, 1987.

[19] A Ritter and W Savage, "Solidification and Solidification Cracking in Nitrogen-Strengthened Austenitic Stainless Steels," *Metallurgical Transactions A*, vol. 17A, pp. 727-737, April 1986.

[20] K Ozbayashi and O Inal, "Thermodynamics and Structure of Solidification in the Fusion Zone of CO2 Laser Welds of 15-5 PH Stainless Steel," *Material Science and Engineering: A*, vol. 130, pp. 205-217, 1990.

[21] J Vitek, A Dasgupta, and S David, "Microstructural Modifications of Austenitic Stainless Steels by Rapid Solidification," *Metallurgical Transactions A*, vol. 14, pp. 1833-1841, September 1983.

[22] J Lippold, "Centerline Cracking in Deep Penetration Electron Beam Welds in Type 304L Stainless Steel," *Welding Journal*, pp. 127-136, 1985.

[23] S Kou and Y Le, "The Effect of Quenching on the Solidification Structure and Transformation Behavior of Stainless Steel Welds," *Metallurgical Transactions A*, vol. 13, pp. 1141-1152, July 1982.

[24] G H Eichelman Jr and F C Hull, "The Effect of Composition on the Temperature of Spontaneous Transformation of Austenite to Martensite in 18-8-Type Stainless Steel ," *Transactions of the American Society of Materials*, vol. 45, pp. 77-104, 1953.

[25] F B Pickering, "Physical Metallurgy of Stainless Steels Developments," *International Metals Reviews*, 1986.

[26] RWK Honeycombe and HKDH Bhadeshia, *Steels—Microstructure and Properties*, Second Edition ed., Edward Arnold, Ed. London, UK, 1995.

[27] C N Hsiao, J R Chiou, and C S Yang, "Aging reactions in a 17-4 PH stainless steel," *Materials Chemistry and Physics*, vol. 74, no. 2, pp. 134-142, 2002.

[28] K Tamaru and S Sekito, "On the quantitative determination of retained austenite in quenched steels," *Science Repository Tohoku Imperial University*, 1931.

[29] A+K Steel, 17-4 PH, 2014.

[30] U K Viswanathan, R Banerjee, and S Krishnan, "Effects of aging on the microstructure of 17-4 PH stainless steel," *Materials Science and Engineering, A*, vol. 104, pp. 181-189, 1988.

[31] L Sandova, H M Urbassek, and P Entel, "The Bain versus Nishiyama–Wassermann path in the martensitic transformation of Fe," *New Journal of Physics*, vol. 11, no. 10, pp. 1-11, 2009.

[32] L Murr et al., "Microstructures and Properties of 17-4 PH Stainless Steel Fabricated by Selective Laser Melting," *Journal of Materials Research and Technology*, vol. 1, no. 3, pp. 167-177, 2012.

[33] H Nakagawa and T Miyazaki, "Effect of Retained Austenite on the Microstructure and Mechanical Properties of Martensitic Precipitaiton Hardening Stainless Steel," *Journal of Materials Science*, vol. 4, pp. 3901-3908, 1999.

[34] V Nikol'skaya, L Pevzner, and N Orekhov, "Effect of Retained Austenite on the Properties of Cast Stainless Steels," *Metal Science and Heat Treatment*, vol. 17, no. 9, pp. 763-767, 1975.

[35] Zenji Nishiyama, *Martensitic Transformation*, Morris Fine, M Meshii, and C M Wayman, Eds. Kawasaki, Japan: Academic Press, 1978.

[36] Rachel Abrahams, The Development of High Strength Corrosion Resistant Precipitation Hardening Cast Steels, 2010.

[37] M Okamoto and R Odaka, *Journal of the Japan Institute of Metals*, vol. 16, no. 81, 1952.

[38] M Izumiyama, "Kinetics of Transformation of Aged Retained-Austenite into Martensite," *Science Repository for the Research Institute for Iron, Steel, and Other Metals*, vol. 14, no. 11, 1962.

[39] J E Hilliard and J W Cahn, *Progress in very high pressure research*. New York, United States: Wiley, 1961.

[40] L Pope and L Edwards, "The Pressure Dependence of the Austenite Start Temperature in Iron-Nickel Base Alloys," *Acta Metallurgica*, vol. 21, no. 3, pp. 281-288, 1972.

[41] Sindo Kou, *Welding Metallurgy*. USA: John Wiley & Sons, 2003.

[42] M Murayama, K Hono, and Y Katayama, "Microstructural Evolution in a 17-4 PH Stainless Steel After Aging at 400 °C," *Metallurgical and Materials Transactions A*, vol. 30, no. 2, pp. 345-353, 1999.

[43] S Thompson, G Krauss, and C Tseng, "A New Model of Interphase Precipitation in Copper-Containing Steels," *Journal of Materials Science Letters*, vol. 7, pp. 2075-2078, 1998.

[44] H Rack and D Kalish, "The Strength, Fracture Toughness, and Low Cycle Fatigue Behavior of 17-4 PH Stainless Steel," *Metallurgical Transactions*, vol. 5, pp. 1595-1605, July 1974.

[45] J Wang, H Zou, and C Li, "The Effect of Microstructural Evolution on Hardening Behavior of Type 17-4PH Stainless Steel in Long-Term Aging at 350C," *Materials Characterization*, vol. 57, pp. 274-280, 2006.

[46] J W Christian, *The Theory of Transformations in Metals and Alloys*, Second Edition ed. Oxford, UK: Pergamon Press, 1975.

[47] U Viswanathan, "Kinetics of Precipitation in 17-4 PH Stainless Steel," *Materials Science and Technology*, vol. 5, pp. 346-349, April 1989.

[48] H Mirzadeh and A Najafizadeh, "Aging Kinetics of 17-4 PH Stainless Steel," *Materials Chemistry and Physics*, vol. 116, no. 1, pp. 119-124, 2009.

[49] J H Hollomon and L D Jaffe, "Time-Temperature Relations in Tempering Steel," *Transactions of AIME*, vol. 162, pp. 223-249, 1945.

[50] Jui-Hung Wu and Chin-Kuang Lin, "Influence of High Temperature Exposure on the Mechanical Behavior and Microstructure of 17-4 PH Stainless Steel," *Journal of Materials Science*, vol. 38, pp. 965-971, 2003.

[51] George E. Dieter, *Mechanical Metallurgy*. United States: McGraw-Hill, 1986.

[52] H Shercliff and M Ashby, "A Process Model for Age Hardening of Aluminum Alloys - I The Model," *Acta Metallurgica et Materialia*, vol. 38, no. 10, pp. 1789-1802, 1990.

[53] K Osakada and M Shiomi, "Flexible Manufacturing of Metallic Products by Selective Laser Melting of Powder," *International Journal of Machine Tools and Manufacture*, vol. 46, no. 11, pp. 1188-1193, 2006.

[54] A Gasser, G Backes, I Kelbassa, and K Wissenbach, "Laser Metal Deposition (LMD) and Selective Laser Melting (SLM) in Turbo-Engine Applications," *Laser Technik Journal*, vol. 2, no. 58-63, 2010.

[55] L Thivillon, P Bertrand, B Laget, and I Smurov, "Potential of Direct Metal Deposition Technology for Manufacturing Thick Functionally Graded Coatins and Parts for Reactors Components," *Journal of Nuclear Materials*, vol. 385, no. 2, pp. 236-241, 2009.

[56] K Taminger and R Hafley, "Electron Beam Freeform Fabrication: A Rapid Metal Deposition Process," in *Proccedings of the 3rd Annual Automotive Composites Conference*, Troy, MI, 2003.

[57] ASM International, "Volume 7: Powdered Metal Technologies and Applications," in *ASM Handbook*, W B Eisen et al., Eds. Materials Park, OH, USA: ASM International.

[58] R Li et al., "Densification Behavior of Gas and Water Atomized 316L Stainless Steel Powder During Selective Laser Melting," *Applied Surface Science*, vol. 256, no. 13, pp. 4350-4356, 2010.

[59] A Simchi, "Direct Laser Sintering of Metal Powders: Mechanism, Kinetics and Microstructural Features," *Materials Science and Engineering: A*, vol. 428, no. 1-2, pp. 148-158, 2006.

[60] D Gu and Y Shen, "Balling Phenomena in Direct Laser Sintering of Stainless Steel Powder: Metallurgical Mechanisms and Control Methods," *Materials & Design*, vol. 30, no. 8, pp. 2903-2910, 2009.

[61] A Simchi, "The Role of Particle Size on the Laser Sintering of Iron Powder," *Metallurgical and Materials Transactions B*, vol. 35, pp. 937-948, October 2004.

[62] R Li, J Liu, Y Shi, L Wang, and W Jiang, "Balling Behavior of Stainless Steel and Nickel Powder During Selective Laser Melting Process," *The International Journal of Advanced Manufacturing Technology*, vol. 59, no. 9-12, pp. 1025-1035, 2012.

[63] H Gu et al., "Influences of Energy Density on Porosity and Microstructure of Selective Laser Melted 17-4PH Stainless Steel," in *Proceedings of the International Freeform Manufacturing Symposium*, Austin, TX, 2013, pp. 474-489.

[64] W O'Neill, C Sutcliffe, R Morgan, A Landsborough, and K K B Hon, "Investigation on Multi-Layer Direct Metal Laser Sintering of 316L Stainless Steel Powder Beds," *CIRP Annals – Manufacturing Technology*, vol. 48, no. 1, pp. 151-154, 1999.

[65] P Fischer et al., "Sintering of Commercially Pure Titanium Powder with a Nd:YAG Laser Source," *Acta Materialia*, vol. 51, no. 6, pp. 1651-1662, 2003.

[66] R Morgan, C J Sutcliffe, and W O'Neill, "Density Analysis of Direct Metal Laser Re-Melted 316L Stainless Steel Cubic Primitives," *Journal of Materials Science*, vol. 39, no. 4, pp. 1195-1205, 2004.

[67] T Starr, K Rafi, B Stucker, and C Scherzer, "Controlling Phase Composition in Selective Laser Melted Stainless Steels," in *Proceedings of the Solid Freeform Fabrication Symposium*, Austin, TX, 2012, pp. 439-446.

[68] J Kruth et al., "Selective Laser Melting of Iron-Based Powder," *Journal of Materials Processing Technology*, vol. 149, no. 1-3, pp. 616-622, 2004.

[69] L Facchini et al., "Metastable Austenite in 17-4 PH Precipitation-Hardening Stainless Steel Produced by Selective Laser Melting," *Advanced Engineering Materials*, vol. 12, no. 3, pp. 184-188, 2010.

[70] B Chalmers, *Principles of Solidification*.: Krieger Pub Co, 1977.

[71] M Masumoto, M Shiomi, K Osakada, and F Abe, "Finite Element Analysis of Single Layer Forming on Metallic Powder Bed in Rapid Prototyping by Selective Laser Processing," *International Journal of Machine Tools and Manufacture*, vol. 42, no. 1, pp. 61-67, 2002.

[72] Luca Facchini, Microstructure and Mechanical Properties of Biomedical Alloys Produced by Rapid Manufacturing Technologies, 2010.

[73] H Conrad, "Thermally Activated Deformation of Metals," *Journal of Metals*, vol. 16, pp. 582-885, 1964.

[74] H Conrad, "The Athermal Component of the Flow Stress in Crystaline Solids," *Materials Science and Engineering*, vol. 6, no. 4, pp. 265-273, 1970.

[75] Alfred Seeger, "LXV. On the Theory of the Low-Temperature Internal Friction Peak Observed in Metals," *Philosophical Magazine*, vol. 1, no. 7, pp. 651-662, 1956.

[76] L E Murr, "Metallurgical Effects of Shock Loading and High-Strain-Rate Loading," in *Materials at High Strain Rates*, T Z Blazynski, Ed. New York, NY, United States: Elsevier Science Publishing Co., Inc., 1987.

[77] J O Campbell, *Dynamic Plasticity of Metals*. Vienna, Austria: Springer-Verlag, 1972.

[78] U S Lindholm, "Deformation Maps in the Region of High Dislocation Velocity," in *High Velocity Deformation of Solids*, K Kawata and J Shioiri, Eds. New York, New York, United States: Springer-Verlag.

[79] P S Follansbee, *Metallurgical Applications of Shock-wave and High-strain-rate Phenomena*, L E Murr, K P Staudhammer, and M A Meyers, Eds. New York, NY, United States: Marcel Decker, 1986, Chapter 24.

[80] R Picu, G Vincze, and F Ozturk, "Strain Rate Sensitivity of the Commercial Aluminum Alloy AA5182-O," *Materials Science and Engineering: A*, vol. 390, no. 1-2, pp. 334-343, 2005.

[81] ASTM International, Standard Test Methods for Tension Testing of Metallic Materials, 2010.

[82] Weinong W Chen and Bo Song, *Split Hopkinson (Kolsky) Bar; Design, Testing, and Applications*. New York, United States: Springer, 2011.

[83] Michael Adam Kaiser, Advancements in the Split Hopkinson Bar Test, 1998, Virginia Polytechnic Institute.

[84] T C LeBrun, K Tanigaki, H Keitaro, and H Kobayashi, "Strain Rate Sensitivity and Mechanical Anisotropy of Selective Laser Melted 17-4 PH Stainless Steel," *Mechanical Engineering Journal*, vol. 1, no. 5, pp. 1-13, Oct. 2014.

[85] Z Shen, R H Wagoner, and W A T Clark, "Dislocation and Grain Boundary Interactions in Metals," *Acta Metallurgica*, vol. 36, no. 12, pp. 3231-3242, December 1988.

[86] S Morito, H Yoshida, T Maki, and X Huang, "Effect of Block Size on the Strength of Lath Martensite in Low Carbon Steels," *Materials Science and Engineering A*, vol. 438-440, pp. 237-240, 2006.

[87] Hengfeng Gu et al., "Influences of Energy Density on Porosity and Microstructure of Selective Laser Melted 17-4PH Stainless Steel," in *Solid Freeform Fabrication Symposium*, Austin, TX, 2013, pp. 474-489.

[88] E C Santos, K Osakada, M Shiomi, Y Kitamura, and F Abe, "Microstructure and Mechanical Properties of Pure Titanium Models Fabricated by Selective Laser Melting," in *Proceedings of the Institution of Mechanical Engineers, Part C: Journal of Mechanical Engineering Science 2004*, 2004, pp. 711-719.

[89] J Lichtenfeld, M Mataya, and C Tyne, "Effect of Strain Rate on Stress-Strain Behavior of Alloy 309 and 304L Austenitic Stainless Steel," *Metallurgical and Materials Transactions A*, vol. 37, pp. 147-161, January 2006.

[90] Z Jiang, Z Guan, and J Lian, "Effects of Microstructural Variables on the Deformation Behavior of Dual-Phase Steel," *Materials Science and Engineering A*, vol. 190, pp. 55-64, 1995.

[91] J A Lichtenfeld, M C Mataya, and C J Van Tyne, "Effect of Strain Rate on Stress-Strain Behavior of Alloy 309 and 304L Austenitic Stainless Steel," *Metallurgical and Materials Transactions A*, vol. 37, pp. 147-161, January 2006.

[92] Fahr, D. "Stress- and strain-induced formation of martensite and its effects on strength and ductility of metastable austenitic stainless steels," *Metallurgical Transactions*, *2*(July), 1883–1892, 1971

[93] N Shirakawa, Y Miyata, H Inui, and T Nakamoto, "Selective Laser Sintering of High Carbon Steel Powders Studied as a Function of Carbon Content," *Journal of Materials Processing Technology*, vol. 209, no. 15-16, pp. 5653-5660, September 2009.

[94] ASTM International, Standard Test Methods for Density of Compacted or Sintered Powder Metallurgy (PM) Products Using Archimedes Principle, 2008, B962-08.

[95] A. Gusarov, I. Yadroitsava, I. Smurov I. Yadroitsev, "Single track formation in selective laser melting of metal powders ," vol. 210, pp. 1624-1631, May 2012.

[96] C. Hauser, M. Badrossamay T. H. C. Childs, "Mapping and Modelling Single Scan Track Formation in Direct Metal Selective Laser Melting," *Manufacturing Technology*, vol. 53, no. 1, pp. 191-194, Jan. 2004.

[97] V. Romano, H.P. Weber, N.P. Karapatis, E. Boillat, R. Glardon P. Fischer, "Sintering of commercially pure titanium powder with a Nd:YAG laser source ," *Acta Materialia* , vol. 51, pp. 1651-1662, Nov. 2002.

[98] H. Azuma, S. Yamazaki, H. Sugimoto, S. Takagi Y. Kizaki, "Phenomenological Studies in Laser Cladding. Part I. Time-Resolved Measurements of the Absorptivity of Metal Powder," *pn. J. Appl. Phys* , vol. 32, no. 1A, pp. 205-212, 1993.

Appendix A

Equation of State During Dynamic Tensile Analysis [83]

When considering how a split-Hopkinson tensile bar (SHTB) may be used to evaluate the mechanical properties of a material under dynamic loading conditions, it is best to start at the beginning to properly derive the state of motion as it exists within a simplified model of such equipment. First, consider a cylindrical bar with an infinite length and a cross-sectional area A_B. Within this bar a differential length-element along the axis will be examined in detail. This differential element is represented with a length of dx and with the same cross-sectional area as the bar, A_B. Figure A.1 details this arrangement visually within a simplified three-dimensional space.

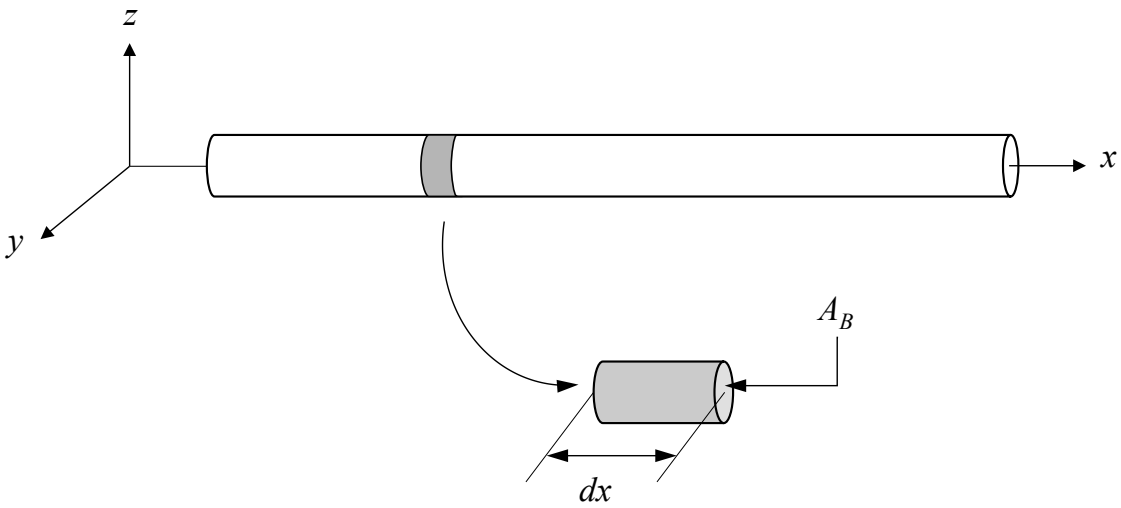


Figure A.1: Differential element along a symbolic representation of a cylindrical bar.

Initially this differential element is at rest. However, at a subsequent instant in time, a tensile load is generated across the length of the differential element.[1] While under tensile load this differential element will experience forces, F_1 and F_2, acting in opposite directions to its faces. This is depicted schematically in Figure A2. For a SHTB that operates with bars loaded within their elastic regime, the relationship of stresses imposed by these tensile forces and their

[1] The origin of this stress wave may be considered a result of events similar to those of a SHTB test where a high-speed impact upon a yoke interface generates a travelling stress wave. However, for the purpose of this derivation, it is not immediately important to distinguish its source or mechanism.

corresponding strain may be expressed in terms of Hooke's Law and the modulus of elasticity for the bar material, *E*. These strains may also be expressed in terms of elemental displacements, *u*, and the following general expression,



Figure A.2: Differential element in tension with forces acting on the opposite faces.

$$F_X = A_B E \frac{\partial u}{\partial x} \tag{A.1}$$

This expression is valid assuming a state of uniaxial stress and neglecting Poisson effects on the through-thickness of the bar. The forces acting on the faces of the differential element may then be expressed using Equation A.1 and Figure A.2 may now be updated to show that change.



Figure A.3: Differential element in tension with expressible forces acting on the opposite faces.

If these forces are then summed in accordance with Newton's second law of motion, $F = ma$, or in this case, $F = m\ddot{x}$, an expression may be written describing both the forces acting on the faces of this differential element with respect to the acceleration therein.

$$A_B E \frac{\partial u_1}{\partial x} - A_B E \frac{\partial u_2}{\partial x} = A_B dx \rho \frac{d^2 u}{dt^2} \tag{A.2}$$

This new expression assumes that the acceleration across the differential element is constant. If the sound speed of the material may be expressed as,

$$C_B = \sqrt{\frac{E}{\rho}} \tag{A.3}$$

where E is modulus of elasticity of the bar material and ρ is the material density of the bar material, Equation A.2 may be rewritten as,

$$C_B{}^2\left[\frac{\partial u_1}{\partial x}-\frac{\partial u_2}{\partial x}\right]=\frac{\partial^2 u}{\partial t^2}dx \tag{A.4}$$

A more recognizable form of the above expression may be written if the displacement at one end of the differential element is written in terms of the other,

$$u_2=u_1+\frac{\partial u_1}{dx}dx \tag{A.5}$$

This expression assumes that the rates of change in displacement of the two sides of the differential element are equal – a reasonable assumption. This expression may then be differentiated and substituted into Equation A.4 to take the form of,

$$C_B{}^2\frac{\partial^2 u_1}{\partial x^2}=\frac{\partial^2 u}{\partial t^2} \tag{A.5}$$

At this point we have arrived at the partial differential wave equation. While this expression may not have any application in practical terms of SHTB operation and data reduction, it will be relevant to later calculating strain and strain rate within the specimen.

For harmonic waves the term describing $\frac{\partial^2 u_1}{\partial t^2}$ may also be expressed as $\frac{\partial v}{\partial t}$, where v is the particle velocity. Additionally, the pressure across the cross-section of the differential element may be expressed as

$$E\frac{\partial}{\partial x}\left(\frac{\partial u_1}{\partial x}\right)=\frac{\partial p}{\partial x} \tag{A.6}$$

where p is the pressure across the cross-section. The equation of motion can now be rewritten by combining these two previous expressions

$$-\frac{\partial p(x,t)}{\partial x} = \rho \frac{\partial v}{\partial t} \tag{A.7}$$

A solution to this equation takes the form of a positive traveling harmonic wave described by

$$p(x,t) = Pe^{i(\omega t - kx)} \tag{A.8}$$

where P is the amplitude of the pressure, ω is the frequency, t is time, k is the wave number ($k = \frac{\omega}{C_B}$), and x is the spatial location of the wave. Using this expression in Equation A.7, particle velocity may be expressed as

$$v(x,t) = \frac{1}{\rho C_B} Pe^{i(\omega t - kx)} \tag{A.9}$$

As the bar is effectively under a state of uniaxial stress, Hook's Law may be used to relate the pressure as a stress with its strain.

$$p(x,t) = \varepsilon(x,t)E \tag{A.10}$$

When Equation A.10 is substituted into Equation A.9, the particle velocity within the bar may be expressed in terms of its strain.

$$v(x,t) = C_B \varepsilon(x,t) \tag{A.11}$$

Strain rate within the specimen may be determined by evaluating the velocities of the two bar-ends relative to each other. The average strain rate at a give time, *t*, is determined by the following

$$\frac{d\varepsilon}{dt} = \frac{v_1 - v_2}{L} \tag{A.12}$$

where the subscripts 1 and 2 for the velocity terms indicate the interfaces by which the specimen is attached to the bar. If we remember that the velocity of the first interface (where the travelling wave first interacts with the specimen from the bar commonly referred to as the incident bar) is determined by the sum of the incident and reflected waves, the velocity at that end may be expressed as

$$v_1 = C_B\varepsilon_I - C_B\varepsilon_R \tag{A.13}$$

The velocity of the second interface, v_2, requires knowledge of only the transmitted wave. The transmitted wave has a direction that is the same sign as the incident wave and may therefore be expressed as

$$v_2 = C_B\varepsilon_T \tag{A.14}$$

Substituting equations A.13 and A.14 into A.12 gives the expression for the strain rate of the specimen in terms of the strains as measured in the two bars attached at the specimen's two ends.

$$\frac{d\varepsilon}{dt} = \frac{C_B}{L}\left(\varepsilon_T - \varepsilon_I + \varepsilon_R\right) \tag{A.15}$$

Under the assumption that uniform deformation occurs in the specimen, the sum of the strains to the incident and reflected waves should equal the strain of the transmitted wave.

$$\varepsilon_I + \varepsilon_R = \varepsilon_T \tag{A.16}$$

The final equation that may be used to determine the strain rate of the specimen can be expressed entirely in terms of the transmitted wave.

$$\frac{d\varepsilon_S}{dt} = \frac{2C_B}{L}\varepsilon_R \tag{A.17}$$

where L is the gauge length of the specimen.

Integrating strain rate over the duration of the tensile test gives the resultant strain of the specimen.

$$\varepsilon_S = \frac{2C_B}{L}\int \varepsilon_R \, dt \tag{A.18}$$

If we remember to use Equation A.16, the same expression may be evaluated in terms of the incident and transmitted waves. This permits flexibility in choosing between the different signals to arrive at the final calculation.

Appendix B

Development of Selective Laser Melting Materials Processing

Introduction and Parameter Variation

It is not uncommon for processing parameters of AM equipment to be held as proprietary information by companies who regularly rely on the technology. As a consequence of this, a duplication of research efforts for these optimized processing parameters is typically required before attempting to build functional hardware or bulk material. Because research into the controllability of microstructures via SLM is still in its early stages of research and development, the "optimization" of processing parameters is usually in reference to attaining the highest relative density compared to what is considered 100% dense material, minimizing embedded porosity to the greatest extent possible. While this effort is not directly related with the evaluation of the mechanical properties, understanding how and why the machine parameters were selected is important. This section will detail that effort as conducted for the powdered 17-4 PH previously described.

Initial bulk material fabrication efforts were conducted at JMP, a private operator of various AM machines located in Takatsuki City, Osaka Prefecture, Japan. The supplier provided some guidance as to the recommended operational parameters that could potentially result in high-density material. However, neither the researchers nor the technicians at JMP had previous experience at SLM processing of 17-4 PH from the material supplier provided. It was therefore necessary to perform a development study to identify these idealized conditions. This investigation involved producing test samples across a matrix of processing parameters and measuring resultant density. As a result of this activity, the future machine settings would be determined.

The primary focus of this study was on powder consolidation and its correlation with the achievable bulk material density against theoretically attainable values. The machine available for use at JMP was a LaserCusing M2 by Concept Laser (GmbH, Germany). Without any additional modifications made to the working material, the operational parameters available for adjustment within the SLM machine were the laser power, laser scanning speed, laser scanning pattern, layer thickness, laser spot diameter, and operational environment (gaseous). All of these were discussed in previously discussed in Chapter 5. However, for the purpose of minimizing the range of variables to

adjust (and as a matter of limited investigation time), the development work focused on adjusting only the laser scanning speed and the laser power.

To work towards the goal of maximum achievable density, thirty-five cubic primitives were designed using Pro/Engineer CAD software. Each specimen was identical except for a positive relief added to the upper-most surface where a letter-based identification tag was built as part of the SLM process. The dimensions of each specimen were 15 mm square in-plane to SLM layers and 17 mm in the vertical building direction. The additional 2 mm added to the height was done for the purpose of ensuring sufficient excess stock. The excess height is sacrificed during the mechanical removal of the samples from the build plate (typically by electro discharge machining). Table B.1 outlines the laser scanning speed and laser power combination settings investigated. For power, the settings chosen were 170, 185, 190, 195, and 200 Watts. For the scanning speed, 500, 550, 600, 650, 700, 750, and 800 mm/s were selected. Figure X depicts the technical drawing of the cubic primitive layout atop the build plate used during fabrication.

Table B.1: SLM processing parameter combinations

Testing Condition Identifier	Laser Scan Rate (mm/s)	Laser Power (Watts)
A	500	170
B	550	170
C	600	170
D	650	170
E	700	170
F	750	170
G	800	170
H	500	185
J	550	185
K	600	185
L	650	185
M	700	185
N	750	185
P	800	190
R	500	190

S	550	190
T	600	190
U	650	190
V	700	190
W	750	190
X	800	190
Y	500	195
Z	550	195
AA	600	195
AB	650	195
AC	700	195
AD	750	195
AE	800	195
AF	500	200
AG	550	200
AH	600	200
AJ	650	200
AK	700	200
AL	750	200
AM	800	200

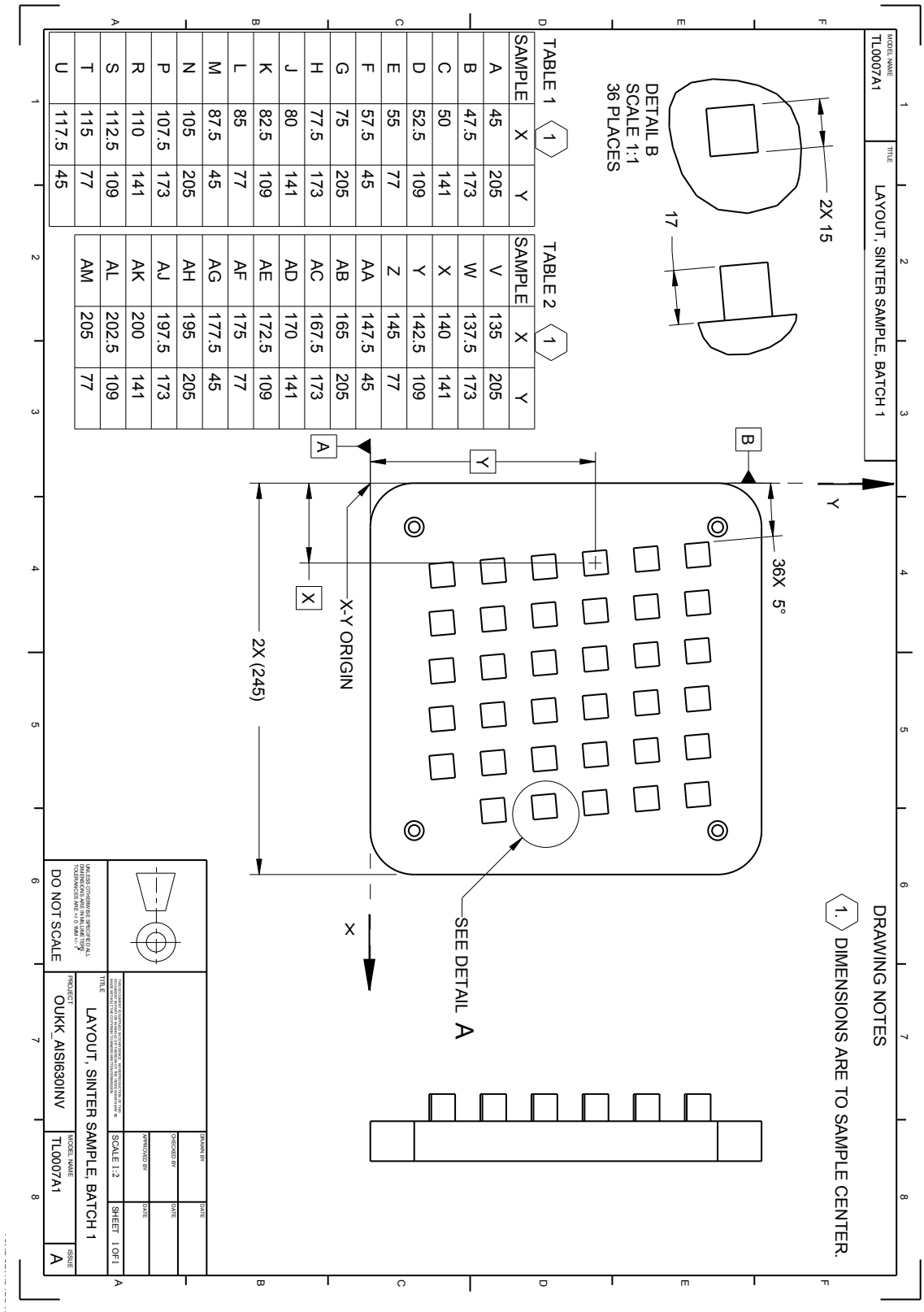


Figure B.1: Technical layout of the settings and the cubic primitives for the initial consolidation study.

Regarding the other machine settings, based on advisement from the technicians' operational experience at JMP, a layer thickness of 30 μm was used. The laser spot diameter was fixed at 150 μm in diameter and operated in

continuous mode (not pulsed or power intensity variant). The scanning pattern deployed was the checkerboard pattern, the same as described in the Chapter 5 on for Batch One.

The thirty-five specimens were arranged in a six-by-six grid pattern with one position in this grid pattern empty. Each specimen was a unique combination of two machine operational settings: laser power and scanning velocity. Two of the most commonly investigated machine settings that affect the melting performance were targeted as part of this initial study [3,59,61,93].

It should be noted that the individual samples were rotated counter clockwise five degrees about the upper-left-most corner of each specimen. Also, each specimen in-line in the columnar-direction was offset by 2 mm in one direction from this pivot point. The offset stacked such that the sixth sample in the columnar-direction was offset a total of 10 mm from the same point of the first in the same column. These two adjustments to the layout were done at the advisement of the machine operators so as to minimize the length of simultaneous contact by the powder distribution mechanism (wiper blade) when traversing a freshly melted and solidified laser surface. The intended goal of this placement was to maximize the proper distribution of powder.

Unlike many commercial AM machines, the M2 has the operational capability of changing the laser settings from part to part in the same build operation. Therefore, the fabrication of all thirty-five samples with different machine settings was possible in the same build operation. Older, commercial variants on the technology would require all samples to be fabricated with the same machine settings during one build operation from start to finish.

Technical Difficulties

The M2 machine has the option of using either a rubber or steel wiper blade for the purpose of applying sequential layers of powder. Both have the accuracy necessary for properly applying each sequential layer of powder at the thickness designated. However, there is an operational difference when defects or irregularities are generated as part of the build process. In the case of the rubber wiper, irregularities that are formed as a part of the laser melting process may protrude above the build volume. Before the start of the next layer, the consolidated material is passed over by the wiper mechanism and a fresh layer is deposited. The effect of the irregularities on the powder laying process has not been investigated thoroughly, but on two occasions during the initial build of

thirty-five specimens the technician stopped the operation. The interruption was necessary to replace the rubber wiper due to mechanical damage. Per the machine operators' prior experience, damage to the wiper is a result of solidified material scratching or scarring the rubber in some way such that the linear edge of the wiper is no longer straight and uninterrupted. The result of which is a linear defect that is generated across the powder in the wiping direction during the laying process. Each sequential layer does fill this linear defect with powder, but the now faulty wiper recreates this linear defect. This prevents the proper laying of an uninterrupted plane of powder for the next layer. As such, the linear defect persists until the wiper is replaced. In the case of a steel wiper blade, the machine stops when it encounters sufficient resistance to the wiping mechanism when a mechanical obstacle impedes its progress. These types of impediments may instead damage a rubber blade. The resulting effect of this linear defect on part density is briefly discussed later in this appendix section.

Density Measurements

Every sample was measured for density using the Archimedes method by the device pictured in Figure B.2. Samples were cleaned in acetone prior to measurement. Each sample was measured for its dry mass in grams (A) and resulting buoyancy force in grams (B) when submerged in distilled water. Buoyancy force was measured using the device shown by first measuring the dry mass, resetting the scale with the sample still present in the dry mass position, and subsequently submerging the mass onto the second measuring tray below the waterline. The recorded value is the force of the displaced water in grams. A negative value will be measured as the dry mass is still accounted in the device setup after resetting the scale. The quotient of these two measured values was adjusted for the density of pure water at the temperature measured. The apparatus used to perform these measurements is show in Figure B.2. The equation used to calculate the density is shown below:

$$\rho_{sample} = \frac{A}{|B|} \times \rho_{water} \tag{B.1}$$

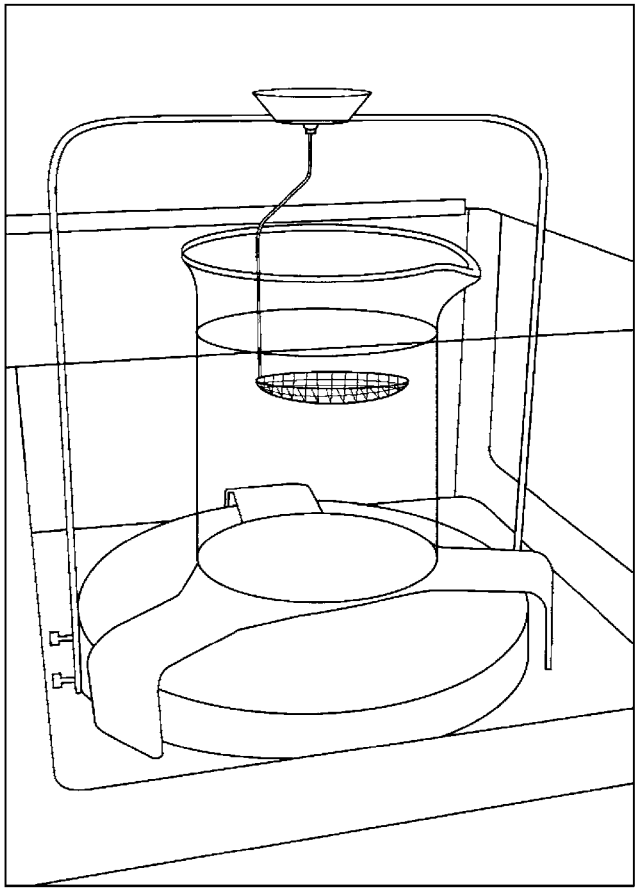


Figure B.2: Archimedes measurement tool [5]

The results of these measurements are shown in Table B.2 as a relative density (unity is 100% dense). The reference density for this material is 7.8 grams per cubic centimeter. When displayed graphically, the fractional density values are more easily understood. As shown in Figure B.3, the densities are plotted as a function of laser power and grouped according to scanning speed. It should be noted that those samples affected by the linear defect described in Technical Difficulties are plotted with hollow dots for reference.

Table B.2: Relative density of processed specimens

	170 (W)	185	190	195	200
500 (mm/sec)	0.9901	0.9916	0.9923	0.9946	0.9901
550	0.9946	0.9927	0.9922	0.9889	0.9917
600	0.9897	0.9904	0.9917	0.9907	0.9934
650	0.9890	0.9901	0.9876	0.9935	0.9884
700	0.9825	0.9822	0.9947	0.9926	0.9934
750	0.9785	0.9937	0.9944	0.9946	0.9928
800	0.9895	0.9911	0.9929	0.9933	0.9913

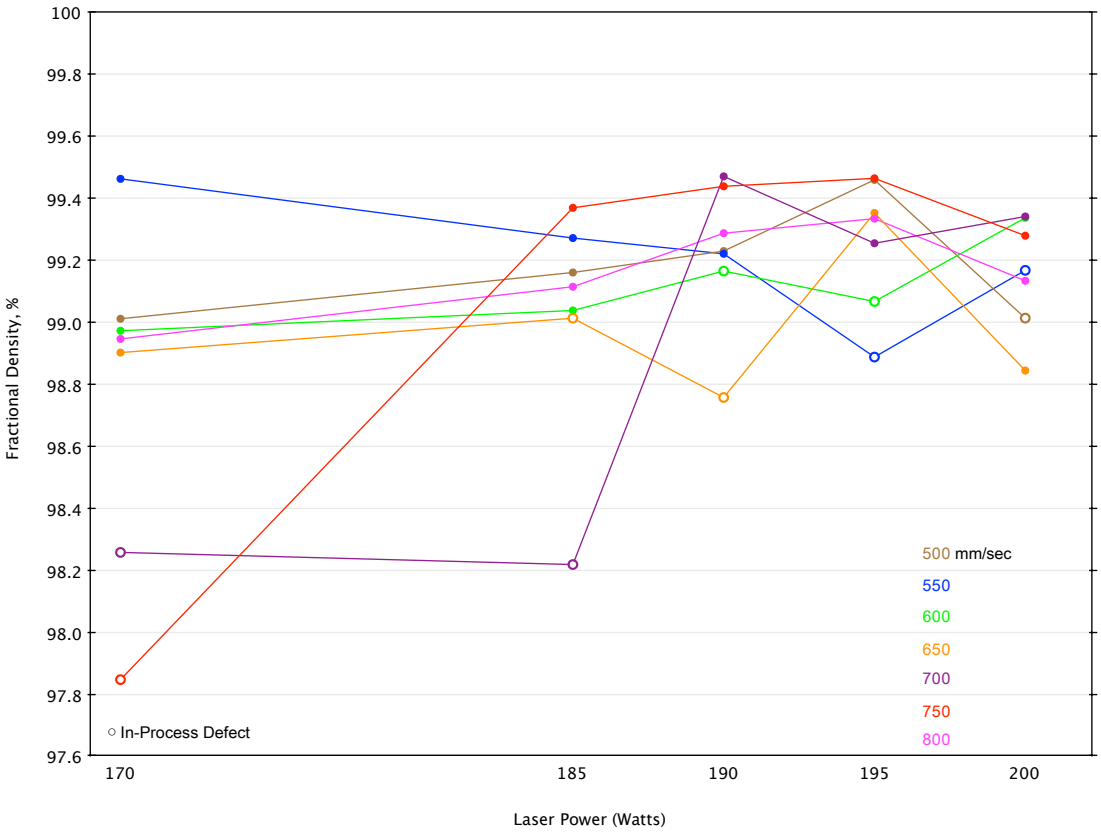


Figure B.3: Fractional density with respect to laser power. Trend lines grouped according to laser scanning speed.

Figure B.4 plots the same density data, but against the scanning speed and group by laser power, yields a slightly different interpretation. There is no relationship between color schemes from these two figures.

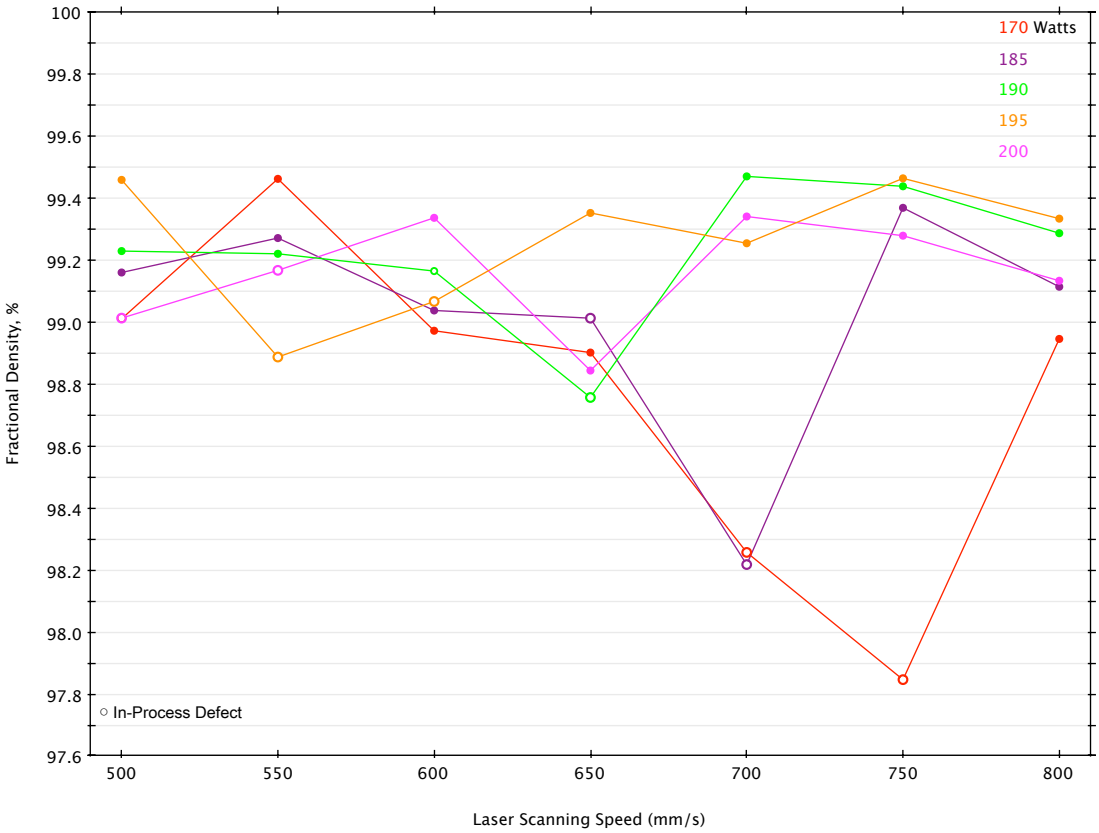


Figure B.4: Fractional density plotted with respect to scanning speed. Trend lines grouped according to laser power.

These plots are not very useful without some additional clarity. As a result of the defects generated by the previously described wiper damage in Section B.2, several densities were viewed as anomalous. The surface texture of these specimens obviously indicated improper consolidation due to poor powder distribution. When these defected samples are removed from the previous two plots, the same data has much more congruency. Figures B.5 and B.6 show the same information as plotted previously, but with the specimens containing build faults removed from the dataset.

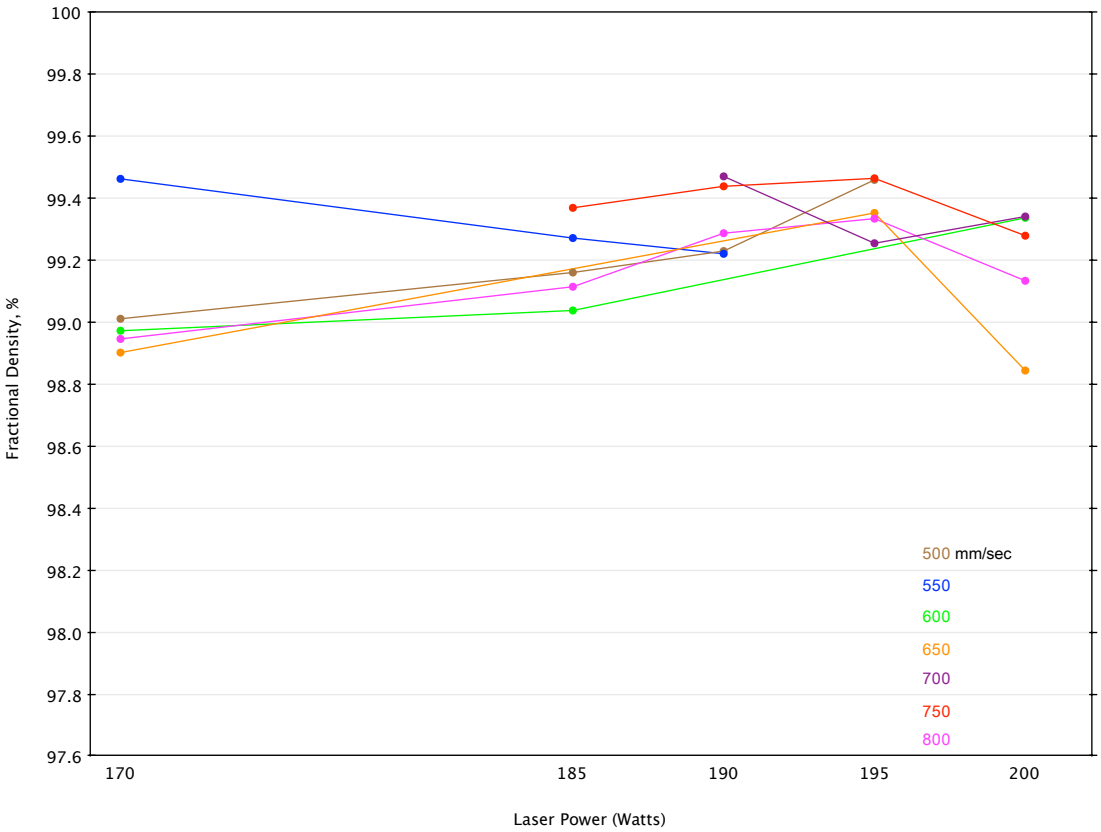


Figure B.5: Fractional density with respect to laser scanning power. Defected specimens have been removed. Trend lines grouped by laser scanning velocity.

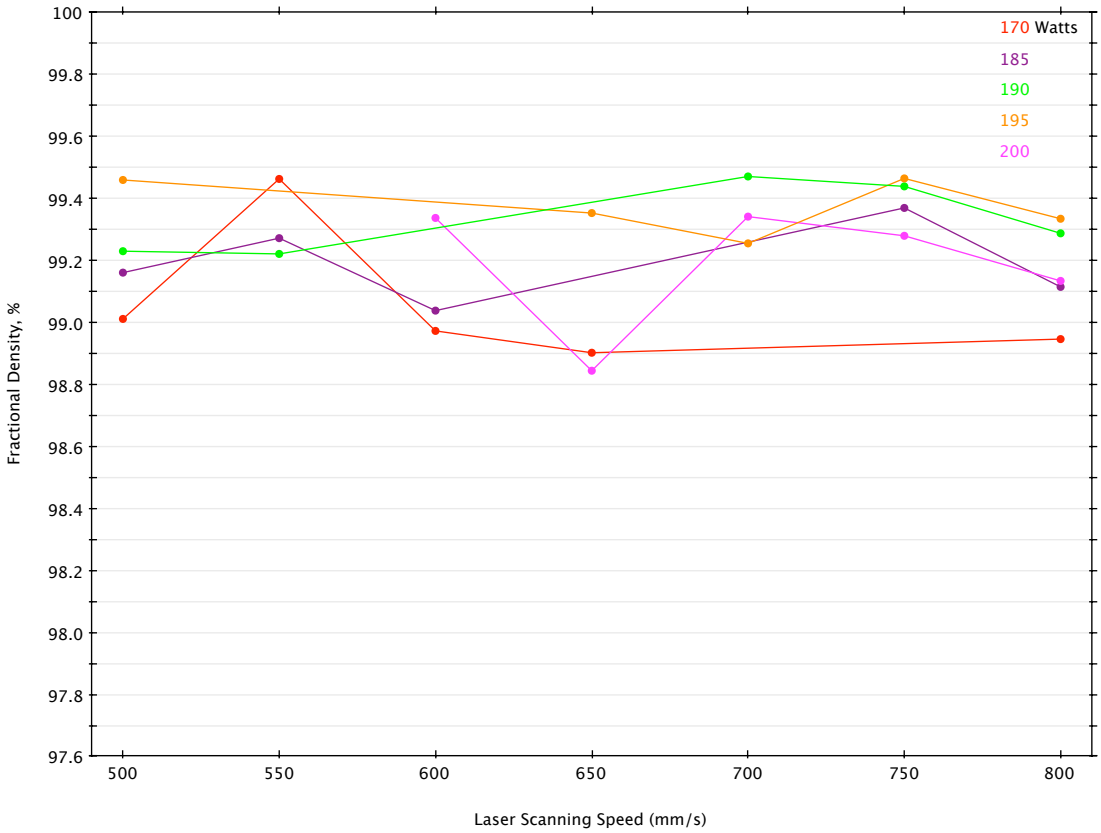


Figure B.6: Fractional density with respect to laser scanning speed. Defected specimens have been removed. Trend lines grouped by laser power.

Based on the recorded density measurements, the data suggests little variability between the samples across the parameter ranges tested. This is especially true when examined in light of the limited number of samples taken at each SLM machine combination. When defected samples are excluded, the total range in variation of density does not exceed 0.7%. This is hardly enough to establish a trend amidst the statistical limitations of a small sample size.

On its own, the data identifies one key piece of information: using this particular powder morphology and chemistry, under the combination of settings chosen for the SLM machine, consolidation performance is exceptionally good. Unfortunately, it is not possible to make very informed predictive conclusions based on this data. How this particular powder will behave at other machine settings outside the envelope previously tested cannot be determined based on this data alone. Therefore, when plotted against data from other researchers, new insights can be made. Simchi examined the role of powder size and composition on the achievable density across a range of SLM machine settings using iron-based powders [59]. This is very similar to the work already presented here. That particular study also processed the data into two additional

quantifiers to better understand the roll and influence of laser power and scanning speed towards measuring the laser melting performance: linear and volumetric density. In the case of linear energy density, laser power is simply normalized against scanning speed and plotted against fractional density, *P/v*.

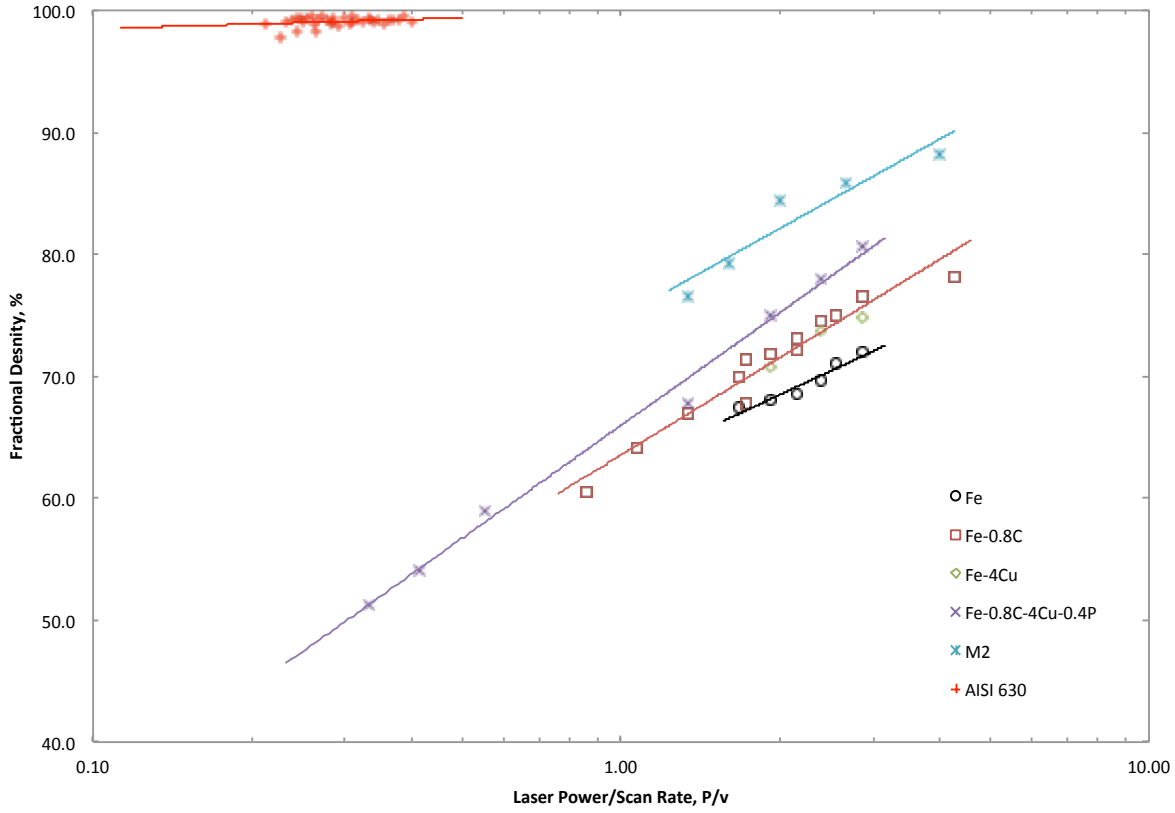


Figure B.7: Laser Power/Scanning Speed plotted against fractional density for a variety of materials and those of this study. This material is identified as AISI 630 in the legend. Source of additional data [2].

The data provided by Simchi would be highly suggestive of increasing fractional density with increasing laser power/scan rate ratio. However, with the addition of the AISI 630 data, that trend would appear to be less certain for more alloyed materials. However, when examining the same experimental data, but taking into account for the volume of the working material, it becomes clear that volumetric energy density is a fairer representation and predictor of laser melting performance.

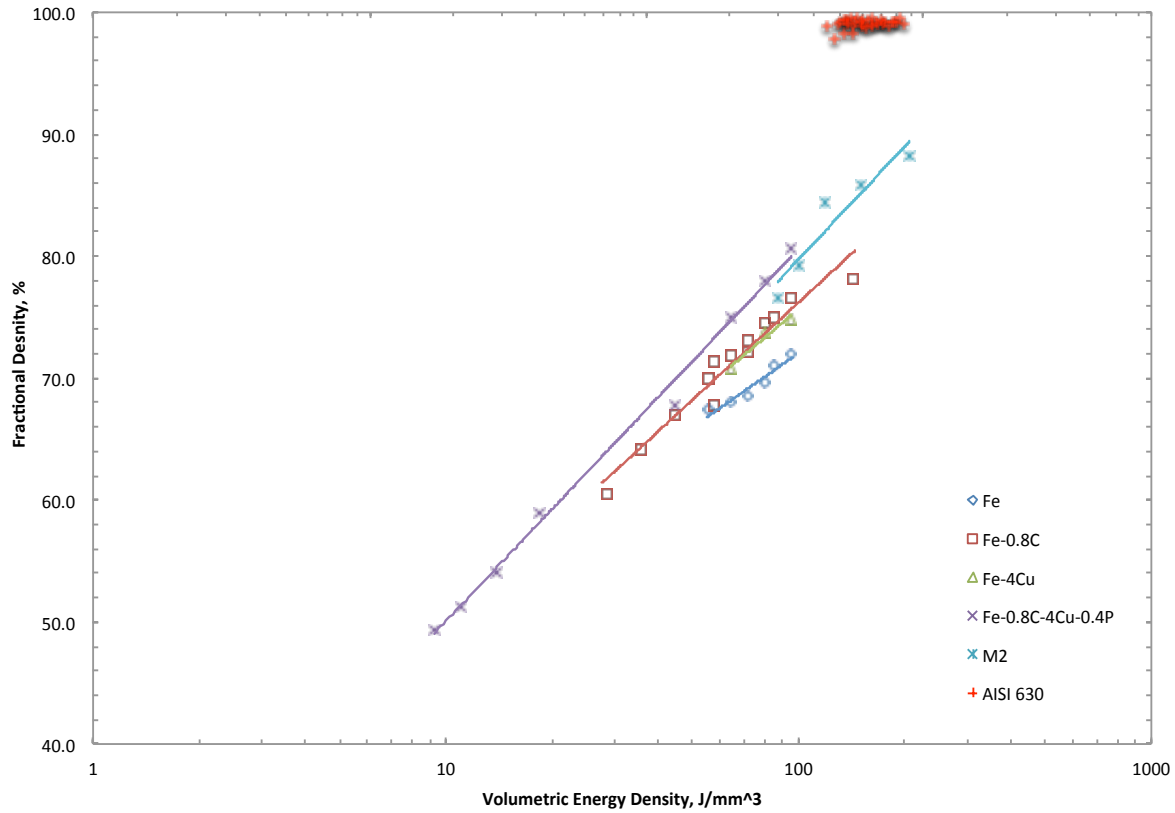


Figure B.8: Volumetric energy density plotted against fractional density for a variety of materials and those of this study. This material is identified as AISI 630 in the legend. Source of additional data [2].

B.4 Discussion on Volumetric Energy Density

At every layer processed by the SLM machine, a discrete volume of material is targeted for complete melting. The energy requirements for that phase change should dictate and properly predict the necessary settings for processing. Such parameters as layer thickness, powder density (at the consequence of morphology), laser scanning speed, and laser power, work to achieve that target of complete melting and binding. Additionally, understanding the energy requirements for re-melt into previously processed layers should be accounted for. The difficult balance of achieving sufficient energy density without exceeding the limits of vaporization, challenges material processing by SLM and is the subject of many research efforts.

Linear energy density can be a good predictor of the melting performance of single laser tracks through powder beds [95,96]. However, the process of consolidating and constructing full geometries of material requires a volumetric approach. The following derivation describes the volumetric energy density on a per layer basis.

Surface energy density can be described firstly as a laser spot over a discrete area of the powder bed

$$\rho_E = \frac{P}{A} \tag{B.2}$$

The area in this case can be described as the total irradiated area by the laser. To characterize that, first the surface area of the laser spot

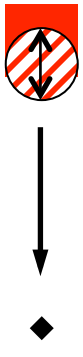
$$\pi r^2 = A \tag{B.3}$$

And with respect to the laser diameter

$$A = \pi \frac{d^2}{4} \tag{B.4}$$

This is not the area characteristic of the surface energy density, but just the laser spot size. The surface energy density is the amount of exposure any one particular point will see from this spot size. The laser spot will traverse any one spot on the surface of the powder bed over a calculated time

$$t = \frac{d}{v} \tag{B.5}$$



Distance of exposure across laser spot diameter

Direction of travel by laser spot

Arbitrary point on powder bed surface to be exposed

An additional, dimensionless term for laser scan overlap must be introduced, where *h* is the scan line spacing distance, center to center:

$$Overlap = \frac{d}{h}$$

(B.6)

The surface energy density can then be shown as

$$\left(\frac{4P}{\pi d^2}\right)\left(\frac{d}{v}\right)\left(\frac{d}{h}\right) = \rho_{SE} \tag{B.7}$$

This reduces to

$$\frac{4P}{\pi hv} = \rho_{SE} \tag{B.8}$$

When divided by the layer thickness, *w*, we arrive at volumetric energy density

$$\frac{4P}{\pi hvw} = \rho_{VE} \tag{B.9}$$

Where *P* is the laser power in Watts, *h* the scan spacing in mm, *v* the scanning velocity, and *w* the layer thickness. This equation gives a volumetric energy density with units of Joules per cubic mm.

In the case of this investigation, the island scanning strategy was utilized in Batch One. For the sake of simplicity, only this scanning strategy will be discussed, but the principles extend to other scanning patterns. Each scanning island can be described as a melting volume unit. Whereas, other linear scanning strategies use scan paths that traverse the entire cross section before returning for another, adjacent pass.[1]

Applying the above energy density calculations and displaying the data in a similar way as Table B.3, we arrive at the following energy densities as inputs into the powder bed:

Table B.3: Volumetric energy input (J/mm^3)

[1] In those cases, the scanning energy must be examined on a per-cross-section basis. This is entirely dependent on the individual cross-section's geometry – a feature that changes throughout the thickness of part geometry. Thermal energy concentration and subsequent dissipation also change based on the shape of the in-work cross-section.

	170 (W)	185	190	195	200
500 mm/sec	137.4	149.6	153.6	157.6	161.7
550	124.9	136.0	139.6	143.3	147.0
600	114.5	124.6	128.0	131.4	134.7
650	105.7	115.0	118.2	121.3	124.4
700	98.2	106.8	109.7	112.6	115.5
750	91.6	99.7	102.4	105.1	107.8
800	85.9	93.5	96.0	98.5	101.1

When examining the individual island unit, a volume of only 0.75 mm^3 is tabulated for the given dimensions and layer thickness of 30 μm. Applying the above densities, the energy per island can be shown in Table B.4.

Table B.4: Volumetric energy densities per individual island (J/mm^3)

	170 (W)	185	190	195	200
500 mm/sec	103.1	93.7	85.9	79.3	73.6
550	112.2	102	93.5	86.3	80.1
600	115.2	104.7	96	88.6	82.3
650	118.2	107.5	98.5	90.9	84.4
700	121.3	110.2	101.1	93.3	86.6
750	103.1	93.7	85.9	79.3	73.6
800	112.2	102	93.5	86.3	80.1

Not all energy that is inputted into the system is properly retained and converted to thermal energy used to raise the temperature of the particles and initiate a phase change. Equation B.10 is therefore modified with a coupling efficiency, η.

$$\eta \frac{4P}{\pi h v w} = \rho_{VE} \tag{B.10}$$

When laser radiation interacts with metal powders, the energy deposition is performed by both bulk-coupling and powder-coupling mechanisms [97]. As previously mentioned, the multiple reflections effect between the powder particles leads to higher optical penetration depths compared to bulk materials. The density change during irradiation and formation of metal agglomerates also affect the coupling efficiency and thus influence the absorbed energy [98]. A coupling efficiency between the directed laser energy attempts to describe the losses associated with reflectance, absorption rates, and other undeterminable losses. Simchi utilized a coupling efficiency of 20% [59]. However, the proper quantization of these losses has yet to be attempted.

Applying the same approximate coupling efficiency of 20% to the previous table yields a striking change to the amount of absorbed and harnessed energy.

Table B.5: Estimated Volumetric Energy Absorption (J/mm^3)

	170 (W)	185	190	195	200
500 mm/sec	20.62	22.44	23.04	23.64	24.26
550	18.74	20.4	20.94	21.5	22.04
600	17.18	18.7	19.2	19.7	20.22
650	15.86	17.26	17.72	18.18	18.66
700	14.72	16.02	16.46	16.88	17.32
750	13.74	14.96	15.36	15.76	16.16

800	12.88	14.02	14.4	14.78	15.16

After estimating the absorbed energy, a rough approximation to the energy necessary to properly melt the powder should be attempted. This approximation can be described as

$$Q = C\Delta T + \Delta H_F \quad \text{(B.11)}$$

Filling in Equation B.11 with some specifics:

Specific heat capacity for solid AISI 630 = 460 J/(g K) (0-100 °C) (decreases with increasing temperature)

Melting temperature for AISI 630 is between 1400-1440 C (1420 average)

Starting, ambient temperature = 20 °C

Using the rule of mixtures, an approximate value for the Heat of Fusion for AISI 630 = 274 J/g

For one layer of solid AISI 630, in a 5 mm x 5 mm x .03 mm island, the required energy to fully melt is ~5.4 J

As previously discussed, because thermal conduction between particles can be ignored, laser energy is not transferred from particle to particle. The heat capacity for the to-be-melted particles remains the same as bulk material. The effective mass of material to be melted is obviously reduced. Because the density of the powder was found to be approximately half of the fully dense material[2], an adjusted mass yields an energy requirement also approximately half the original value, **~ 2.5** Joules per island.

The difference in energy requirements and those inputted into the system have some unintended consequences. Extra energy beyond that required for a solid to liquid phase change can raise the liquid melt pool temperature as high as the vaporization temperature. Figure B.9 shows an example of the vaporization and ejection effect commonly seen inside the build chambers of SLM machines.

[2] The value of the as-delivered powder with its given morphology was measured to be 3.63 g/cm^3. The bulk density for AISI 630 powder is 7.75-7.86 g/cm^3 (depending on temper). The fractional density of the powder under the operational conditions of the SLM machine is approximately 47%.

The process of material ejection and re-deposition on the in-process surface has other deleterious effects on melting performance.

Globular deposits from the ejection phenomena have the potential to interfere with the laser-powder interaction previously discussed. These larger, spherical particles prevent proper penetration of the laser energy. An example of these deposits is shown in a SEM image of the upper surface of a fabricated bulk primitive in Figure B.10.

In addition to the potential for vaporization, higher energy densities than what is immediately necessary to liquefy the as-deposited powder may also be used to re-melt previously consolidated material. This is previously discussed in observations of the height of the last layer relative to the machine setting for layer thickness.

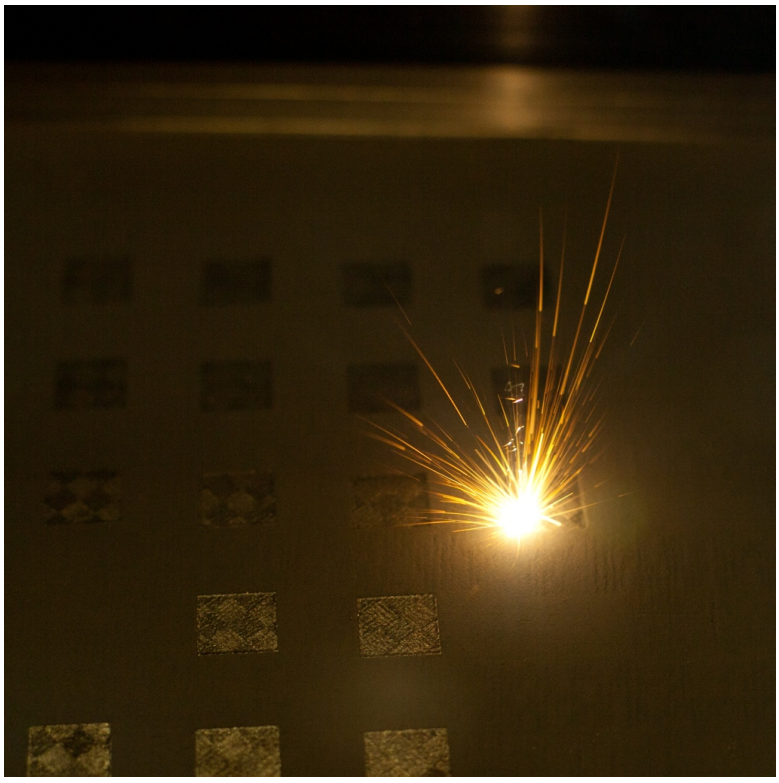


Figure B.9: Ejection of molten material by expanding gas shock

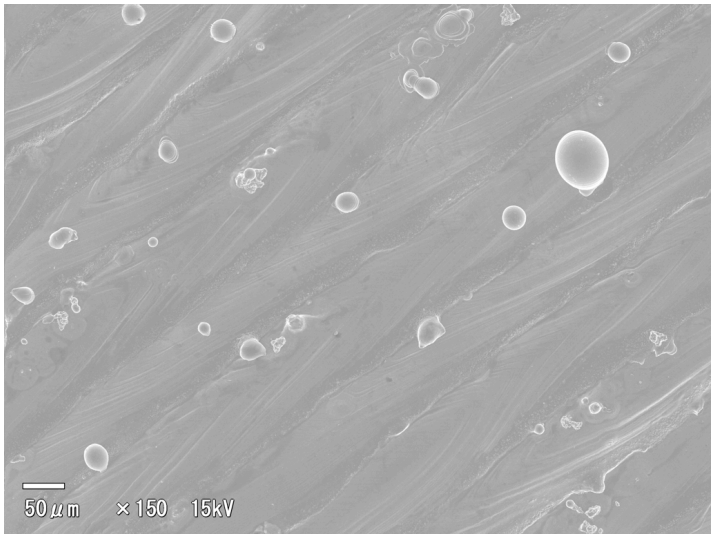


Figure B.10: Molten spheres as deposited onto a processed layer after ejection from a neighboring site on the surface of the SLM build operation.

List of Publications, Conferences, and Awards

Published Publications

1. T. LeBrun, K. Tanigaki, K. Horikawa, H. Kobayashi, “Strain rate sensitivity and mechanical anisotropy of selective laser melted 17-4 PH stainless steel”, *Mechanical Engineering Journal* JSME, 2014, vol. 1 (5), pp.1-13.

Publications Submitted and Under Ongoing Revision and Review

2. T. LeBrun, K. Tanigaki, K. Horikawa, H. Kobayashi, “Micro and Macroscopic Alloy Segregation in Selective Laser Melted 17-4 PH Stainless Steel”, *Metallurgical and Materials Transactions A.*

3. “Effect of Retained Austenite on Subsequent Thermal Processing and Resultant Mechanical Properties of Selective Laser Melted 17-4 PH Stainless Steel”, *Materials & Design*.

Publications Preparing for Submission

4. “Quasi-Static and Dynamic Strain rate sensitivity from retained austenite in 17-4 PH stainless steel processed by selective laser melting”, Expected submission 2015/3

Conference Presentations and Proceedings

1. Presentation on “Microstructural Evolution and Resultant Porosity of Selective Laser Melted of AISI 630 Stainless Steel by Additive Manufacturing”, Japan Institute of Metals, Kanazawa University, 2013 (Oral presentation)

2. Presentation on “Effect of Strain Rate on Mechanical Properties of Additive Manufactured AISI 630 Stainless Steel.” (Oral presentation)

3. Proceeding and Presentation on “Strain Rate Sensitivity And Material Anisotropy Of Additive Manufactured AISI 630 Stainless Steel”, International Conference of Materials and Processing (ICM&P) JSME, Detroit, United States, 2014 (Oral presentation and peer-reviewed conference proceeding)

4. Presentation on “Macroscopic Alloy Segregation Resulting from the Selective Laser Melting of 17-4 PH Stainless Steel”, European Mechanics of Materials 2014, Gothenburg, Sweden (Oral presentation)

Awards

“Certificate of Merit for Young Engineer's Excellent Paper of the Conference”, Awarded by the Materials & Processing Division of the Japan Society of Mechanical Engineers, 2013